

**DEVELOPMENT OF BIOCOMPATIBLE MANGANESE
IRON OXIDE NANOSTRUCTURES FOR
MAGNETICALLY ACTIVATED HYPERTHERMIA
THERAPY**

A THESIS SUBMITTED TO
**D. Y. PATIL EDUCATION SOCIETY
(DEEMED TO BE UNIVERSITY), KOLHAPUR**



FOR THE DEGREE OF
DOCTOR OF PHILOSOPHY
IN
PHYSICS
UNDER THE FACULTY OF
INTERDISCIPLINARY STUDIES
BY

Mr. SATISH SAMBHAJI PHALAKE

M.Sc.

UNDER THE GUIDANCE OF
Dr. VISHWAJEET M. KHOT

M.Sc. PhD.

DEPARTMENT OF MEDICAL PHYSICS,
CENTRE FOR INTERDISCIPLINARY RESEARCH,
D. Y. PATIL EDUCATION SOCIETY (DEEMED TO BE
UNIVERSITY), KOLHAPUR- 416 006, MAHARASHTRA,
(INDIA)

2024

DECLARATION

I hereby declare that the thesis entitled “**Development of biocompatible manganese iron oxide nanostructures for magnetically activated hyperthermia therapy**” submitted for the degree of **Doctor of Philosophy (Ph.D.) in Physics** at **Department of Medical Physics, Centre for Interdisciplinary Research, D. Y. Patil Education Society (Deemed to be University), Kolhapur** is completed and written by **Mr. Satish Sambhaji Phalake**, under the supervision of **Dr. Vishwajeet M. Khot**, has not before made the basis for the award of any degree/diploma/other related heading of this or any other university in India/any other country/examining body to the best of my knowledge. Further, I assert that, I have not dishonored any of the requirements under copyright and piracy/cyber/IPR act amended by UGC from time to time.

Date: 24/10/2024

Place: Kolhapur

Research Student



Mr. Satish Sambhaji Phalake
Department of Medical Physics,
Centre for Interdisciplinary Research,
D. Y. Patil Education Society,
(Deemed to be University),
Kolhapur- 416 006

**D. Y. Patil Education Society (Deemed to be University),
Kolhapur
Centre for Interdisciplinary Research**



Certificate

This is to certify that the thesis entitled “**Development of biocompatible manganese iron oxide nanostructures for magnetically activated hyperthermia therapy**”, which is being submitted here for the award of the degree of **Doctor of Philosophy in Physics** under the faculty of **Interdisciplinary Studies**, at **D. Y. Patil Education Society, (Deemed to be University), Kolhapur** is the result of original Research work completed by **Mr. Satish Sambhaji Phalake** under my supervision and guidance and to the best of my knowledge and belief the work bound in this thesis has not formed earlier the basis for the award of any Degree or similar title of this or any other university or examining body.

Date: 24/10/2024

Place: Kolhapur

Research Guide

Dr. Vishwajeet M. Khot

Associate Professor

Department of Medical Physics,
Centre for Interdisciplinary Research

Dr. Vishwajeet M. Khot

Associate Professor

Department of Medical Physics,
Centre for Interdisciplinary Research,
D.Y.Patil Education Society, Kolhapur.
(Institution Deemed to be University)
Kolhapur-416 006. (India)

Forwarded through,

Prof. C. D. Lokhande

Research Director and Dean,

Centre for Interdisciplinary Research

Research Director

D. Y. Patil Education Society

(Institution Deemed to be University)

869, 'E', Kasaba Bawada

KOLHAPUR- 416006

ACKNOWLEDGEMENT

This was a beautiful journey, a journey of expanding the boundaries of knowledge, a journey of finding your strengths and weaknesses, and a journey of becoming mentally and emotionally strong. It became more beautiful and exciting because of the people I met along the way. I would like to take this opportunity to acknowledge those fascinating people.

*First and foremost, I would like to express my deepest gratitude to my supervisor, **Dr. Vishwajeet M. Khot**, whose expertise, guidance, and unwavering support were invaluable throughout my Ph.D. journey. Your encouragement and insightful feedback have been instrumental in shaping my research and bringing this work to fruition. I am grateful not only for his guidance in the realm of research but also for instilling in me a deep passion for science, thereby illuminating my life path. My association with him for the past few years was a rewarding experience I will cherish all along.*

*I am sincerely thankful to **Prof. C. D. Lokhande**, Dean and Research Director, Centre for Interdisciplinary (CIR) Studies, D. Y. Patil Education Society (Deemed to be University), Kolhapur for the generous support, very fruitful discussions, helpful guidance and constructive compliments.*

*I sincerely thank Vice-Chancellor **Prof. R. K. Mudgal** and Registrar **Dr. V. V. Bhosale** for their inspiration and support. I also express gratitude to **Dr. Jayavanat Gunjekar**, **Dr. Umakant Patil**, **Dr. Sharad Patil**, **Dr. Shivaji Kasthe**, **Dr. K Mayakanana**, **Dr. Ashwini Jadhav**, **Ms. Pooja Patil** and **Dr. Pravin Pawar** for their assistance in analyzing the results with their empathy and cooperative mindset. Also, I am thankful to **Mr. Nirmal Sir**, **Mrs. Namrata Mam**, **Mr. Ramdas sir**, **Mr. Omkar sir** and other staff of the Centre for Interdisciplinary research, D. Y. Patil Education Society, for cooperation in many ways during my Ph.D.*

*I am always grateful to **Dr. Ashwini B. Salunkhe** (Physics department, Rajaram College, Kolhapur), **Dr. Nanasaheb Thorat** (Marie Curie, Visiting Scientist, Department of Oncology; Medical Sciences Division UNIVERSITY OF OXFORD, U.K.) and **Prof. Deepak Dubal** (Queensland University of Technology, Australia) for constantly inspiring, encouraging, and guiding me. Additionally, I acknowledge the contributions of **Prof. Syed A. M. Tofail** (Department of Physics and Bernal Institute, Limerick Digital Cancer Research Centre (LDCRC), University*

of Limerick, Castletroy), and **Dr. Suvra S. Laha** (Research Assistant Professor Clemson University, USA) for providing important sample characterization data throughout my research endeavor. I am thankful to **Dr. Sarita P. Patil**, Head Department of Physics, Sanjay Ghodawat University, Kolhapur, for her good wishes and support.

I would like to thank my colleagues, **Manohar, Sagar and Ketaki** for their assistance and support in my research endeavors. I want to express sincere thanks to my seniors, **Dr. Shrikant, Dr. Shivaji, Dr. Suraj, Dr. Rohini, Dr. Satish, Dr. Sachin, Dr. Dhanaji, Mr. Vikas, Mr. Yogesh, Ms. Sargun, and Ms. Sayali** for their insightful guidance, scientific discussions, and valuable suggestions on the present work. I extend my heartfelt gratitude for always being there for me in every situation and your unwavering support and assistance. I want to acknowledge my colleagues and juniors at the Centre for Interdisciplinary Research, **Sambhaji Khot, Sambhaji Kumbar, Rushiraj, Vinod, Shraddha, Tejaswini, Shahabaj, Anuja, Shivani, Apurva, Ranjit, Sumita, Shivprasad, Ganesh, Prashant, Shweta, Shraddha, Sohel, and Dilip Patil** for their wonderful collaboration. Thanks to **Dr. Mahesh, Dr. Snehal, and Ms. Ashwini** from Shivaji University, Kolhapur, for their help with sample characterizations, insightful guidance and research support.

I am also thankful to D. Y. Patil Education Society (Institution Deemed to be University), Kolhapur for financial support through the research project (sanction no. DYPES/DU/R&D/2021/276). In addition, I acknowledge the funding support from Chhatrapati Shahu Maharaj Research, Training and Human Development Institute (**SARTHI**), Pune Government of Maharashtra State for the SARTHI Junior Research Fellowship (**CSMNJRF-2021**) sanctioned to me (sanction No. CSMNRF-2021/2021-22/896). I would like to acknowledge my friends and well-wishers for their moral support and motivation, which drives me to give my best, the list of friends is endless thanks to one and all. I feel proud to have friends like them. I extend my sincere word of thanks to University academic staff.

My heartfelt appreciation goes to my late father, **Sambhaji**, my mother, **Kalpana**, and my lovely brother, **Anil**, for their continuous support and love. Finally, I thank everyone who made this journey possible and memorable.

~Satish

Place: Kolhapur

SUMMARY OF RESEARCH WORK

Indian Patents (Published) (02)

- 1) Aminated iron oxide nanoparticles for magnetic hyperthermia application
Dr. Vishwajeet M. Khot, **Mr. Satish S. Phalake**, Dr. Ashwini B. Salunkhe
(Application No.: 202321038532)
- 2) A method for the preparation of ascorbic acid functionalized cobalt iron oxide nanoparticles and application thereof
Dr. Vishwajeet M. Khot, Mr. Manohar S. Lad, **Mr. Satish S. Phalake**, Mr. Sagar A. Patil, Ms. Prajakta V. Londhe, Prof. C. D. Lokhande, (Application No.: 202321073714)

Papers Accepted at International Journals (03)

- 1) **S S Phalake**, S B Somvanshi, S A Tofail, N D Thorat, V M Khot. Functionalized manganese iron oxide nanoparticles: a dual potential magneto-chemotherapeutic cargo in a 3D breast cancer model. Nanoscale. 2023; 15 (38):15686-99. **(I.F- 8.3)**.
- 2) **S S Phalake**, M S Lad, K V Kadam, S A Tofail, N D Thorat, V M Khot. Application of $Mn_xFe_{1-x}Fe_2O_4$ ($x = 0 - 1$) nanoparticles in magnetic fluid hyperthermia: correlation with cation distribution and magnetostructural properties. ACS omega. 2022 Nov 22; 7 (48):44187-98. **(I.F- 4.1)**.
- 3) K V Kadam, **S S Phalake**, M S Lad, V G Parale, J L Gunjekar, V M Khot. Low-temperature glycine nitrate combustion synthesis of nanostructured zinc ferrites for enhanced visible-light-driven methylene blue degradation. Emergent Materials. 2024 Mar 18:1-3. **(I.F- 3.8)**.

Book Chapter (01)

- 1) **Satish S. Phalake**, Sayali A. Chougule, Vishwajeet M. Khot, Potential of Polyoxometalate (POMs) in Bio-medicinal Applications, **(Accepted in Book 'Polyoxometalate-based Materials and Applications'- 2024)**

Attended/ Presented, National/International Conference, Workshop and Seminar (10)

- 1) Poster presentation in the 8th Interdisciplinary Symposium on Materials Chemistry (ISMC-2020) June 17-19th, 2021, Bhabha Atomic Research Centre, Mumbai – 400085, INDIA.
- 2) Attend two days of the International Workshop on the Topic "Research Methodology in Drug Discovery and Life-Sciences" organized by the School of Pharmaceutical Sciences, Sanjay Ghodawat University, Kolhapur, on May 7th and 8th, 2021.
- 3) Attending five days of "Hands-on Training Workshop on Basic Techniques in Nanoscience and Nanotechnology" organized by the School of Nanoscience and Technology, Shivaji University, Kolhapur, from the 21st to 25th March 2022.
- 4) Attended One Day "International Symposium: Nanotechnology for healthcare: clinical and industrial perspectives" organized by Nuffield Department of Women's and Reproductive Health, Medical Sciences Division, University of Oxford (U.K.) on 10th June 2022. (Online)
- 5) Attending Seven days "Hands-on Training Workshop on "Advanced Instrumentation Techniques for Material Characterization & Analysis" at the Central Instrumentation Laboratory (CIL) and Department of Physics, Deenbandhu Chhotu Ram University of Science and Technology, Murthal, organized in collaboration with Sophisticated Analytical Instrumentation Facility (SAIF)/Central Instrumentation Laboratory (CIL), Panjab University, Chandigarh scheduled from 12th July to 19th July 2022.
- 6) Attended one day International Conference on "Recent trends in fabrication of nanomaterials and their applications " organized by Rajarshi Chhaatrapati Shahu College, Kolhapur, on 15th March 2023.
- 7) Attended the 7th International Conference on Nanoscience and Nanotechnology (ICONN-2023) organized by SRM Institute of Science and Technology, Kattankulathur, Tamil Nadu, India, on March 27-29, 2023. (Online)
- 8) Paper presentation "National Conference on Physics of Materials and Materials Based Device Fabrication 2023 (NCPM-MDF-2023)" from 25- 26 November 2023, organized by the Department of Physics, Shivaji University, Kolhapur.
- 9) Paper presentation at the "International Conference on Nanotechnology Addressing the Convergence of Materials Science, Biotechnology, and Medical Science (IC-NACMBM-2024)" held at D. Y. Patil Education Society, Kolhapur, from 12th -14th February 2024.
- 10) Poster presentation in the International Conference "International Conference on Advanced Functional Materials and Devices - 2024 (AFMD-2024)" held at Nanotechnology Research Centre (NRC), SRM Institute of Science and Technology (SRMIST), from February 26th -29th, 2024.

CONTENTS

Chapter 1: Introduction

1.1	Introduction	1
1.2	Overview of cancer	4
1.3	Challenges in cancer diagnosis and treatment	7
1.3.1	Early diagnosis	8
1.3.2	Conventional treatments	9
1.4	Cancer nanotechnology	13
1.5	Nanomaterial based cancer treatments	14
1.5.1	Photodynamic therapy	16
1.5.2	Sonodynamic therapy	17
1.5.3	Chemodynamic therapy	19
1.5.4	Hyperthermia therapy	20
1.6	Statement of the problem	21
1.7	References	24

Chapter 2: Theoretical Background of Magnetic Nanoparticles and its Applications

2.1	Introduction	27
2.2	Magnetic nanoparticles in hyperthermia (Literature survey)	29
2.2.1	Types of magnetic nanoparticles	29
2.2.2	Properties of magnetic nanoparticles	30
2.2.3	Iron oxide based magnetic nanoparticles	32
2.2.4	Manganese iron oxide nanoparticles (MnFe_2O_4)	34
2.3	Biomedical applications of magnetic nanoparticles	37
2.3.1	Targeted drug delivery (Magnetically triggered)	38
2.3.2	Magnetic Resonance Imaging	41
2.3.3	Magnetic hyperthermia therapy	43
2.4	Magnetic Hyperthermia Therapy	46
2.4.1	Modes of hyperthermia	46
2.4.2	Heat loss processes in MHT	48
2.4.3	Specific Absorption Rate (SAR)	52
2.4.4	Intrinsic Loss Power (ILP)	52
2.5	Influencing Parameters on SAR	53
2.6	Magnetic Nanoparticles: Toxicity, Biodistribution, Pharmacokinetics	57
2.7	References	60

Chapter 3: Experimental and Characterization Techniques for Magnetic Iron Oxide Nanoparticles

3.1	Introduction	64
3.2	Synthesis of iron oxide nanoparticles	64
3.2.1	Co-precipitation method (Spherical)	64

	3.2.2	Thermal Decomposition method (Nanocubes)	66
3.3		Characterization techniques	69
	3.3.1	X-ray diffractometer	69
	3.3.2	Fourier Transform Infrared Spectroscopy	71
	3.3.3	Thermogravimetric Analysis-Differential Thermal Analysis	74
	3.3.4	Transmission Electron Microscopy	76
	3.3.5	Vibrating Sample Magnetometer	82
	3.3.6	Zeta Potential and Dynamic Light Scattering	84
	3.3.7	UV-Vis Spectroscopy	87
	3.3.8	Fluorescence Microscopy	89
	3.3.9	Confocal microscopy	90
	3.3.10	Flow cytometry	92
	3.3.11	Biocompatibility study: Cytotoxicity assays	94
	3.3.12	Magnetic Induction heating system for hyperthermia	96
3.4		References	99
Chapter 4: Synthesis of Manganese Iron Oxide Nanoparticles			
4.1		Introduction	103
4.2		Synthesis and characterizations of $\text{Mn}_x\text{Fe}_{3-x}\text{O}_4$ ($x = 0$ to 1) MNPs by Co-precipitation method	105
4.3		Results and Discussion	106
	4.3.1	Structural analysis	106
	4.3.2	Morphological Analysis	108
	4.3.3	Thermogravimetric Analysis	112
	4.3.4	Magnetic properties	113
	4.3.5	Cation Distribution	115
	4.3.6	Induction Heating Study	122
4.4		Synthesis and characterizations of $\text{Mn}_x\text{Fe}_{3-x}\text{O}_4$ ($x = 0$ to 1) MNPs by Thermal decomposition method	127
4.5		Results and Discussion	128
	4.5.1	Structural analysis	128
	4.5.2	Morphological Analysis	131
	4.5.3	Thermogravimetric Analysis	132
	4.5.4	Magnetic properties	132
	4.5.6	Induction Heating Study	134
4.6		Conclusion	138
4.7		References	140

Chapter 5:	Surface Functionalization of Optimized Manganese Iron Oxide Nanoparticles by using Chitosan for Hyperthermia Application	
5.1	Introduction	144
5.2	Need of functionalization	145
5.3	Strategies and choice of polymer	146
5.4	Surface functionalization of manganese iron oxide nanoparticles with chitosan	147
5.5	Experimental details	147
5.5.1	Surface modification of MIONPs with chitosan	148
5.5.2	Structural and magnetic characterization	148
5.5.3	Magnetic hyperthermia experiment	148
5.6	Results and discussions	149
5.6.1	Structural analysis	149
5.6.2	Morphological analysis	150
5.6.3	Thermogravimetric analysis	153
5.6.4	Magnetic properties	154
5.6.5	Stability study	155
5.6.6	Induction heating study	156
5.7	Conclusions	159
5.8	References	161
Chapter 6:	Surface Functionalization of Optimized Manganese Iron Oxide Nanoparticles by using m-PEG for Hyperthermia Application	
6.1	Introduction	164
6.2	Need of functionalization	166
6.3	Strategies and choice of polymer	167
6.4	Surface functionalization of manganese iron oxide nanoparticles with m-PEG	168
6.5	Experimental details	168
6.5.1	Surface modification	168
6.5.2	Structural and magnetic characterization	168
6.5.3	Magnetic hyperthermia experiment	168
6.6	Results and discussions	169
6.6.1	Structural analysis	169
6.6.2	Morphological analysis	170
6.6.3	Thermogravimetric analysis	171
6.6.4	Magnetic properties	172
6.6.5	Stability study	175
6.6.6	Induction heating study	175
6.7	Conclusions	178
6.8	References	180

Chapter 7:	<i>In vitro</i> Magnetic Hyperthermia Study of m-PEG and Chitosan Functionalized Manganese Iron Oxide Nanoparticles	
7.1	Introduction	183
7.2	The principles of nanotoxicology	184
7.3	Cytotoxicity	185
7.4	Experimental details for biocompatibility analysis	186
	7.4.1 Hemolysis assay	186
	7.4.2 Reactive oxygen species (ROS) assay	186
	7.4.3 Angiogenesis activity/ in Ovo cytotoxicity assay	187
	7.4.4 MTT assay	187
7.5	Cell culture	188
	7.5.1 Cell viability by MTT assay	188
	7.5.2 Trypan blue dye exclusion	188
	7.5.3 <i>In vitro</i> Anti-cancer activity	188
	7.5.4 <i>In Vitro</i> magnetic hyperthermia Study	189
7.6	Results and discussions	189
	7.6.1 Hemolysis assay	189
	7.6.2 Reactive oxygen species (ROS) assay	192
	7.6.3 Angiogenesis activity/ in Ovo cytotoxicity assay	194
	7.6.4 <i>In vitro</i> cytotoxicity of CS coated manganese iron oxide nanoparticles	196
	7.6.5 <i>In vitro</i> magnetic hyperthermia therapy with m-PEG coated manganese iron oxide nanocubes	197
	7.6.6 <i>in vitro</i> anti-cancer activity of m-PEG manganese iron oxide nanocubes under AC magnetic field	197
7.7	Conclusions	199
7.8	References	200
Chapter 8:	Summary and Conclusions	202
Chapter 9:	80 - Recommendation	208
Publications and Conferences		

List of Figures

Chapter 1 Introduction

- Figure 1.1** Characteristic features of benign tumor and malignant tumor
- Figure 1.2** The projected number of cancer cases in India for 2024, classified by region and cancer type
- Figure 1.3** The projected distribution of cancer cases in India for 2024, classified by cancer type
- Figure 1.4** Schematic illustration of nanotechnology applications in cancer detection and diagnosis
- Figure 1.5** External beam radiation therapy setup
- Figure 1.6** Metallic nanotherapeutic applications in cancer theranostics
- Figure 1.7** Schematic representation of PDT by using MNPs
- Figure 1.8** Illustration of potential SDT mechanisms
- Figure 1.9** Formation of copper peroxide (CP) nanodots for H_2O_2 self-supplying CDT
- Figure 1.10** Schematic illustration of MNP-mediated MHT for tumor cell apoptosis
- Figure 1.11** Specific absorption rates concerning the shape of iron oxide nanoparticles

Chapter 2 Theoretical Background of Magnetic Nanoparticles and its Applications

- Figure 2.1** Various forms of theranostic magnetic nanoparticles, including their modifications and biomedical applications
- Figure 2.2** Schematic representation of magnetic dipole arrangements in various materials, including diamagnetic, paramagnetic, ferromagnetic, ferrimagnetic, and antiferromagnetic substances, both in the absence and presence of an external magnetic field (H).
- Figure 2.3** Crystal structure of spinel ferrite
- Figure 2.4** Structure of manganese ferrite showing tetrahedral (T_d) and octahedral (O_h) sites
- Figure 2.5** Applications of manganese iron oxide nanoparticles in various fields

Figure 2.6	Drug targeting approaches: (a) Passive targeting, (b) Active targeting
Figure 2.7	Hydrogen nuclei (a) magnetic field is absent (b) magnetic field is present
Figure 2.8	Magnetic hyperthermia therapies
Figure 2.9	Different heat generation models in MNPs in response to the AC magnetic field (H)
Figure 2.10	The hysteresis loop of a multi-domain magnetic material
Figure 2.11	Schematics of magnetic easy and hard axes for (a) fcc-Co and (b) hcp-Co crystals
Chapter 3	Experimental and Characterization Techniques for Magnetic Iron Oxide Nanoparticles
Figure 3.1	Schematic representation of co-precipitation method
Figure 3.2	Schematic illustrations for the formation kinetics of iron oxide nanoparticles
Figure 3.3	Schematic diagram of the thermal decomposition method
Figure 3.4	Schematic representation of X-ray diffractometer
Figure 3.5	Basic working principle of the FTIR system
Figure 3.6	TG-DTA measurement unit
Figure 3.7	Schematic representation of TEM
Figure 3.8	Mechanism of X-ray emission in EDS
Figure 3.9	Basic principle of VSM
Figure 3.10	Working Principle of Vibrating Sample Magnetometer Applications
Figure 3.11	Basic working principle of the DLS system
Figure 3.12	Basic working principle of zeta potential system
Figure 3.13	Schematic diagram of UV–Vis–NIR Spectrophotometer
Figure 3.14	A schematic diagram of a wide-field fluorescence microscope
Figure 3.15	A schematic diagram of confocal microscopy
Figure 3.16	A schematic diagram of Flow cytometry
Figure 3.17	Biocompatibility study on L929 mouse fibroblast cell lines

Figure 3.18 Schematic representation of induction heating system

Figure 3.19 Induction heating system instrument

Chapter 4 Experimental and Characterization Techniques for Magnetic Iron Oxide Nanoparticles

Figure 4.1 (a)- XRD patterns for $\text{Mn}_x\text{Fe}_{1-x}\text{Fe}_2\text{O}_4$ ($x = 0.0, 0.25, 0.50, 0.75$, and 1.0) NPs; (b)- Shift view of the region around (311) peak at different Mn^{2+}

Figure 4.2 The variation of $\text{Mn}_x\text{Fe}_{1-x}\text{Fe}_2\text{O}_4$ ($x = 0.0, 0.25, 0.50, 0.75$, and 1.0) NPs with Mn^{2+} content x in terms of their lattice parameter a (nm), crystallite size D_{xrd} (nm), and x-ray density d_x (g/cm^3)

Figure 4.3 Images of (a-b, c, d), (e-f, g, h) and (I, j, k, l) represent TEM Images, SAED patterns and histograms of samples $\text{Mn}_x\text{Fe}_{1-x}\text{Fe}_2\text{O}_4$ at $x = 0, 0.25$ and 0.75 respectively

Figure 4.4 EDX spectra of the $\text{Mn}_x\text{Fe}_{1-x}\text{Fe}_2\text{O}_4$ ($x = 0.0, 0.25, 0.50, 0.75$, and 1.0) along with their respective analyzed results as given in the inset

Figure 4.5 FTIR spectra of $\text{Mn}_x\text{Fe}_{1-x}\text{Fe}_2\text{O}_4$ ($x = 0.0, 0.25, 0.50, 0.75$, and 1.0) NPs

Figure 4.6 Thermogravimetric spectra of MIONPs

Figure 4.7 Magnetization (M) versus field (H) curves of the $\text{Mn}_x\text{Fe}_{1-x}\text{Fe}_2\text{O}_4$ ($x = 0.0, 0.25, 0.50, 0.75$, and 1.0) NPs

Figure 4.8 Strain graph of $\text{Mn}_x\text{Fe}_{1-x}\text{Fe}_2\text{O}_4$ ($x = 0.0, 0.25, 0.50, 0.75$, and 1.0) NPs

Figure 4.9 The growth in temperature versus time for $\text{Mn}_x\text{Fe}_{1-x}\text{Fe}_2\text{O}_4$ ($x = 0.0, 0.25, 0.50, 0.75$, and 1.0) NPs at different concentrations (0.5, 1, 2, 5 and 10 mg/ml) and applied fields 13.3 kA/m to 26.7 kA/m, with constant frequency (≈ 277 kHz)

Figure 4.10 SAR value of the $\text{Mn}_x\text{Fe}_{1-x}\text{Fe}_2\text{O}_4$ ($x = 0.0, 0.25, 0.50, 0.75$, and 1.0) NPs at different concentrations (0.5, 1, 2, 5 and 10 mg/ml) and applied fields 13.3 kA/m to 26.7 kA/m, with constant frequency (≈ 277 kHz)

Figure 4.11 (a) XRD patterns, (b) FTIR spectra of $\text{Mn}_x\text{Fe}_{3-x}\text{O}_4$ ($x = 0.0, 0.25, 0.50, 0.75$, and 1.0) MIONCs

Figure 4.12 The variation of $\text{Mn}_x\text{Fe}_{3-x}\text{O}_4$ ($x = 0.0, 0.25, 0.50, 0.75$, and 1.0) MIONCs with Mn^{2+} content x in terms of their lattice parameter, crystallite size, and x-ray density

- Figure 4.13** (a, b) TEM, (c), HRTEM image, (d), histogram of $\text{Mn}_x\text{Fe}_{3-x}\text{O}_4$ ($x = 1.0$) MIONCs
- Figure 4.14** Thermogravimetric spectra of $\text{Mn}_x\text{Fe}_{3-x}\text{O}_4$ ($x = 1.0$) MIONCs
- Figure 4.15** Magnetization (M) versus field (H) curves of the $\text{Mn}_x\text{Fe}_{3-x}\text{O}_4$ ($x = 0.0, 0.50, \text{ and } 1.0$) MIONCs with an inset image showing the coercivity values
- Figure 4.16** The growth in temperature versus time for samples $\text{Mn}_x\text{Fe}_{3-x}\text{O}_4$ ($x = 0.0, 0.25, 0.50, 0.75, \text{ and } 1.0$) MIONCs at different field amplitudes (≈ 277 kHz)
- Figure 4.17** SAR value of the $\text{Mn}_x\text{Fe}_{3-x}\text{O}_4$ ($x = 0.0, 0.25, 0.50, 0.75, \text{ and } 1.0$) MIONCs at different concentrations (1, 2, and 5 mg/ml) and applied fields 13.3 kA/m to 26.7 kA/m, with constant frequency (≈ 277 kHz)
- Figure 4.18** ILP value of the ($x = 0.0, 0.0, 0.25, 0.50, 0.75, \text{ and } 1.0$) MIONCs at different concentrations (1, 2, and 5 mg/ml) and applied fields 13.3 kA/m to 26.7 kA/m, with constant frequency (≈ 277 kHz)
-
- Chapter 5** **Surface Functionalization of Optimized Manganese Iron Oxide Nanoparticles by using Chitosan for Hyperthermia Application**
- Figure 5.1** Schematic shows the procedure for the synthesis of MIONPs and their surface modification using CS
- Figure 5.2** (a) XRD patterns of bare MIONPs, CS and CS- MIONPs, (b) FT-IR spectra of bare MIONPs, CS and CS- MIONPs
- Figure 5.3** TEM, HRTEM image, SAED patterns and Histogram of bare MIONPs (a, b, c, d) and CS- MIONPs (e, f, g, h)
- Figure 5.4** TEM-EDX chemical mapping of the samples MIONPs and CS-MIONPs
- Figure 5.5** Stoichiometric % concentrations of the constituent elements of the $\text{Mn}_{0.75}\text{Fe}_{0.25}\text{Fe}_2\text{O}_4$ by EDX
- Figure 5.6** Thermogravimetric spectra of (a) uncoated MIONPs and (b) CS-MIONPs
- Figure 5.7** Magnetization (M) versus field curves of the bare MIONPs and CS-MIONPs
- Figure 5.8** (a) Zeta potential studies at various pH of CS-MIONPs, (b, c) Hydrodynamic diameter of MIONPs and CS-MIONPs
- Figure 5.9** Temperature versus time curves for (a) 0.5 mg/mL, (b) 1 mg/mL, (c) 2 mg/mL, (d) 5 mg/mL and (e) 10 mg/mL of MIONPs at the applied field, 13.3 kA/m- 26.6 kA/m

- Figure 5.10** Temperature versus time curves for **(a)** 0.5 mg/mL, **(b)** 1 mg/mL, **(c)** 2 mg/mL, **(d)** 5 mg/mL and **(e)** 10 mg/mL of CS-MIONPs at the applied field, 13.3 kA/m- 26.6 kA/m
- Figure 5.11** The SAR values of bare MIONPs **(a)** and CS-MIONPs **(b)**, the ILP values of bare MIONPs **(c)** and CS-MIONPs **(d)**
- Chapter 6 Surface Functionalization of Optimized Manganese Iron Oxide Nanoparticles by using m-PEG for Hyperthermia Application**
- Figure 6.1** **(a)** XRD patterns of MIONCs NCs, **(b)** FTIR spectra of MIONCs and m-PEG MIONCs
- Figure 6.2** **(a, b)** TEM, **(c)** HRTEM image, **(d)** Histogram **(e)** TEM-EDX chemical mapping of the MIONCs
- Figure 6.3** Thermogravimetric spectra of **(a)** MIONCs and **(b)** m-PEG MIONCs
- Figure 6.4** Magnetization vs applied magnetic field curves of **(a)** MIONCs and **(c)** m-PEG MIONCs samples at 300 K and 10 K **(b, d)** Temperature dependence of the magnetization (ZFC and FC) over the temperature range 0–300 K for **(b)** MIONCs and **(d)** m-PEG MIONCs
- Figure 6.5** Temperature versus time curve of MIONCs **((a)** 1mg/mL, **(b)** 2 mg/mL, **(c)** 5 mg/mL) and m-PEG MIONCs **((d)** 1 mg/mL, **(e)** 2 mg/mL), **(f)** 5mg/mL at field amplitudes 13.3 to 26.7 kA/m and frequency ≈ 277 kHz.
- Figure 6.6** SAR vs applied magnetic field for **(a)** MIONCs and **(b)** m-PEG MIONCs, the ILP values of bare MIONCs **(c)** and m-PEG -MIONCs **(d)**
- Chapter 7 *In vitro* Magnetic Hyperthermia Study of m-PEG and Chitosan Functionalized Manganese Iron Oxide Nanoparticles**
- Figure 7.1** Physicochemical characteristics of engineered nanomaterials that contribute to nanotoxicity
- Figure 7.2** The concentration Vs. the absorbance of **(a)** MIONPs **(c)** CS-MIONPs, Percentage of hemolysis Vs concentration of **(b)** MIONPs **(d)** CS-MIONPs
- Figure 7.3** The concentration Vs. the absorbance of **(a)** m-PEG MIONCs, **(c)** MIONCs, and the percentage of hemolysis Vs concentration of **(b)** m-PEG MIONCs, **(d)** MIONCs

- Figure 7.4** Shows the ROS determination of MIONPs and CS-MIONPs samples at a concentration of 30 mg in gram-positive and gram-negative bacteria in **a)** *E. coli* and **b)** *S. aureus*
- Figure 7.5** Shows the ROS determination of MIONCs and m-PEG MIONPs samples at a concentration of 30 mg in gram-positive and gram-negative bacteria in **a)** *E. coli* and **b)** *S. aureus*.
- Figure 7.6** Angiogenesis analysis of MIONPs and CS-MIONPs and histological analysis of CAM using H&E staining
- Figure 7.7** Angiogenesis analysis m-PEG MIONCs and MIONCs and histological analysis of CAM using H&E staining
- Figure 7.8** Concentration-dependent anti-cancer activity of **(a)** CS-MIONPs, **(b)** m-PEG MIONCs conjugated nanoformulations on MCF7 cells for 24h and 48h
- Figure 7.9** **(a)** The cytotoxicity of m-PEG MIONCs in Control, MIONCs, and m-PEG MIONCs with and without AMF, **(b)** Time dependent Cytotoxicity effects of m-PEG MIONCs

List of Tables

- Chapter 2 Theoretical Background of Magnetic Nanoparticles and its Applications**
- Table 2.1** Literature survey on MNPs used for hyperthermia application
-
- Chapter 4 Synthesis of Manganese Iron Oxide Nanoparticles**
- Table 4.1** Lattice constant (a), Average crystallite size by XRD (D_{xrd}) and TEM (D_{TEM}), X-ray density (dx), specific surface area (S) of $Mn_xFe_{1-x}Fe_2O_4$ NPs ($x = 0.0, 0.25, 0.50, 0.75, \text{ and } 1.0$)
- Table 4.2** Stoichiometric % concentration of the constituent elements of the $Mn_xFe_{1-x}Fe_2O_4$ ($x = 0.0, 0.25, 0.50, 0.75, \text{ and } 1.0$) NPs by EDX
- Table 4.3** Tetrahedral band (ν_1), the octahedral band (ν_2), force constants (f_T and f_O) of $Mn_xFe_{1-x}Fe_2O_4$ ($x = 0.0, 0.25, 0.50, 0.75, \text{ and } 1.0$) NPs
- Table 4.4** Magnetization (M_s), remanence (M_r) and remanence ratio (M_r/M_s), magnetic moment (n_B) of the $Mn_xFe_{1-x}Fe_2O_4$ ($x = 0.0, 0.25, 0.50, 0.75, \text{ and } 1.0$) NPs
- Table 4.5** Distribution of cations among A- and B-sites

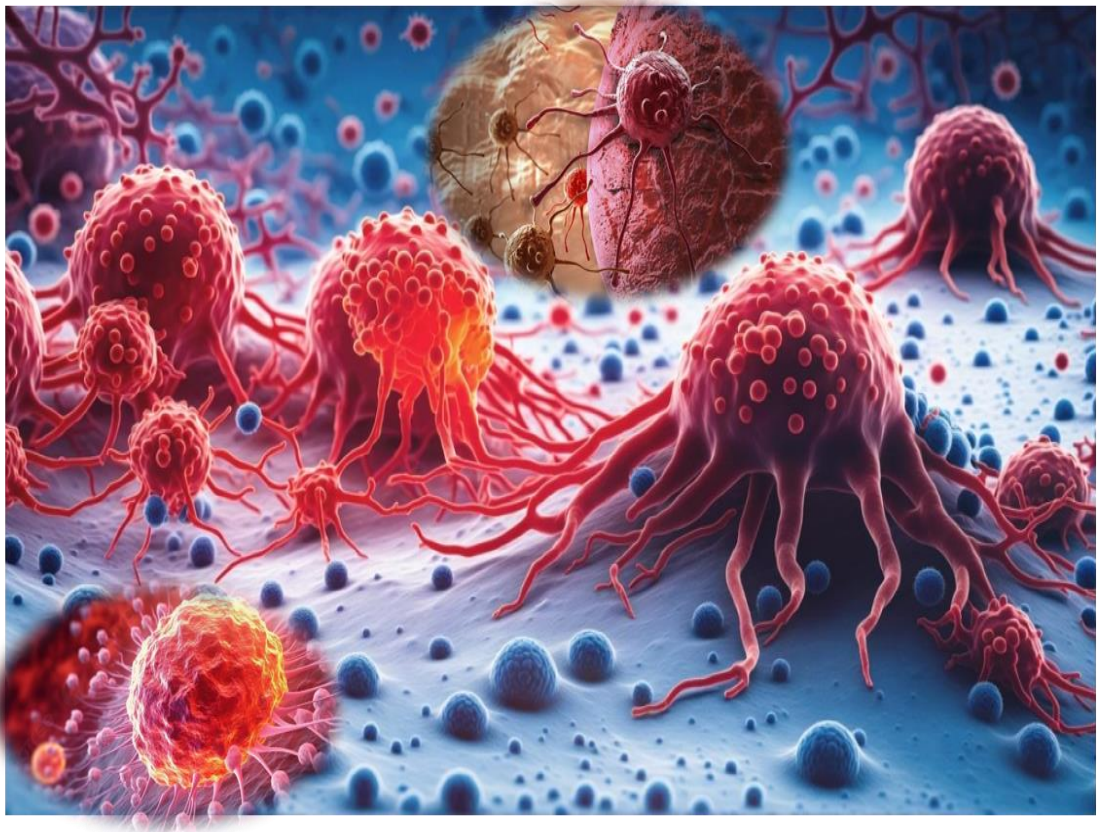
Table 4.6	Hopping length (L_A) and (L_B), tetrahedral bond length (d_{Ax}), octahedral bond length (d_{Bx}), tetrahedral edge (d_{AxE}), shared (d_{BxE}) and unshared (d_{BxEu}) octahedral edges as a function of x for $Mn_xFe_{1-x}Fe_2O_4$ ($x = 0.0, 0.25, 0.50, 0.75$, and 1.0) NPs
Table 4.7	Calculation of distances between cations and anions and between cations and cations for $Mn_xFe_{1-x}Fe_2O_4$ ($x = 0.0, 0.25, 0.50, 0.75$, and 1.0) nanocrystals
Table 4.8	Calculated values of hopping lengths and inter-ionic bond angles for $Mn_xFe_{1-x}Fe_2O_4$ ($x = 0.0, 0.25, 0.50, 0.75$, and 1.0) nanocrystals
Table 4.9	SAR and ILP values of $Mn_xFe_{1-x}Fe_2O_4$ ($x = 0.0, 0.25, 0.50, 0.75$, and 1.0) NPs with an increase in amplitudes from 13.3 kA/m to 26.7 kA/m for $0.5, 1, 2, 5$ and 10 mg/ml respectively
Table 4.10	Tetrahedral band (ν_1), the octahedral band (ν_2), force constants (f_T and f_O) of $Mn_xFe_{3-x}O_4$ ($x = 0.0, 0.25, 0.50, 0.75$, and 1.0) MIONCs
Table 4.11	Summary of Saturation Magnetization (M_s), Remanence magnetization (M_r), Coercivity (H_c), Reduced Remanence (M_r/M_s), and Magnetic Moment (η_B) of the $Mn_xFe_{3-x}O_4$ ($x = 0.0, 0.50$, and 1.0) MIONCs
Table 4.12	SAR and ILP values of $Mn_xFe_{3-x}O_4$ ($x = 0.0, 0.25, 0.50, 0.75$, and 1.0) MIONCs with an increase in amplitudes from 13.3 kA/m to 26.7 kA/m for $1, 2$, and 5 mg/ml respectively
Chapter 5	Surface Functionalization of Optimized Manganese Iron Oxide Nanoparticles by using Chitosan for Hyperthermia Application
Table 5.1	Stoichiometric percentage of the constituent elements of the $Mn_{0.75}Fe_{0.25}Fe_2O_4$ by EDX
Chapter 6	Surface Functionalization of Optimized Manganese Iron Oxide Nanoparticles by using m-PEG for Hyperthermia Application
Table 6.1	Summary of Saturation Magnetization (M_s), Coercivity (H_c), Reduced Remanence (M_r/M_s), Magnetic Moment (η_B), effective magnetic anisotropy constant (K_{eff}) obtained from the Hysteresis Loops at 300 and 10 K
Chapter 7	<i>In vitro</i> Magnetic Hyperthermia Study of m-PEG And Chitosan Functionalized Manganese Iron Oxide Nanoparticles
Table 7.1	Hemolytic efficiency of MIONPs, CS-MIONPs, MIONCs and m-PEG MIONCs

LIST OF ABBREVIATIONS

A.C.	Alternating Current	MNPs	Magnetic nanoparticles
AMF	Alternative Magnetic Field	m-PEG	Methoxy- Polyethylene glycol
CDT	Chemodynamic therapy		
CLSM	Confocal microscopy	m-PEG-MIONCs	Methoxy- Polyethylene glycol coated Manganese iron oxide nanocubes
CS	Chitosan		
CS-MIONPS	Chitosan-coated Manganese iron oxide nanoparticles	MTT	3-(4,5-dimethylthiazol-2-yl)-2,5-diphenyl tetrazolium bromide
DLS	Dynamic Light Scattering	MRI	Magnetic resonance imaging
DSC	Differential Scanning Calorimetry	NCI	National Cancer Institute
		NPs	Nanoparticles
EDS/EDX	Energy-dispersive X-ray spectroscopy	PDT	Photodynamic therapy
FC	Field Cooling	PEG	Polyethylene glycol
FDA	Food and Drug Administration	PTT	Photothermal therapy
FTIR	Fourier Transform Infrared Spectroscopy	R.F.	Radiofrequency
FWHM	Full width at half maximum	ROS	Reactive oxygen species
GSH	Glutathione	SAED	Selected area electron diffraction
HDD	Hydrodynamic diameter	SAR	Specific absorption rate
HRTEM	High-resolution transmission electron microscopy	SDT	Sonodynamic therapy
ILP	Intrinsic Loss Power	SPM	Superparamagnetic
IONPs	Iron oxide nanoparticles	TEM	Transmission Electron Microscopy
MCT	Magneto-chemotherapy	TG-DTA	Thermogravimetric Analysis-Differential Thermal Analysis
MR	Magnetic resonance	TME	Tumor microenvironment
MHT	Magnetic hyperthermia Therapy	VSM	Vibrating Sample Magnetometer
MIONCs	Manganese iron oxide Nanocubes	XRD	X-ray Diffraction
MIONPs	Manganese iron oxide nanoparticles	ZFC	Zero Field Cooling

CHAPTER-1

Introduction



1.1 Introduction

Cancer is a group of diseases characterized by the uncontrolled growth and spread of abnormal cells that can result in death if not treated. Although the exact cause of many cancers remains unclear, several factors are known to elevate risk, including modifiable ones such as tobacco use and obesity, as well as non-modifiable factors like inherited genetic mutations [1]. In recent years, control of cancer has been considered to be a foremost communal health issue. Due to the high number of deaths from cancer, cancer is a serious health problem worldwide [2]. The World Health Organization (WHO) has projected that approximately 13.1 million cancer-related deaths will occur by the year 2030.

Additionally, it is expected that over 1.9 million new cancer cases will be diagnosed in 2024. In the United States alone, it is anticipated that around 611,720 Americans will succumb to cancer in 2024, equating to roughly 1,680 deaths each day. This emphasizes the fact that, after heart disease, cancer is the second most common cause of mortality. Cancer diagnosis and treatment were delayed in 2020 due to the COVID-19 pandemic because of hospital closures, disruptions in work, health insurance, and worries about viral exposure [3].

The global rise in cancer cases in recent years is attributed to epidemiological shifts driven by increased life expectancy, an aging population, and the growing prevalence of unhealthy lifestyles [4]. Cancer survival rates significantly differ depending on the type and late-stage diagnosis. Metastatic spread, defining late-stage cancer, is responsible for 90% of cancer-related deaths. It is worth considering that widespread screening and early cancer detection could significantly improve cancer morbidity and mortality outcomes. Notwithstanding the pressing demand for early cancer detection, screening tests with established clinical effectiveness are infrequent. The emergence of high-throughput technologies and computational resources holds the promise of enabling early diagnosis in the future. In cases where early detection is viable and treatment choices are available, our restricted knowledge of patient categorization for informed treatment decisions frequently hinders successful outcomes. Clinical protocols for diagnosing and determining treatment paths commonly rely on procedures such as tissue biopsy, imaging modalities, and cytology. The information obtained through these approaches is coarse-grained, offering limited molecular details about the cancer. This lack of molecular specificity

can complicate treatment decisions, as interpatient tumor heterogeneity often governs the response to existing therapies [5]. Current cancer treatment approaches, such as chemotherapy and radiotherapy, regrettably have the potential to harm healthy tissues in the body and can lead to a decline in the patient's overall health. Consequently, the quest for less detrimental and more efficacious treatments is growing significantly.

Despite intensive research endeavors spanning the past few decades, cancer continues to stand as a prominent contributor to mortality and a significant public health concern. Cancer manifests as a complex cascade of pathological states, advancing incrementally to form a cluster of cells characterized by unbridled proliferation and the capacity to evade the body's inherent mechanisms for cell apoptosis. Chemotherapy is a significant treatment modality for both localized and metastasized cancers. It involves administering free drugs into the bloodstream to target cancer cells. However, as anticancer drugs are not specific to cancer cells, there is a strong interest in selectively increasing their uptake in tumor tissues. The current state of cancer therapy still faces challenges, as the potent drugs used in chemotherapy can harm healthy cells that overgrow, in addition to cancer cells. Existing diagnostic and prognostic categorizations lack the precision required to forecast treatment success and patient prognosis accurately. Consequently, there is a pressing demand and a substantial impetus to create novel and inventive technologies capable of eradicating an entire tumor and ascertaining whether a cancer has been thoroughly excised [6]. Currently, traditional methods for cancer treatment include tumor removal through surgery, immunotherapy, radiation therapy, chemotherapy, or a combination of these approaches [7].

Magnetic iron oxide nanoparticles are a prominent example of multifunctional nanomaterials, gaining increasing use in various biomedical fields such as magnetic resonance imaging (MRI), biological catalysis, magnetic hyperthermia, magnetic targeting, magnetic separation, photo-responsive therapy, and drug delivery. They are now widely used in the diagnosis and treatment of cancer. New therapies at different stages of development include angiogenesis inhibitors, biological treatments, bone marrow and peripheral blood stem cell transplants, laser therapy, hyperthermia, photodynamic therapy, and targeted cancer therapies [8]. Current chemotherapy faces several challenges, including non-specificity, cytotoxicity, short half-life, poor solubility, the development of multi-drug resistance, and the growth of stem-like cancer cells. To address these issues, advanced treatment methods such as

nanomaterial-based chemotherapy, targeted therapies, molecular therapy, photodynamic therapy (PDT), photothermal therapy (PTT), chemodynamic therapy (CDT), magnetic hyperthermia therapy (MHT) and sonodynamic therapy (SDT) are being employed in cancer treatment [9]. MHT has recently gained prominence as a non-invasive approach to cancer therapy, offering several advantages in contrast to conventional treatments. Hyperthermia is defined as a very high body temperature. This could be from an infection, heat exposure, or an adverse effect of the drugs. Additionally, body tissue can be exposed to extremely high temperatures as part of hyperthermia therapy to either kill or damage cancer cells or to increase their susceptibility to the effects of radiation and specific anticancer drugs. Hyperthermia, in essence, involves elevating body temperature beyond the normal range. This elevation can be induced as part of a treatment, as a result of infection, or due to exposure to heat. Magnetic hyperthermia, employing $\text{Fe}_3\text{O}_4/\gamma\text{-Fe}_2\text{O}_3$ nanoparticles, offers the distinct advantage of selectively eliminating cancerous cells while sparing healthy ones. This selectivity is achieved by raising the temperature to approximately 42-43 °C within the specific target area of these nanoparticles [10 -11].

Magnetic nanoparticles (MNPs) are among the most significant nanomaterials in healthcare and life sciences. When their size is reduced to the nanoscale (1–100 nm), they display distinct physical, chemical, and biological properties highly dependent on their size. The ability to control and utilize magnetic properties in medical applications makes them particularly valuable for cancer diagnosis and treatment. MNPs hold great promise for biomedical applications due to their small size, enabling interactions with living organisms like cells and bacteria. Their magnetic properties allow remote control and guidance within the human body. Consequently, there has been extensive research in recent years to explore their potential biomedical uses, such as MRI, drug delivery, biosensing, and MHT [12]. Nanotechnology research and developments allow the synthesis of MNPs with particular morphologies, surface modification, and property manipulation at the nanoscale. The efficiency of MHT is primarily influenced by the specific absorption rate (SAR) of the heat mediator, which is further affected by the applied magnetic field (AMF), the magnetic characteristics of the nanoparticles, and the properties of the surrounding biological medium.

1.2 Overview of Cancer

Cancer comprises a collection of conditions marked by the uncontrollable proliferation and dissemination of abnormal cells, posing a significant threat if left untreated. The fundamental hallmark of cancer is the abnormal increase in the number of cells, which results from alterations in the mechanisms that govern cell birth and proliferation. Although the precise origins of cancer remain partially veiled, various factors that heighten the risk are recognized, encompassing those that are amenable to modification, such as tobacco consumption and excessive body weight, as well as those that are innate, like hereditary genetic mutations. Cancer is a leading cause of death worldwide, affecting both developed and underdeveloped countries, with a higher prevalence in middle-income countries, potentially linked to poor socioeconomic conditions. Geographic variations in cancer prevalence can be attributed to several factors, including early diagnosis, age, risk factors, screening tests, and access to quality treatment. Recent research has shown that reduced cell death or apoptosis rates play a role in developing certain types of cancer [13]. Cancers are categorized based on the kind of fluid or tissue from which they arise or where they first show themselves in the body. Cancerous cells, in their somewhat self-sufficiency, remain unresponsive to the signals that typically initiate the normal cell cycle. This lack of responsiveness leads to the uncontrolled growth and proliferation of transformed cells, which, if unchecked, can result in a fatal outcome. About 90% of cancer-related deaths are attributed to metastasis or the spread of cancer cells to other tissues. In normal cells, the process of mitosis relies on external growth factors, and cell growth occurs coordinately. When the supply of these growth signals becomes limited or is halted, normal cells cease their reproduction. Furthermore, normal cells exhibit contact inhibition, a mechanism where they break cell division when they reach a certain threshold, responding to the presence of a sufficient number of neighboring cells.

Conversely, cancer cells lack this contact inhibition capacity, forming unwanted cell masses. The lifecycle of a normal cell is well-regulated, dividing around 50 times before undergoing apoptosis or programmed cell death, after which it is replaced by a new cell. This is consistent with the restricted efficiency of DNA replication, as repeated repetition leads to the shortening of telomeres. Conversely, cancer cells exhibit high telomerase enzyme activity, constantly replenishing telomeres' lost and worn-out ends, enabling unrestricted cell proliferation [14]. In

addition, some cancers are of mixed types. A new growth of abnormal tissue that is often uncontrolled and progressive. Cancer initiates when healthy cells undergo alterations, leading to uncontrolled growth and the formation of a mass known as a tumor. Tumors can be broadly categorized into benign (noncancerous) tumors and malignant (cancerous) tumors. A benign tumor comprises cells that do not invade unrelated tissues or organs in the body, although it may continue to grow in size excessively.

On the other hand, malignant or cancerous tumors can spread into nearby tissues, glands, and other parts of the body. They exhibit invasive properties, making them a more serious health concern. **Fig. 1.1** represents the difference between benign tumors and malignant tumors.

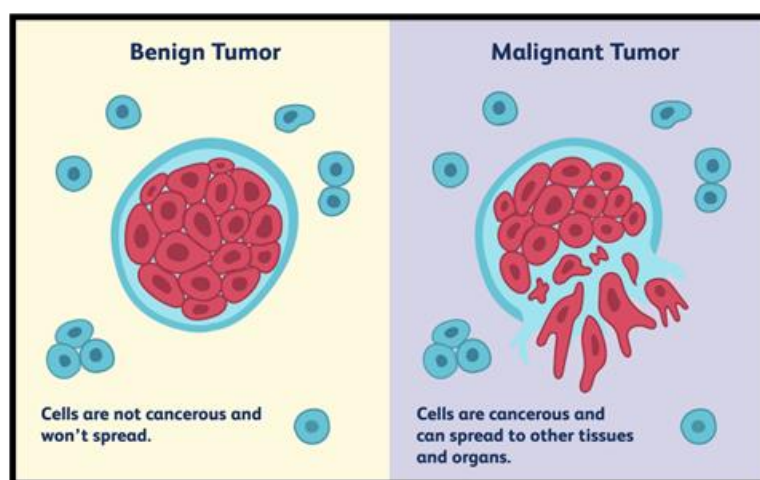


Figure 1.1 Characteristic features of benign tumor and malignant tumor

The tumor-specific cells are not aberrant or noticeably distinct from neighboring cells and are contained within the tumor. Cancer cells, the basis of malignant tumors, have the potential to spread to neighboring tissues and proliferate uncontrolled. A malignant tumor usually contains cancer cells that differ significantly from the healthy tissue around it in terms of abnormality and morphology.

Types of cancer depend on the location (organ-specific) [15]

Breast cancer Cancer that begins in the cells of the breasts is known as breast cancer

Prostate cancer Prostate cancer, on the other hand, occurs in the prostate gland of men, a small walnut-sized organ responsible for producing seminal

	fluid.
Melanoma	Melanoma is regarded as the most severe form of skin cancer.
Colon cancer	Colon cancer originates in the colon or rectum and may initially manifest as noncancerous polyps.
Lung cancer	Lung cancer primarily begins in the lungs and is often linked to tobacco use.
Leukemia	Leukemia is a type of cancer that affects blood-forming tissues, compromising the body's ability to combat infections.
Stomach Cancer	Stomach cancer, or gastric cancer, initiates in the cells that line the stomach.
Liver cancer	Liver cancer pertains to malignant cells forming in the tissues of the liver, termed primary liver cancer.

As of 2024, cancer remains a significant public health challenge in India, with approximately 2.5 million individuals currently living with the disease and over 1.46 million new cases diagnosed annually. **Fig. 1.2** illustrates the estimated number of cancer cases in India for 2024, categorized by region and type of cancer. The most prevalent cancers differ by gender: lung cancer is most common among men, while breast cancer predominates among women. Additionally, childhood cancers, particularly lymphoid leukemia, are becoming increasingly concerning. By 2025, India is expected to see a 12.8% rise in cancer cases compared to 2020, especially in the northern and northeastern regions. This increase is influenced by lifestyle factors such as tobacco use, alcohol consumption, and poor dietary habits. Tobacco-related cancers, especially oral cancer, represent a significant portion of male cases, while breast, cervix, oral cavity, and lung cancers together account for more than 50% of cancer-related fatalities. The five-year survival rates for certain cancers, like cervical cancer (51.7%) and breast cancer (66.4%), show considerable variation based on region and healthcare access. **Fig. 1.3** represents the estimated distribution of cancer cases in India for 2024, categorized by type of cancer [3]. Based on the data presented in the table, it is evident that the number of estimated new cancer cases exceeds the estimated number of deaths. This indicates a rapid increase in cancer incidence compared to previous years. To address the growing prevalence of cancer, there is a critical need for advancements in new medical treatments [2]. The following section provides a comprehensive overview of existing and emerging cancer treatments.

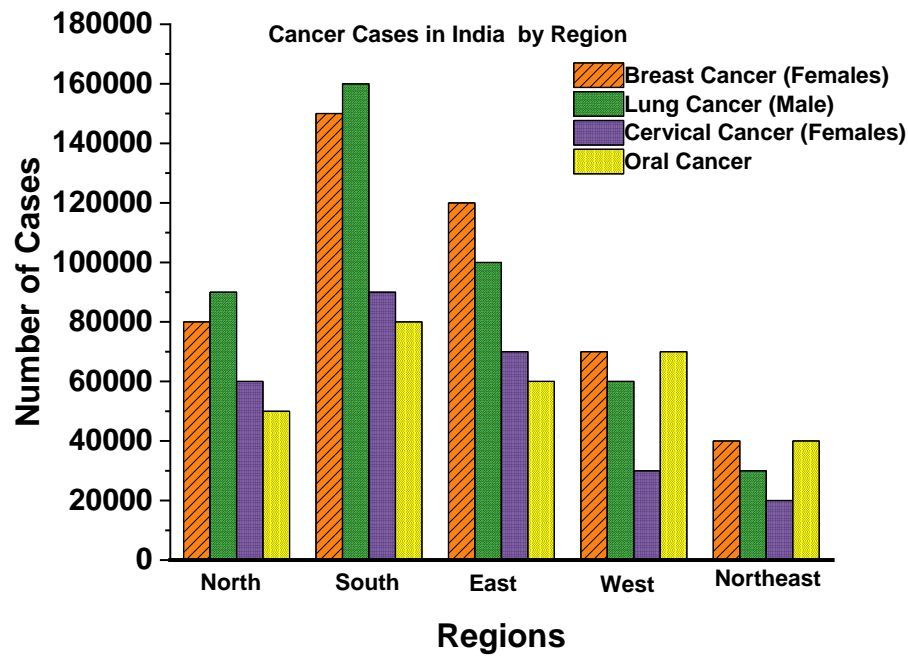


Figure 1.2 The projected number of cancer cases in India for 2024, classified by region and cancer type [3]

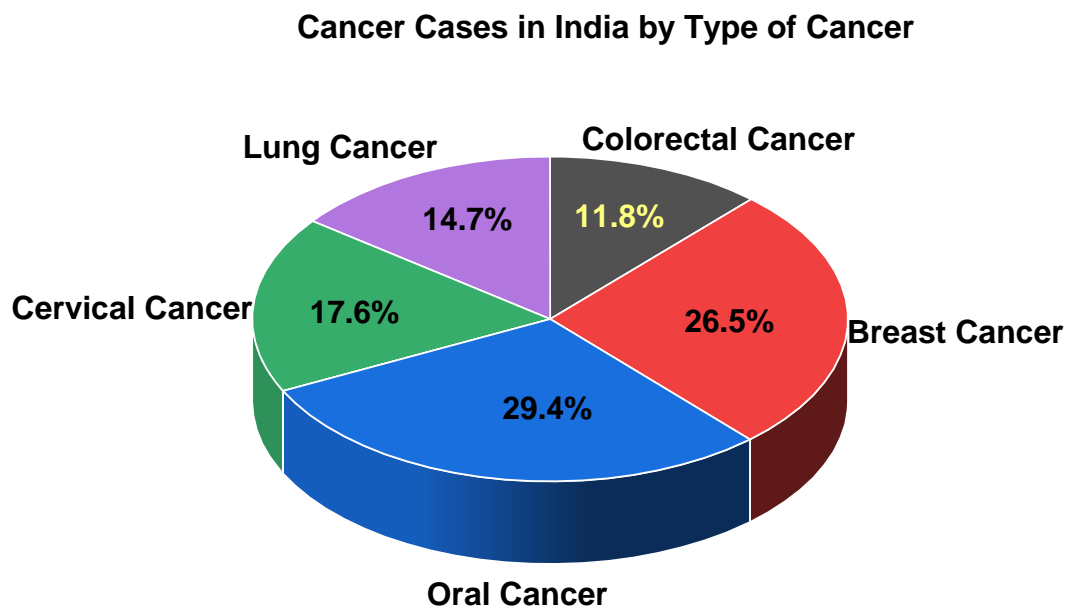


Figure 1.3 The projected distribution of cancer cases in India for 2024, classified by cancer type [3]

1.3 Challenges in Cancer Diagnosis and Treatment

Cancer treatments encompass a range of approaches, including surgery, chemotherapy, radiation therapy, and innovative techniques like interventional

radiology and immunotherapy. Ongoing research focuses on discovering innovative and effective treatment methods for cancer. Currently, more than 60% of medical trials worldwide concentrate on cancer. Treatment selection and progress depend on the cancer type, location, and stage of advancement. Conventional treatments such as surgery, radiation-based techniques, chemotherapy, and radiotherapy continue to be commonly utilized. At the same time, new methods include hormone therapies, anti-angiogenic strategies, stem cell treatments, immunotherapy, and dendritic cell-based immunotherapies. Notably, traditional treatments may have side effects, underscoring the importance of exploring novel cancer treatment methods. Novel approaches for treating cancer involve targeting cancer's ability to generate blood vessels, utilizing oncolytic virotherapy, genetic manipulation of pathways related to apoptosis and tumor suppression [16].

Cancer treatment typically relies on three primary methods: surgery, radiotherapy, and chemotherapy. Surgery and radiotherapy are highly effective for removing tumors, especially in early-stage cases, but their application becomes limited in high-stage tumors. In such cases, chemotherapy is often necessary, although it doesn't ensure a cure. Therefore, developing innovative drugs and combination therapies is crucial to maximize the effectiveness of cancer treatment for malignant tumors [17]. Numerous methods and medications exist for cancer treatment, and ongoing research is exploring even more. These treatments can be categorized into 'local' approaches like surgery and radiation therapy, which target specific tumor areas of the body. 'Systemic' treatments, such as chemotherapy, immunotherapy, or targeted therapy, can potentially impact the entire body [18].

1.3.1 Early Diagnosis

Diagnostic tools that detect specific molecular changes in tumors are crucial in precision medicine. In recent years, the Food and Drug Administration (FDA) has frequently approved companion diagnostic tests alongside new targeted therapies. These tests help determine whether a patient's tumor possesses the target for a particular treatment, potentially saving patients from the costs and side effects of therapies that may be ineffective for their cancer [19]. Recent research has focused on developing effective methods to minimize the side effects of conventional cancer therapies and diagnostics. Early cancer detection aims to identify symptomatic patients as soon as possible, offering them the best chance for successful treatment.

Delays in cancer care can lead to lower survival rates, increased treatment complications, and higher healthcare costs. Early diagnosis enhances cancer outcomes by enabling intervention at the earliest stage, making it a crucial public health strategy in all contexts. Some MNPs-based nanotechnology applications in cancer detection and diagnosis are shown in **Fig. 1.4**.

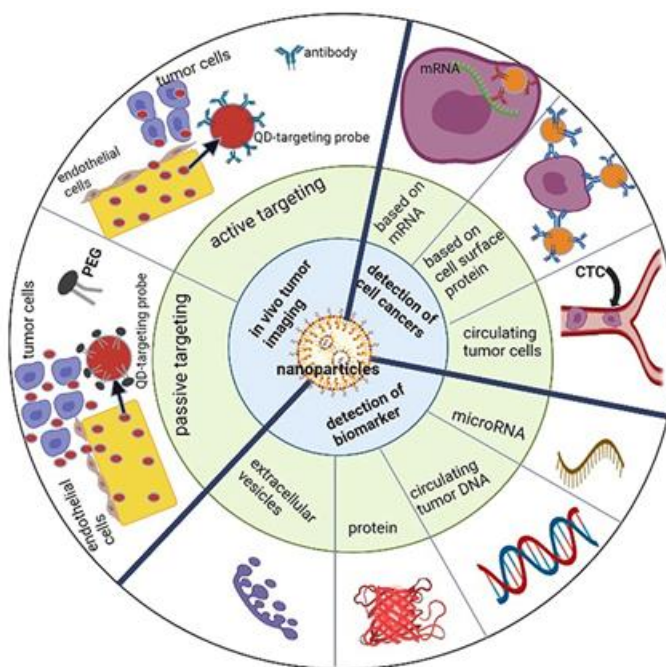


Figure 1.4 Schematic illustration of nanotechnology applications in cancer detection and diagnosis [20]

Early diagnosis programs are relatively simple and cost-effective because they focus on symptomatic patients, making them less extensive than screening programs that target entire populations. In this context, magnetic nanoparticles have garnered significant interest due to their unique physical properties, including magnetic susceptibility, biocompatibility, and stability. For *in vivo* biomedical applications, MNPs must meet specific conditions such as appropriate size, size distribution, surface charge, biodegradability or bio-limnality, and if needed, the presence of well-chosen ligands for targeted delivery.

1.3.2 Conventional Treatments

Conventional cancer treatments typically contain the surgical removal of tumors, followed by radiotherapy using X-rays and chemotherapy using drugs. Surgical resection is most effective in the early stages of the disease. Radiation therapy may damage healthy cells, organs, and tissues, while chemotherapy, though

effective in lowering morbidity and mortality, also affects healthy cells, particularly those that rapidly divide. A significant challenge with chemotherapy is the development of drug resistance in cancer cells, leading to decreased drug effectiveness. Conventional chemotherapy has limitations such as difficulty in selecting the proper dosage, lack of specificity, rapid drug metabolism, and significant side effects [21].

(a) Radiotherapy

Radiation therapy, often referred to as radiotherapy, is a method for treating cancer that uses high doses of radiation to target and kill cancer cells, which helps to reduce the size of tumors. In contrast, lower doses of radiation are commonly employed in medical procedures like X-rays, which are used to capture internal images, such as those of teeth or fractured bones. In contrast, high doses of radiation in radiation therapy target cancer cells, causing damage to their DNA. Cancer cells with irreparable DNA damage either cease dividing or undergo cell death. The body subsequently breaks down and eliminates these damaged cells. It's essential to understand that radiation therapy doesn't kill cancer cells instantly; it takes several days or weeks of treatment to cause enough DNA damage to ultimately lead to cancer cell death. After radiation therapy concludes, cancer cells continue to perish over several weeks or even months. Radiation specialists have a dual objective: to safely enhance the radiation dose delivered to the tumor and shield surrounding healthy tissues from this dose, minimizing potential side effects at the treatment site. Significant advancements have been made in achieving these objectives by integrating state-of-the-art technology into radiation oncology.

In cancer therapy, radiation is a potent tool to eliminate cancer cells. This therapy's specific type of radiation is known as ionizing radiation. Radiation interacting with biological tissues induces an electrical charge in the particles within these bodies, rendering it "ionizing." In this process, energy is transmitted from the radiation to the body's cells, which it traverses. This energy can lead to the direct destruction of cancer cells or genetically modify them, compelling them to undergo apoptosis or programmed cell death. Radiation therapy, whether used on its own or in conjunction with other treatment methods, has demonstrated substantial enhancements in tumor remission rates. Presently, two primary radiation treatment modalities exist: external beam radiation and internal radiation, commonly referred to

as brachytherapy [21]. Using a machine to target the malignant spot with radiation is known as external beam radiation therapy. As a focused treatment, it targets a particular bodily part. Conversely, internal radiation therapy, also known as brachytherapy, involves the implantation of a radioactive implant inside or close to the physical tumor. The external beam radiation therapy setup is shown in **Fig. 1.5**.

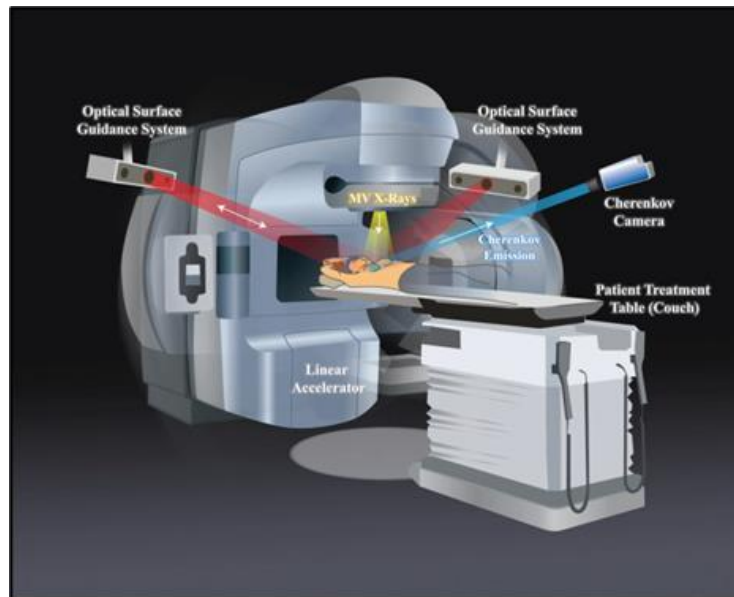


Figure 1.5 External beam radiation therapy setup [22]

Radiation therapy, while effective at targeting and inhibiting the growth of cancer cells, can also impact neighboring healthy cells. This can lead to side effects, such as hair loss at the treatment site (sometimes permanent), skin irritation at the treatment site, and fatigue.

(b) Surgery

Surgery is a well-established treatment method for various types of cancer. The history of cancer surgery can be traced back thousands of years, with records of surgical procedures to remove breast tumors dating as far back as ancient Egypt (Edwin Smith papyrus; 1600 BC). Over time, advancements in surgical techniques have led to improved cancer outcomes. Surgical oncologists play a crucial role in enhancing these outcomes and minimizing the impact of cancer treatments on a patient's quality of life. Surgery is most effective in cases where the cancer is localized, meaning it is confined to the original site and hasn't spread to other parts of the body, a condition known as metastasis. Surgery remains the primary treatment approach for most cancers. However, surgical oncologists now collaborate as part of a

comprehensive multidisciplinary team, where healthcare professionals with diverse skills work together to optimize patient outcomes. Technological advancements have significantly minimized the impact of surgery on patient's quality of life, allowing cancer survivors to enjoy longer and better lives. Like all cancer treatments, surgery comes with benefits, risks, and side effects, which may vary from person to person depending on various factors such as the cancer's location and type, the specific surgical procedure, prior treatments like chemotherapy and radiation therapy, general health, and any symptoms experienced before the surgery. After surgery, it is expected to have some pain from the surgery's effect on the body. Surgery serves multiple purposes in the context of cancer.

Common side effects: Surgery, while an effective cancer treatment, is not without its associated risks. These risks include potential complications like bleeding, injury to neighboring tissues, and adverse reactions to the anesthesia used during the procedure. After surgery, it's common for individuals to experience pain in the area where the operation was performed. There is a risk of post-operative infections that can develop after surgery.

(c) Chemotherapy

Chemotherapy was first used to treat cancer at the beginning of the 20th century, both for targeted treatments and as a means of developing novel medications. Chemotherapy includes the use of various chemicals to eliminate cancer cells. Specifically, cancer chemotherapy entails administering cytotoxic chemicals, which have cell-killing properties. The objective is to eradicate the tumor in some cases or, at the very least, reduce its size and alleviate tumor-related symptoms, potentially extending the patient's life. Chemotherapy, which primarily employs cytotoxic drugs, is often administered intravenously. The fundamental mechanism of chemotherapy is to impede the progression of tumors by inhibiting their ability to divide and promoting apoptosis. These cytotoxic drugs are typically administered in carefully selected combinations of two or more medications. This approach serves several purposes: it enhances the chances of overcoming tumor cell resistance, broadens the activity of the regimen against various tumor cell variants, and minimizes the risk of significant toxicity to healthy tissues. In a healthy body, the natural biological processes regulate cell renewal by eliminating excess or damaged cells and facilitating the production of new ones. In contrast, tumor cells exhibit an increased

capacity for division and seemingly endless replication, as they are not subject to apoptosis control. Consequently, whereas cell proliferation to cell death is balanced and regulated in healthy bodies, cancerous masses display a significantly skewed ratio with increased cell proliferation and diminished cell death [23].

Combination chemotherapy is frequently employed to achieve optimal treatment responses. This approach aims to prevent the development of drug-resistant clones by increasing cytotoxicity in both resting and dividing cells. Many chemotherapy drugs are available, all potent chemicals designed to combat cancer by interfering with specific cell cycle phases. The cell cycle is the process of producing new cells, and all cells go through this cycle. However, cancer cells progress through this cycle faster than normal cells, making chemotherapy particularly effective against these rapidly dividing cells. It's important to note that chemotherapy drugs target cancer cells and all fast-growing cells in the body, potentially leading to side effects. Moreover, it can enhance the effectiveness of other treatment modalities, such as surgery or radiation therapy.

Common side effects of chemotherapy include fatigue, hair loss, easy bruising and bleeding, and issues in the mouth, tongue, and throat, such as sores and pain while swallowing. Currently, around one-third of patients with localized tumors at the time of diagnosis can achieve a cure through local treatment strategies like surgery, radiotherapy, and chemotherapy.

1.4 Cancer Nanotechnology

Cancer nanotechnology is an emerging interdisciplinary field that integrates biology, chemistry, engineering, and medicine and is anticipated to bring significant progress in cancer detection, diagnosis, and treatment. Designing more effective cancer therapies by manipulating materials at the nanoscale offers a promising solution for selectively targeting cancer cells while minimizing harm to normal cells. Nanomedicine holds immense promise for transforming cancer treatment and diagnostics by creating innovative biocompatible nanocomposites, particularly for drug delivery, one of the most significant applications of nanoparticles [24]. Nanotechnology in cancer treatment can potentially improve therapy and minimize side effects by explicitly directing drugs to target cancer cells. Nano-based approaches could also aid in more precise surgical tumor removal and increase the

effectiveness of radiotherapies and other treatment methods, reducing patient risk and improving chances of survival [25].

Extensive research has demonstrated that nanotechnology can effectively create systems that enhance the pharmacokinetics of drugs and reduce associated toxicities. Beyond drug delivery, nanotechnology research also explores the development of novel therapeutics that leverage the unique properties of nanomaterials themselves. Firstly, specific physical properties of nanoparticles, such as their ability to absorb and re-radiate energy, can be utilized to disrupt diseased tissue, as demonstrated in laser ablation and hyperthermia treatments. Secondly, nanoparticles are small enough to accumulate at tumor sites and large enough to carry numerous therapeutic agents, such as radionuclides and active pharmaceutical compounds. Thirdly, their surfaces can be modified with ligands like DNA or RNA strands, peptides, aptamers, or antibodies, explicitly targeting their delivery within the body [26]. The engineered properties of nanoparticles enable innovative, non-invasive cancer therapy approaches that were not previously feasible, including advanced techniques like PDT, radiotherapy, radiofrequency therapy, and theranostics. Combining diagnosis and treatment into a single process is a developing biomedical approach known as theranostics. Many theragnostic methods use nanoparticles to deliver both diagnostic agents and therapeutic drugs. Biocompatible nanoparticles are being developed as theragnostic agents for cancer, allowing for non-invasive diagnosis and targeted therapy. They offer unique advantages in designing and customizing properties that traditional drugs cannot achieve, positioning them as a promising new generation of cancer therapies. Additionally, multifunctional nanoparticles may eventually be capable of detecting and eliminating cancer cells simultaneously [27].

1.5 Nanoparticle-Based Cancer Treatments

Currently, the most prevalent cancer treatments are chemotherapy, radiation therapy, and surgery. In addition to these established methods, there are emerging treatments at various stages of development. These therapies include angiogenesis inhibitors, biological treatments, bone marrow and peripheral blood stem cell transplants, laser therapy, MHT, PDT, and targeted cancer treatments. Extensive research and application of nanotechnology in cancer treatment have highlighted the significant potential of nanoparticles as drug delivery systems. Nanoparticle-based

drug delivery offers several advantages over conventional drugs, including improved stability, biocompatibility, enhanced permeability and retention effect, and targeted delivery. Hybrid nanoparticles, combining the properties of different nanoparticles, have further advanced this drug-carrier system. Moreover, nanoparticle-based drug delivery systems have demonstrated promise in overcoming drug resistance associated with cancer treatment [28].

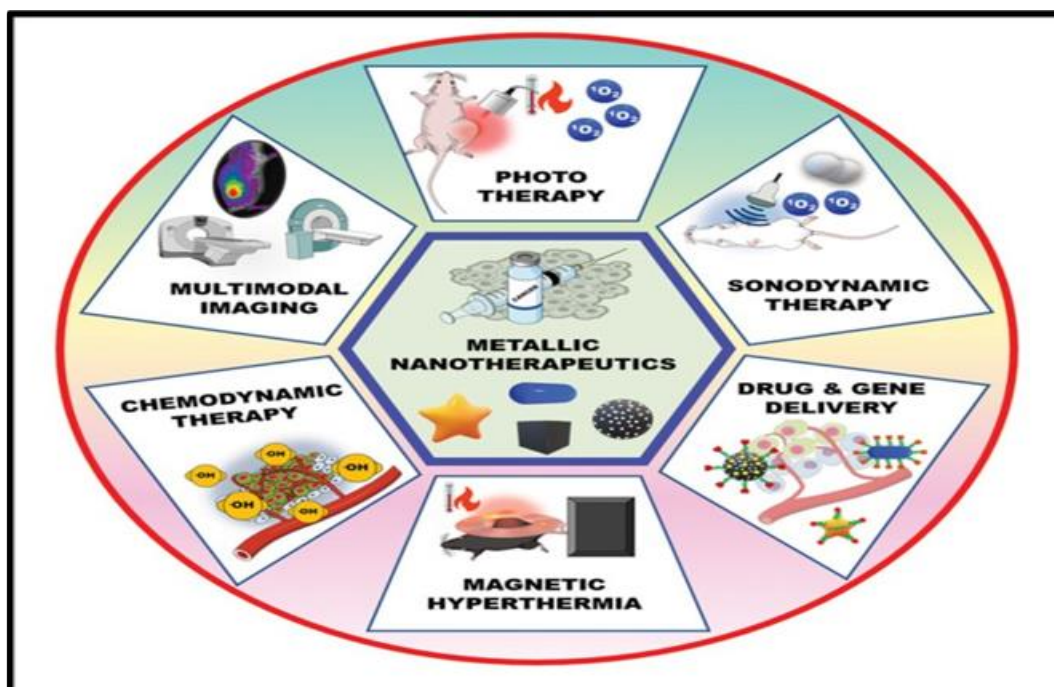


Figure 1.6 Metallic nanotherapeutic applications in cancer theranostics [30]

In the past twenty years, a wide array of nanoscale and nanostructure-based agents has been created to treat and diagnose cancer. These approaches can be employed individually or in conjunction with other cancer treatments, which can actively or passively target tumors, respond to internal or external stimuli, and transport therapeutic genes to cell nuclei [29]. Advancements in materials science and nanotechnology have significantly expanded the range of nanosized materials utilized for drug delivery in cancer treatment. Various synthetic materials, encompassing inorganic, organic, and natural compounds, have been developed, modified, and harnessed as nanosized carriers for anticancer therapeutics, mainly systemic delivery [30]. MNPs can be used in conjunction with different stimuli, such as light, ultrasound, and an AMF, to increase the effectiveness of anticancer treatments. **Fig. 1.6** depicts using stimulus-triggered metallic nanotherapeutics in various cancer therapies such as PTT, PDT, MHT, SDT, and CDT to kill cancerous cells.

1.5.1 Photodynamic Therapy (PDT)

PDT employs a photosensitizer, which becomes active when exposed to visible or near-infrared light. It then transfers energy to molecular oxygen, producing reactive oxygen species (ROS) such as singlet oxygen, free radicals, and peroxides. PDT employs a light-activated drug to eliminate cancer and other abnormal cells. PDT triggers the oxidation of lipids, amino acids, and proteins, resulting in cell death. PDT is an approved and minimally invasive therapeutic method known for its selective cytotoxicity against malignant cells. The process involves giving a photosensitizing agent and exposing the area to light at a wavelength that matches the agent's absorbance band. In the presence of oxygen, this exposure triggers a series of reactions that result in direct destruction of tumor cells, damage to the microvasculature, and local inflammatory response. Clinical research has demonstrated the effectiveness of PDT in treating early-stage tumors, extending the lives of patients with inoperable cancers, and significantly improving their quality of life. PDT is noted for its minimal toxicity to normal tissues, negligible systemic side effects, reduced long-term morbidity, and lack of resistance mechanisms. This makes it a valuable choice for combination treatments. Recent technological advancements have further improved PDT's potential to become an integral part of mainstream cancer treatment [31].

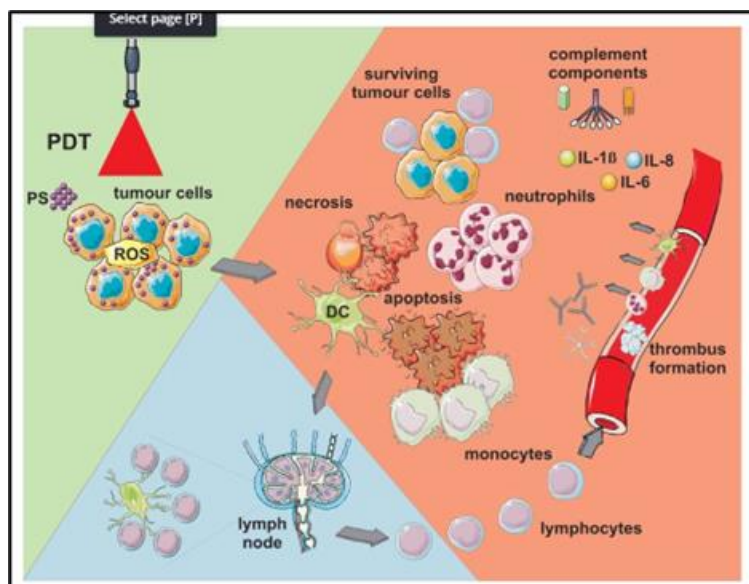


Figure 1.7 Schematic representation of PDT by using MNPs [36]

PDT is a two-step procedure that uses light energy in conjunction with a photosensitizing drug to destroy cancerous and precancerous cells selectively upon

activation by light. A Commonly used sensitizer is Porphyrins, Chlorines, Purpurins, Phthalocyanines, Hematoporphyrin derivative (HpD), Photofrin, Aminolevulinic acid (5-ALA), Temoporfin or m-THPC (Foscan®), etc [32]. The photosensitizer remains non-toxic until it is exposed to a specific wavelength of light energy, often delivered through a laser. Once activated by light, the photosensitizer becomes toxic to the targeted tissue. The photosensitizer depends on the treatment area and duration; the cancer cells absorb the drug. Subsequently, light is applied to the treated area, causing the drug to react and generate a particular type of oxygen molecule that kills the cells. PDT may also destroy the blood vessels that nourish the cancer cells and activate the immune system to attack the cancerous cells. PDT is well-known for its ability to provide precise targeting via intravenous or topical injection to the skin.

After minimal invasiveness and toxicity, it has been found to have extensive clinical use in treating different tumors, particularly those on the surface. Nevertheless, the tumor microenvironment (TME) often exhibits hypoxia, stemming from insufficient oxygen (O₂) supply due to irregular blood vessel formation in neoplastic tissues and heightened O₂ consumption triggered by the rapid growth of tumor cells. This hypoxic TME can impede the effectiveness of oxygen-dependent PDT [33]. In addition to having negative consequences, PDT might damage healthy cells in the treated area. H. Hou et al. present a novel cancer treatment combining PDT with the Fenton reaction using multifunctional MNPs. These nanoparticles enhance the generation of ROS when exposed to light and magnetic fields, improving the effectiveness of PDT in targeting and destroying cancer cells. This approach offers a synergistic method to increase cancer cell death and potentially reduce side effects compared to conventional treatments [34]. Jiong Li et al. describes the development of nanoparticles coated with cancer cell membranes. These nanoparticles are designed for dual-modal imaging using magnetic resonance (MR) and near-infrared (NIR) fluorescence, enhancing the accuracy of tumor imaging. Additionally, they facilitate targeted PDT, using light to activate the nanoparticles and destroy cancer cells, offering a precise and effective cancer treatment strategy [35]. **Fig. 1.7** shows the PDT-induced effect based on MNPs.

1.5.2 Sonodynamic Therapy (SDT)

SDT is a treatment strategy that uses ultrasound to kill cancer cells by inducing the overproduction of ROS activated by sonosensitizers. Due to the unique

properties of ultrasound, SDT is particularly effective for treating deep-seated tumors. This therapy leverages the synergistic effects of ultrasound and chemical agents, with ultrasound stimulation, especially cavitation, causing cytotoxicity, making SDT one of the least invasive approaches for solid tumor treatment [37]. Initially, ultrasound is applied to focus energy in the target area of sensitizers. Cavitation processes create intense conditions that enable sonochemical reactions. These reactions take place in three specific zones. High temperatures and pressures Within the collapsing bubbles generate suitable pyrolysis conditions, producing hydroxyl radicals ($\bullet\text{OH}$) and hydrogen atoms ($\bullet\text{H}$) in aqueous environments. Secondly, the bubble-liquid interface forms steep pressure and temperature gradients, which can break down nearby solutes. Thirdly, the ROS generated during bubble collapse can trigger chemical reactions in the surrounding solution. Extensive studies have explored the link between cavitation and ROS production, with sonoluminescence being connected to the formation of ROS [38]. In SDT, ultrasound penetrates deep tissue and focuses energy precisely on tumor cells, activating sonosensitizers to produce ROS, which induces cytotoxicity in tumors while minimizing harm to surrounding healthy tissue. The principle behind SDT is similar to that of PDT. However, SDT offers several advantages: i) ultrasound is a widely used, safe, and affordable imaging technique, and ii) it can be focused on pathological tissue with penetration depths of up to several centimeters. SDT depends on the interplay of ultrasound, sonosensitizer, and oxygen [39]. However, three potential mechanisms have been proposed (**Fig. 1.8**): the generation of ROS, mechanical disruption, and thermal effects.

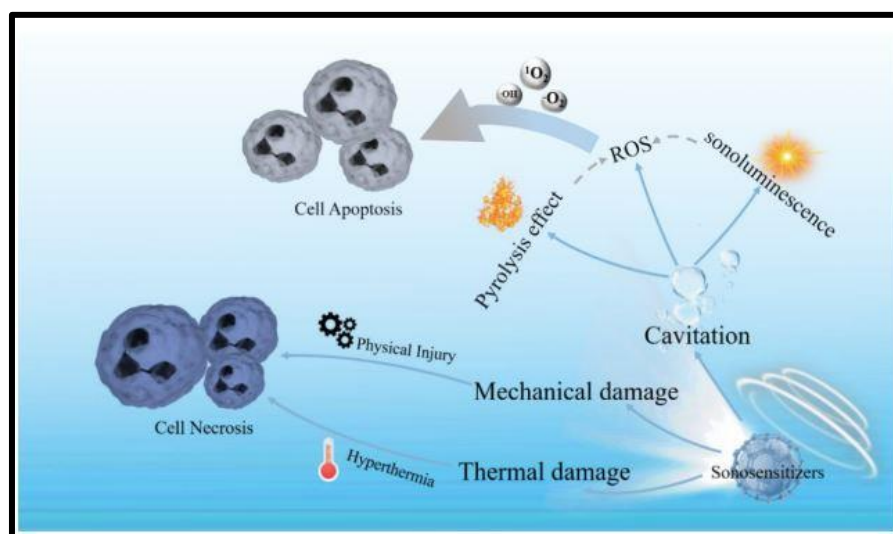


Figure 1.8 Illustration of potential SDT mechanisms [39]

Focused ultrasound can target deeper areas within the body where light would be obstructed or require invasive delivery methods. It can also deliver a precise dose of energy, triggering apoptosis across the entire tumor. Additionally, it enables localized toxicity while minimizing damage to surrounding healthy tissues. Ma et al. Study the use of metalloporphyrin complex-based nanosonosensitizers in SDT for treating deep-tissue tumors. These nanosonosensitizers are activated by ultrasound, enabling precise, non-invasive therapy and imaging of tumors located deep within the body [40].

1.5.3 Chemodynamic Therapy (CDT)

CDT is a novel treatment method that harnesses Fenton-type reactions to produce the exceptionally cytotoxic hydroxyl radical ($\bullet\text{OH}$), the most potent ROS. The production of $\bullet\text{OH}$ through Fenton chemistry involves the interaction between hydrogen peroxide (H_2O_2) and catalysts, requiring no external energy input or oxygen (O_2). This unique ROS generation mechanism in CDT overcomes challenges associated with hypoxia-related resistance and limited light penetration depth observed in tumor PDT, a widely used ROS-based therapeutic strategy. Recent advancements have investigated different nanoparticles for controlled delivery of Fenton catalysts in cancer CDT, using endogenous H_2O_2 as the substrate for Fenton-type reactions. However, although specific tumor cells exhibit higher intracellular H_2O_2 levels than normal cells, the amount of H_2O_2 produced naturally is often inadequate to achieve optimal chemodynamic efficiency [41]. CDT utilizes iron-triggered Fenton chemistry to eradicate cancer cells by transforming the body's hydrogen peroxide (H_2O_2) into harmful hydroxyl radical ($\bullet\text{OH}$). Although Fenton-like reactivity has been noticed in metal ions apart from Fe^{2+} , there's a scarcity of metal-based CDT agents exhibiting Fenton-like traits [42].

Regrettably, intracellular glutathione (GSH), recognized for its capability to neutralize $\bullet\text{OH}$, considerably impedes the effectiveness of CDT. The elevated GSH levels in tumor cells pose a considerable challenge for CDT. Although GSH plays a vital role in cellular protection against various harmful agents, its overexpression in cancer cells also leads to increased resistance to chemotherapy, radiotherapy, and PDTs. GSH, known for its robust intracellular antioxidant properties, counteracts the potent hydroxyl radicals ($\bullet\text{OH}$) produced by chemodynamic agents, strengthening cancer cells' resistance to oxidative stress and diminishing the effectiveness of CDT.

Consequently, reducing intracellular GSH levels is pivotal for CDT nano agents to conquer tumor resistance and boost the effectiveness of CDT.

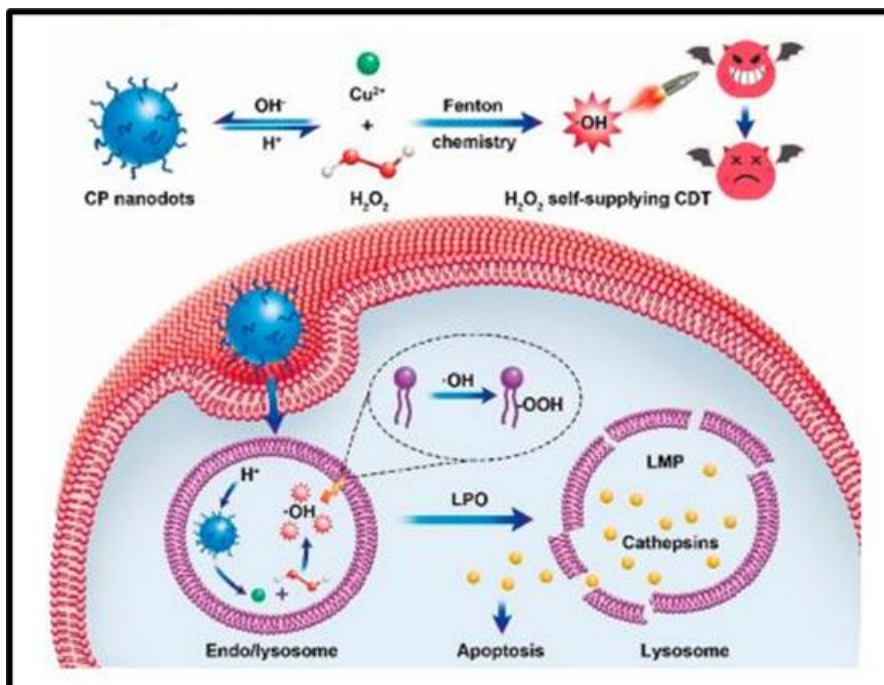


Figure 1.9 Formation of copper peroxide nanodots for H_2O_2 self-supplying CDT [43]

To achieve this, innovative nanoformulations have been developed for the controlled generation of highly toxic ROS. In particular, the recent advances in CDT use nanoparticles containing transition metals like ferro or ferric oxide, antiferromagnetic pyrite, and iron-based nanoparticles to catalyze the production of hydroxyl radicals ($\cdot\text{OH}$) shown in **Fig. 1.9**.

1.5.4 Hyperthermia Therapy

In the oncology field, hyperthermia has been explored as a complementary approach alongside radiotherapy or chemotherapy for addressing different cancer types, including brain, breast, liver, prostate, and lung cancer. Elevating the tumor's temperature to a specific range, usually between 40 to 45 °C, induces damage to tumor cells and enhances their responsiveness to conventional treatment methods. Significantly, this approach minimizes adverse effects on healthy cells, as they are less susceptible to temperature elevation [44]. In the 42 to 46 °C temperature range, hyperthermia is employed with simultaneous radiotherapy or chemotherapy. This combination triggers cell death through diverse mechanisms, including nucleus condensation, membrane blebbing, DNA damage, protein denaturation, protein

folding, disruption of cellular signaling, stimulation of anticancer immune responses, and apoptosis. At higher temperatures ($>46\text{ }^{\circ}\text{C}$, up to $55\text{ }^{\circ}\text{C}$), also known as "thermoablation," cancer cells are directly killed through coagulation, carbonization, or necrosis. **Fig. 1.10** shows the schematic illustration of MNP-mediated MHT for tumor cell apoptosis.

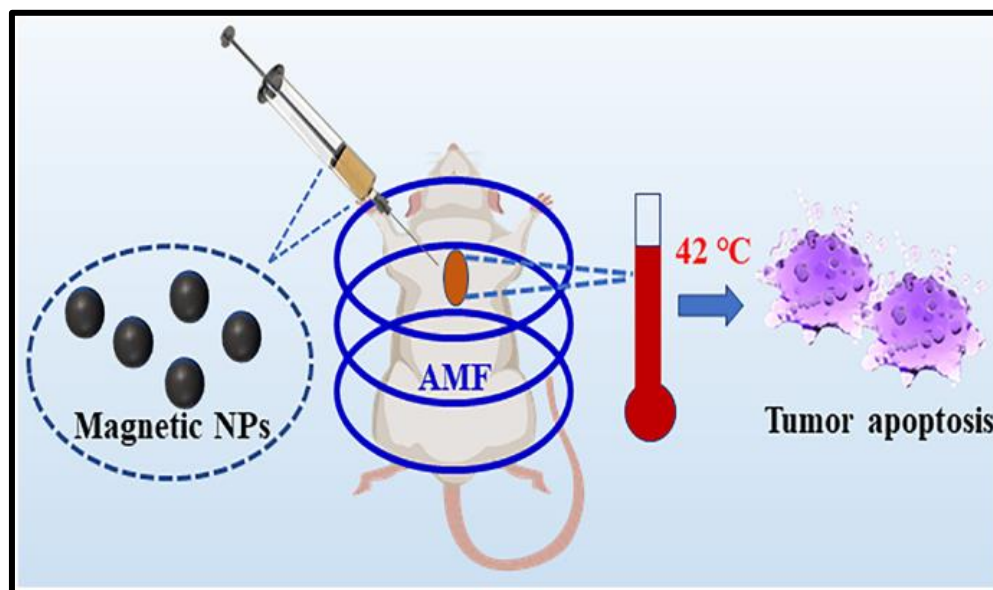


Figure 1.10 Schematic illustration of MNP-mediated MHT for tumor cell apoptosis

Hyperthermia employs different external sources like hot water, microwaves, ultrasonic waves, and radio waves to elevate the temperature. Despite advancements in clinical routines, conventional hyperthermia techniques still face challenges such as burns, blisters, unregulated tissue growth, limited heat wave penetration, imprecise localization of thermal energy, and inadequate tumor targeting. MHT achieves precise heat localization within deep tissues noninvasively due to the presence of MNPs and the penetrating power of the magnetic field. Iron oxide nanoparticles have notably featured in numerous theranostic applications [45].

1.6. Statement of the Problem

Cancer nanotechnology has substantially contributed to personalized diagnostics, healthcare, and monitoring. In the context of hyperthermia therapy, research has primarily concentrated on tailoring the size, composition, and surface properties of MNPs to enhance the SAR of the MHT agent. However, despite these endeavors, conventional cancer treatments such as chemotherapy, PDT, and PTT face challenges that constrain their effectiveness and efficacy [46]. Therefore, various

strategies are being investigated to enhance the effectiveness of traditional therapies or target tumor cells directly. One approach is to utilize diverse morphologies, different sizes, various chemical properties, and the tunable structure of MNPs.

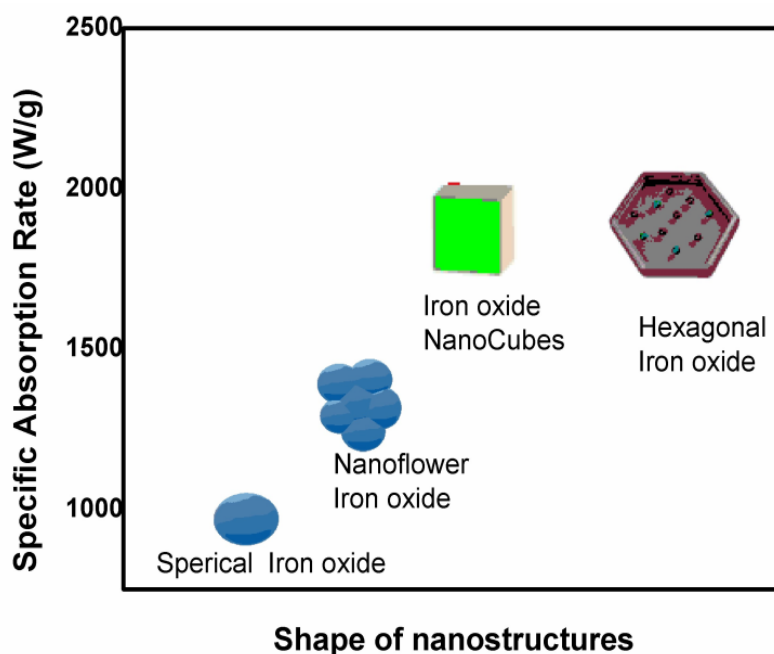


Figure 1.11 Specific absorption rates concerning the shape of iron oxide nanoparticles

It is observed that nanoparticles with non-spherical shapes (e.g., cubical, hexagonal) demonstrate higher heating efficiency compared to their spherical counterparts. **Fig. 1.11** represents various values of SAR concerning the formation of magnetic nanostructures. The heating efficiency of nanoparticles can further be improved by changing both the shape and composition of nanoparticles. It is well-established that introducing specific metals into iron oxide in precise ratios can boost its magnetic properties and enhance heating efficiency. In this regard, intense efforts have been taken to develop biocompatible shape selective nanostructures of manganese iron oxide, which are expected to generate the high value of a specific absorption rate under a physiologically safe range of AC magnetic field and frequency [47-50]. The present work is subjected to three objectives as follows:

- 1) To optimize the synthesis method (co-precipitation and reflux method) for preparation of magnetic manganese iron oxide nanostructure in different shapes such as nanocubes, nanosphere, & nanoflowers.

- 2) To surface functionalize manganese iron oxide nanostructure with m-polyethylene glycol to improve stability and biocompatibility for possible biomedical applications.
- 3) To evaluate the anticancer activity of m-polyethylene glycol coated manganese iron oxide nanostructure on MCF7 breast cancer cell line under AC magnetic field.

1.7 References

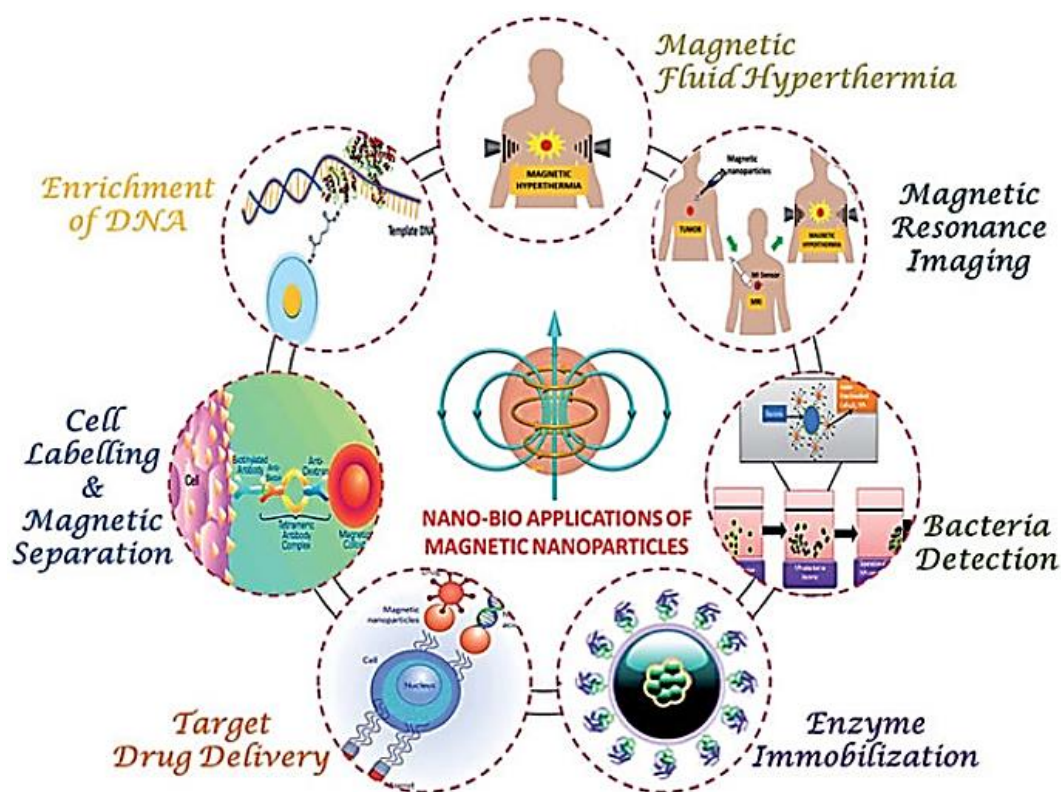
1. Cancer Facts & Figures 2024, American Cancer Society, (2024); 1-82.
2. A. Salunkhe, V. Khot, S. Pawar, *Curr. Top. Med. Chem.*, 14 (5) (2014) 572-594.
3. R. Siegel, A. Giaquinto, A. Jemal, *CA Cancer J Clin.*, 74(1) (2024) 12-49.
4. S. Sahoo, M. Verma, P. Parija, *Oncology Journal of India*, 2(4) (2018) 86-89.
5. S. Bratulic, F. Gatto, J. Nielsen, *J Tissue Eng Regen Med.*, 7 (2021) 312-352.
6. Z. Nemati, J. Alonso, L. Martinez, H. Khurshid, E. Garaio, J. Garcia, M. Phan, H. Srikanth, *J. Phys. Chem. C*, 120 (15) (2016) 8370-8379.
7. S. Thakkar, D. Sharma, K. Kalia, R. Tekade, *Acta Biomater.*, 101 (2020) 43-68.
8. A. Tres, M. Valladares, A. González-Fernández, *Cancers*, 3 (2011) 3279-3330.
9. S. Bajpai, S. Tiwary, M. Sonker, A. Joshi, V. Gupta, Y. Kumar, N. Shreyash, S. Biswas, *ACS Appl. Nano Mater.* 4(7) (2021) 6441-6470.
10. P. Das, M. Colombo, D. Prosperi, *Colloids Surf. B Biointerfaces.*, 174 (2019), 42-55.
11. A. Roca, L. Gutiérrez, H. Gavilán, M. Brollo, S. Veintemillas-Verdaguer, M. del Puerto Morales, *Adv. Drug Deliv. Rev.* 138 (2019) 68-104.
12. Z. Nemati, J. Alonso, I. Rodrigo, R. Das, E. Garaio, J. García, I. Orue, M. Phan, H. Srikanth, *J. Phys. Chem. C*. 122 (4) (2018) 2367-2381.
13. S. Jackson, M. Marks, H. Katki, M. Cook, N. Hyun, N. Freedman, L. Kahle, P. Castle, B. Graubard, A. Chaturvedi, *Cancer*, 128 (19) (2022) 3531-40.
14. Z. Abbas, S. Rehman, *Neoplasms*. 1 (2018) 139-57.
15. <https://www.cancer.net>
16. D. Debela, S. Muzazu, K. Heraro, M. Ndalama, B. Mesele, D. Haile, S. Kitui, T. Manyazewal, *SAGE Open Med.* 9 (2021) 20503121211034366.
17. K. Kim, D. Khang, *Int J Nanomedicine.*, (2020) 5719-5743.
18. <https://www.cancer.org/cancer/managing-cancer/treatment>.
19. <https://www.cancer.gov/research/areas/diagnosis#recent-research-findings-in-cancer-diagnosis-research>
20. M Dessale, G. Mengistu, H. Mengist. *Int J Nanomedicine*. 17 (2022) 3735-3750.
21. D. Abshire, M. Lang, *Semin. Oncol. Nurs.* 34 (2) (2018) 151-157.

22. R. Hachadorian, P. Bruza, M. Jermyn, D. Gladstone, B. Pogue, L. Jarvis, *Nat. Commun.*, 11(1) (2020), 2298-2307.
23. T. Högberg, B. Glimelius, P. Nygren, *Acta Oncol.*, 40 (2-3), (2001) 340-360.
24. M. Ferrari, *Nat. Rev. Cancer*, 5(3) (2005) 161-171.
25. M. Verma, P. Sheoran, A. Chaudhury, *Advances in animal biotechnology and its applications*, (2018) 161-178.
26. J. Kemp, Y. Kwon, *Nano Converg.*, 8(1): (2021) 34 - 72.
27. R. Misra, S. Acharya, S. Sahoo, *Drug Discov. Today*, 15 (19-20) (2010) 842-850.
28. Y. Yao, Y. Zhou, L. Liu, Y. Xu, Q. Chen, Y. Wang, S. Wu, Y. Deng, J. Zhang, A. Shao, *Front. Mol. biosci.*, 7 (2020) 193 - 207.
29. M. Arruebo, N. Vilaboa, B. Sáez-Gutierrez, J. Lambea, A. Tres, M. Valladares, A. González-Fernández Á. *Cancers*. 3(3) (2011) 3279-3330.
30. Z. Lu, P. Qiao, *Mol. Pharmaceutics.*, 15(9) (2018) 3603-3616.
31. A. Mohapatra, S. Uthaman, I. Park, *Front. Mol. biosci.*, 7 (2021) 597634-68.
32. J. Kou, D. Dou, L. Yang, *Oncotarget*. 8(46) (2017) 81591–81603.
33. C. Zhang, X. Hu, L. Jin, L. Lin, H. Lin, Z. Yang, W. Huang, *Adv. Healthc. Mater.* (2023) 2300530.
34. H. Hou, X. Huang, G. Wei, F. Xu, Y. Wang, S. Zhou, *ACS Appl. Mater. Interfaces.*, 11(33) (2019) 29579-92.
35. J. Li, X. Wang, D. Zheng, X. Lin, Z. Wei, D. Zhang, Z. Li, Y. Zhang, M. Wu, X. Liu, *Biomater. Sci.*, 6(7) (2018) 1834-45.
36. A. Karagianni, N. Tsierkezos, M. Prato, M. Terrones, K. Kordatos, *Carbon*, 203 (2023) 273-310.
37. T. Yamaguchi, S. Kitahara, K. Kusuda, J. Okamoto, Y. Horise, K. Masamune, Y. Muragaki, *Cancers*, 13 (24) (2021) 6184-6196.
38. M. Lafond, S. Yoshizawa, S. Umemura, *J. Med. Ultrasound*, 38(3) (2019) 567-580.
39. P. Yan, L. Liu, P. Wang, *ACS Appl. Bio Mater.*, 3 (6) (2020) 3456-75.
40. A. Ma, H. Chen, Y. Cui, Z. Luo, R. Liang, Z. Wu, Z. Chen, T. Yin, J. Ni, M. Zheng, L. Cai, *Small*, 15 (5) (2019) 1804028-39.
41. B. Ma, S. Wang, F. Liu, S. Zhang, J. Duan, Z. Li, Y. Kong, Y. Sang, H. Liu, W. Bu, L. Li, *JACS*, 141 (2) (2018) 849-857.

42. L. Lin, J. Song, L. Song, K. Ke, Y. Liu, Z. Zhou, Z. Shen, J. Li, Z. Yang, W. Tang, G. Niu, *Angew. Chem.*, 130 (18) (2018) 4996-5000.
43. L. Lin, T. Huang, J. Song, X. Ou, Z. Wang, H. Deng, R. Tian, Y. Liu, J. Wang, Y. Liu, G. Yu, *JACS*, 141 (25) (2019) 9937-9945.
44. M. Vicentini, R. Ferrero, A. Manzin, *Adv. Theory Simul.* (2023) 2300234-2300246.
45. H. Etemadi, P. Plieger, *Adv. Therap.*, 3 (11) (2020) 2000061-2000110.
46. H. Burachaloo, P. Gurr, D. Dunstan, G. Qiao, *ACS Nano*, 12 (2018) 11819-11837.
47. S. Kossatz, J. Grandke, P. Couleaud, A. Latorre, A. Aires, K. Crosbie-Staunton, R. Ludwig, H. Dähring, V. Ettelt, A. L. Carrillo, I. Hilger, *Breast Cancer Research*, 17 (2015) 66-83.
48. O. Arriortua, M. Insausti, L. Lezama, I. Muro, E. Garaio, J. Martínezde, I. Fuente, M. Fratila, M. Morales, R. Costa, M. Eceiza, M. Aizpurua, *Colloids Surf. B Biointerfaces.*, 165 (2018) 315-324.
49. J. Lee, J. Jang, J. Choi, S. Moon, S. Noh, J. Kim, J. Kim, L. Kim, K. Park, J. Cheon, *Nat. Nanotechnol.*, 6 (2011) 418-422.
50. S. Noh, W. Na, J. Jang, J. Lee, E. Lee, S. Moon, Y. Lim, J. Shin; J. Cheon, *Nano Lett.*, 13 (2012) 3716–3721.

CHAPTER-2

Theoretical Background of Magnetic Nanoparticles and its Applications



2.1 Introduction

Recent progress in the field of nanomedicine holds excellent potential for the precise delivery of anticancer agents using specially designed nanomaterials. These nanomaterials, typically existing at the nanoscale, fall into two main categories: organic nanoparticles, including lipids, polymers, liposomes, dendrimers, and nucleic acids and inorganic nanoparticles including metal oxide-based nanoparticles, metal nanoparticles, and carbon nanoparticles are depicted in **Fig. 2.1**. Compared to traditional chemotherapy, nanoparticle-based drug carriers provide the advantages of well-tailored drug formulations and enhanced pharmacokinetics, allowing for targeted drug delivery to tumors while minimizing systemic toxicity [1]. MNPs have garnered substantial attention in biomedical research due to their versatile properties, encompassing crystallite size, structure, composition, rapid magnetic response, and excellent biocompatibility, making them prime contenders for drug delivery systems.

MNPs have gained significant recognition as versatile nanomaterials, finding applications in numerous biomedical domains such as MRI, MHT, magnetic targeting, magnetic separation, phototherapeutic responses, and targeted drug delivery [2-4]. Ongoing research and advancements in nanotechnology have enabled the precise fabrication of MNPs with specific morphologies, tailored surface modifications, and manipulating properties at the nanoscale [5]. MNPs typically comprise a magnetic core-shell enclosed by a polymer shell. The surface coating of MNPs improves their colloidal stability, providing the capability for covalent or electrostatic attachment of therapeutic payloads, targeting agents, and even supplementary imaging agents. Furthermore, this coating plays a pivotal role in adjusting various aspects of MNP properties, including their pharmacokinetics, systemic toxicity, clearance rate, non-specific protein adsorption, interactions with cells, and controlled drug release, among other factors.

Nanoparticles are solid colloidal structures with sizes ranging from 10 to 1000 nanometers. These small particles have specific advantages over bigger ones, such as a higher surface-to-volume ratio and unique physical, chemical, electrical, mechanical, thermal, and magnetic properties. Notably, ferromagnetic nanomaterials represent a significant class of materials, with their magnetic properties being greatly influenced by anisotropy factors such as structure, shape, and surface anisotropy [6]. Ferromagnetism in materials arises from interactions between free electrons, including spin-spin, spin-orbit, and coherent exchange interactions, causing the

alignment of their magnetic moments. When reduced to the nanoscale, ferromagnetism becomes size-dependent due to limited electron interactions. Adjusting the material's size, shape, and surface characteristics allows precise control over magnetic properties like coercivity and magnetization.

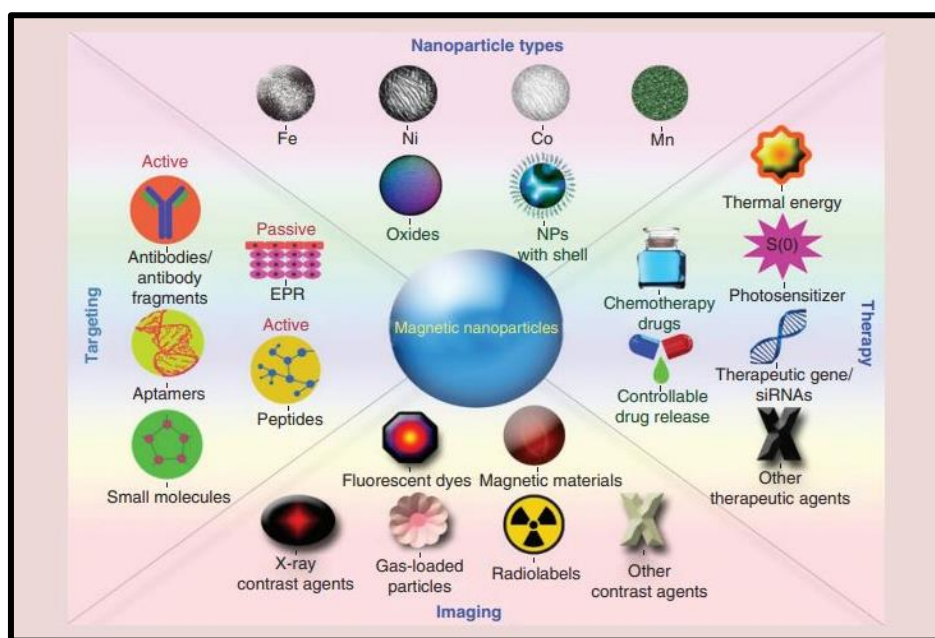


Figure 2.1 Various forms of theranostic magnetic nanoparticles, including their modifications and biomedical applications [7]

Nanostructured MNPs are synthesized using both physical and chemical techniques. Chemical methods are mainly based on solution-phase reactions. They have received significant attention due to their unique bottom-up approaches, enabling the creation of monodisperse MNPs with precise control over their dimensions, composition, and shape. These MNPs produced via chemical methods can be stabilized with organic surfactants and dispersed in different solvents. This provides two fundamental systems, both in solution and solid-state, for exploring various applications related to magnetism, magneto-optics, and magneto-electronics [8]. MNPs present several benefits: (i) their small size allows for intravenous injection and delivery through the bloodstream, reaching tumors that might be challenging to access (ii) The substantial surface-to-volume ratio of MNPs enables precise surface modifications with single or multiple targeting molecules, facilitating specific targeting of tumor tissues (iii) remote heating of MNPs using an externally AMF restricts heat generation exclusively to the area where the nanoparticles have accumulated [9].

Chapter I discusses the fundamental concepts of MNPs and their use in biomedical applications. Preliminary aspects of magnetic hyperthermia, modes of hyperthermia, and material properties used for MHT are discussed in this chapter. The effects of various physical properties on the heating of MNPs in MHT applications are addressed at the end.

2.2 Magnetic Nanoparticles in Hyperthermia

MNPs engineered for medical use hold the promise to bring about a paradigm shift in the field of medicine, diagnostic, therapeutic, and theranostic tools. Due to its abundance in living organisms and its vital role in numerous biological processes like oxygen transport and cellular respiration, iron emerges as a promising material for applications in the biomedical field. Iron oxide nanoparticles (IONPs), such as maghemite ($\gamma\text{-Fe}_2\text{O}_3$) and magnetite (Fe_3O_4), are particularly noteworthy among nanomaterials, as they can be safely injected into the body and metabolized naturally. Magnetite-based MNPs have gained recognition as promising candidates for biological applications due to their exceptional magnetic properties, biocompatibility, and biodegradability. The FDA has approved several magnetite-based MNP products for human use [10]. Pure iron oxides are commonly used in biomedical applications; IONPs doped with magnetically susceptible elements or metal alloy nanoparticles are less employed due to potential toxicity and rapid oxidation despite their more vital magnetism. The toxicity, metabolic pathways, and pharmacokinetics of IONPs administered intravenously have been subject to comprehensive research. Specific IONP-based MRI contrast agents have undergone clinical trials [11].

2.2.1 Types of Magnetic Nanoparticles

MNPs are classified based on their magnetic behavior, encompassing diamagnetic, paramagnetic, ferromagnetic, ferrimagnetic, and antiferromagnetic materials, contingent on the orientation of magnetic dipoles in the presence or absence of an external magnetic field shown in **Fig. 2.2**. Diamagnetic nanomaterials lack magnetic dipoles without a magnetic field but generate dipoles opposing when applied to the external field. Paramagnetic nanomaterials exhibit randomly oriented dipoles without a magnetic field yet align in response to an external magnetic field. Ferromagnetic materials have permanent magnetic dipoles, maintaining their orientation regardless of the magnetic field. In antiferromagnetic materials,

neighboring dipoles are antiparallel and mutually cancel each other out when no magnetic field is present.

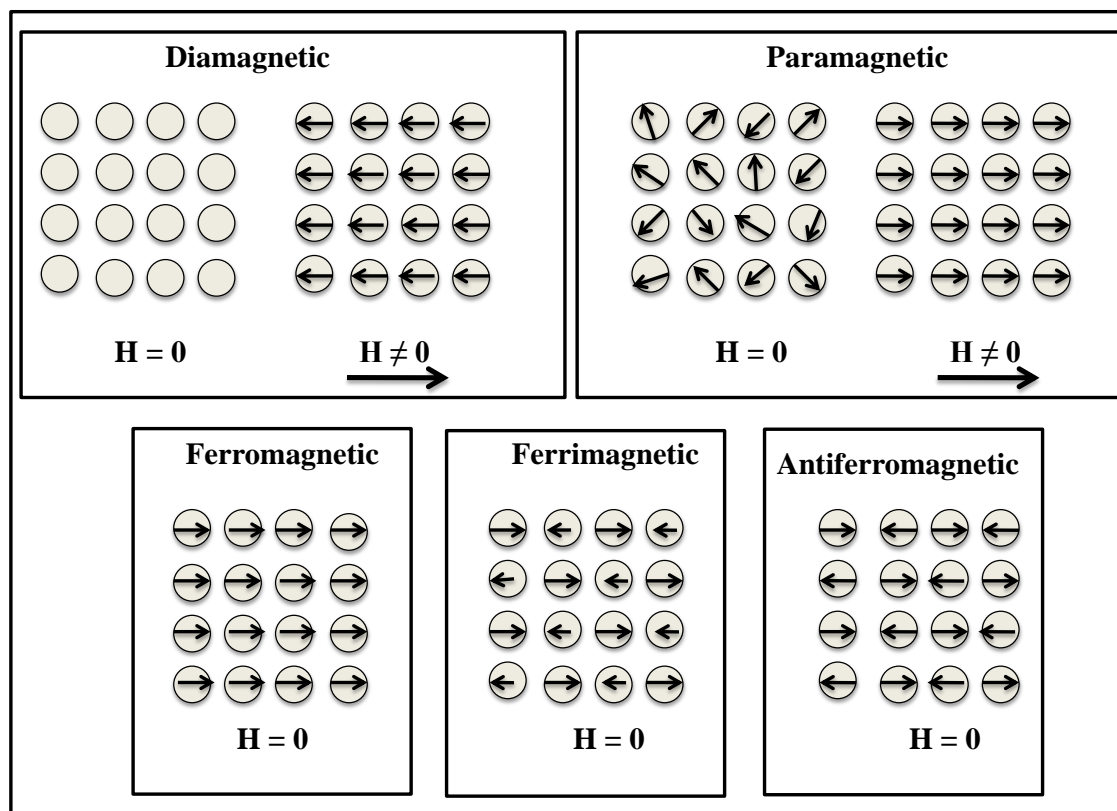


Figure 2.2 Schematic representation of magnetic dipole arrangements in various materials, including diamagnetic, paramagnetic, ferromagnetic, ferrimagnetic, and antiferromagnetic substances, both in the absence and presence of an external magnetic field (H).

2.2.2 Properties of Magnetic Nanoparticles

The hysteresis curve of ferromagnetic materials reveals key parameters such as saturation magnetization (M_s), remanent magnetization (M_r) at zero applied field, and coercivity (H_c), which is the external field needed to bring the magnetization to zero. Above the blocking temperature (T_B), both ferromagnetic and ferrimagnetic materials exhibit (Superparamagnetic) SPM behavior. Zero Field Cooling (ZFC) curves measure the magnetization of a material as it is cooled without an external magnetic field. In contrast, Field Cooling (FC) curves assess the magnetization when the material is cooled under the influence of an external magnetic field. The experimental determination of T_B relies on the point where the ZFC and field-cooled FC magnetization curves converge. T_B can be calculated using the formula:

$$T_B = \frac{KV}{25K_B} \quad (2.1)$$

where K stands for the anisotropy constant, V refers to the volume of the MNPs, and K_B represents the Boltzmann constant. In bulk magnetic materials, the magnetic properties, such as hysteresis, are mainly determined by a magnetic structure of magnetic domains separated by domain walls. However, when the particle size drops below a certain threshold, having a single magnetic field rather than multiple domains becomes more energetically favorable. This critical size for a monodomain depends on a balance of several energies within the material, which is determined by factors such as the composition and shape of the MNPs and the domain wall energy. Most magnetic materials show magnetic anisotropy, indicating they align a specific direction for magnetization, usually aligned with one of the crystal axes. Monodomain MNPs generally possess two stable magnetic orientations that are antiparallel to each other, aligned along this easy axis of magnetization. An energy barrier separates these orientations called the anisotropic energy (E_a), which is directly proportional to the product of the magneto-crystalline anisotropy constant (K) and the magnetic volume (V) of the MNPs ($E_a = KV$). As the size of the nanoparticles decreases, the energy barrier for reversing the magnetic spin also decreases. When the thermal energy ($K_B T$) becomes sufficiently high, the particle spins switch randomly between these energy minimis. Below a specific critical diameter, thermal activation causes the magnetic moments of the particles to reverse spontaneously and continuously, leading to an average total magnetic moment of zero for the particle [12].

The nano size of MNPs also leads to a decrease in their M_s values despite M_s being an intrinsic property. This reduction in M_s for very small MNPs is attributed to surface effects. When a magnetic field is applied, the magnetic moments of MNPs align with the magnetic field, increasing magnetization (M). Once all the magnetic moments align with the magnetic field, the material reaches magnetic saturation, exhibiting its M_s . Magnetic materials exhibit exciting properties based on their response to magnetic fields. When the direction of the magnetic field is reversed, the magnetization decreases. Still, some alignment of magnetic moments continues even when the magnetic field decreases to zero, resulting in what is known as M_r . To eliminate this magnetization, the magnetic field must be reversed, and the magnetic field required to achieve this is referred to as the coercive field or coercivity (H_c).

Magnetic materials are generally classified as soft-magnetic or hard-magnetic based on their H_c . Soft-magnetic materials have low H_c values and exhibit narrow magnetic hysteresis loops.

On the other hand, hard-magnetic materials possess wide hysteresis loops, substantial coercivity values, and significant remanent magnetization. These materials are typically used to produce permanent magnets. Hard-magnetic materials include rare-earth transition-metal alloys, hexaferrites based on $MFe_{12}O_{19}$ (usually $M =$ barium or strontium), and $\gamma\text{-Fe}_2\text{O}_3$.

The electronic structure of the magnetic atoms or ions and the material's crystal structures shape the basic properties of magnetic materials. These factors impact the strength of the magnetic coupling within the material, thereby influencing its M_s and magnetocrystalline anisotropy. In particular, the value of M_s depends on the magnetic moments of the atoms/ions and the distance and angle between neighbouring magnetic atoms/ions.

2.2.3 Iron Oxide-Based Magnetic Nanoparticles

Ferrite is a ceramic-like material with magnetic properties that make it useful in various electronic devices. It is hard brittle, contains iron, and is typically grey or black. Ferrites are polycrystalline, meaning they are composed of many small crystals. Ferrites are typically ferrimagnetic ceramic compounds derived from iron oxides, with magnetite (Fe_3O_4) being a well-known example. Like most ceramics, ferrites are brittle, hard, and poor conductors of electricity. IONPs, with diameters typically ranging from 1 to 100 nm, are a focus of extensive research due to their biocompatibility and ease of synthesis. These nanoparticles often comprise nanocrystalline magnetite (Fe_3O_4) or maghemite ($\gamma\text{-Fe}_2\text{O}_3$) and have a spinel crystal structure. The unique magnetic properties of MNPs are achieved by varying the types of cations occupying these crystal positions. Metal ferrites can be adjusted in composition, typically $M\text{Fe}_2\text{O}_4$, where M represents divalent cations such as Mn, Fe, Co, or Ni, with a valence of +2. This compositional adjustment allows for fine-tuning of specific magnetic properties. When the particle size is reduced, these nanoparticles exhibit SPM behavior, preventing them from self-aggregating. SPM nanoparticles only display magnetic properties in an external magnetic field. To enhance the stability of MNPs in aqueous solutions, surfactants like silica, phosphoric compounds,

or silicones are often used to modify the nanoparticle surfaces [13-14]. These surface-modified nanoparticles are used for biomedical applications.

Spinel ferrites have a general AB_2O_4 formulation, where A and B represent metal ions arranged in A-O tetrahedra and B-O octahedra, respectively. Within the crystal structure, a unit cell consists of 32 oxygen atoms and 24 cations in various positions. These positions contain six octahedral and eight tetrahedral sites, resulting in 32 octahedral and 64 tetrahedral sites. Spinel materials, like spinel ferrites, are divided into three categories based on the distribution of divalent metal ions and Fe^{3+} on cationic sites: normal, inverse, and complex. These rigid ferrimagnetic oxide materials comprise Fe^{3+} and other bi- and trivalent cations. A cubic unit cell contains eight formula units. Oxygen (O_2) creates a cubic close-packed structure, with metal cations occupying 8 of the 64 tetrahedral sites (A-sites) and 16 of the 32 octahedral sites (B-sites).

Bivalent metal cations occupy the tetrahedral sites in a normal spinel structure, while trivalent cations exist in the octahedral sites. Most ferrite nanoparticles exhibit SPM properties when their size is below or around 20 nm in diameter. In a single unit cell of spinel ferrite, 64 available tetrahedral positions and 32 octahedral positions for cations, but only eight tetrahedral and 24 octahedral sites are occupied. In an inverse spinel structure, eight bivalent cations occupy octahedral sites, while eight trivalent cations fill the tetrahedral sites, with the remaining eight trivalent cations also occupying octahedral sites. Smaller cations tend to prefer the tetrahedral sites, and since trivalent cations are smaller than bivalent ones, they favor the tetrahedral sites, making inverse spinel structures more common in ferrites [6]. These ferrites comprise 32 oxygen atoms distributed among 32 trivalent octahedral sites and 64 divalent tetrahedral sites. Specifically, in these structures, divalent cations (M^{2+}) and trivalent cations (Fe^{3+}) occupy specific sites to maintain an electrically balanced state. In the standard or typical spinel ferrite structure, divalent cations (M^{2+}) are found in tetrahedral sites, while trivalent cations (Fe^{3+}) are in octahedral sites. Examples of this structure include $ZnFe_2O_4$ and $CdFe_2O_4$. In an inverse spinel ferrite structure, divalent cations (M^{2+}) occupy only octahedral sites, whereas trivalent cations (Fe^{3+}) are equally distributed between tetrahedral and octahedral sites. Examples of this structure include Fe_3O_4 , $NiFe_2O_4$, and $CoFe_2O_4$. Complex spinel ferrite structures randomly distribute M^{2+} and Fe^{3+} cations across tetrahedral and octahedral sites.

Examples of complex spinel ferrites include MnFe_2O_4 and MgFe_2O_4 [15]. **Fig 2.3** shows the crystal structure of spinel ferrite.

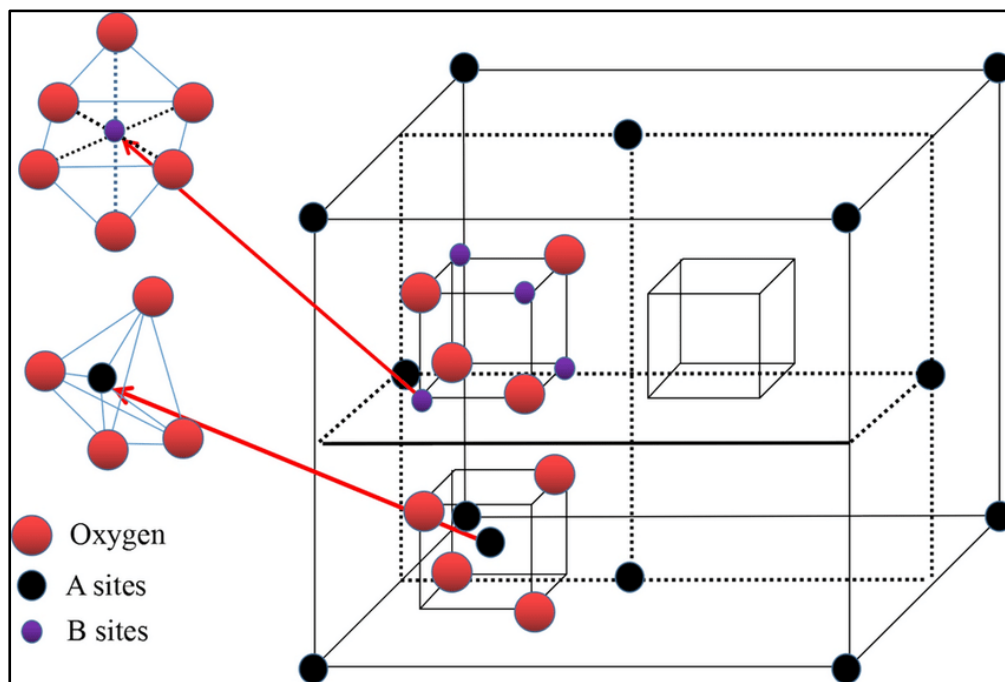


Figure 2.3 Crystal structure of spinel ferrite [16]

2.2.4 Manganese Iron Oxide Nanoparticles (MnFe_2O_4)

MnFe_2O_4 , a well-known soft magnetic material, has gained significant attention from researchers due to its remarkable magnetic and electromagnetic properties, low cost, large surface area, good chemical stability, mechanical hardness, catalytic properties, and environmental friendliness. MnFe_2O_4 nanoparticles exhibit a mixed spinel structure (**Fig. 2.4**), where Mn^{2+} and Fe^{3+} cations occupy A (tetrahedral) and B (octahedral) sites within a face-centered close-packed arrangement of oxygen anions.

$$[\text{Mn}_{1-i}^{2+}\text{Fe}_i^{3+}]_A [\text{Mn}_i^{2+}\text{Fe}_{2-i}^{3+}]_B \text{O}_4 \quad (2.2)$$

In this formula, 'i' represents the inversion parameter, which indicates the degree of inversion. In normal spinels ($i = 0$), all Mn cations occupy tetrahedral sites, while in inverse spinels ($i = 1$), they are located in octahedral sites [17]. MnFe_2O_4 nanoparticles have garnered significant attention in electronic systems due to their soft-magnetic properties, including low coercivity, high magnetic permeability, and moderate saturation magnetization. Additional benefits of MnFe_2O_4 nanoparticles include their SPM nature, ease of preparation, high chemical stability, high electrical resistivity, and high crystal symmetry. Additionally, MnFe_2O_4 nanoparticles have

been identified as effective heat sources in magnetic hyperthermia-based cancer therapy, as they generate heat when exposed to AMF. The heating efficiency of MnFe_2O_4 nanoparticles in an oscillating magnetic field is closely tied to their saturation magnetization, which is heavily influenced by particle size, shape, and the distribution of cations between tetrahedral and octahedral sites. These properties can be regulated by the synthesis methods and conditions used [18,19].

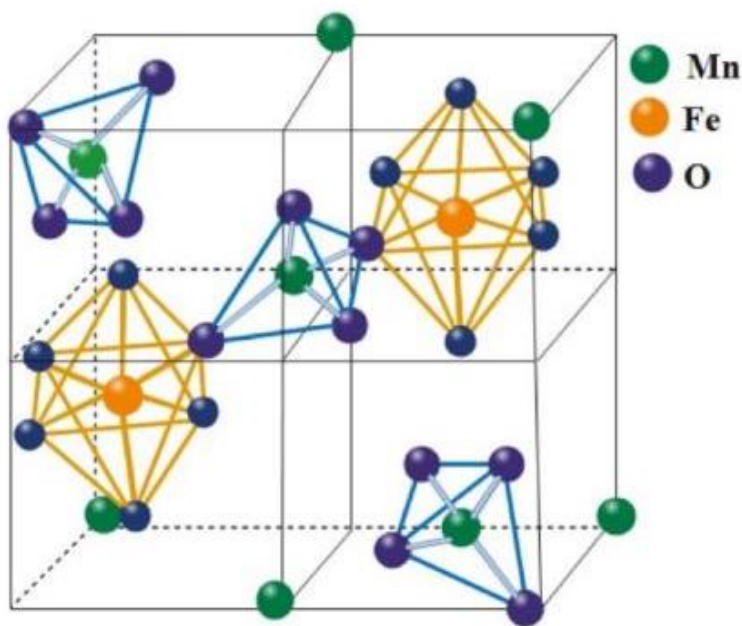


Figure 2.4 Structure of manganese ferrite showing tetrahedral (T_d) and octahedral (O_h) sites [20]

In particular, spinel manganese-iron oxide ($\text{Mn}_x\text{Fe}_{3-x}\text{O}_4$) systems exhibit distinctive features such as high magnetic moment values around five μ_B per unit cell, excellent chemical stability, high saturation magnetization, minimal or nearly zero coercivity, and surfaces well-suited for ligand functionalization and bioconjugation. Manganese has garnered special interest in biomedicine among various cations due to its multiple oxidation states. Manganese's most common valence states are Mn^{2+} , Mn^{3+} , and Mn^{4+} . Mn^{2+} ions are the most stable compared to Mn^{3+} and Mn^{4+} ions, thanks to their half-filled outer 3d electron shell. Additionally, the manganese valence states influence the magnetic properties of the nanoparticles; Mn^{2+} ions, with their five unpaired electrons, exhibit the highest relaxivity, followed by Mn^{3+} and Mn^{4+} ions. MnFe_2O_4 has been of primary interest among spinel ferrites due to its suitability for biological applications. MnFe_2O_4 has a bulk saturation magnetization (M_s) of 80 emu/g, similar to the M_s values of bulk Fe_3O_4 and $\gamma\text{-Fe}_2\text{O}_3$ (approximately 90 emu/g

and 80 emu/g, respectively). Additionally, it has an anisotropy constant of $K = 2.5 \times 10^3 \text{ J/m}^3$ at room temperature [21]. **Table 2.1** presents various synthesis methods, highlighting how variations in shape, size, magnetic saturation, and the choice of capping agents impact the effectiveness of hyperthermia applications.

Table 2.1: Literature survey on MNPs used for hyperthermia application

Sr. No.	Synthesis Method	Morphology	Size (nm)	Magnetic saturation M_s (emu/g)	Capping agent	SAR (W/g)	Ref. No.
1	Co-condensation	Cubic-spinel	23	63.4	Poly (l-lysine)	201	[22]
2	Seed-mediated growth method	Spherical	≈ 12.1 to 18	40.2- 31.2	Chitoson/ Dimercapto Succinic Acid (DMSA)	1.15-1.20	[23]
3	Hydrothermal	Cubic	9.3	38.4	Polystyrene-Poly Ethylene Glycol (PS-PEG)	145	[24]
4	Thermal Decomposition	Cube-like	60	-	Polyvinyl pyrrolidine (PVP)	215	[25]
5	Co-precipitation	Spherical	10-14	40.6 to 63.4	Polyamidoamin edendrimer (PAMAM)	49.8-129.3	[26]
6	Thermal decomposition	Nanocubes	27	62.1	Poly-maleic anhydride-alt-1-octadecene) (PMAO)	-	[27]
7	Co-precipitation	Spherical	≈ 20	54	Silica	217.62	[28]
8	Polyol method	Multicore structure	30-80	54-18	Polyethylene Glycol (PEG)	965	[29]
9	Seed-mediated growth method	Nanostar	16-20	71-68.1	Dimethylformamide (DMF)	15-140	[30]

It is observed in the literature that non-spherical MNPs can generate more heat than conventional spherical MNPs of the same size. Controlling the shape of MNPs is key to achieving the desired temperature. With this intention, in the present

work, manganese iron oxide nanostructures (such as nanocube, polyhedron) will be synthesized. The effect of manganese composition in iron oxide will also be evaluated to optimize magnetocrystalline anisotropy, thereby improving induction heating. Properly tuned, such magnetic nanostructures are expected to produce a high value of SAR.

2.3 Biomedical Applications

The magnetic anisotropy and magnetization of nanoscale MNPs can better those of bulk materials. Multiple factors influence the magnetic properties of these materials, with chemical composition, particle size, shape, morphology, and nanoparticle interactions being the primary determinants [31]. Among ferrite nanoparticles, those doped with manganese are particularly promising for biomedical applications. These nanoparticles have a high Curie temperature, mild saturation magnetization, high coercivity, high magneto-crystalline anisotropy, and chemical stability. Researchers have explored their potential uses in MHT and as contrast agents in MRI [32]. The Different properties and possible applications of MnFe_2O_4 -based nanostructures are shown in **Fig. 2.5**.

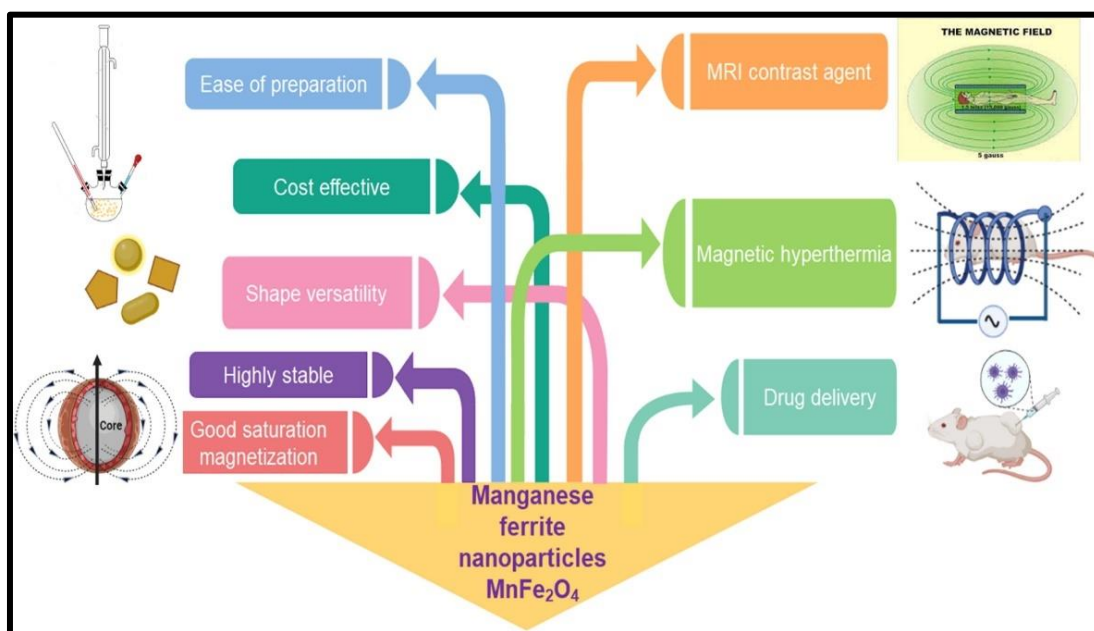


Figure 2.5 Applications of manganese iron oxide nanoparticles in various fields [21]

Stable and biocompatible functionalized MNPs can serve various roles in theranostics. They can be utilized as agents for MRI, MHT when exposed to high-frequency AMF, and magnetic drug targeting and delivery. MNPs offer a crucial

advantage due to their controllable sizes, which can be much smaller than cells (9-99 μm), proteins (4-49 nm), or viruses (19-451 nm). Their key attributes, such as biocompatibility and the ability to aggregate precisely in desired tissues, make them an ideal choice for biomedical applications. These particles need to be of a size that allows for biological circulation, are small in scale, and are explored in numerous applications [33 -35].

2.3.1 Targeted Drug Delivery (magnetically triggered)

Targeted drug delivery is a method that enhances the concentration of medication in specific areas of the body compared to others. This approach is primarily based on nanomedicine, which aims to use nanoparticle-based drug delivery to overcome the limitations of traditional methods. The nanoparticles are loaded with drugs and directed to areas with diseased tissue, minimizing interaction with healthy tissue. A magnetic field is the control mechanism that ensures efficient drug delivery to the desired location. Using MNPs in drug delivery is crucial for cancer treatment, targeted drug delivery to tumors, and improving efficient gene delivery systems. These systems offer precise targeting of specific locations within the body, a reduction in the necessary drug quantity to achieve the desired concentration at the target site, and a decrease in drug concentration at non-target sites, ultimately mitigating severe side effects. MNPs serve as carriers for drugs, directing them to the tumor. Once the drug enters the bloodstream, a magnetic field is applied to retain the particles at the tumor site. This has emerged as a highly promising treatment for cancer. When coupled with an external magnetic field, these nanoparticles can be manipulated to transport the drug to the target site, anchor the particles in place, release the medication, and accomplish magnetic drug targeting [36- 38].

Drug delivery using nanostructures occurs through two primary mechanisms: passive and self-delivery. In passive delivery, drugs are bounded within the structure's inner cavity, primarily through hydrophobic interactions. In self-delivery, drugs meant for release are directly linked to the carrier nanostructure, ensuring efficient delivery. Drug targeting within nanoformulations can be further categorized as active or passive, as diagrammatically shown in **Fig.2.6**.

Active targeting in drug delivery involves the attachment of specific moieties like antibodies and peptides to drug delivery systems. These moieties bind the drug delivery system to receptor structures at the target site. Active targeting relies

on the overexpression of distinct epitopes or receptors in tumor cells and specific physical characteristics. Consequently, carriers that respond to physical stimuli such as temperature, pH, electric charge, light, sound, and magnetism have been created and linked to drugs. Active targeting can also be achieved by utilizing the overexpression of specific molecules, such as low molecular weight ligands like folic acid, thiamine, and sugars, along with peptides, proteins antibodies, lectins, polysaccharides like hyaluronic acid, peptides, DNA, and others.

Passive targeting involves drug carrier complexes that circulate through the bloodstream and reach the target site based on properties like pH, temperature, molecular size, and shape, leading to affinity or binding. Common targets in the body include cell membrane receptors, lipid components of cell membranes, and cell surface antigens or proteins. Passive targeting frequently depends on the enhanced permeability and retention effect and is commonly linked to drug-conjugated dendrimers and dendritic polymers [39].

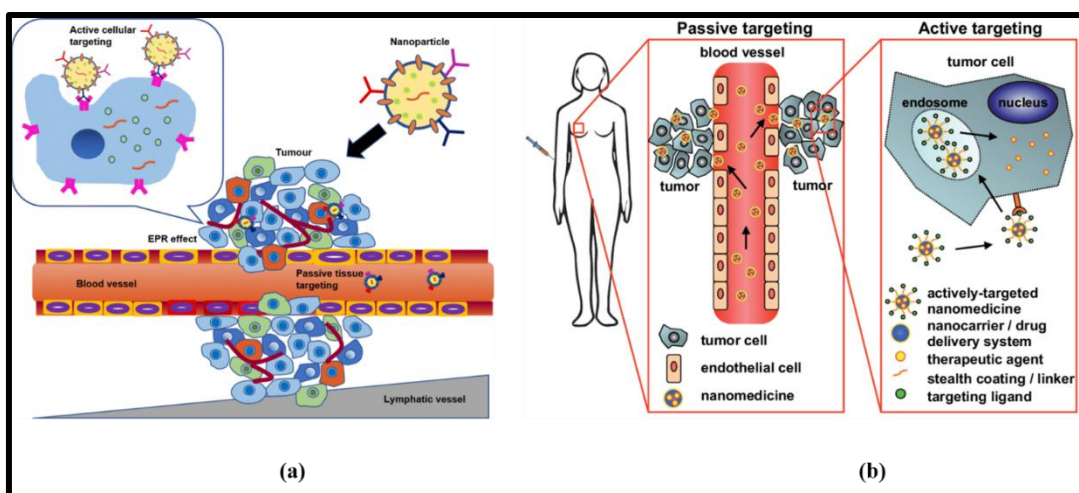


Figure 2.6 Drug targeting approaches: (a) Passive targeting, (b) Active targeting [40, 41]

The localization of drugs using magnetic delivery systems relies on the interaction between forces acting on the particles from the bloodstream and the magnetic forces generated by an applied field, such as a magnet. When the magnetic forces exceed the linear blood flow rates in arteries (10 cm/s) or capillaries (0.05 cm/s), the MNPs are retained at the desired target site. They may also be absorbed by the endothelial cells in the targeted tissue. MNPs are introduced via an intra-arterial route using a catheter. These drug-loaded magnetic carriers are introduced into an artery specifically selected for its connection to the tumor. A permanent dipole

magnet is positioned directly over the cancer on the patient's body to concentrate the particles. Following a specified duration, during which the particles have migrated into the surrounding tissues, the magnet is removed. The particles remain trapped in the tumor, where the drug is released. The loading and release of bioactive material from the polymer coating is a significant parameter that decides the efficiency of magnetic polymeric particles in therapy [37].

Methods for loading drugs onto magnetic particles can be broadly classified into two primary categories: chemical bonding and physical bonding. Chemical bonding typically involves the formation of covalent bonds using the amino, carboxyl, and thiol groups found on the surfaces of both the MNPs and the drug. Polymer coating often introduces These functional groups to the magnetic particle surface. The same chemical groups can also attach peptides, antibodies, and viruses, thereby improving targeting. External factors like a controlled temperature increase or internal factors, such as a change in pH, can trigger drug release after magnetic stimulation. Physical binding involves electrostatic, hydrophilic/hydrophobic, and affinity interactions. These interactions offer advantages such as rapid binding and high efficiency but often result in early drug release. Magnetic fields are suitable for medical applications as they do not disrupt biological processes. Nevertheless, several challenges are linked to utilizing magnetic carriers and vectors in targeted drug delivery systems [42].

Advantages

Disadvantages

It prevents the medication from degrading.	Leakage and fusion of the medication within is observed.
The patient's dose required decreases.	Short half-life because of its chemical and physical instability
Deliver the most insoluble medicines.	The low loading capacity of drug ejection during crystallization and the comparatively high-water content of the dispersions are some disadvantages of nano delivery.
Targeted drug delivery with the aid of liposomes and exosomes to targeted organs	Disruption of autonomic imbalance directly impacts heart and vascular function.

2.3.2 Magnetic Resonance Imaging (MRI)

MRI is a non-invasive imaging technique that produces detailed cross-sectional images of internal structures using non-ionizing electromagnetic radiation. It is based on the principle of nuclear magnetic resonance, where atomic nuclei, exposed to a strong magnetic field, absorb and emit electromagnetic waves at specific resonant frequencies in the radiofrequency (RF) range. This signal contains rich information about tissues' biochemistry and gross structural properties, making MRI an incredibly versatile imaging tool. MRI techniques can be customized to enhance specific features of interest, providing high-resolution images of particular structures like white matter tracts, lesions, and arteries. While MRI was initially used for anatomical depiction, it is now evolving to capture functional properties and localized spectra. MRI finds diverse clinical uses encompassing neurological, psychiatric, cardiac, abdominal, musculoskeletal, and vascular imaging. This versatility positions MRI as one of the most influential and versatile medical imaging technologies [43].

MRI is a medical imaging technique used to visualize thin slices of soft tissues in the human body in two and three dimensions. It relies on the interaction of water within our bodies. The hydrogen nuclei in water align themselves with an applied external magnetic field. To produce MRI images, an RF signal is employed to change the orientation of these hydrogen nuclei, and the RF signal's frequency must match that of the hydrogen nuclei. When the directions of these nuclei change due to the RF signal, they re-align with the applied magnetic field, releasing energy in the form of an RF signal, which is then detected by MRI equipment. The realignment rate of these nuclei varies among different body tissues, aiding in precisely imaging these tissues. The duration required for this realignment is referred to as relaxation time, which is categorized into two types: T1 (longitudinal or spin-lattice relaxation) and T2 (transverse or spin-spin relaxation). These relaxation times are based on how long the components of the respective magnetization vectors are to return to their original thermal equilibrium state. Relaxivities (r_1 and r_2) are inversely related to the relaxation times (i.e., $r_1 = 1/T_1$; $r_2 = 1/T_2$). The ratio of relaxivities is crucial in determining whether nanoparticles will be used as a positive or negative contrast agent in MRI. The saturation magnetization of nanoparticles and their interactions with protons in the surrounding water molecules affect T1 and T2 relaxations. The process involving the precession of nuclei in the direction of a magnetic field is akin

to a device with a spinning wheel or gyroscopes, known as Larmor precession. The ‘Frequency of Larmor precession’ (ω_0) is determined by **Equation 2.3**, and it is directly correlated with the intensity of the applied magnetic field [44].

$$\omega_0 = \gamma B_0 \quad (2.3)$$

Where B_0 is the applied magnetic field strength, γ is the gyromagnetic ratio and is the nuclei-specific constant. The value of γ for hydrogen is 42.6 MHz/Tesla. **Fig. 2.7** displays the hydrogen atoms nuclei aligned in the direction of the applied magnetic field.

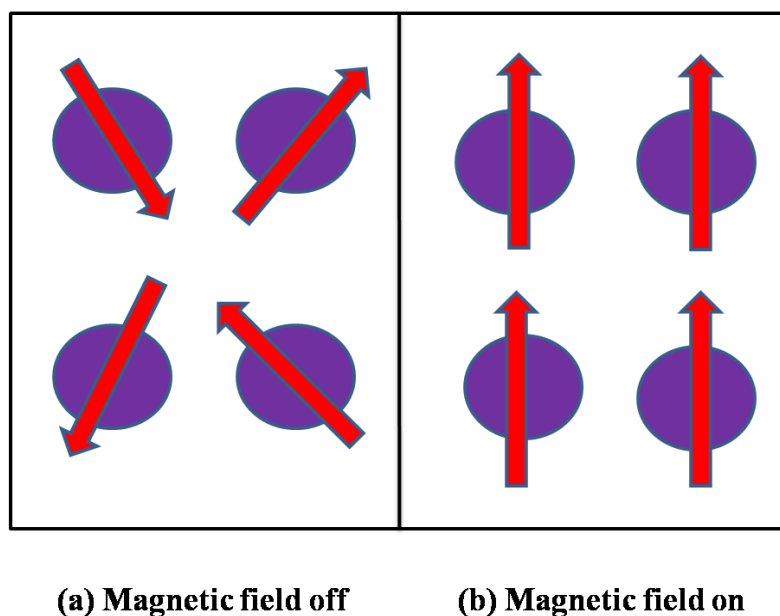


Figure 2.7 Hydrogen nuclei (a) magnetic field is absent (b) magnetic field is present.

At a mechanical level, variations in the pathological characteristics of biological samples create different chemical and physical environments. These differences lead to distinct outcomes in the computation of nuclear relaxation via MRI. MNPs influence the nuclear relaxation of magnetic nuclei in their vicinity by generating a local magnetic field. This accelerates the relaxation process and reduces the relaxation time of nearby protons, ultimately enhancing the contrast in MRI images. Throughout this process, two primary relaxation mechanisms are consistently employed in MRI: longitudinal and transverse relaxation, abbreviated as T1 and T2 relaxation, respectively. Depending on the specific magnetic properties of MNPs, various MNPs used as contrast agents can significantly augment the contrast in either T1-weighted or T2-weighted MRI [45-46].

Advantages	Disadvantages
Highly effective for the precise scanning and detection of abnormalities in soft tissue structures, including cartilage and delicate organs like the brain and heart	Performed in an enclosed area and some people may become afraid to be in a closely contained area during the scan due to the loud noises produced by the magnets
It does not expose individuals to radiation, making it a safe imaging option, particularly for those vulnerable to radiation's effects, such as pregnant women and infants.	Particular ear protection may be necessary due to loud noises, generally known as clicking and beeping, as well as sound intensities up to 120 dB in some MR scanners

2.3.3 Magnetic Hyperthermia Therapy (MHT)

Hyperthermia is the medical context involves the therapeutic exposure of a specific region to elevated temperatures above average body temperature (around 37°C in humans). The effectiveness of this treatment is rooted in the distinct heat tolerance of healthy tissue compared to cancerous cells. Due to their rapid growth and compromised vascular supply, tumor cells are more vulnerable to elevated temperatures, and temperatures above 42°C can significantly impact their survival. In recent years, hyperthermia has been recognized as an alternative or complementary approach to treating cancer. Moderate temperature increases (41-46°C) can alter cellular functions, induce cellular degradation, and eventually lead to controlled cell death or apoptosis.

In contrast, temperatures exceeding 50°C cause rapid cell death, resulting in tissue necrosis, a procedure known as thermoablation. By utilizing the heat generated when MNPs are exposed to an alternating current (AC) magnetic field, MHT is created. Gilchrist et al. initially presented this method in 1957 with a revolutionary study involving locally heating lymph nodes laden with MNPs [47]. In MHT, MNPs are selectively introduced as heat mediators into the tumor, exposing the cancer to an external AMF. This process raises the tumor's temperature by generating heat from the internalized magnetic nanoparticles under high-frequency AMF. This heat is produced due to the dissipation of magnetic energy in single-domain particles through internal Néel and Brownian relaxation. The actual MHT setup is shown in **Fig. 2.8**



Figure 2.8 Magnetic hyperthermia therapies [48]

The increased temperature eliminates cancer cells through various direct mechanisms, including protein denaturation, folding, aggregation, apoptosis, necrosis, and coagulation. Additionally, it indirectly activates the immune system by promoting the overexpression of heat shock proteins. MHT has not reached its full clinical potential due to challenges in efficiently and locally heating malignant cells. To address this, MNPs can be intravenously administered, explicitly targeting cancer cells accumulating in the tumor. Magnetite and maghemite nanoparticles are commonly used materials for MHT. The heat generated by MNPs in response to an AMF is primarily due to two mechanisms: hysteresis and relaxation losses. In MHT, electromagnetic energy is converted into heat. MNPs are distributed near the target region, and an AMF is employed. This field supplies the requisite energy for the magnetic moments within the nanoparticles to surpass their energy barriers for reorientation. Consequently, energy is emitted as the magnetic moments within the nanoparticles gradually revert to their equilibrium state. This sequence of events results in the heating of the nanoparticles through mechanisms such as Brownian rotation or Néel relaxation [49].

MNPs are delivered to tumors using intertumoral, intra-arterial, intracavitary, and intravenous administration. Oral administration is not feasible due to nanoparticle

excretion. Intertumoral and intracavitary approaches localize MNPs effectively for primary tumor heating. However, intravenous administration is the most versatile for treating various oncological conditions. Iron oxide MNPs, when delivered intravenously, accumulate in tumors partly due to the enhanced permeability and retention effect, which capitalizes on tumor vasculature permeability and poor lymphatic drainage. Attaching target ligands like antibodies, receptor-specific ligands, peptides, and aptamers to MNPs enhances uptake by malignant cells. This causes the targeted heating of the tumor while protecting neighboring healthy tissues when exposed to an AMF. Despite promising preclinical results in MHT, several challenges remain, including establishing optimal magnetic field strength and frequency limits, their correlation with treatment duration, the toxicity of MNPs (which depends on specific ligands), and determining the ideal nanoparticle concentration in the affected organ [50-52].

Advantages

Disadvantages

In contrast to near-infrared (NIR) laser-based hyperthermia, MHT exhibits superior tissue penetration capabilities for the magnetic field and enhanced accumulation of MNPs in the tumor through magnetic targeting, making it a more potent approach for cancer treatment.

Safety, Effectiveness, and Dosing: The safety, effectiveness, and appropriate dosage of MHT remain uncertain. This includes determining the optimal amount of MNPs administered, selecting magnetic parameters, and determining the power of the AMF, all of which are critical for achieving effective hyperthermia.

Hyperthermia can improve the efficacy of other cancer treatments, such as chemotherapy and radiation therapy.

Lack of Temperature Measurement: Precisely measuring the local temperature rise achieved *in vivo* during treatment is a challenge

Because of their synergistic effects, MHT-based multimodal cancer therapies, particularly when combined with chemotherapy, are more successful in treating cancer.

The normal tissues in the treated area may experience bleeding, edema, clots of blood, and other side effects. However, the majority of these adverse effects become better with therapy. After total body hyperthermia, diarrhea, nausea, and vomiting are frequently experienced.

2.4 Magnetic Hyperthermia Therapy (MHT)

2.4.1 Modes of Hyperthermia

The two main components of hyperthermia treatment are internal and exterior hyperthermia. While internal hyperthermia involves the introduction of specific substances into the body to serve as heat sources, external hyperthermia is induced by applying heat from sources outside the body, which can include various methods like microwaves, radiofrequency, ultrasound, and more. The National Cancer Institute (NCI) classifies hyperthermia into three categories, and these classifications are based on the size of the treated area:

a-) **Local Hyperthermia**

In hyperthermia therapy, heat is applied explicitly to a localized area, often a tumor, using various energy sources like microwaves, radiofrequency, or ultrasound. Tumors typically have leaky blood vessels, which allow MNPs to passively enter the tumor cells based on the particles' biophysiochemical properties [53, 54]. Hyperthermia therapy comes in various forms tailored to the location and depth of the tumor:

- **External hyperthermia** is employed for tumors near or just below the skin. Devices generating heat are placed around or near the treatment area.
- **Intraluminal or endocavitary hyperthermia** is a treatment approach designed for tumors located within or close to body cavities, such as the esophagus or rectum. This method involves the insertion of heat-emitting probes into the cavity, directing them toward the tumor.
- **Interstitial hyperthermia** is suitable for deep-seated tumors, such as those in the brain, and allows for higher-temperature heating. Under anesthesia, probes or needles are carefully inserted into the cancer, with the aid of imaging techniques like ultrasound, to ensure precise probe placement. Subsequently, a heat source is introduced for the procedure.

b-) **Regional hyperthermia**, employed in treating locally advanced cancer through perfusion or microwaves, utilizes techniques like external applicators or regional perfusion to heat substantial tissue volumes, including body cavities, organs, or limbs. When a patient has regional hyperthermia, medical professionals provide heat to sizable body parts like a cavity, organ, or limb. Deep tissue procedures, regional

perfusion, and continuous hyperthermic peritoneal perfusion are methods utilized to treat regional hyperthermia.

- **Deep tissue** procedures are employed to address internal tumors, such as those found in cases like bladder or cervical cancer. Heat-delivering devices are positioned around it to boost the temperature of the cavity or organ to be treated, and energy is directed there.
- **Regional perfusion** techniques are applied to manage cancers in the arms and legs, like melanoma, or in specific organs, such as the liver or lung. In this process, a portion of the patient's blood is extracted, heated, and re-circulated into the affected limb or organ. In some cases, chemotherapy is administered concurrently with this treatment.
- **Continuous hyperthermic peritoneal perfusion** is a method for treating cancer in the peritoneal cavity, the abdominal space housing organs like the intestines, stomach, and liver. It's administered during surgery while the patient is under anesthesia. In this procedure, heated chemotherapy drugs are dispersed through the peritoneal cavity via a warming device, raising the local temperature to about 106 to 108°F.

c-) **Whole-body hyperthermia** is a method employed to treat metastatic cancer that has spread all over the body. During this treatment, patients are placed in thermal chambers or wrapped in hot water blankets, elevating their body temperature to approximately 107 to 108°F for short periods.

Among various hyperthermia approaches such as microwave, laser, and ultrasonic wave-based treatments, MHT stands out for its potential to selectively target tumor cells. The magnetic fluid carrying MNPs can be delivered to the tumor in four ways:

1. **Arterial injection** involves the injection of a fluid containing MNPs into the arterial supply of the tumor, creating a route for targeted drug delivery.
2. **Direct injection:** The fluid is directly injected into the tumor, with most particles in the tumor tissue, particularly in the interstitial space. This approach ensures that heat is generated primarily outside the cells. Additionally, MNP synthesis with specific tumor antibodies can enable selective ingestion by tumor cells, minimizing uptake by normal cells (differential endocytosis).
3. Formation of **in situ** implants involves injectable formulations that transform into gels, effectively trapping magnetic particles within the tumor.

4. **Active targeting:** A more complex delivery method involves antibody targeting and the enrichment of particles in the tumor region using an external magnetic field gradient, known as magnetic targeting.

2.4.2 Heat Loss Processes in MHT

In MHT, heat generation from MNPs is responsible for using two mechanisms: relaxation losses and hysteresis losses. In the case of multi-domain ferro or ferrimagnetic nanoparticles, heat is produced when exposed to a magnetic field. This heating effect is a result of a phenomenon called domain wall displacement. However, heat generation is primarily due to hysteresis losses for nanoparticles with multiple magnetic domains. On the other hand, in single-domain nanoparticles like SPM nanoparticles, the primary mechanism responsible for heat generation is Brownian-Néel relaxation. Different heat generation models in MNPs in response to the AC magnetic field are shown in **Fig. 2.9**.

➤ Hysteresis losses

Hysteresis losses are typically observed in multi-domain ferro or ferrimagnetic nanoparticles. These losses occur when these nanoparticles are exposed to a magnetic field, leading to heat dissipation. The underlying mechanism for this heat generation is the displacement of domain walls, and it tends to be more prominent in larger nanoparticles, usually exceeding 100 nm in size. Ferromagnetic materials are analyzed by the alignment of magnetic moments resulting from unpaired electron spins on neighboring atoms. This alignment occurs spontaneously, allowing ferromagnetic materials to maintain a net magnetization without an external magnetic field. The saturation magnetization value, denoted as M_s , represents the maximum magnetization achievable when all magnetic moments in the ferromagnet align. When a material exhibits hysteresis behavior, where magnetization curves for rising and decreasing magnetic field amplitudes do not overlap, it produces heat when subjected to an AC magnetic field. The quantity of heat produced per unit volume is dictated by the magnetic field's frequency and the area enclosed within the hysteresis loop. In an AC magnetic field, the hysteresis loss can be represented as,

$$A = \int_{-H_{Min}}^{-H_{max}} \mu M(H) dH \quad (2.4)$$

And thus, the SAR is,

$$SAR = A * f \quad (2.5)$$

The area of the hysteresis loop is determined by several factors, including the size of the MNPs, their anisotropy, and the frequency and amplitude of the applied AC magnetic field. In larger particles, coercivity (H_c) and remanence (M_r) are diminished, primarily due to reduced energy loss per cycle. In contrast, more minor particles experience heightened anisotropy energy barriers that separate various orientation states, leading to increased energy loss. This effect can potentially result in magnetization blockage, particularly in the case of SPM nanoparticles.

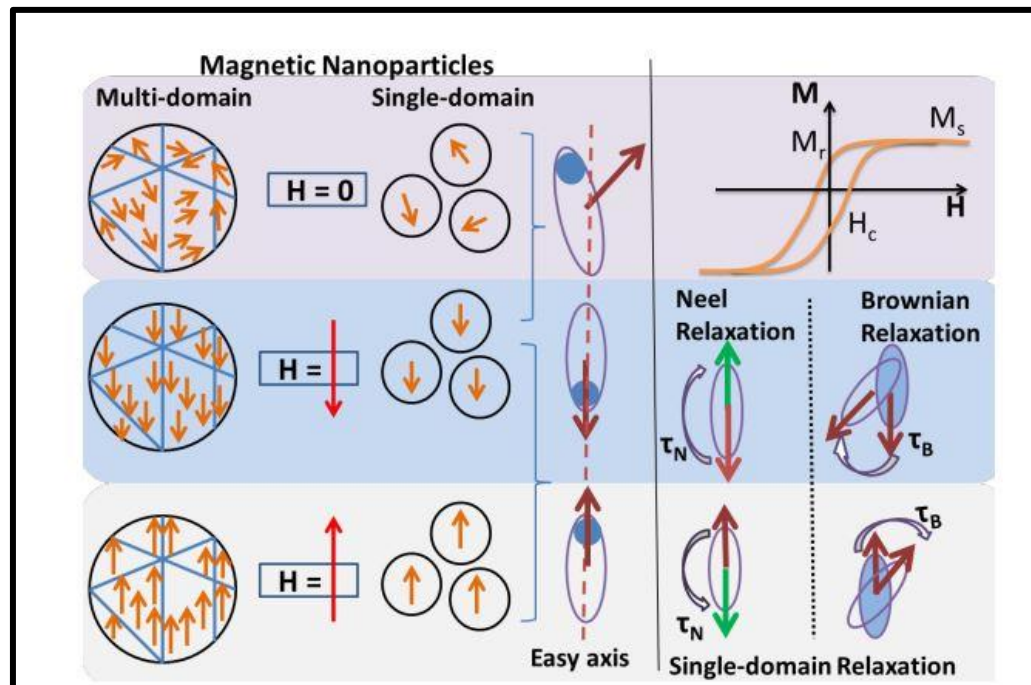


Figure 2.9 Different heat generation models in MNPs in response to the AC magnetic field (H)

Fig. 2.10 The hysteresis loop of a multi-domain magnetic material, where H represents the applied magnetic field, and M represents the magnetization of the material, illustrates domain wall displacements within such a material. In the case of multi-domain materials, arrows on the cycle indicate the path taken when increasing or decreasing the field amplitude. Ferromagnetic materials exhibit a multi-domain system and hysteresis loss, which refers to the energy converted into heat during each cycle of the magnetization reversal process. In a multi-domain system, domain walls can shift in response to an AMF. The external magnetic field can instigate these domains' formation, expansion, and dissolution by providing a favored direction for the magnetic moments. To alter the orientation of spins within a particular domain, it is necessary to reposition the walls of that domain, a phenomenon known as the

Barkhausen effect. This effect is irreversible, relying on structural imperfections in atomic arrangements, including defects, dislocations, vacancies, etc [55].

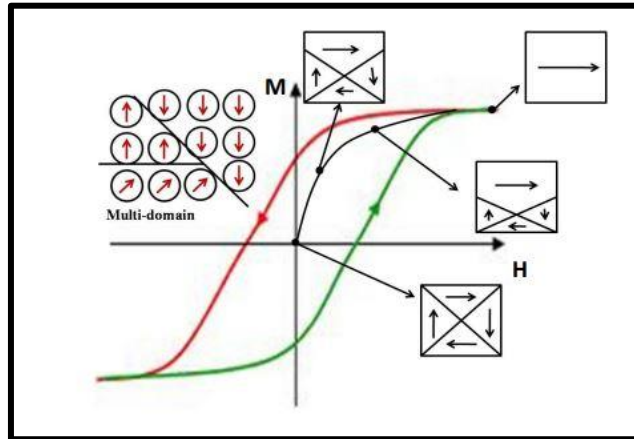


Figure 2.10 the hysteresis loop of a multi-domain magnetic material

➤ Eddy current losses

Eddy currents are produced as a consequence of the law of electromagnetic induction, and they are not limited to magnetic materials but are relevant to all macroscopic conductive materials. Eddy current loss represents the Joule loss resulting from these eddy currents induced by an AMF, and the material's electrical resistivity primarily determines the extent of this loss. Residual loss has a more complex physical origin that cannot be easily distinguished from either eddy current loss or hysteresis loss. Nonetheless, many ferrite materials exhibit high electrical resistivity, leading to low eddy current loss. The heat loss resulting from eddy currents can be mathematically expressed as follows:

$$ED = \frac{(\mu\pi dfH)^2}{20\rho} \quad (2.6)$$

In the equation, ' μ ' represents the material's permeability, ' d ' stands for the diameter of the particle, and ' ρ ' corresponds to the material's resistivity. The heating of small magnetic particles induced by eddy currents is significantly minimal compared to magnetic losses. Hence, the induction of magnetic heating in ferrite materials is predominantly due to hysteresis loss and residual loss within an alternating magnetic field [55].

➤ **Néel and Brownian- relaxation**

In MHT, two mechanisms, Brownian-Néel relaxation and hysteresis losses, generate heat from MNPs in sizes < 100 nm. Hysteresis losses cause heating in nanoparticles with multiple magnetic domains. On the other hand, Brownian-Néel relaxation primarily occurs in single-domain nanoparticles, like SPM nanoparticles. When exposed to an external magnetic field, Néel relaxation involves the rapid reorientation of magnetic moments within the nanoparticle. The time it takes to return to equilibrium depends on the effective anisotropy of the crystal, which considers factors such as magnetocrystalline energy, shape anisotropy, and surface effects. Simultaneously, the magnetic moments of the MNPs interact with the externally applied AC magnetic field, causing the nanoparticles to rotate due to Brownian physical motion. This rotational friction is influenced by the surrounding liquid's viscosity (η) and the hydrodynamic diameter of the nanoparticle (V_H) [56]. The following equations give the Néel (τ_N) and Brownian (τ_B) relaxation times:

$$\tau_N = \tau_o e^{\frac{KV}{KT}} \quad (2.7)$$

$$\tau_B = \frac{3\eta V_H}{KT} \quad (2.8)$$

$$\tau = \frac{\tau_B \tau_N}{\tau_B + \tau_N} \quad (2.9)$$

Where τ denotes the effective relaxation time, τ_o represents the characteristic flipping frequency, K is the magnetic anisotropy constant, V refers to the nanoparticle volume, k is the Boltzmann constant, T signifies the temperature, η stands for the fluid's viscosity, and V_H corresponds to the hydrodynamic volume of the nanoparticles.

The Néel relaxation time is strongly influenced by nanoparticle size, while Brownian relaxation time depends on nanoparticle hydrodynamic size and is highly affected by fluid viscosity. Smaller MNPs are better suited for efficient intracellular hyperthermia because they require less energy for magnetic moment rotation and experience fewer restrictions to rotation in high-viscosity cellular environments. Heat is generated in MNPs since their magnetic moments take longer to relax under an external AMF than the relaxation times of the nanoparticles. The following equation gives the heat dissipation:

$$P = \mu_o \pi \chi'' f H^2 \quad (2.10)$$

Where P is the value of heat dissipation, μ_0 is the permeability of free space, χ'' is the magnetic susceptibility, f is the frequency of the AMF, and H is the strength of the AMF, respectively. Changes in nanoparticle size introduce shape anisotropy, which strongly influences SAR. In the monodomain range, larger nanoparticles reduce anisotropy because they are inversely proportional to size, enhancing SAR. However, excessive anisotropy can hinder the Néel and Brownian relaxation mechanisms, becoming detrimental [57].

2.4.3 Specific Absorption Rate (SAR)

SAR holds significant importance in the development of MNPs for MHT. This parameter measures the absorbed power per unit mass of MNPs when subjected to a specific frequency and intensity of an applied AMF. Simply put, SAR serves as a metric to assess how efficiently MNPs convert magnetic energy into heat in colloid form. The process of converting magnetic energy into thermal energy, facilitated by MNPs when exposed to an external AMF, can be determined through the value of SAR, also known as Specific Loss Power (SLP).

$$\text{SAR} = C \left(\frac{dT}{dt} \right) \left(\frac{M_s}{M_m} \right) \quad (2.11)$$

In this equation, ' C ' denotes the specific heat capacity of the water, ' (dT/dt) ' represents the initial rate of temperature change, ' M_m ' refers to the mass of dispersed MNPs, ' M_s ' stands for the mass of the suspension, ' H ' corresponds to the magnetic field, and ' f ' represents the frequency.

To achieve optimal SAR per Hysteresis value through hysteresis losses, it is necessary to employ high magnetic field amplitudes, at least equal to the coercive field value. This allows for the full utilization of the hysteresis loop area; however, due to various physiological and technical constraints on field amplitudes, such as the safety condition (e.g., $H \cdot f < 5 \times 10^9 \text{ Am}^{-1}\text{s}^{-1}$) that must be observed to prevent harm to the patient; the hysteresis loop can seldom be fully exploited. Modern particles utilized for hyperthermia purposes predominantly rely on Néel relaxation. This is because SPM particles tend to yield a higher SAR when working with smaller field amplitude than ferromagnetic MNPs [58].

2.4.4 Intrinsic Loss Power (ILP)

To compare the heating efficiency across various samples and field conditions, SAR values can be standardized using the ILP. The SAR is a commonly

employed metric to describe the heat-producing capacity of a system. Nevertheless, the SAR value for a specific sample is influenced by the strength and frequency of the AMF, making it challenging to directly compare results across diverse experimental configurations. As a result, an alternative parameter, the ILP, has been suggested to standardize the SAR values.

$$\text{ILP} = \frac{P}{\rho f H^2} = \frac{\text{SAR}}{f H^2} \quad (2.12)$$

In this equation, 'P' stands for volumetric power dissipation, calculated as $P = \mu_0 \pi \chi''(f) f H^2$, where $\chi''(f)$ represents the imaginary part of the magnetic susceptibility, ' ρ ' is the density of the magnetic material, ' H ' denotes the strength of the magnetic field, and ' f ' is the frequency. This parameter enables a straightforward comparison of outcomes across various research groups since it does not rely on the strength and frequency of the AC field. ILP parameter, being the most appropriate model, depends on the magnetic field's frequency and magnitude, offering a convenient means to compare results from multiple experiments.

2.5 Influencing Parameters on SAR

2.5.1 Magnetic Field Amplitude & Frequency

The heating efficiency of a ferrofluid is indicated by its SAR value. Nevertheless, the amount of heat produced is not exclusively dictated by the structure and composition of nanoparticles. Still, it is also influenced by the frequency and amplitude of the AMF. SAR values generally increase with higher frequencies and field amplitudes. Currently, most SAR measurements reported in the literature fall within the frequency range of 300–700 kHz and field strengths between 10 and 30 kAm⁻¹. However, there is still uncertainty regarding the safety of these values at the clinical level. To address safety concerns, the Brezovich criterion, introduced in 1988 by Atkins and Brezovich, establishes a safety threshold for magnetic hyperthermia. According to this criterion, the product of $H \cdot f$ should not surpass $4.85 \times 10^9 \text{ Am}^{-1}\text{s}^{-1}$ to prevent the occurrence of eddy current effects. In simpler terms, this safety limit was defined to avoid unintentional heating or harm to the human body. However, this threshold was determined based on feedback from healthy patients who underwent MH treatment on their entire torso to gauge discomfort and tolerance levels [59-61]. Currently, the NanoActivator® system (MagForce AG, Germany) is the only therapeutically available AMF system in the world. It has a frequency of 100 kHz and

can apply magnetic fields of up to 18 kAm^{-1} , according to Jordan et al. in 2001. The frequency of 100 kHz was chosen to reduce the formation of eddy currents while increasing the temperature difference between normal tissues and tumor regions containing MNPs. Eddy currents refer to electrical currents induced within a conductor, in this context, the human body, due to changes in the magnetic field, as explained by Faraday's law of electromagnetic induction [62].

2.5.2 Particle size

As we previously discussed different heat loss mechanisms, it becomes evident that the size of the nanoparticle core, mainly whether it is monodomain or not, plays a crucial role. Hysteresis losses are the dominant mechanism for relatively large blocked particles exceeding 100 nm. Moreover, the specific type of relaxation mechanism, whether Néel or Brownian, is contingent on the anisotropy of the NPs. Enhancing anisotropy decreases the critical size of the transition from Néel to Brownian mechanisms. This is a crucial factor to consider when assessing a system's heating capability in a biological environment because cellular internalization may hinder the Brownian mechanism.

Additionally, the surface coating of the MNPs can also influence their heating capabilities by affecting Brownian relaxation and subsequently controlling the transfer of heat into the surrounding medium [63]. The discrepancies in determining the ideal particle size for treatments arise from variations in the heating process setup, including magnetic field strength and frequency. Even when comparing results using ILP, variations exist across different studies due to differences in parameters such as anisotropy. The particle size and all other relevant factors must be carefully optimized to achieve the highest possible heating effect. Nanoparticles sized at the boundary between exhibiting single-domain behavior in superparamagnetic and being in a blocked domain state are likely optimal for magnetic hyperthermia treatments.

2.5.3 Effect of Particle Morphology

The characteristics of nanoparticles are significantly influenced by their surface properties, and any modifications to these properties can result in changes in their physical, chemical, and biological attributes. Various investigations have been conducted to explore the relationship between surface properties and shape morphologies, focusing on understanding the magnetic characteristics and their

impact on magneto-hyperthermia. Core-shell MNPs belong to the category of hybrid materials, where the composition and microstructure vary radially, enabling the provision of multiple functionalities. **Fig.1.10 (Chapter 1, Section 1.6)** shows that nanoparticles with non-spherical shapes (e.g., cubical, hexagonal) demonstrate superior heating efficiency compared to their spherical counterparts. It represents various values of SAR concerning the formation of magnetic nanostructures. The heating efficiency of nanoparticles can further be improved by changing both the shape and composition of nanoparticles.

2.5.4. Anisotropy in magnetic materials

The size of the particles has a notable impact on the outcome of SAR. Moreover, magnetic anisotropy plays a critical role in determining the effectiveness of hyperthermia treatment. Modeling studies have shown that as the anisotropy constant increases, the nanoparticle size at which the highest heating power is generated decreases. Carrey et al. estimate the optimal anisotropy required for achieving the best heating results; an analytical calculation can be carried out using the proposed formulation. The anisotropy constant can be manipulated by altering the nanoparticle synthesis methods. Additionally, the shapes of nanoparticles play a role in determining magnetic anisotropy.

The effective anisotropy of a nanoparticle system plays a significant role in heat dissipation, as demonstrated by its exponential dependence on Néel relaxation time. Consequently, adjustments in the anisotropy of nanoparticles can offer the means to control the heating potential of such a system. The effective anisotropy of nanoparticles is primarily influenced by crystal or magnetocrystalline anisotropy, shape anisotropy, and surface effects. When no external magnetic field is applied, the magnetization aligns with the direction of minimum energy or the easy axis. Two main strategies can be employed to enhance the effective particle anisotropy and improve heating efficiency: Varying the magnetocrystalline anisotropy of the material and shape anisotropy.

a. Magnetocrystalline Anisotropy

The strength of magnetic anisotropy in crystalline ferromagnetic materials is determined by the atomic stacking patterns, a characteristic referred to as magnetocrystalline anisotropy. This type of anisotropy is intrinsic to the material and is contingent upon its structure and composition. For instance, magnetite exhibits the

maximum anisotropy among iron oxides, ranging from 11 to 14 kJ m⁻³, while maghemite has an anisotropy value of about 4.6 kJ m⁻³. However, it's possible to enhance the anisotropy value by incorporating other transition metals, such as cobalt, manganese, or nickel, into the inverse spinel structure. Introducing these transition metals as dopants in iron oxide has been proposed to improve the SAR [64]. The energy needed to reverse the magnetization direction is called magnetocrystalline anisotropy energy. Magnetization aligns along the magnetic easy axes in a crystal structure with minimal anisotropy energy. In contrast, directions requiring more energy to align magnetization are termed magnetic hard axes. The most commonly studied crystal structures for ferromagnetic materials are cubic and hexagonal are shown in **Fig. 2.11**.

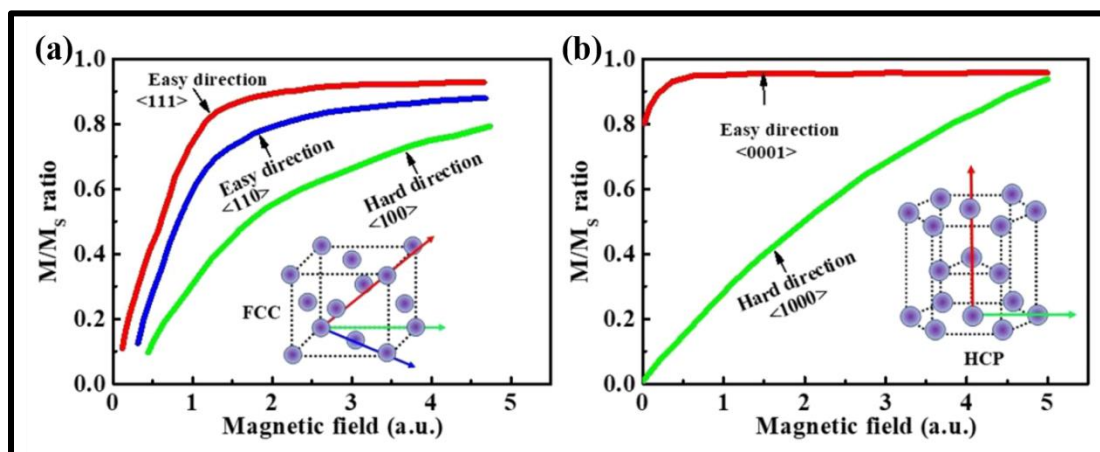


Figure 2.11 Schematics of magnetic easy and hard axes for (a) fcc-Co and (b) hcp-Co crystals [65]

Materials with cubic structures typically possess multiple easy axes and demonstrate low magnetocrystalline anisotropy, falling into the category of ‘soft magnetic materials’. In contrast, materials with hexagonal structures possess high magnetocrystalline anisotropy and substantial coercivity, earning them the label of ‘hard magnetic materials’. For example, in a face-centered cubic (*fcc*) structure, like *fcc*-Co, the magnetic easy axes align with three $\langle 111 \rangle$ directions. In a hexagonal-close-packed (*hcp*) crystal structure, such as *hcp*-Co, the magnetic easy axis coincides with the $\langle 0001 \rangle$ direction, often called the uniaxial axis. The magnetocrystalline anisotropy in *hcp*-Co (530 kJ/m³) is significantly greater than that of *fcc*-Co (270 kJ/m³).

b. Shape Anisotropy

The changing shape of nanoparticles can enhance effective anisotropy, with surface effects playing a more significant role. On the nanoparticle's surface, changes in neighboring atoms and crystal orientation result in variations in local magnetization about the surface. In the case of faceted particles, when subjected to a nonzero magnetic field, domain wall motion tends to align toward forming flat domains, reducing energy and increasing surface anisotropy. Simultaneously, cubic morphology appears to reduce spin canting compared to spherical particles. As a result, it has been observed that faceted or cubic-shaped nanoparticles tend to display higher SAR values compared to their spherical counterparts [66]. Shape anisotropy, arising from dipole-dipole interactions in ferromagnetic materials, is a fundamental aspect of magnetism. When dealing with equally magnetized magnetic ellipsoid bodies, shape anisotropy can be quantitatively characterized using the demagnetization tensor (N), which is solely determined by the object's shape. This method provides a simple and effective way to control the local effective anisotropy field for micro- and nanoscale magnetic components. However, achieving uniform magnetization under a finite magnetic field is challenging for a magnet with an irregular, non-ellipsoidal shape. Due to this non-uniform magnetization, the values of N estimated using the constant magnetized ellipsoid approximation may need to be more accurate and suitable for describing shape anisotropy [67].

2.6 Magnetic Nanoparticles: Toxicity, Biodistribution, Pharmacokinetics

Ensuring the safety and effectiveness of MNPs in clinical applications hinges on understanding their toxicity, pharmacokinetics, and biodistribution within the body. Several factors, including hydrodynamic size, surface potential, coating, and NP interactions, play vital roles in the pharmacokinetics and pharmacodynamics of MNPs in the body. In contrast, the liver and spleen may take up larger particles before undergoing eventual degradation or excretion via the hepatobiliary route. Moreover, the physicochemical characteristics of nanomaterials, including size, structure, composition, surface charge, and surface modification, collectively contribute to the toxicity profile of formulated MNPs. Specifically, nanoparticles with less than 10 nm are effectively removed from circulation through renal clearance, while core sizes exceeding 200 nm are more susceptible to sequestration by the spleen.

Additionally, MNPs with a neutral surface charge exhibit prolonged circulation times compared to nanoparticles with positive or negative surface charges. Surface coating represents another crucial determinant affecting the circulation of MNPs. Accumulation of MNPs in the liver and spleen can lead to unintended off-target toxicity. Furthermore, *in vivo* toxicity is influenced by several additional critical factors, including the synthesis procedure, purity, nanoparticle size, surface charge, biodistribution within the body, and the pharmacokinetic properties of these nanoparticles [68]. The effectiveness of heating induced by an AMF is closely tied to the concentration of MNPs within the tumor. In clinical trials, patients with glioblastoma have been administered up to 31.36 mg of iron per cubic centimeter (Fe/cm^3) of tumor in the form of MNPs via intratumoral injection (as reported by Maier-Hauff et al. in 2011). Feraheme® (AMAG Pharmaceuticals, USA), an IONP approved by the FDA for iron replacement therapy, has been safely administered intravenously in substantially larger quantities than most other FDA-approved inorganic nanoparticles. The standard dosing regimen typically involves the administration of 510 mg of iron in the form of Feraheme®, followed by a second injection within a time frame ranging from 3 to 8 days [69].

a. Viscosity of the fluid

When MNPs exhibit a magnetic anisotropy characterized by an energy barrier significantly surpassing the thermal energy at room temperature, the predominant mechanism for magnetic relaxation shifts to Brownian rotation. The hydrodynamic diameter of MNPs and the viscosity of the surrounding medium are crucial factors in determining the SAR. Additionally, the type of medium employed can impact the treatment outcome. In an experiment where the same material concentration and magnetic field conditions were maintained, the temperature rose most significantly in water, followed by glycerol, while the temperature increase was the lowest in collagen. This disparity can be attributed to collagen's high viscosity, which hampers the Brownian relaxation effect. The inhibition of Brownian relaxation was confirmed through an *in vitro* experiment involving living cells. Various types of nanoparticles were introduced into cell cultures as part of this study. Creating perfectly uniform particles is exceptionally challenging, so for practical applications, the variation in particle diameters (polydispersity) must be considered when calculating optimized heat generation. Research has been undertaken to investigate the influence of polydispersity on the heat-generation capabilities of MNPs [70].

b. Effect of coating with organic ligands

The chemicals that stabilize the nanoparticles also discover their magneto-hyperthermia once exposed to bodily fluids due to developing a protein corona that modulates the particles' behavior. MNPs that are coated with various organic ligands, such as polyethyleneimine (PEI), polyethylene glycol (PEG), dextran, oleic acid, and Pluronic F-127, exhibit different behaviors compared to uncoated MNPs, according to *in-vivo* and *in-vitro* magnetic hyperthermia tests. Effective stabilization enhances the biocompatibility of nanoparticles, minimizing immune reactions and preventing the formation of protein-nanoparticle aggregates that could obstruct blood capillaries. Improving the biocompatibility of nanoparticles involves the introduction of organic ligands on their surface, resulting in enhanced uptake by tumors and cells. The use of organic ligands serves to extend the circulation time of nanoparticles in the bloodstream and minimize toxicity. Although these organic ligands may not directly affect the heat dissipation of MNPs, they do influence the hydrodynamic sizes and dispersion of the particles, consequently impacting the process of Brownian relaxation. Selecting a biocompatible capping agent can lead to increased nanoparticle uptake in tumors, prolonged circulation in the bloodstream, improved heating efficiency, and reduced particle aggregation *in vivo* [71-73].

2.7 References

1. L. Zhu, Z. Zhou, H. Mao, L. Yang, *Nanomed.*, 12 (1) (2017) 73-87.
2. K. Hayashi, Y. Sato, W. Sakamoto, T. Yogo, *ACS Biomater Sci Eng.*, 3 (1) (2017) 95-105.
3. S. Liébana-Viñas, k. Simeonidis, U. Wiedwald, Z. Li, Z. Ma, E. Myrovali, A. Makridis, D. Sakellari, G. Vourlias, M. Spasova, M. Farle, *RSC Adv.*, 6 (77) (2016) 72918-25.
4. S. Laurent, S. Dutz, U. Häfeli, M. Mahmoudi, *Adv. Colloid Interface Sci.*, 166(1-2) (2011) 8-23.
5. S. Avugadda, M. Materia, R. Nigmatullin, D. Cabrera, R. Marotta, T. Cabada, E. Marcello, S. Nitti, E. Artés-Ibañez, P. Basnett, C. Wilhelm, *Chem. Mater.*, 31 (15) (2019) 5450-63.
6. D. Lisjak, A. Mertelj, *Prog. Mater. Sci.*, 95 (2018) 286-328.
7. L. Zhu, L. Yang, Z. Zhou, *Nanomedicine and Nanotoxicology*, (2017) 173–206.
8. K. Zhu, Y. Ju, J. Xu, Z. Yang, S. Gao, Y. Acc. *Chem. Res.*, 51 (2) (2018) 404-13.
9. P. Guardia, R. Corato, L. Lartigue, C. Wilhelm, A. Espinosa, M. Hernandez, F. Gazeau, L. Manna, T. Pellegrino, *ACS Nano*, 6 (4) (2012) 3080-91.
10. Y. Wang, *World J Gastroenterol.*, 21(47) (2015) 13400–13402.
11. D. Ling, T. Hyeon, *Small*, 9 (2013) 1450-1466.
12. H. Gavilán, S. Avugadda, T. Fernández-Cabada, N. Soni, M. Cassani, B. Mai, R. Chantrell, T. Pellegrino, *Chem. Soc. Rev.*, 50 (20) (2021) 11614-67.
13. L. Zhou, J. Yuan, Y. Wei, *J. Mater. Chem.*, 21 (9) (2011) 2823-2840.
14. M. Singh, S. Manikandan, A. Kumaraguru, *J. Nanosci. Nanotechnol.*, 1(1) (2011) 1-1.
15. L. Yu, A. Sun, N. Suo, Z. Zuo, X. Zhao, W. Zhang, *Appl. Phys. A*. 126 (2020) 1-3.
16. A. Hao, X. Ning, *Front. Mater. Sci.*, 8 (2021) 718869 -718878.
17. K. Vamvakidis, M. Katsikini, D. Sakellari, E. Paloura, O. Kalogirou, C. Dendrinou-Samara, *Dalton Trans.*, 43(33) (2014) 12754-65.
18. K. Asghar, M. Qasim, D. Das, *Materials Today: Proceedings*, 26 (2020) 87-93.

19. M. Cruz, L. Ferreira, J. Ramos, S. Mendo, A. Alves, M. Godinho, M. Carvalho, J. Alloys Compd., 703 (2017) 370-380.
20. N. Akhlaghi, G. Najafpour-Darzi, J. Ind. Eng. Chem., 103 (2021) 292-304.
21. C. Kalaiselvan, S. Laha, S. Somvanshi, T. Tabish, N. Thorat, N. Sahu, Coord. Chem. Rev., 473 (2022) 214809-214841.
22. M. Salimi, S. Sarkar, R. Saber, H. Delavari, A. Alizadeh, H. Mulder, Cancer Nanotechnol., 9 (2018) 1-9.
23. D. Kim, D. Nikles, C. Brazel, Materials, 3(7) (2010) 4051-4065.
24. L. Feng, B. Liu, R. Xie, D. Wang, C. Qian, W. Zhou, J. Liu, D. Jana, P. Yang, and Y. Zhao, Adv. Funct. Mater., 31 (2020) 2006216-2006230.
25. S. Yin, Prof. G. Song, Y. Yang, Y. Zhao, P. Wang, L. M. Zhu, Prof. X. Yin, Prof. X.-B. Zhang, Adv. Funct. Mater., 29 (2019) 1901417-1901427.
26. F. Benyettou, G. Das, A. Nair, T. Prakasam, D. Shinde, S. Sharma, J. Whelan, H. Traboulsi, O. Abdullah, R. Pasricha, R. Jagannathan, Z. lai, L. Motte, F. Gandara, C. Sadler, A. Trabolsi, JACS, 142 (2020) 18782-18794.
27. M. Arciniegas, A. Castelli, R. Brescia, D. Serantes, S. Ruta, O. Hovorka, A. Satoh, R. Chantrell, T. Pellegrino, Small, 16 (2020) 1907419-1907430.
28. S. Patade, D. Andhare, B. Somvanshi, A. Jadhav, V. Khedkar, K. Jadhav, Ceram. Int., 46 (2020) 25576-25583.
29. C. Iacovita, A. Florea, L. Scorus, E. Pall R. Dudric, A. I. Moldovan, R. Stiuftuc, R. Tetea, C. Lucaciu, Nanomater., 9 (2019) 1489-1512.
30. A. Espinosa, J. Reguera, A. Curcio, A. Noval, C. Kuttner, A. Walle, Luis M. Liz-Marzán, and C. Wilhelm, Small, 16 (2020) 1904960-1904974.
31. K. Buschow, Handbook of magnetic materials. Elsevier, (2003) 1-86.
32. I. Diniz, C. Chen, X. Xu, S. Ansari, H. Zadeh, M. Marques, S. Shi, A. Moshaverinia, J. Mater. Sci.: Mater. Med., 26 (2015) 1-0.
33. L. Katz, A. Burkhalter, W. Dreyer, Nature, 310(5977) (1984) 498-500.
34. L. Mohammed, H. Gomaa, D. Ragab, J. Zhu, Particuology, 30 (2017) 1-4.
35. R. Ismail, G. Sulaiman, S. Abdulrahman, T. Marzooq, Mater. Sci. Eng. C, 53 (2015) 286-297.
36. M. Namdeo, S. Saxena, R. Tankhiwale, M. Bajpai, Y. Mohan, S. Bajpai, J. Nanosci. Nanotechnol., 8(7) (2008) 3247-3271.
37. J. Ritter, A. Ebner, K. Daniel, K. Stewart, J. Magn. Magn. Mater., 280(2-3) (2004) 184-201.

-
38. J. Dobson, *Drug Dev. Res.* 67(1) (2006) 55-60.
 39. M. Arruebo, R. Fernández-Pacheco, M. Ibarra, J. Santamaría, *Nano Today*, 2(3) (2007) 22-32.
 40. B. Subramaniam, Z. Siddik, N. Nagoor, *J. Nanoparticle Res.*, 22 (2020) 1-29.
 41. R. Meel, S. Oliveira, I. Altintas, R. Heukers, E. Pieters, P. Henegouwen, G. Storm, W. Hennink, R. Kok, R. Schiffelers, *Mol. Pharmaceutics*, 10(10) (2013) 3717-3727.
 42. C. Bárcena, A. Sra, J. Gao, *Nanoscale magnetic materials and applications*, Springer-Verlag New York Inc. (2009) 591-626.
 43. T. Yousaf, G. Dervenoulas, M. Politis, *Int. Rev. Neurobiol.*, 141 (2018) 31-76.
 44. G. Kandasamy, D. Maity, *Int. J. Pharm.*, 496(2) (2015) 191-218.
 45. R. Gordon, J. Hines, D. Gordon, *Med. Hypotheses*, 5(1) (1979) 83-102.
 46. S. Wang, J. Xu, W. Li, S. Sun, S. Gao, Y. Hou, *Chem. Rev.* 122(6) (2022) 5411-5475.
 47. I. Hilger, W. Kaiser, *Nanomedicine*, 7 (9) (2012) 1443-1459.
 48. R. Gilchrist, R. Medal, W. Shorey, R. Hanselman, J. Parrott, C. Taylor, *Ann. Surg.* 146(4) (1957) 596 - 606.
 49. P. Das, M. Colombo, D. Prosperi, *Colloids Surf. B Biointerfaces.*, 174 (2019) 42-55.
 50. K. McNamara, S. Tofail, *Adv. Phys.*, 2(1) (2017) 54-88.
 51. A. Iyer, G. Khaled, J. Fang, H. Maeda, *Drug Discov. Today*, 11(17-18) (2006) 812-818.
 52. S. DeNardo, G. DeNardo, A. Natarajan, L. Miers, A. Foreman, C. Gruettner, G. Adamson, R. Ivkov, *J. Nucl. Med.*, 48(3) (2007) 437 - 444.
 53. R. Gupta, D. Sharma, *ACS Chem. Neurosci.*, 10(3) (2019) 1157-1172.
 54. M. Mahmoudi, S. Sant, B. Wang, S. Laurent, T. Sen, *Adv. Drug Deliv. Rev.*, 63(1-2) (2011) 24-46.
 55. H. Etemadi, P. Plieger, *Adv. Therap.*, 3(11) (2020) 2000061- 2000110.
 56. S. Laurent, S. Dutz, U. Häfeli, M. Mahmoudi, *Adv. Colloid Interface Sci.*, 166 (1-2) (2011) 8-23.
 57. R. Hergt, S. Dutz, *J. Magn. Magn. Mater.*, 311(1) (2007) 187-92.
 58. C. Blanco-Andujar, A. Walter, G. Cotin, C. Bordeianu, D. Mertz, D. Felder-Flesch, S. Begin-Colin, *Nanomedicine*, 11(14) (2016) 1889-1910.
 59. C. Dennis, R. Ivkov, *Int. J. Hyperth.*, 29 (2013) 715–729.

-
60. M. Anik, M. Hossain, I. Hossain, A. Mahfuz, M. Rahman, I. Ahmed, *Nano Select*, 2 (6) (2021) 1146-1186.
 61. G. Glöckl, R. Hergt, M. Zeisberger, S. Dutz, S. Nagel, W. Weitschies, J. *Condens. Matter Phys.* 18(38) (2006) S2935–S2949.
 62. I. Brezovich, *Med. Phys. Monogr.* 16 (1988) 82-111.
 63. D. Chang, M. Lim, J. Goos, R. Qiao, Y. Ng, F. Mansfield, M. Jackson, T. Davis, M. Kavallaris, *Front. Pharmacol.* 9 (2018) 831-851.
 64. X. Liu, H. Fan, J. Yi, Y. Yang, E. Choo, J. Xue, J. Ding, J. Mater. Chem. 22(17) (2012) 8235-8244.
 65. Z. Ma, J. Mohapatra, K. Wei, J. Liu, S. Sun, *Chem. Rev.* 123(7) (2021) 3904-3943.
 66. C. Kumar, F. Mohammad, *Adv. Drug Deliv. Rev.* 63 (9) (2011) 789-808.
 67. B. Cullity, C. Graham, *Introduction to magnetic materials*. John Wiley & Sons, (2011).
 68. X. Fan, H. Zhou, J. Rao, X. Zhao, J. Zhao, F. Zhang, D. Xue, *Sci. Rep.* 5(1) (2015) 16139-16148.
 69. S. Mukherjee, L. Liang, O. Veisheh, *Pharmaceutics*, 12 (2) (2020) 147-167.
 70. Suriyanto, E. Ng, S. Kumar, *Biomed. Eng. Online* 16 (2017) 1-22.
 71. M. Naguib, I. Mekkawy, U. Mahmoud, A. Sayed, *Scientific African.* (2022) e01260 -e01271.
 72. S. Del Sol-Fernández, Y. Portilla-Tundidor, L. Gutiérrez, O. Odio, E. Reguera, D. Barber, M. Morales, *ACS Appl. Mater. Interfaces.*, 11 (30) (2019) 26648-26663.
 73. H. Köçkar, O. Karaagac, F. Özel, J. Magn. Mater., 474 (2019) 332-336.

CHAPTER-3

Experimental and Characterization Techniques for Magnetic Iron Oxide Nanoparticles



3.1 Introduction

MNPs have garnered significant interest for their potential applications in various fields, including biomedicine, catalysts, and magnetic data storage. To effectively utilize MNPs in these applications, it is crucial to have precise control over the particle's morphology, uniformity, and chemical composition. This level of control is essential because these parameters significantly influence the physical and chemical properties of MNPs. MNPs can be synthesized using biological, chemical, and physical processes. Recently, numerous wet chemical approaches such as co-precipitation, hydrothermal, polyol, solvothermal, electrochemical, and reverse micelle syntheses have been widely employed to form MNPs of diverse sizes and forms [1]. Among MNPs, iron oxide-based nanoparticles are of interest in the present work.

3.2. Synthesis of Iron Oxide Nanoparticles

3.2.1. Co-precipitation Method

The most widely used method for synthesizing magnetic IONPs is co-precipitation. This method is favored due to its cost-effectiveness, environmentally friendly precursor materials, and simple experimental procedures. However, optimizing co-precipitation syntheses remains a challenge because of particle formation mechanisms. Co-precipitation involves the simultaneous precipitation of ferrous and ferric ions in an aqueous solution by adding a base. One of the reasons for the popularity of this method is the use of inexpensive chemicals and relatively simple experimental procedures carried out at moderate temperatures (typically below 100 °C) without the involvement of toxic reactants or by-products. Despite its advantages, co-precipitation synthesizes IONPs with relatively low magnetization and a significant polydispersity. This variation in IONP core sizes and the presence of agglomerates can limit the uniformity of the resulting nanoparticles. These agglomerates present new challenges related to stabilizing and utilizing the IONPs. For instance, the distribution of IONPs within body tissues is significantly influenced by both the core size and the presence of agglomerates. Variations in core size are likely due to simultaneous nucleation and particle growth processes, along with the formation of intermediate phases before or during the emergence of the desired magnetic phases, such as magnetite (Fe_3O_4) or maghemite ($\gamma\text{-Fe}_2\text{O}_3$). It is expected to vary based on different synthesis conditions, including the choice of precursors, their

concentrations, temperature, pH, and the sequence of reagent and stabilizer additions, among other factors. Only a limited number of recent studies have successfully provided some insights into particle formation mechanisms in the context of co-precipitation [2-4].

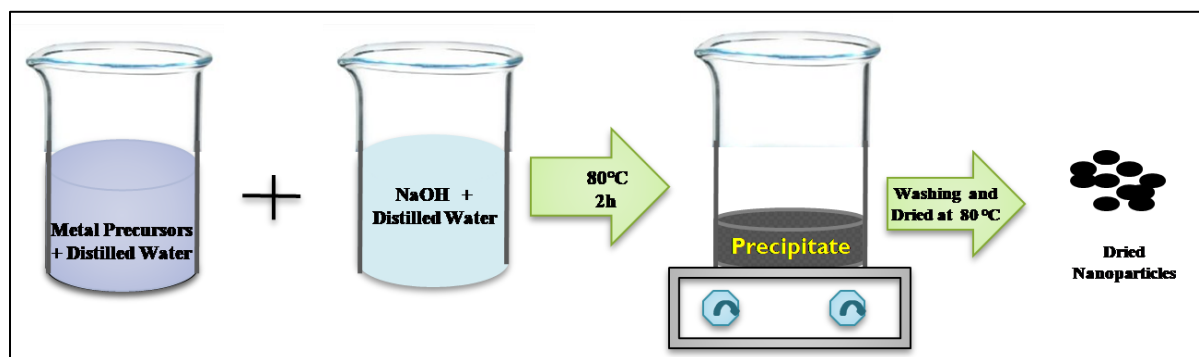
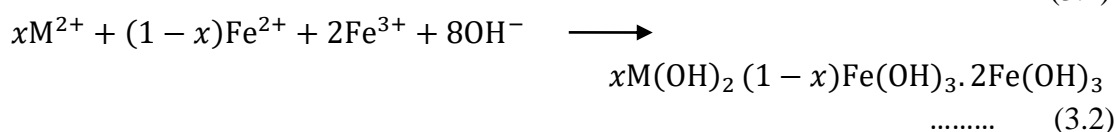
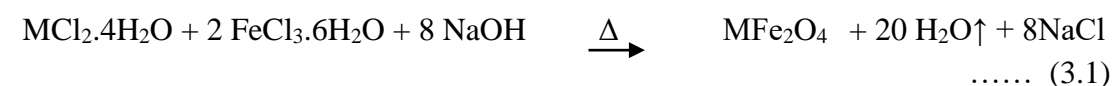


Figure 3.1 Schematic representation of co-precipitation method

Typically, the synthesis process involves introducing a reducing or precipitating agent into the aqueous solution containing the metal precursors. This addition initiates the formation of MNPs as the reaction progresses. The aqueous solution generally consists of metal salts and a base. The reaction can take place at a variety of temperatures, ranging from room temperature to higher temperatures. Multiple factors, including the reaction temperature, the type and ratio of precursors, the solution's volume, and the medium's pH, can be adjusted to modify the composition, shape, and size of the resulting MNPs [5]. In general, precursor salts such as chlorides, nitrates, perchlorates, and sulphates are used. **Fig. 3.1** shows the schematic diagram of the co-precipitation method. The following equations describe the mechanism involved in the co-precipitation method of creating MNPs.



Puspitasari et al. reported varied sizes of manganese iron oxide generated by adjusting the pH of the solution via a co-precipitation approach. The experiment involved

changing the amount of sodium hydroxide injected to get three varied pH levels of 8, 10, and 12. The morphological study of the synthesized particles demonstrated a decrease in particle size, magnetic properties, and medium pH [6].

Advantages

Disadvantages

The preparation method is simple, easy to use, and straightforward, making it convenient for researchers and practitioners.	The particles generated through this method exhibit irregular morphology, lacking a consistent and well-defined shape.
Short processing time and performed at relatively low temperatures, usually below 100°C	The wide range of particle sizes and high polydispersity indicate significant particle size variation.
Practical and energy-efficient method	It lacks precise particle size and shape control and is less suitable for highly uniform applications.

3.2.2. Thermal Decomposition

Recently, thermal decomposition syntheses have become one of the essential methods for obtaining IONPs. However, recent studies have shown that similar thermal decomposition mechanisms may first produce a nonmagnetic Wüstite phase, from which the magnetic magnetite/maghemite phases may eventually arise due to oxidation upon exposure to ambient oxygen. This synthesis method is carried out in a liquid phase at elevated temperatures, using multivalent alcohol as the solvent. In producing nanoparticles, bottom-up liquid-phase methodologies are appealing due to their versatility. Numerous organic chemical reactions have prolonged reaction times; heat is commonly employed to accelerate these reactions. Organic substances have low boiling temperatures and high vapor pressures, making them volatile.

Thermal decomposition is a chemical process that entails heating a reaction for a predetermined amount while employing a condenser to cool the vapours produced back into a liquid form. The vapours generated on top of the reaction undergo continuous condensation and return as a liquid condensate into the reaction flask. This method ensures that the reaction temperature remains constant. Monodisperse IONPs were synthesized through the thermal decomposition of iron oleate in the presence of oleic acid as a surfactant using a ‘heating up’ process. In this process, different solvents with varying boiling points, such as 1-octadecene (~320°C), eicosane (~360°C), and docosane (~380°C), were chosen to examine the

effects of reaction temperature on the size and morphology of the IONPs. Due to the distinct temperature dependence of nucleation and development, the production of monodisperse IONPs was ascribed to their separation. Nucleation occurred at approximately 240°C, while growth occurred at a higher temperature. Surfactants, such as long-chain alkyl compounds with heteroatom or polar groups, played an essential role in determining the size and shape of the nanoparticles. Surfactants could interact with and bind to the nanoparticle's surface through covalent, electrostatic, or coordination bonds. Increasing the concentration of the reactants promotes the generation of more monomers. When the concentration of monomers in the solution exceeded a critical supersaturation level, it overcame the energy barrier, resulting in rapid nucleation. These lead to the creation and aggregation of stable nuclei. The equation provided below defines the minimum radius required for a nucleus to remain stable and grow spontaneously within the supersaturated solution:

$$r = \frac{2\gamma V_m}{RT \ln S} \quad (3.4)$$

Where γ is the amount of free energy on the surface per unit area, the variables V_m , R , T , and S represent the molar volume, temperature, supersaturation, and molar constant of bulk particles. The size of a nucleus that can persist is determined by the minimum radius, and any nucleus with a size smaller than this minimum radius will dissolve. The minimum radius of a stable nucleus is inversely proportional to the degree of supersaturation.

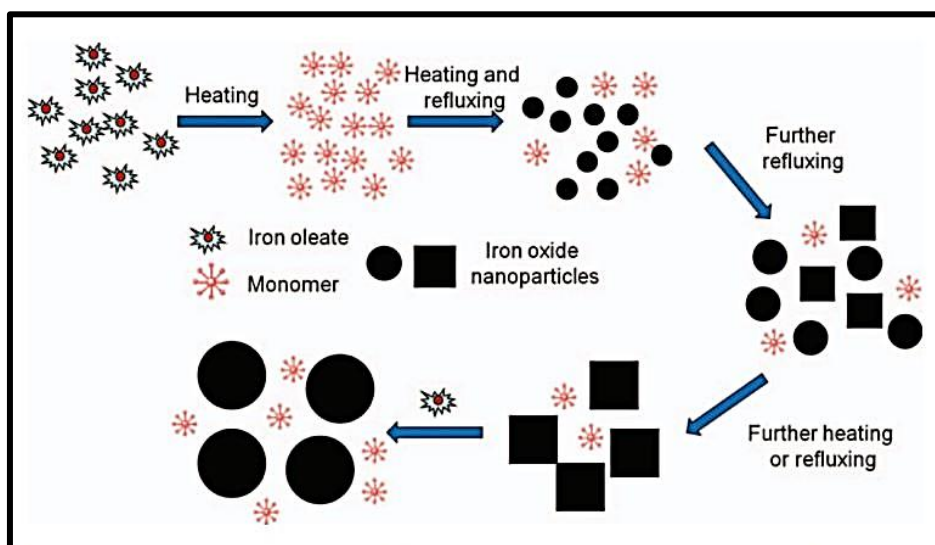


Figure 3.2 Schematic illustrations for the formation kinetics of iron oxide nanoparticles [7]

The heating rate was crucial for synthesizing monodisperse IONPs, even though its impact on the nanoparticle morphology was limited. The synthesis of monodisperse IONPs was essential to ensure the separation of nucleation and growth processes (**Fig. 3.2**). If the heating rate were exceptionally high, the reaction system would be rapidly heated to the temperature at which growth occurred, even while nucleation was still in progress. This was due to a temperature variation between the nucleation and growth phases. When nucleation and growth processes overlap, the growth of individual nanoparticles becomes uneven, resulting in a broad size distribution. Nuclei more significant than the critical radius will continue to grow to form nanoparticles.

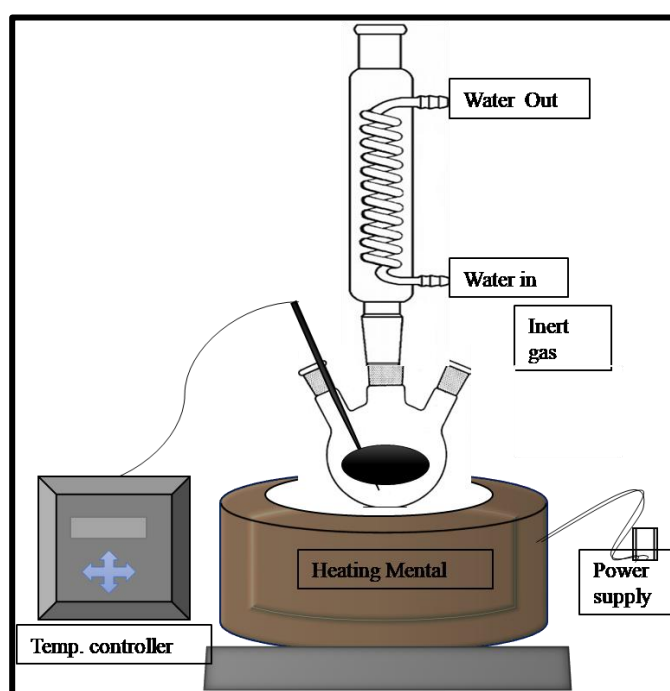


Figure 3.3 Schematic diagram of the thermal decomposition method

Particles with a smaller critical radius dissolve and contribute to monomers, while high reactant concentrations promote small nanoparticles; nanoparticle growth at high monomer levels is thermodynamically controlled, resulting in spherical shapes, and higher temperatures from iron complex decomposition generate more monomers, leading to larger nanoparticles. For example, cubic nanoparticles are generated when spherical nanoparticles experience kinetically controlled growth along the $\langle 111 \rangle$ crystallographic directions. This typically occurs when the monomer concentration is low. To produce larger nanoparticles, adding more iron oleate is necessary to ensure an adequate monomer supply for continued growth. This growth

mechanism aligns with the ‘Ostwald Ripening principle, often called seed-mediated growth [7].

A magnetic stir bar can prevent violent boiling and ensure uniform heating when working with reactants in the round-bottom flask that are not overly dense. As depicted in **Fig. 3.3**, if a magnetic stir bar is utilized, a hot plate should replace a heating mantle because it includes a magnetic stirrer that automatically spins the bar during the thermal decomposition. Maintaining a constant water supply in the condenser is crucial to facilitate effective cooling. As the vapors generated from the liquid reaction mixture release heat and transition from the gaseous phase to the liquid phase, they promote the return of the fluid mixture to the round-bottom flask.

Advantages	Disadvantages
The high boiling point permits syntheses at elevated temperatures, promoting the formation of well-crystallized materials.	Complex synthesis procedure, making it challenging to carry out.
The solvent's reducing properties protect metal particles from oxidation while in the medium.	There is a need for high temperatures and relatively long reaction times, which can span from hours to days.
The medium's high viscosity enables diffusion-controlled particle growth, resulting in well-defined structures and morphology.	Medium yield of nanoparticles.

3.3. Characterization Techniques

In this section, we provide a concise overview of the fundamental principles, operational mechanisms, and experimental arrangements of the instruments employed to investigate the structural, magnetic, and thermal characteristics of the MNPs that are produced. The following instruments and their functionalities are outlined below:

3.3.1. X-ray Diffractometer (XRD)

XRD is one of the most commonly employed techniques for nanoparticle characterization. It is a fundamental, robust, and non-destructive method that finds widespread use in the characterization of nanoparticles. XRD is primarily utilized to extract information about the material's crystalline structure, phase characteristics, lattice parameters, and crystalline grain size. The **Fig. 3.4** displays the schematic representation of the X-ray diffractometer.

Working principle

The XRD technique is based on the reflection of X-rays from crystallographic planes and is defined by Bragg's equation;

$$2d \sin\theta = n\lambda \quad (3.5)$$

where d = interplanar spacing, θ = diffraction angle, λ = wavelength of X-ray and n = order of diffraction. The crystallite size of a sample can be determined using Scherrer's equation (**Equation 3.6**) by measuring the full width at half maximum (FWHM) of the most prominent diffraction peak.

$$D_{xrd} = \frac{K\lambda}{\beta \cos\theta} \quad (3.6)$$

Here, D_{xrd} represents the crystallite (grain) size, λ is the X-ray wavelength, β is the FWHM of the diffraction peak in radians, θ is the Bragg's angle, and K is the shape factor. The value of K typically ranges from 0.89 to 1.39, with ~ 1 being used in most cases. XRD is based on constructive interference of monochromatic X-rays and a crystalline sample. These X-rays are generated by a cathode ray tube, filtered to produce monochromatic radiation, collimated to concentrate, and directed toward the sample. The interaction of the incident rays with the sample produces constructive interference when conditions satisfy Bragg's Law.

Instrumentation and Working

In the XRD process, X-rays are produced using a cathode ray tube. This is accomplished by heating a filament to release electrons, which are then accelerated toward a target through voltage application. These accelerated electrons collide with the inner shell electrons of the target material. As a result of these collisions, characteristic X-ray spectra are emitted. These spectra encompass numerous constituents, the most prevalent ones being $K\alpha$ and $K\beta$. The $K\alpha$ component can be divided into $K\alpha_1$ and $K\alpha_2$, where $K\alpha_1$ has a slightly shorter wavelength and is twice as intense as $K\alpha_2$. These wavelengths are unique to the target material, such as copper (Cu), iron (Fe), molybdenum (Mo), or chromium (Cr). In diffraction experiments, it is necessary to generate monochromatic X-rays by employing filters like foils or crystal monochrometers. Since $K\alpha_1$ and $K\alpha_2$ have closely related wavelengths, a weighted average is typically used for this purpose. With $\text{CuK}\alpha$ radiation = 1.5418 Å, copper is the most often used target material for single-crystal diffraction [8-10].

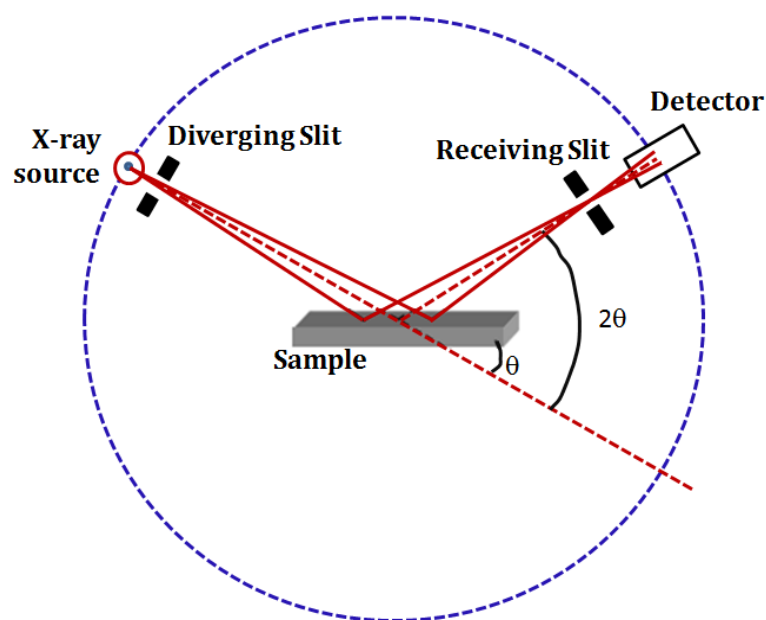


Figure 3.4 Schematic representation of X-ray diffractometer

In XRD, focused X-rays are directed at the sample, and the sample and detector are rotated to measure the reflected X-ray intensity. When the incident X-rays satisfy the conditions of Bragg's Equation, constructive interference produces an intensity peak. A detector captures the X-ray signal, converts it into a count rate, and displays it on a device such as a computer monitor. In the XRD setup, the sample rotates at an angle θ within the focused X-ray beam while the detector moves at 2θ to collect the diffracted X-rays. A goniometer controls the rotation of the sample in the X-ray beam path.

Applications

- Characterizations of crystalline materials
- Determination of unit cell dimension and sample purity
- To determine the structure of biological macromolecules
- Identification of different phase formation

In the present study, the XRD patterns of as-synthesized MNPs using Rigaku miniflex 600 with Cu $K\alpha$ characteristic radiation ($\lambda=1.5406\text{\AA}$) operated at 35 kV in $\theta/2\theta$ mode at a D. Y. Patil Education Society, Kolhapur.

3.3.2. Fourier Transform Infrared Spectroscopy (FTIR)

Infrared spectroscopy, often called IR spectroscopy, is crucial in organic chemistry for identifying specific functional groups within a molecule. It can accurately determine the characteristics of pure compounds and pinpoint particular

impurities through the distinctive patterns of absorption bands. This technique operates on the principle that molecules vibrate at distinct frequencies, typically within the range of approximately 4000 to around 200 cm^{-1} in the infrared region of the electromagnetic spectrum [11].

Working principle

In an electromagnetic field, the energy gap between two levels (E_1 and E_2) of a material is expressed as the product of Planck's constant (h) and the frequency (ν) of the incident radiation, represented as:

$$\Delta E = h \nu \quad (3.7)$$

When exposed to IR radiation, a sample selectively absorbs energy at frequencies corresponding to its molecular vibration frequencies while allowing other frequencies to pass through. An infrared spectrometer detects the frequencies of absorbed radiation, generating a plot of absorbed energy versus frequency known as an 'infrared spectrum.'

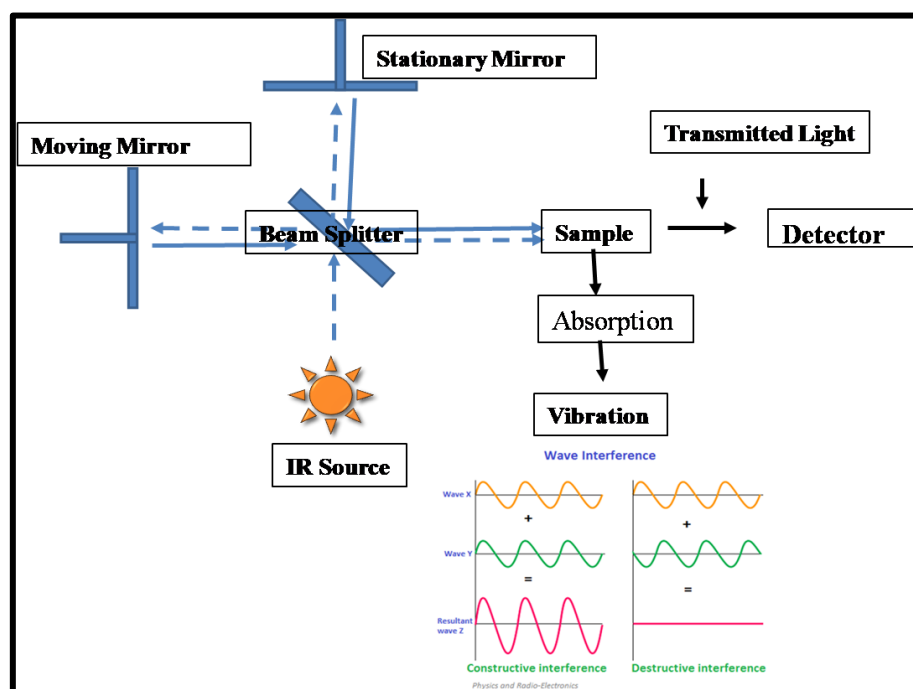


Figure 3.5 Basic working principle of the FTIR system

Since different materials exhibit distinct vibrations and produce unique infrared spectra, this method enables the identification of specific molecules. A nonlinear molecule composed of N atoms, it undergoes $3N-6$ vibrational motions for its constituent atoms, often referred to as fundamental vibrations or normal modes. Only those molecular vibrations considered IR active are observed in the IR

spectrum, meaning they absorb IR light. For a vibration to be IR active, it must cause a change in the dipole moment of the vibrating molecule. In a molecule that has a center of symmetry, the vibrations that exhibit symmetry for the center are considered IR inactive. However, any molecular vibrations that lack symmetry are IR active and thus manifest in the spectrum. This leads to the simultaneous detection of all chemical groups in the material. Intriguingly, this technique can detect amino acids and water molecules, which can be challenging to see using other spectroscopic methods.

Chemical groups with a permanent dipole moment, such as polar bonds, exhibit strong absorption in the infrared region. Consequently, IR spectra of proteins include absorption peaks arising from the carbonyl groups in polypeptide chains [12]. Using the FTIR spectrometer involves several key components within its optical system. The IR radiation first passes through an interferometer, which modulates it by performing an optical inverse Fourier transform. This modulated IR beam is then directed through a gas specimen, which gets absorbed at different wavelengths due to various molecules in the sample. Finally, an IR detector measures the intensity of the absorbed IR radiation. A computer digitizes and performs a Fourier transform on the detected signal, ultimately producing the IR spectrum of the gas sample [13]. The essential components of the optical system in an FTIR spectrometer consist of an interferometer with two mirrors, an IR source, an IR detector, and a beamsplitter, as shown in **Fig. 3.5**. The half-silvered mirror in an interferometer splits incident light into reflected and transmitted beams, which are reflected by rotating and stationary mirrors, creating an interference pattern at the beamsplitter; the moving mirror alters the path length, leading to variations detected as IR energy changes, providing spectral information [14].

Applications

FTIR spectroscopy equipment is widely employed in various applications:

- It is used in quality control to analyze and maintain the consistency of industrially manufactured materials.
- The material analysis showed shifts in absorption bands signal changes in composition or contamination.
- It is used in drying processes for polymers, photoresist materials, and polyimides.
- FTIR spectrum analysis aids in diagnosing organ diseases and quantifying biomolecules such as proteins, nucleic acids, and lipids.

The FTIR Alpha (II) Bruker unit in the range of 400–4000 cm^{-1} is used in the present study.

3.3.3. Thermogravimetric Analysis-Differential Thermal Analysis (TG-DTA)

Thermal analysis (TA) encompasses a range of measurement techniques united by a common principle: they assess how a material responds to heating, cooling, or isothermal conditions. The aim is to establish a relationship between temperature and distinct physical properties of materials. Among the most widely employed techniques are:

1. **Thermogravimetric Analysis (TGA):** TGA measures changes in a material's weight as a function of temperature, typically used to investigate decomposition, volatilization, or oxidation processes.
2. **Differential Scanning Calorimetry (DSC):** DSC measures the heat flow into or out of a material as it undergoes physical or chemical transformations. It is beneficial for studying phase transitions and reactions.
3. **Differential Thermal Analysis (DTA):** A sample property is continuously measured as the sample is programmed through a predetermined temperature profile.

Thermogravimetric Analysis (TGA)

The demand for controlled heating processes and precise temperature regulation led to the development advanced heating furnaces in TGA. The development of accurate thermometers and temperature scales marked a significant milestone in the eighteenth century, with Celsius introducing its temperature scale in 1742. During this period, temperature was primarily determined by observing the thermal expansion of materials. These advancements laid the foundation for the precise control and measurement of temperature, integral to various thermal analysis techniques, including TGA [15].

Working principle

TGA is a valuable analytical technique used to investigate how the mass of a substance changes in response to controlled variations in temperature and time within a specified environment. Commercial TGA instruments often offer an impressive upper-temperature limit, typically reaching 1000 $^{\circ}\text{C}$ or beyond. A controlled atmosphere is established within the instrument to carry out TGA effectively. This atmosphere is created by introducing a purge gas, which can be chosen to be inert

(nitrogen, argon, or helium), oxidizing (typically air), or reducing. These different atmospheres allow us to investigate how materials respond to diverse thermal conditions, shedding light on their stability, decomposition, and other relevant characteristics. Typically, measured substances exhibit mass loss, but it's also possible to observe mass gain before degradation occurs, especially when heating rates are slow and the atmosphere is oxidizing. The mass loss can be attributed to volatile components, which include absorbed moisture, residual solvents, or low-molecular-mass additives or oligomers. These components tend to evaporate within the temperature range of ambient conditions to around 300 °C. In addition, reaction products such as water and formaldehyde can be generated while curing phenolic and amino resins. These reaction products are typically observed within the 100 to 250 °C temperature range. Furthermore, the degradation of volatile products can lead to chain scissions, which occur in the temperature range of 200 to 800 °C [16].



Figure 3.6 TG-DTA measurement unit [17]

Thermogravimetric instruments have various components to ensure flexibility in obtaining specific analytical data. These key components include balance, which is used to measure the weight of the sample accurately. The furnace provides controlled and linear heating to the sample. A temperature programmer is used for precise temperature measurement and control during the analysis. The recorder records and displays the unit for weight changes and temperature variations throughout the study. These components work in tandem to enable comprehensive TGA and to capture essential data regarding weight loss and temperature changes in the sample over time

[18]. The weight of the sample causes a balance beam to shift from its normal position in TGA instruments. Two main types of balances are employed for this purpose: null and deflection balances.

Null Balance: In this type, a sensor detects the deviation of the balance beam from the null point, and a reset force is applied to bring it back into balance. Various methods, such as photographic recording, electrical signals, or electrochemical devices, are used to measure the conducted beam deflection and convert it into a recognizable weight.

Deflection Balance: These balances directly measure the deflection of the balance beam and do not rely on a null point. The change in position of the beam is used to determine the weight. Several factors can influence the sensitivity of the balance, leading to alterations in the shape of the TGA curves. To ensure accurate results, it is crucial to calibrate the instruments before conducting new experiments [19-20]. In this study, the thermal and oxidative stability of the prepared samples were analyzed using TG-DTA, performed with an SDT-2960 instrument from TA Instruments, USA (Fig. 3.6).

Applications

- DTA can provide valuable insights into the thermal properties of materials, including specific heat capacity, thermal conductivity, and thermal diffusivity.
- In metallurgy, DTA is extensively used to examine the behavior of metals and alloys during thermal treatments like annealing, quenching, and tempering.
- It is instrumental in determining phase transitions and assessing the kinetics of phase transformations during these processes.
- Analysis of polymers, organic and inorganic materials and determining the effect of oxidative or reductive atmospheres on materials

3.3.4. Transmission Electron Microscopy (TEM)

The TEM is a potent tool in materials science. The TEM functions based on the same fundamental principles as a light microscope but employs electrons rather than visible light. Due to the significantly smaller wavelength of electrons compared to light, TEM can achieve a level of resolution that is orders of magnitude superior to that of a light microscope. High-resolution TEM can be utilized to analyze the quality, shape, size, and density of structures like quantum wells, wires, and dots. One of the key advantages of TEM is that electrons, which are used as the probing

particles, have a significantly shorter wavelength than light. While light microscopes depend on shorter wavelengths for increased resolution, in TEM, as electrons illuminate the specimen, the longer electron wavelength boosts resolution. The wavelength of electrons is approximately 0.005 nm, which is 100,000 times shorter than that of light. This fundamental difference in wavelength contributes to TEM's superior resolution, offering about 1,000 times greater.

Working principle

The electron beam produced by the electron gun is focused into a compact, coherent beam through the condenser lens. The condenser aperture is then employed to eliminate high-angle electrons, refining the beam further. Subsequently, the beam strikes the specimen, and depending on its thickness and electron transparency, parts of it are transmitted through. The portion of the electron beam that passes through the specimen is then focused by the objective lens, creating an image on either a phosphor screen or a charge-coupled device (CCD) camera. Optional objective apertures can block high-angle diffracted electrons to enhance contrast. The image then travels through the column, passing through intermediate and projector lenses at each stage, where it is successively magnified. The high-resolution power they produce, which enables their application in numerous fields, powers their functioning mechanism. The schematic representation of TEM shown in **Fig. 3.7**, and its three functional components are as follows:

a) Electron gun

The TEM electron beam-producing section is located at the electron gun. A cathode forms electrons in a tungsten filament that is V-shaped, and it is usually heated. The tungsten filament is covered by a control grid known as a Wehnelt cylinder with a central hole that lies columnar to the tube. The cathode lies on top of or below the cylindrical column hole. The cathode and the control grid are negatively charged with an end of the anode, which is disk-shaped and has an axial hole. The transmission of electrons from the cathode to the anode through a columnar aperture (hole) at a high voltage and consistent energy. This process effectively focuses the specimen to create a precisely defined image. The TEM incorporates a condenser lens system crucial in concentrating the electron beam onto the specimen. It controls the energy intensity and the column hole of the electron gun, ensuring precise imaging and analysis. The TEM uses two condenser lenses to converge the beam of electrons to the specimen. The two condenser lenses each function to produce an image, i.e.,

the first lens, which has strong magnification, produces a smaller image of the specimen, to the second condenser lens, directing the image to the objectives.

b) Image- Producing system

The TEM consists of several critical components contributing to its imaging capabilities: The objective lens is a fundamental element of the TEM near the specimen. It has a short focal length, typically 1 to 5 millimeters. This lens plays a crucial role in forming an intermediate image from the sample, which is then transmitted to the projector lenses for further magnification. The intermediate lens is one of the types of projector lenses. It allows for substantial magnification of the intermediate image, contributing to the overall magnification of the specimen. The projector lens is another type of projector lens in the TEM. It imparts additional magnification beyond that provided by the intermediate lens. This combination of lenses ensures that the final image is highly magnified. For optimal performance and the production of high-quality images, both the objective and projector lenses require high-power supplies with excellent stability to achieve the highest resolution standards.

c) Image-Recording System

The TEM is equipped with various components that enable the visualization and capture of images. A fluorescent screen is used in TEM to view and focus on the images. It plays a critical role in the formation and visualization of images. A digital camera is also incorporated into the microscope, which records the images permanently after viewing. The TEM features a vacuum system that maintains a vacuumed environment within the microscope. This vacuum system is essential for preventing electron movement and focusing disruption caused by collisions with air molecules. It ensures that electrons travel in a straight path to form images. The vacuum system consists of several key elements, including a pump, gauge, valves, and a power supply, all working together to create and maintain the vacuum.

The images produced by TEM are monochromatic, typically appearing in shades of grey or black and white. Electrons can pass through a fluorescent screen positioned at the microscope's base to make these images visible to the human eye. The images captured by TEM can also be recorded digitally. They can be displayed on a computer screen and stored in formats like JPEG or TIFF. It's possible to manipulate the monochromatic images and add color during storage and processing. When the electron beam hits the phosphor screen, it generates light, making the image visible.

The darker areas of the image represent regions of the sample where fewer electrons have passed through. In contrast, the lighter areas of the image represent areas of the sample through which more electrons were transmitted [22-24].

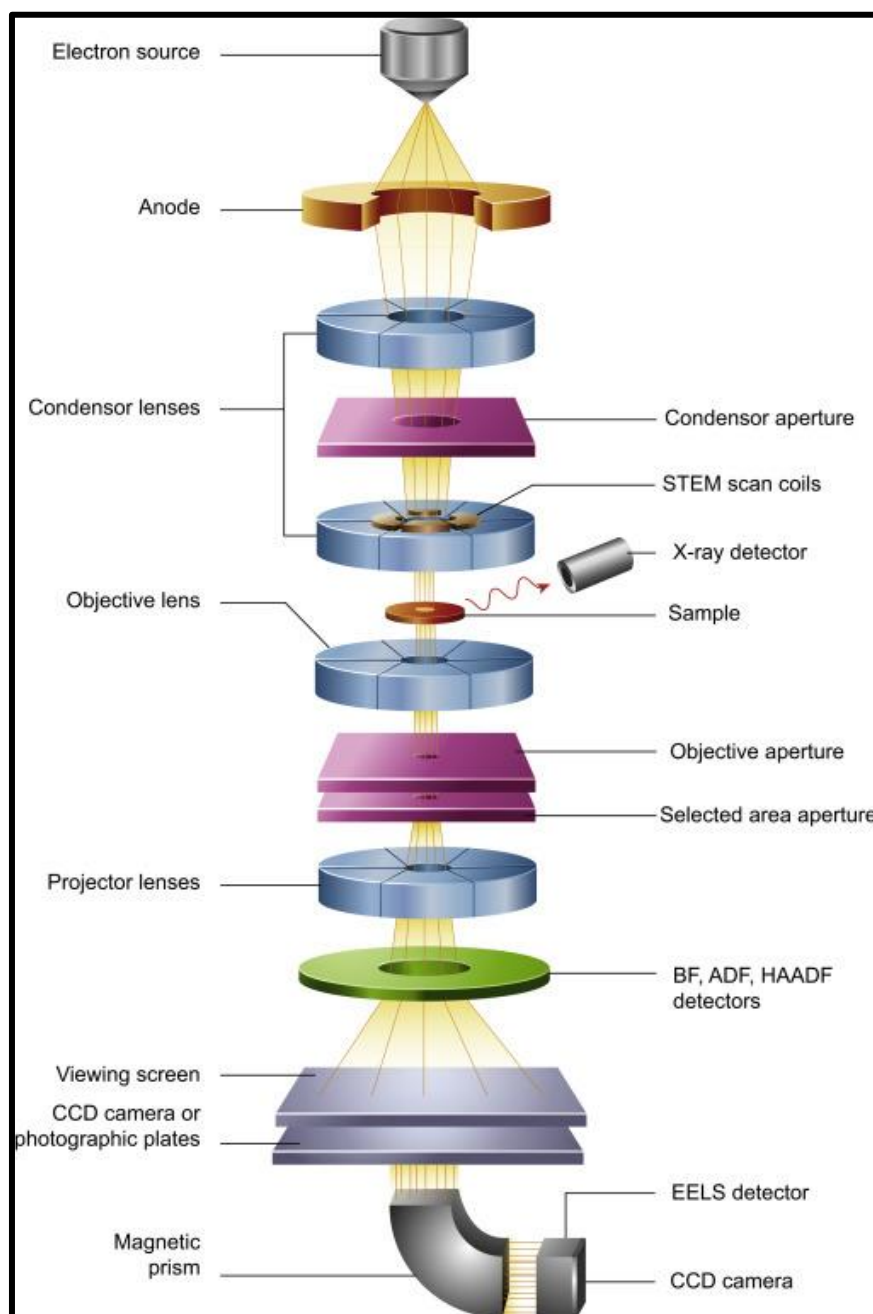


Figure 3.7 Schematic representation of TEM [21]

Applications of TEM

TEM is utilized in a wide range of applications. Biology, microbiology, nanotechnology, and forensic studies are:

- It is used for visualizing and researching the intricate cell structures of bacteria, viruses, and fungi.
- TEM is used to determine nanoparticle size, shape, and distribution.
- TEM aids in examining the diverse forms and sizes of microbial cell organelles, deepening our understanding of microorganisms.
- This technique is instrumental in investigating and differentiating between plant and animal cells, shedding light on their unique features.

Energy dispersive X-ray Spectroscopy (EDS)

EDS, or EDX or EDXA, is a highly effective technique to analyze an object's elemental composition. The fundamental principle underlying EDS operation relies on high-energy electromagnetic radiation interaction with the electrons within an atom, specifically X-rays. This interaction removes 'core' electrons, which are those not situated in the outermost electron shell. This principle is articulated by Moseley's Law, which established a direct relationship between the emitted light's frequency and the element's atomic number. Vacancies are created after removing these core electrons, and higher-energy electrons can fill these gaps. As the filling electrons transition to their lower energy states, they release energy. Notably, the energy emitted during this relaxation is unique to each element found on the periodic table. Consequently, by irradiating a sample with X-rays, EDS can be employed to ascertain elements' presence and relative proportions within the sample.

Here is an illustrative example of how EDS functions: Electrons in different electron shells are denoted by letters K, L, and M, with K electrons closest to the nucleus and having an n value of 1. The terms α and β are used to signify the magnitude of the transition. The transition from M to L or L to K is designated as $L\alpha$ or $K\alpha$ while transitioning from M to K is termed a $K\beta$ transition, as shown in **Fig. 3.8**. These transitions are collectively described using the Siegbahn notation. EDS relies on a system comprising three primary components: an emitter, a collector, and an analyzer.

Typically, these components are integrated into electron microscopes, such as scanning electron microscopes (SEM) or TEM. The collaborative operation of these three elements facilitates the assessment of the quantity of emitted X-rays and their energy levels concerning the initial X-ray emission. The data obtained through EDS analysis is visually represented as a graph, where the x-axis represents energy in kilo-

electronvolts (KeV), and the y-axis represents peak intensity. To deduce the elements associated with the energy variations, a computer program is employed to convert the peak positions on the x-axis into the specific atoms responsible for the energy transitions observed. This process assists in identifying the elemental composition of the analyzed sample [25-28].

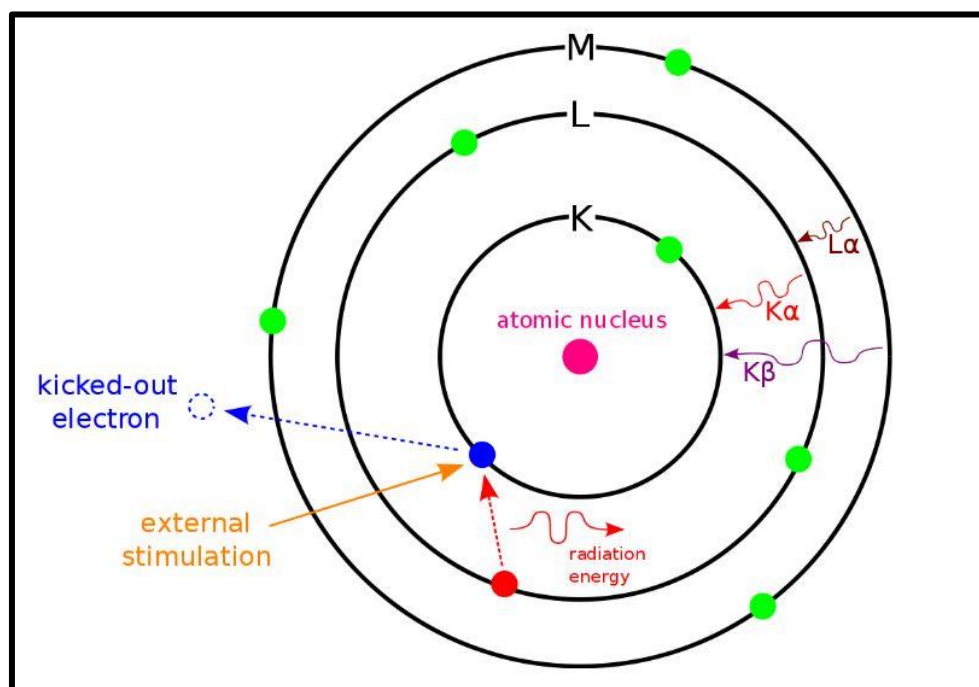


Figure 3.8 Mechanism of X-ray emission in EDS

EDS systems are most commonly integrated into SEMs and electron microprobes. SEMs rely on a cathode and magnetic lenses to generate and focus an electron beam. The energy of the electron beam is a critical parameter that must be carefully chosen to balance the need for high-resolution and efficient X-ray production. The X-rays generated within the specimen are analyzed using two focused crystal spectrometers. An EDS X-ray detector is commonly employed and typically constructed as a solid-state device using lithium-drifted silicon. This detector measures the relative abundance of emitted X-rays as a function of their energy. When an incident X-ray interacts with the detector, it generates a charge pulse, and the magnitude of this pulse is directly proportional to the energy of the X-ray. Following the generation of a charge pulse, it is converted into a voltage pulse by a charge-sensitive preamplifier. These voltage signals are then transmitted to a multichannel analyzer, categorizing the pulses according to their voltage levels. The energy of each incident X-ray is determined from the voltage measurement and is

subsequently sent to a computer for visualization and in-depth data analysis. The X-ray spectrum, which illustrates the relationship between X-ray energy and the corresponding counts, is scrutinized to infer the elemental composition of the sample volume under investigation.

It is important to note that elements with low atomic numbers can be challenging to detect using EDS. To address this, the silicon (Si) detector is often protected by a beryllium (Be) window. However, the presence of the Be window limits the detection of elements with atomic numbers below 11 (Na). In windowless systems, elements with atomic numbers as low as 4 (Be) have been detected, but the challenges associated with lower atomic numbers become increasingly significant [29-30].

In the present study, Transmission Electron Microscopy with a JEOL TEM-2100 microscope operating at 200 kV, and an EDXS (energy-dispersive X-ray spectroscopy) detector was used for size, shape and composition of given studies.

3.3.5. Vibrating Sample Magnetometer (VSM)

The VSM is a straightforward yet precious technique used to characterize the properties of magnetic materials. This method is based on Faraday's law, which describes how an electromagnetic force is induced in a coil when there is a change in the magnetic flux linked with the coil [31]. The basic principle of VSM is shown in **Fig. 3.9**.

The VSM operates with a straightforward principle. It involves subjecting a sample to vibration between two pickup coils while simultaneously applying a direct current (DC) magnetic field to the sample, generally in a direction perpendicular to the coils. This magnetic field leads to the sample's magnetization, causing the vibrating magnetic moment to create a flux that fluctuates over time. By Faraday's Law, this temporal flux change results in the induction of an alternating current (AC) voltage in the detection coils. The signals generated in the coils are then detected using a lock-in amplifier. This instrument is chosen because it features a narrow bandwidth (for a given relative frequency) and very high gain. The lock-in amplifier yields a DC voltage output directly proportional to the magnetic moment of the material. As a result, this setup enables the measurement of sample magnetization as a function of the applied magnetic field, yielding a magnetization curve.

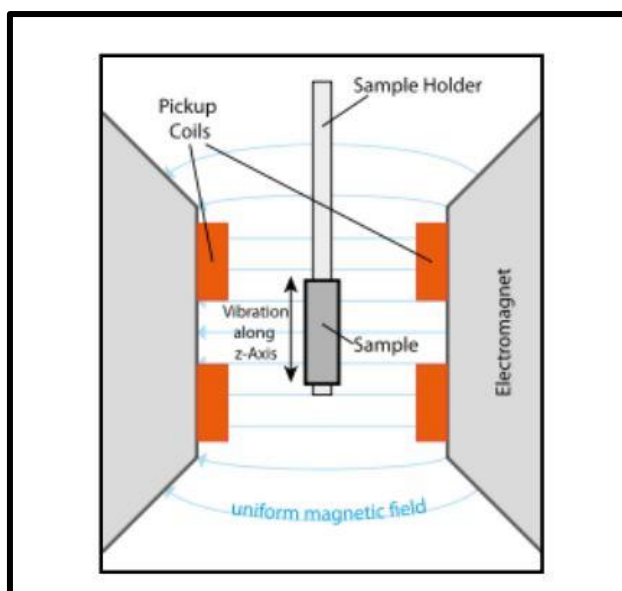


Figure 3.9 Basic principle of VSM

Working principle

The fundamental VSM measurement process involves oscillating the sample close to a detection (pickup) coil while synchronously detecting the induced voltage. This is accomplished using a compact gradiometer pickup coil arrangement, which allows for relatively large oscillation amplitudes, typically in the range of 1-3 mm at its peak, and operates at 40 Hz. This configuration enables the system to detect magnetization variations smaller than 10^{-6} electromagnetic units (emu) at a frequency of 1 Hz. It includes a VSM linear motor transport for vibrating the sample, a detection coil set puck, electronics for driving the motor and processing signals from the coils, and software for automation and control. The sample is mounted on the end of a rod that moves in a sinusoidal pattern. The oscillation center is precisely positioned at the vertical midpoint of the gradiometer pickup coil. The VSM motor module, guided by an optical linear encoder signal from the motor transport, ensures accurate control of both the position and amplitude of the oscillation. The voltage generated in the pickup coil is amplified and processed using lock-in detection within the VSM detection module, which employs the position encoder signal as a reference for synchronized detection. The VSM motor module generates the encoder signal by processing raw signals from the VSM linear motor transport. In the VSM detection module, the in-phase and quadrature-phase signals from the encoder and the amplified voltage signal from the pickup coil are detected. These signals are averaged and transmitted to the

VSM application on the PC for further analysis and processing. The schematic working principle of VSM is shown in **Fig. 3.10**.

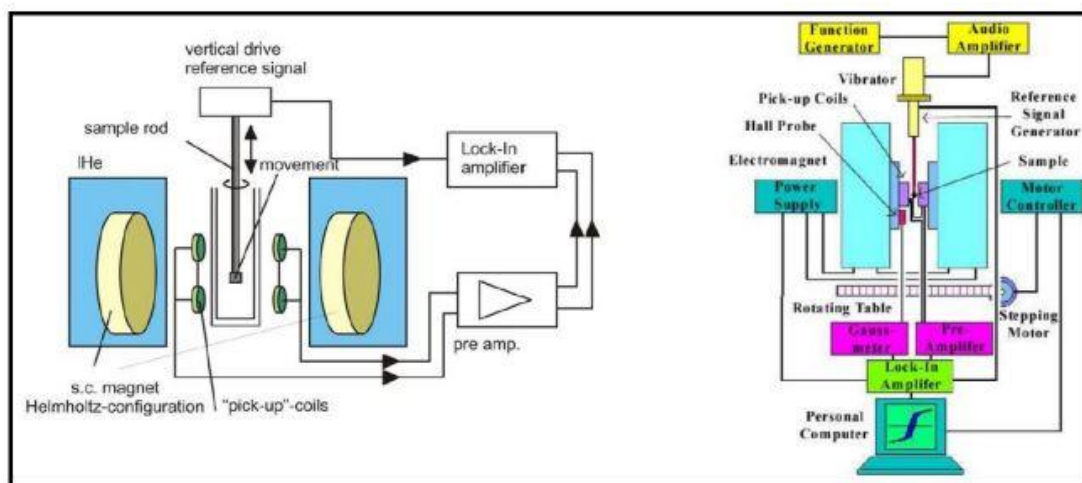


Figure 3.10 Working Principle of Vibrating Sample Magnetometer [32]

Applications

- The VSM is widely used to characterize the magnetic properties of diamagnetic, paramagnetic, ferromagnetic, and antiferromagnetic materials.
- An essential application is measuring domain sizes in ferromagnetic minerals, offering valuable insights into their magnetic properties [32-34].

In the present study, all magnetic characterizations of prepared MNPs were carried with Lake Shore 7307 model under the applied field of $\pm 10,000$ Oe at room temperature and low temperature.

3.3.6. Zeta Potential and Dynamic Light Scattering

Dynamic Light Scattering (DLS) is a well-established and highly accurate method for determining particle sizes in suspensions and emulsions. Its fundamental principle relies on the Brownian motion of particles within a liquid medium, where smaller particles exhibit faster movements while larger ones move at a slower pace. By analyzing the light scattered by these particles, DLS can extract valuable information about their diffusion rates, consequently providing insights into the size distribution of particles within the sample. DLS is a useful method for particle size analysis, offering a comprehensive size range capability spanning from 0.3 nm to 10,000 nm. Unlike Laser Diffraction, which tends to encounter limitations for particles smaller

than 100 nm due to weak signals and small angular change in scattering, DLS excels in precisely this size range. Its particular strength lies in the analysis and characterization of nanoparticles. DLS provides additional advantages, such as measuring highly concentrated and extremely dilute samples. Moreover, it can determine important parameters like Zeta Potential, molecular weight, and concentration, making it a comprehensive tool embedded in many DLS analyzers.

Working principle

A typical DLS system has six essential components. To begin with, a laser (1) serves as the light source, illuminating the sample particles within a cell (2). Although most of the laser beam travels directly through the sample, a portion scatters when it interacts with the particles. A detector (3) captures the scattered light, and because particles scatter light in all directions, the detector can theoretically be positioned at any angle and still detect the scattering.

Depending on the specific DLS model, the detector is positioned at either 175° or 90° . For precise measurements, the intensity of the scattered light must remain within a particular range. If the detected light is too intense, the detector can become overloaded. To prevent this, an "attenuator" decreases the laser's intensity, reducing the scattering intensity. In cases where samples scatter minimal light, as with tiny particles or samples of low concentration, the attenuator permits more laser light to pass through to the sample.

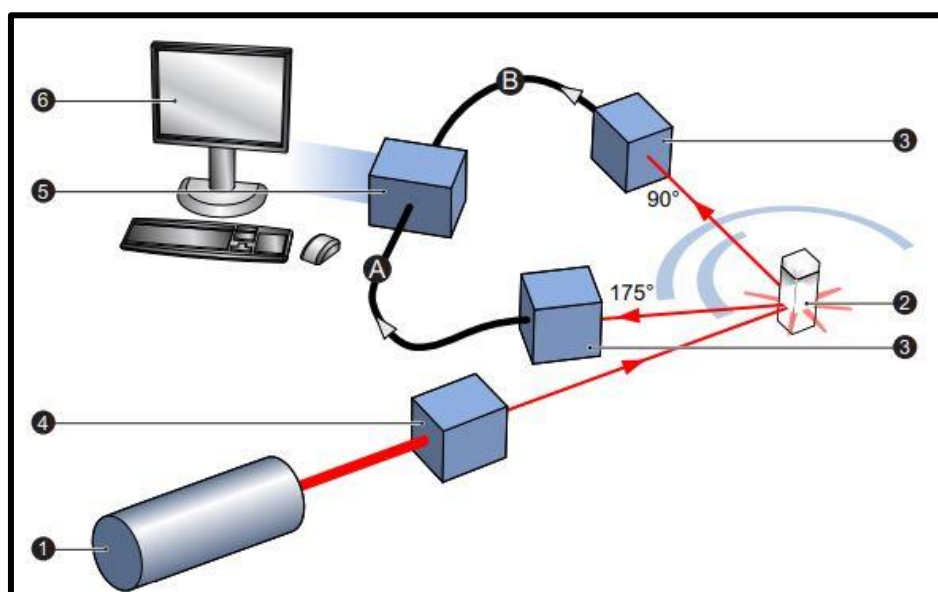


Figure 3.11 Basic working principle of the DLS system

Conversely, for samples that scatter more light, such as larger particles or samples with higher concentrations, the attenuator decreases the laser light reaching the sample. This precise control allows for accurate DLS measurements. The basic working principle of the DLS system is shown in **Fig. 3.11**.

The particle-liquid interface affects the physical properties of colloids and suspensions, with zeta potential being a key factor in optimizing formulations and predicting interactions; particles with zeta potentials above +30 mV or below -30 mV are considered stable. In a zeta potential measurement system, six essential components are at play. Initially, a laser (1) serves as the light source to illuminate the particles in the sample for zeta potential measurements. This laser light is split into an incident beam A and a reference beam B, modulated to create the required Doppler Effect for the measurement. The laser beam is directed through the center of the sample cell (2), and a scattering beam C is detected at an angle of 12.8° .

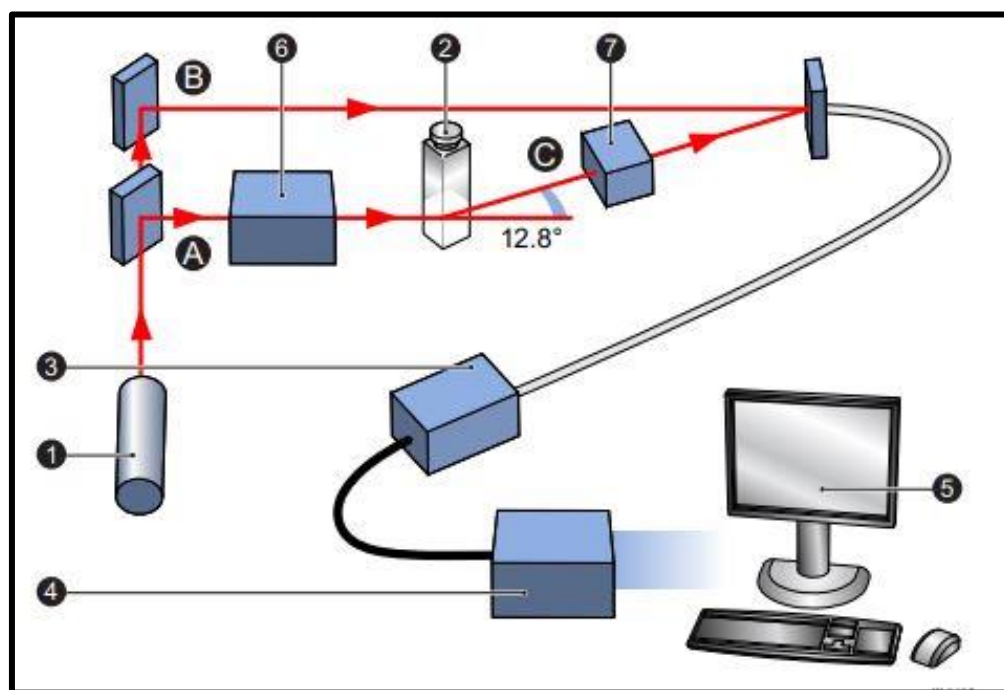


Figure 3.12 Basic working principle of zeta potential system

When an electric field is applied to the cell, particles moving through the measurement volume create fluctuations in the intensity of the detected light. A detector (3) transmits this information to a digital signal processor (4). This information is subsequently forwarded to a computer (5), where the Zetasizer generates a frequency spectrum to calculate electrophoretic mobility and,

consequently, zeta potential information. For precise measurements, it is essential to maintain the intensity of the scattered light within a specific range, as overloading the detector can lead to inaccuracies. To address this concern, an 'attenuator' (6) is utilized to decrease the laser's intensity, thereby reducing the intensity of the scattering.

Furthermore, compensation optics (7) are integrated into the path of the scattering beam to account for potential differences in cell wall thickness and refractive properties of the dispersant, ensuring the alignment of the scattering beams is maintained. This helps to correct for potential sources of error in the measurements [35-37]. The basic working principle of the zeta potential system is shown in **Fig. 3.12**.

Applications

- DLS system is used in many industries and research labs to measure the size of nanoparticles.
- Droplet size and zeta potential are critical indicators of emulsion stability.
- To measure protein size and aggregation and measure the isoelectric point.
- The particle size of pigment used in ink and paints is an essential physical characteristic affecting appearance and functionality.

The colloidal stability was assessed by determining the zeta potential using Malvern Instruments.

3.3.7 UV-Vis Spectroscopy

A spectrophotometer allows for the analysis of liquids, gases, and solids by utilizing radiant energy across the electromagnetic spectrum's far and near ultraviolet, visible, and near-infrared regions. The specific wavelengths of electromagnetic radiation are defined as follows: ultraviolet (UV) from 300 to 400 nm, visible (Vis) from 400 to 765 nm, and near-infrared (NIR) from 765 to 3200 nm.

The instrument operates by passing a beam of light through a sample and measuring the wavelength of light that reaches the detector. The wavelength provides insights into the chemical structure, while the intensity is proportional to the number of molecules, indicating the quantity or concentration. Analytical information can be revealed regarding transmittance, absorbance or reflectance of energy in the wavelength range between 160 and 3500 mill microns [38]. The operation of a UV-Vis spectrophotometer begins when the integrated lamp emits either UV or visible

light, depending on the wavelength required. Different lamps are used for each type of light; for example, a deuterium lamp produces ultraviolet light, while a tungsten lamp emits visible light. The monochromator then plays a key role in the process.

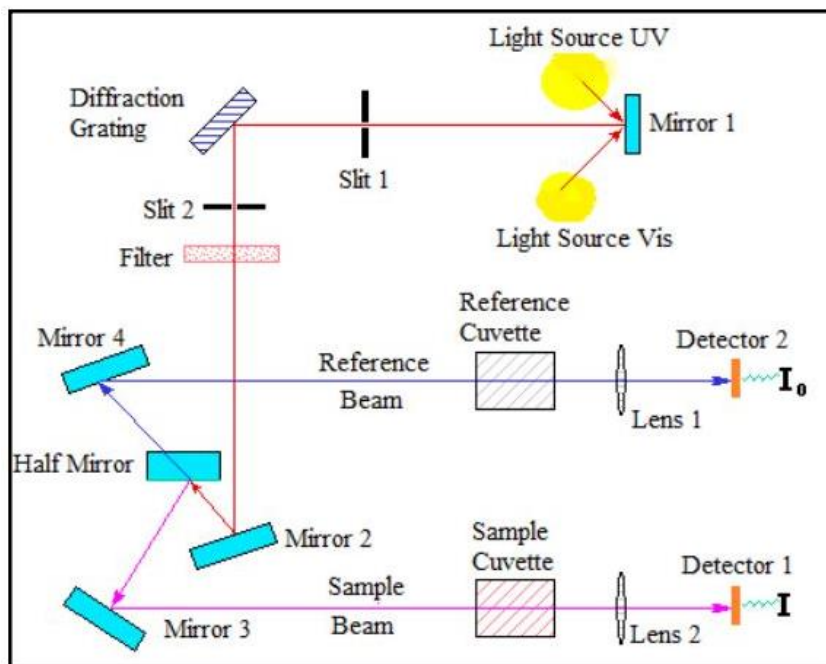


Figure 3.13 Schematic diagram of UV–Vis–NIR Spectrophotometer [39]

A monochromator utilizes two slits separated by a prism or diffraction grating to create a light beam with a very narrow bandwidth, essentially isolating the light of a single color. The initial beam passes through the first slit and, upon hitting the prism, disperses into a spectrum of colors. Each wavelength is directed to a specific location, but only one wavelength passes through the second slit. The component in the UV-Vis spectrometer is the beam splitter, which separates the light into two parallel beams of equal intensity. These beams are directed toward two cuvettes—one containing the sample and the other holding the reference. After passing through the cuvettes, the beams reach the detector. The detector converts the impact of photons into electrical current via computational programs [39]. The schematic diagram of the UV–Vis–NIR spectrophotometer is shown in **Fig. 3.13**

Applications

- The determination of the physical and chemical properties of the specimen
- Material science, pharmaceutical research, Life Science

3.3.8 Fluorescence Microscopy

A fluorescence microscope operates similarly to a standard light microscope but includes additional features to enhance its functionality. While a traditional microscope uses visible light (400-700 nm) to illuminate and magnify a sample, the fluorescence microscope is designed for more advanced imaging. A fluorescence microscope uses high-intensity light to excite fluorescent molecules, which emit lower-energy light to create a magnified image, allowing visualization of specific features in small specimens by filtering out background light and targeting specific areas with fluorescent tags. The schematic diagram of a wide-field fluorescence microscope is shown in **Fig. 3.14**.

A light source, like a Xenon or Mercury Arc Lamp, emits light across a wide wavelength range from ultraviolet to infrared. This light is directed through an excitation filter that selects the appropriate wavelength. A dichroic mirror, which reflects only the excitation wavelength, directs the light toward the sample. The light then passes through the objective lens, focusing it onto the fluorescent specimen. The emitted light from the specimen travels back through the objective for magnification and then through the dichroic mirror. The light is filtered by a barrier filter that selects for the emission wavelength, eliminating any unwanted light from the arc lamp or other sources reflected off the microscope components. The resulting filtered fluorescent emission is then directed to a detector for digitization.

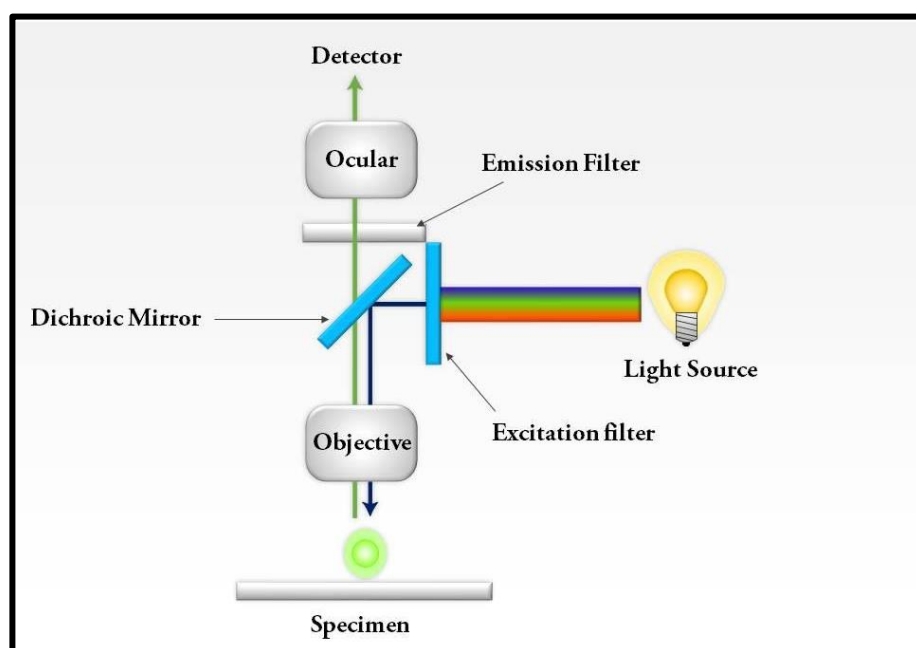


Figure 3.14 A schematic diagram of a wide-field fluorescence microscope [40]

The specimen under observation is stained or labeled with a fluorescent dye and illuminated with high-intensity ultraviolet light from a mercury arc lamp. This light passes through an exciter filter, allowing only blue light. The blue light then reaches a dichroic mirror, which reflects it downward onto the specimen. The specimen, labeled with the fluorescent dye, absorbs the blue light (shorter wavelength) and emits green light. This emitted green light travels upward, passing through the dichroic mirror, which reflects the blue light and allows only the green light to pass through the objective lens. Finally, the green light is filtered through the barrier filter before reaching the detector for digitization [42].

Applications

- It is used in biomedical research and clinical pathology.
- It enables multicolor staining, labeling cellular structures, and the assessment of a cell's physiological state.
- The fluorescence microscope aids in examining the texture and structure of coal.
- Fluorescent dyes are used to investigate porosity in ceramics.

3.3.9 Confocal microscopy

Confocal microscopes generate clear images of objects that appear blurred under conventional microscopes. They capture light solely from the microscope's focal plane, effectively filtering most surrounding light. This technique reduces haze, improves contrast, and enables detailed 3D reconstructions by compiling thin slices of the object along the vertical axis. The schematic diagram of confocal microscopy is shown in **Fig. 3.15**.

A conventional microscope uses broad light to illuminate a large specimen area, often producing unclear, crowded images due to lacking a focal point. To overcome these issues, a Confocal Microscope is utilized. The entire specimen is illuminated in wide-field or fluorescent microscopes, leading to total excitation and light emission, which is then detected by a photodetector on the microscope. In contrast, the confocal microscope operates on the principle of point illumination. A specimen stained with fluorochrome is analyzed, and when a focused beam of light is directed at a specific point on the fluorochrome specimen, it generates illumination that is concentrated by the objective lens onto a plane above the objectives. The objective features an aperture on the focal plane above it, primarily designed to block

stray light from reaching the specimen. The illumination points measure approximately 0.25 to 0.8 μm in diameter, influenced by the objective's numerical aperture, and is about 0.5 to 1.5 μm deep with the highest intensity.

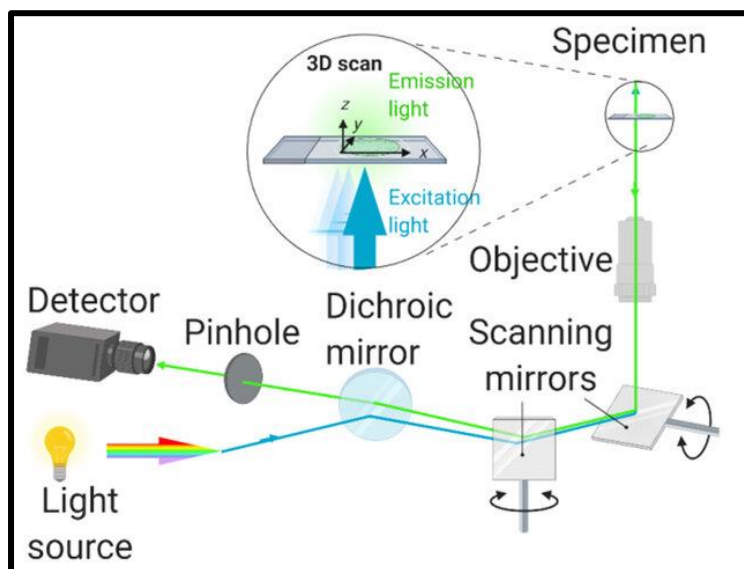


Figure 3.15 A schematic diagram of confocal microscopy

The specimen is typically positioned between the camera lens and the optimal focus point, referred to as the plane of focus. Using the laser from the microscope, the laser scans a plane on the specimen through beam scanning or by moving the stage (stage scanning). A detector then measures the illumination, creating an optical section image. Multiple optical sections are scanned and compiled into a computerized system, generating a 3D image that can be measured and quantified. The aperture above the objective blocks stray light and enhances the final result. Confocal microscope images have excellent contrast and resolution, regardless of the specimen's thickness. The images are saved as high-resolution 3D images of cellular structures and complexes. A key feature of the confocal microscope is its ability to detect only what is in focus, rendering out-of-focus areas black [43].

The specimen's image is generated as the microscope scanner directs the focused beam across a designated area, controlled by two high-speed oscillating mirrors powered by galvanometer motors. One mirror shifts the beam horizontally along the X-axis, while the other moves it vertically along the Y-axis. After completing a scan on the X-axis, the beam swiftly returns to the starting point to begin a new scan, a process referred to as flyback. No information is collected during

the flyback process. Therefore, the laser scanner illuminated the end of focus, which is the area of interest [44].

Applications

- In biomedical sciences, it is applied to analyze corneal infections by quantitatively and qualitatively assessing corneal endothelial cells.
- It also detects fungal elements in the corneal stroma during keratomycotic infections, enabling rapid diagnosis and timely therapeutic intervention.

3.3.10 Flow cytometry

The fundamental principle of flow cytometry involves cells passing individually in front of a laser for detection, counting, and sorting. The cell components are tagged with fluorescent labels, which the laser excites to emit light at different wavelengths. The schematic diagram of flow cytometry is shown in **Fig. 3.16**.

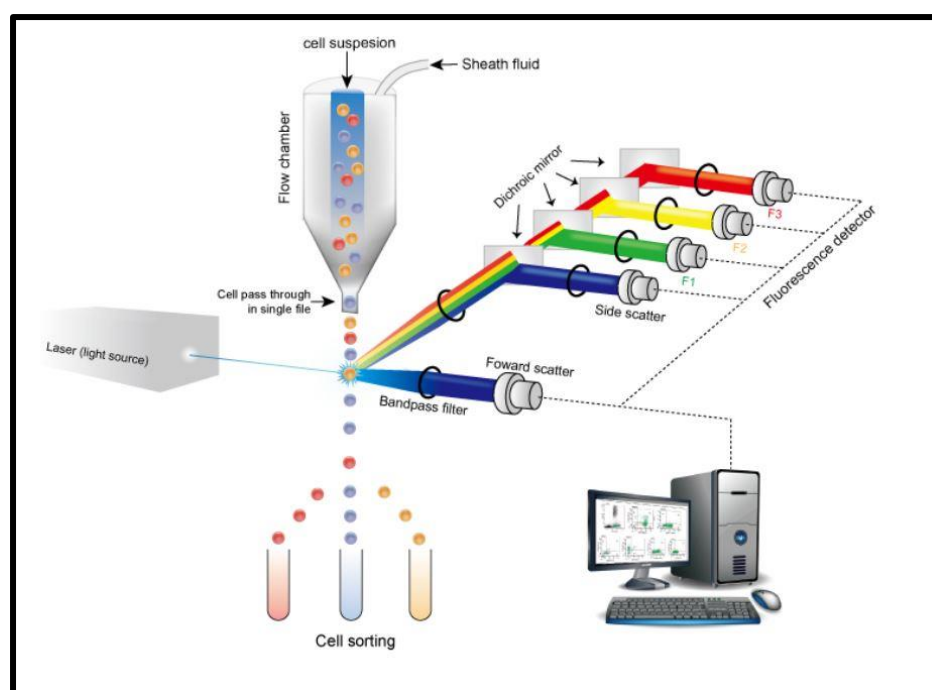


Figure 3.16 A schematic diagram of Flow cytometry [45]

The emitted fluorescence quantifies and identifies cells in a sample as thousands flow through a liquid stream, with a focused laser and strategically placed detectors measuring Forward Scatter (FSC) and Side Scatter (SSC). Fluorescent detectors are also present to identify different cell types or components using fluorescent labels. Particles or cells, ranging from 0.2 to 150 μm in size, move

through a light beam, causing the light to scatter. Fluorescently labeled cell components are excited by the laser, emitting light at longer wavelengths. The detectors capture both the scattered and fluorescent light and the data is processed by a computer equipped with specialized software for analysis. The intensity of each detector, corresponding to each fluorescent emission peak, is calibrated for optimal detection. Various details about the cells' physical and chemical properties can be obtained based on these light measurements. Generally, FSC can detect the cell volume, whereas the SSC reflects the inner complexity of the particle, such as its cytoplasmic granule content or nuclear structure [45].

A flow cytometer consists of three core components: the fluidics system, the optics system, and the electronics system.

- a) **Fluidics:** The fluidics system delivers particles in a fluid stream to the laser beam. This is done by injecting the sample into a stream of sheath fluid, typically a buffered saline solution, within the flow chamber. The chamber's design focuses on the sample core in the middle of the sheath fluid, where the laser beam interacts with the particles. The focusing occurs as the sample suspension is injected into the sheath fluid, guiding the particles to the center of the sample core.
- b) **Optics System:** The optical system of the cytometer is made up of excitation optics and collection optics. The excitation optics include the laser and lenses that shape and focus the laser beam onto the sample flow. The collection optics feature a lens that captures the light emitted after the particle interacts with the laser, along with a set of optical mirrors that redirect specific wavelengths of the collected light to designated detectors. Once a cell or particle passes through the laser light, the emitted rays and fluorescence signals are directed to photomultiplier tubes (PMTs) while a photodiode gathers the signals. A filter is placed in front of the tubes to ensure a detector is specific to a particular fluorescent dye, allowing only a narrow wavelength range to reach the detector.
- c) **Electronics system:** The electronic system transforms the signals from the detectors into digital signals that a computer can process. When light signals hit one side of the PMT or photodiode, they are converted into a relative number of electrons, which are multiplied to produce a more robust electrical current. This electrical current is sent to the amplifier, which converts it into a voltage pulse.

The peak of this pulse occurs when the particle passes through the center of the beam, resulting in the highest levels of scatter or fluorescence. The Analog-to-Digital Converter (ADC) then converts the pulse to a digital number [46-47].

Applications

- It is utilized in clinical laboratories to detect malignancies in bodily fluids, such as in cases of leukemia.
- Cytometers, such as cell sorters, can physically isolate and collect specific cells of interest into separate tubes.
- It can be utilized to measure DNA content through fluorescent markers.
- Flow cytometers allow the analysis of replication cells using fluorescent dye for four stages of the cell cycle.

3.3.11. Biocompatibility study: Cytotoxicity assays

Cell culture assays use isolated cells cultured *in vitro* to evaluate a material's or extract's biocompatibility. These methods help determine a material or chemical's potential for toxicity or irritation. Before doing *in vivo* studies, they offer excellent screening materials. Before receiving FDA approval, medical devices intended for human implantation must undergo preclinical testing consisting of both *in vitro* and *in vivo* evaluations.

a) Qualitative Cytotoxicity Tests

Qualitative cytotoxicity tests for medical devices often involve three standard methods. The Direct Contact method is particularly suitable for low-density materials like contact lens polymers. In this process, a sample of the test material is placed directly onto cells grown in a culture medium. The cells are then incubated, allowing any chemicals leaching from the test material to diffuse into the medium and interact with the cell layer. The presence of cell malformation, degeneration, and lysis around the test material serves as an indicator of the sample's reactivity.

The *Agar Diffusion assay*, on the other hand, is ideal for assessing dense materials such as elastomeric closures. This method spreads a nutrient-rich agar layer over the cultured cells. The test material, or its extract dried on filter paper, is then placed on the agar surface, and the cells are incubated. The appearance of a zone containing malformed, degenerative, or lysed cells beneath and around the test material is a clear indicator of cytotoxicity.

The *MEM Elution assay* involves using various extracting media and extraction conditions to assess devices under realistic usage conditions or conditions that magnify potential risks. Extracts derived from the medical device can be titrated to evaluate cytotoxicity semi-quantitative. These extracts are subsequently applied to a layer of cells and then incubated. Following incubation, the cells are carefully examined under a microscope to detect any indications of malformation, degeneration, or cell lysis. It is generally advisable to perform at least one cytotoxicity test on each constituent component of a specific medical device.

b) Quantitative Cytotoxicity – 3-(4,5-dimethylthiazol-2-yl)-2,5-diphenyl tetrazolium bromide (MTT) Assay

Recent regulatory changes on the biocompatibility of medical devices highlight that although qualitative cytotoxicity tests, such as direct contact, MEM elution, and agar diffusion, are effective for initial screening, quantitative assessments are preferred for more accurate evaluation. One such quantitative method is the MTT cytotoxicity assay, which can accurately quantify cell viability with as few as 950 cells. This assay relies on a colorimetric approach that measures the reduction of a yellow compound called MTT by mitochondrial succinate dehydrogenase. Since this reduction reaction only occurs in living cells, it enables the quantification of the percentage of viable cells in a solution.

The MTT assay evaluates the cytotoxicity of various substances, including medical device materials and potential anti-cancer drugs, offering quantitative results, flexibility in testing methods, and reduced subjectivity in interpretation. Moreover, the MTT assay can be conducted using 96-well microplates in a standard reader, like the Bio-Tek ELx808, enabling rapid screening of multiple samples (**Fig. 3.17**). The toxic effects of nanoparticles depend on cell type and organ, as cell physiology and membrane traits influence outcomes, with MNPs introduced through biomedical applications like intravenous or intramuscular pathways. Depending on the affected organ, different cell types may be selected for cytotoxicity studies, ranging from those affecting the liver, nervous system, and blood to the kidneys. It's essential to optimize the conditions and cell numbers when choosing the appropriate cell type for cytotoxicity assessment. In this study, L929 mouse fibroblast cell lines and MCF7 (adenocarcinoma cell line of human breast) cell lines were chosen to evaluate nanoparticle cytotoxicity [48-50].

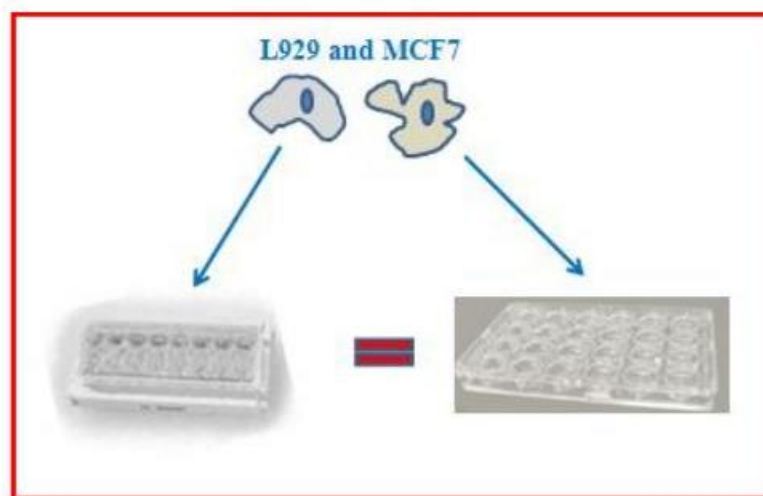


Figure 3.17 Biocompatibility study on L929 mouse fibroblast cell lines

The MTT assay, while recommended, doesn't distinguish between cell death mechanisms and may underestimate early damage, highlighting the need for standardized dose metrics in MNP cytotoxicity studies. *In vitro*, the dosage of MNPs should be defined at various levels, considering their mode and site of action. These dose metrics are advantageous for accounting for differences in cellular uptake that can be particle-dependent. Additionally, the dispersion state of nanoparticles plays a crucial role in nanotoxicological studies. Therefore, selecting the appropriate dose of nanoparticles is essential for conducting cytotoxicity assays and gaining a better understanding of the toxic effects of MNPs [51-54].

3.3.12. Magnetic Induction Heating System for Hyperthermia

Induction heating operates through a process where a high-frequency alternating current is first applied to the coil, which serves as the primary winding. As a result, an AMF is generated, following the principles of electromagnetism. Subsequently, the workpiece, which effectively acts as a single, short-circuited secondary winding, is positioned within the coil.

MHT entails introducing a colloidal magnetic nanofluid into an AC magnetic field with adequate strength and frequency. This process results in the heating of the particles due to mechanisms such as magnetic hysteresis losses or Neel relaxation. **Fig. 3.18** depicts a high-frequency induction machine alongside its schematic representation. Magnetic hyperthermia therapy can be carried out using four primary methods: arterial embolization hyperthermia (AEH), direct injection hyperthermia

(DIH), and intracellular hyperthermia (IH). Magnetic mediators for cancer hyperthermia therapy are promising due to their superior temperature control and magnetic properties.

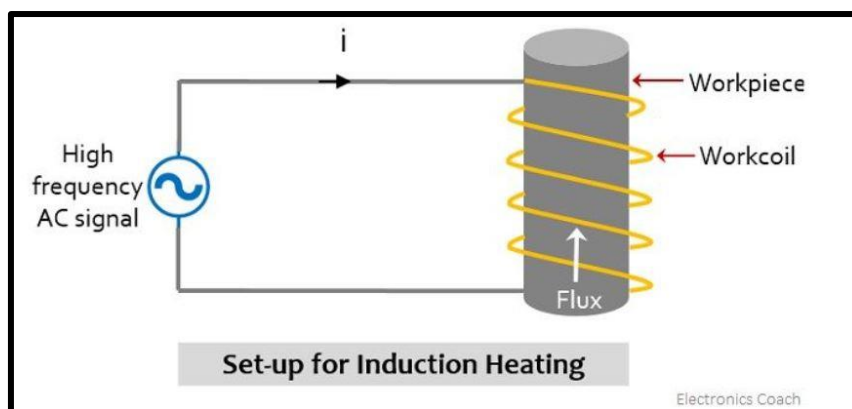


Figure 3.18 Schematic representation of induction heating system [55]

Furthermore, the distribution of magnetic nanoparticles in tissues can be visualized through MRI before the heating process [56]. Various magnetic mediators have been developed due to their effective heat dissipation characteristics in AMF. Magnetic mediators primarily target heat release through magnetic losses, representing the conversion of magnetic field energy into heat during magnetization reversal processes in particle systems. These processes include hysteresis, Nèel, or Brownian relaxation and losses resulting from friction in viscous suspensions.

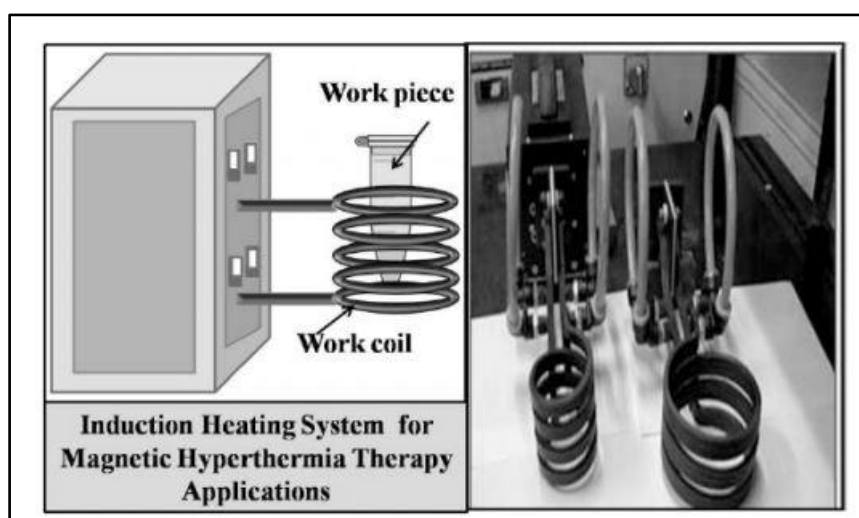


Figure 3.19 Induction heating system instrument

To study the material's potential for hyperthermia applications, induction heating was performed in a 1.5 mL plastic microcentrifuge tube using an induction

heating device (Easy Heat 8310, Ambrell; UK) with a 6 cm diameter and four turns heating coil (**Fig. 3.19**). The MNPs were dispersed in 1 mL of distilled water and positioned at the center of the coil. A frequency of 265 kHz was then applied. The heat generated by the magnetic fluid in response to the applied magnetic field is quantified using a SAR, measured in watts per gram (W/g), and calculated according to **equation 2.11** (**Section 2.2.3**).

3.4 References

1. L. Lu, N. Dung, L. Tung, C. Thanh, O. Quy, N. Chuc, S. Maenosono, N. Thanh, *Nanoscale*, 7 (46) (2015) 19596-19610.
2. J. Scheck, B. Wu, M. Drechsler, R. Rosenberg, A. Van Driessche, T. Stawski, D. Gebauer, *J. Phys. Chem. Lett.*, 7(16) (2016) 3123-3130.
3. S. Sun, D. Gebauer, H. Cölfen, *Angew. Chem. Int. Ed.*, 56(14) (2017) 4042-4046.
4. M. Besenhard, A. LaGrow, A. Hodzic, M. Kriechbaum, L. Panariello, G. Bais, K. Loizou, S. Damilos, M. Cruz, N. Thanh, A. Gavriilidis, *J. Chem. Eng.*, 399 (2020) 125740- 125760.
5. S. Salih, W. Mahmood, *Heliyon*, 9 (6) (2023) 2405-8440.
6. C. Kalaiselvan, S. Laha, S. Somvanshi, T. Tabish, N. Thorat, N. Sahu, *Coord. Chem. Rev.*, 473 (2022) 214809- 214841.
7. Z. Chen, *Inorg. and Nano-Met. Chem.*, 42(7) (2012) 1040-1046.
8. S. Pillai, *Solid State Physics*, 6th Edition New Age Science Publishing (2009) 429-431.
9. B. Sharma, *Instrumental method for chemical analysis*, 24th Edition, Goel Publishing house, Meerut (2005) 494-536.
10. B. Cullity, S. Stock, 3rd Edition, Prentice Hall, New York, (2001).
11. G. Socrates, *Infrared and Raman characteristic group frequencies: tables and charts*. John Wiley & Sons, 3rd Edition (2004) 1-362.
12. R. Meier, *Chem. Soc. Rev.*, 34 (9) (2005) 743-752.
13. G. Bellisola, C. Sorio, *Am. J. Cancer Res.*, 2 (1) (2012) 1-21.
14. M. Pillingb, P. Gardner, *Chem. Soc. Rev.*, 00 (2013), 1-3.
15. C. Keattch, D. Dollimore, *J. Therm. Anal.*, 37 (1991) 2089-2102.
16. J Menczel, R Prime, *Thermal Analysis of Polymers: Fundamentals and Applications* (2009) 241-317.
17. <https://mse.engin.umich.edu/ta-sdt-2960-simultaneous-dsc-tga>.
18. Haines PJ. Springer Science & Business Media; (2012) 22-62.
19. M. Saroj, R. Payal, *Analytical Methods in Chemical Analysis*, Walter de Gruyter GmbH & Co KG; (2023)147-169.
20. N. Zainal, J. Saiter, S. Halim, R. Lucas, C. Chan, *Chem. Teach. Int.*, 3(2) (2020) 59-75.

21. J. Inkson, In Materials characterization using non-destructive evaluation (NDE) methods, Woodhead publishing, 1st Edition (2016) 17- 43.
22. D. Williams, C. Carter, Transmission Electron Microscopy: Spectrometry, IV Edition, (1996) 3-17.
23. P. Harris, Transmission electron microscopy of carbon: a brief history. C. 4 (1) (2018) 4-21.
24. G. Nair, S. Survase, P. Raote, R. Naik, S. Barve, Material Characterization Techniques for Beginners, BFC Publications, 1st Edition, (2023) 19-27.
25. R. Mishra, A. Zachariah, S. Thomas, In Microscopy methods in nanomaterials characterization, 1st Edition, 1 (2017) 383-405.
26. A. Girão, G. Caputo, M. Ferro, In Comprehensive analytical chemistry, Elsevier 75 (2017) 153-168.
27. M. Scimeca, S. Bischetti, H. Lamsira, R. Bonfiglio, E. Bonanno, European journal of histochemistry: EJH, 62 (1) (2018) 2841- 2852.
28. L. Corbari, M. Cambon-Bonavita, G. Long, F. Grandjean, M. Zbinden, F. Gaill, P. Compere, Biogeosciences, 5 (2008) 1295–1310.
29. P. Flewitt, R. Wild, Physical methods for materials characterization. CRC Press; 3rd Edition (2017) 28-118.
30. D. Brandon, W. Kaplan, Microstructural Characterization of Materials, 2nd Edition, (2013) 1-30.
31. K. Buschow, F. Boer, Physics of magnetism and magnetic materials, 1st Edition (2003) 85-89.
32. V. Lopez-Dominguez, A. Quesada, J. Guzmán-Mínguez, L. Moreno, M. Lere, J. Spottorno, F. Giacomone, J. Fernández, A. Hernando, M. García, Rev. Sci. Instrum., 89(10) (2018) 10I112- 10I117.
33. B. Dodrill, J. Lindemuth, Magnetic measurement techniques for materials characterization, Springer, Cham., (2021) 15-37.
34. M. Mariyanto, D. Ramadhan, T. Purba, F. Nabilah, J. Phys. Conf., 2309 (1) (2022) 012025-012033.
35. B. Berne, R. Pecora, Dynamic Light Scattering, Courier Corporation, 1st Edition, (1976) 24-53.
36. S. Thomas, R. Thomas, A. Zachariah and R. Mishra, Thermal and Rheological Measurement Techniques for Nanomaterials Characterization, 1st Edition, 3 (2017) 37-50.

37. D. Titus, E. Samuel, S. Roopan, Nanoparticle characterization techniques. In Green synthesis, characterization and applications of nanoparticles, Elsevier, 1st Edition, (2019) 303-319.
38. F. Rocha, A. Gomes, C. Lunardi, S. Kaliaguine, G. Patience, Can. J. Chem. Eng., 96(12) (2018) 2512–2517.
39. E. Tomaszewska, K. Soliwoda, K. Kadziola, B. Tkacz-Szczesna, G. Celichowski, M. Cichomski, W. Szmaja, J. Grobelny, J. Nanomater., 1 (2013) 313081-313091.
40. U. Kubitscheck, Fluorescence microscopy: from principles to biological applications, 2nd Edition, John Wiley & Sons; (2017) 85-132.
41. B. Herman, Fluorescence microscopy. Garland Science, 1st Edition (2020) 1-10.
42. A. Elliott, Curr Protoc Cytom., 92 (1) (2020) 68-79.
43. W. Jerome, R. Price, Basic confocal microscopy, 2nd Edition, (2018) 1-20.
44. K. McKinnon, Current protocols in immunology 120 (1) (2018) 1-11.
45. A. Adan, G. Alizada, Y. Kiraz, Y. Baran, A. Nalbant, Crit. Rev. Biotechnol. 37(2) (2017) 163-176.
46. Aysun Adan et al.; Flow cytometry: basic principles and applications. Crit. Rev. Biotechnol., 2016, 37(2): 163-176.
47. A. Nemmar, M. Hoylaerts, P. Hoet, D. Dinsdale, T. Smith, H. Xu, J. Vermeylen, B. Nemery, Am J Respir Crit Care Med, 166(7) (2002) 998-1004.
48. N. Lewinski, V. Colvin, R. Drezek, Small, 4(1) (2008) 26-49.
49. P. Nguyen, E. Clark, S. Ananthakrishnan, K. Lenz, H. Canavan, Biointerphases, 15(3) (2020) 31201- 31216.
50. B. Diaz, C. Sánchez-Espinel, M. Arruebo, J. Faro, E. de Miguel, S. Magadán, C. Yagüe, R. Fernández-Pacheco, M. Ibarra, J. Santamaria, A. González-Fernández Small, 4(11) (2008) 2025-2034.
51. Z. Lacava, R. Azevedo, E. Martins, L. Lacava, M. Freitas, V. Garcia, C. Rebula, A. Lemos, M. Sousa, F. Tourinho, M. Da Silva, J. Magn. Magn. Mater., 201(1-3) (1999) 431-434.
52. A. Jordan, P. Wust, H. Föhling, W. John, A. Hinz, R. Felix, Int. J. Hyperth., 25(7) (2009) 499-511.

53. S. Laurent, D. Forge, M. Port, A. Roch, C. Robic, L. Elst, R. Muller, *Chem. Rev.*, 108(6) (2008) 2064-2110.
54. A. Lu, E. Salabas, F. Schüth, *Angew. Chem. Int. Ed.*, 46(8) (2007) 1222-1244.
55. T. Kobayashi, *Biotechnol. J.*, 6(11) (2011) 1342-1347.
56. A. Salunkhe, V. Khot and S. Pawar, *Curr. Top. Med. Chem.*, 14 (2014) 572-594.

CHAPTER-4

Synthesis of Manganese Iron Oxide Nanoparticles

The part of this chapter has published as a research article



<http://pubs.acs.org/journal/acsodf>



Article

Application of $\text{Mn}_x\text{Fe}_{1-x}\text{Fe}_2\text{O}_4$ ($x = 0-1$) Nanoparticles in Magnetic Fluid Hyperthermia: Correlation with Cation Distribution and Magnetostuctural Properties

Satish S. Phalake, Manohar S. Lad, Ketaki V. Kadam, Syed A. M. Tofail, Nanasaheb D. Thorat,* and Vishwajeet M. Khot*

Cite This: *ACS Omega* 2022, 7, 44187–44198

Read Online

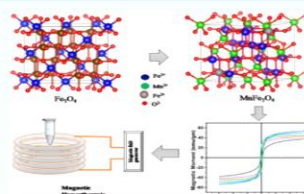
ACCESS |

Metrics & More

Article Recommendations

Supporting Information

ABSTRACT: Optimization of manganese-substituted iron oxide nanoferrites having the composition $\text{Mn}_x\text{Fe}_{1-x}\text{Fe}_2\text{O}_4$ ($x = 0-1$) has been achieved by the chemical coprecipitation method. The crystallite size and phase purity were analyzed from X-ray diffraction. With increases in Mn^{2+} concentration, the crystallite size varies from 5.78 to 9.94 nm. Transmission electron microscopy (TEM) analysis depicted particle sizes ranging from 10 ± 0.2 to 13 ± 0.2 nm with increasing Mn^{2+} substitution. The magnetization (M_s) value varies significantly with increasing Mn^{2+} substitution. The variation in the magnetic properties may be attributed to the substitution of Fe^{3+} ions by Mn^{2+} ions inducing a change in the superexchange interaction between the A and B sublattices. The self-heating characteristics of $\text{Mn}_x\text{Fe}_{1-x}\text{Fe}_2\text{O}_4$ ($x = 0-1$) nanoparticles (NPs) in an AC magnetic field are evaluated by specific absorption rate (SAR) and intrinsic loss power, both of which are presented with varying NP composition, NP concentration, and field amplitudes. $\text{Mn}_{0.75}\text{Fe}_{0.25}\text{Fe}_2\text{O}_4$ exhibited superior induction heating properties in terms of a SAR of 153.76 W/g. This superior value of SAR with an optimized Mn^{2+} content is presented in correlation with the cation distribution of Mn^{2+} in the A or B position in the Fe_2O_4 structure and enhancement in magnetic saturation. These optimized $\text{Mn}_{0.75}\text{Fe}_{0.25}\text{Fe}_2\text{O}_4$ NPs can be used as a promising candidate for hyperthermia applications.



4.1 Introduction

MNPs have received much attention in recent decades because of their potential biological uses. These applications include targeted drug delivery, biological separation, magnetoresistive biosensing, MRI, and their use as heat dissipation agents in activities such as gene transcription, neural stimulation, and cancer treatment [1]. IONPs are the most frequently employed materials in magnetic hyperthermia due to their low toxicity. Additionally, exploration into other ferrite nanoparticles, such as manganese ferrite, has been undertaken due to their elevated magnetization within the ferrite family and their stability against oxidation [2, 3]. Maghemite ($\gamma\text{-Fe}_2\text{O}_3$) and magnetite (Fe_3O_4) NPs are particularly well-suited for diverse biomedical applications thanks to their distinctive physical characteristics, established biocompatibility, ease of production, and high tunability at the nanoscale [4, 5]. Magnetization in Fe_3O_4 can be adjusted by replacing iron ions with transition metal cations, particularly manganese ions, which have higher magnetic moments [6]. Many applications are being investigated, including catalysts, humidity sensors, biomedicine, MRI, microwave technologies, drug delivery, and MHT.

The unique properties of manganese ferrites, including high electrical resistance, a high Curie temperature (bulk MnFe_2O_4 with T_c of 577 K), low coercivity value, and minimal eddy current loss, make them versatile for various applications [7, 8]. The study has focused on integrating secondary cations, such as Mn^{2+} , in Fe_3O_4 and the reproducibility of synthesis [9]. In the last decade, the general term MFe_2O_4 (where M = Co, Mg, Ni, etc.) for spinel ferrites has been widely utilized in various technological and biomedical applications [10, 11]. The synthesis process, chemical content, annealing temperature, and cation distribution significantly influence these compounds magnetic and electrical properties. Investigating the cation distribution among the two interstitial sites in the structure of spinel ferrites remains challenging due to its impact on the properties of these materials [12]. Shahane *et al.* reported the MnFe_2O_4 MNPs showing the antiparallel spin moments between Fe^{3+} , Mn^{2+} and Fe^{2+} ions at A-sites and inverse spinel structures [13]. The sol-gel auto-combustion process with the Co substitution produces the polycrystalline spinel ferrite $\text{Co}_x\text{Ni}_{1-x}\text{Fe}_2\text{O}_4$ ($x = 0.0, 0.25, 0.50, 0.75$, and 1.0). Because of the increased magnetocrystalline anisotropy and smaller particle size in Co^{2+} substituted nickel ferrite, the density is higher than in Ni^{2+} ions. The saturation magnetization (M_s) was increased to $x = 0.8$, at which point M_s for CoFe_2O_4 decreased somewhat [14]. Numerous proposals have been made for

substituted magnetite nanoparticles for diverse bio-applications, denoted as $M_xFe_{3-x}O_4$ (where $M = Ni, Zn, Mn, Co$, and $0 < x \leq 1$). These substituted magnetite nanoparticles offer tunable magnetic properties by facilely replacing divalent or trivalent metal ions. This substitution can be achieved without altering the crystal structure through complete or partial replacement of these ions.

Manganese-doped IONPs, specifically $Mn_xFe_{3-x}O_4$, exhibit superior magnetization (M_s), low coercivity (H_c), and reduced inherent toxicity compared to other doped ferrite materials. They demonstrate higher magnetization in certain instances than the well-studied IONPs currently available. These manganese ferrites possess good chemical stability and biocompatibility. Moreover, their properties can be modified, enabling the tuning of hyperthermic therapeutic temperatures making them suitable for self-controlled hyperthermia treatment [15]. The precise formula for a metal ferrite material is expressed as $(M_xFe_{1-x}) [M_xFe_{2-x}] O_4$, where the 'A' tetrahedral site and 'B' octahedral site are denoted by parentheses and square brackets, respectively. The parameter 'x' represents the inversion parameter, quantifying the distribution of M^{2+} , Fe^{2+} , and Fe^{3+} cations among these sites. In the synthesis process, manganese substitution was carried out by varying the molar concentration of Mn^{2+} , resulting in the formation of $Mn_xFe_{1-x}Fe_2O_4$ with different molar ratios of Mn^{2+} to Fe^{2+} , where 'x' ranges from 0 to 0.75. Manganese ferrites, specifically $MnFe_2O_4$, are regarded as highly promising materials due to their remarkable magnetization capacity [16]. Muhammad *et al.* synthesized yttrium-substituted manganese ferrites using a reverse micelle micro-emulsion method and found that the lattice constant increased with an increase in the Yttrium content [17]. Various metal ions in spinel ferrite lead to structural distortions, which affect the material's physical and structural characteristics and parameters [18]. The distribution of ions between the tetrahedral and octahedral sites and their interaction ultimately decides the magnetic characteristics of NPs [19].

There are different methods for the synthesis of ferrite NPs, such as chemical co-precipitation [6], a sol-gel auto-combustion method [20], combustion synthesis [21], ultrasonically assisted co-precipitation method [22], and thermal decomposition method [23]. Thermal decomposition and co-precipitation methods are commonly used for the synthesis of NPs. The former approach may easily produce ferrite NPs of regulated size in an organic substrate. Chemical co-precipitation is the most basic method for synthesizing MNPs in an aqueous solution. The size of the NPs can be

changed by optimizing synthesis parameters such as concentration, pH, and temperature [13]. Despite significant progress in material chemistry, developing MNPs with better magnetic characteristics and monodisperse nature remains a problem for the scientific community in this sector.

MHT utilizes MNPs in cancer treatment, offering a non-invasive approach where nanoparticles at the tumor site elevate the temperature to 42–46°C. The SAR quantifies the heating effectiveness of MNPs, a parameter influenced by factors such as the size and shape of NPs, magnetization, strength of the AMF, frequency, and other relevant parameters. Additionally, the cation distribution in ferrites plays a significant role in affecting the magnetic properties of the NPs [24, 25]. The temperature response exhibited by MNPs under an AC magnetic field is influenced by various factors, including interparticle interaction, particle concentration in the carrier liquid, viscosity, heat capacity, and surface modification [26]. In this chapter, a comprehensive assessment of the substitution of Mn^{2+} into $\text{Mn}_x\text{Fe}_{1-x}\text{Fe}_2\text{O}_4$ (with x values of 0.0, 0.25, 0.50, 0.75, and 1.0) has been conducted, establishing a correlation between induction heating studies of MNPs and their cation distribution.

4.2. Synthesis and Characterizations of $\text{Mn}_x\text{Fe}_{1-x}\text{Fe}_2\text{O}_4$ ($x = 0.0, 0.25, 0.50, 0.75$, and 1.0) MNPs by Co-precipitation Method

In the typical synthesis of $\text{Mn}_{0.25}\text{Fe}_{0.75}\text{Fe}_2\text{O}_4$, (0.25 mmol) manganese (II) chloride, (2 mmol) iron (III) chloride hexahydrate, and (0.75 mmol) iron (II) chloride tetrahydrate were separately dissolved in double distilled water with constant stirring. Then, until co-precipitation occurs at pH 12, (8 mmol) sodium hydroxide (NaOH) was added directly to the above solution as a precipitating agent and kept at 70 – 80 °C for 2h. The precipitate was collected by magnetic decantation and washed with double distilled water. The washed precipitate was dried at room temperature overnight. $\text{Mn}_x\text{Fe}_{1-x}\text{Fe}_2\text{O}_4$ ($x = 0.0, 0.50, 0.75$, and 1.0) were prepared using the same procedure.

Characterizations

XRD patterns of powder samples with various concentrations were recorded using Cu- K_α radiation at the wavelength (λ) = 1.546 Å. The crystallite size of the samples was calculated using Scherrer equation 3.6 (Section 3.3.1),

The formula has been used to derive the lattice constant ‘ a ’ using the calculated corresponding d values,

$$a = d_{hkl} \sqrt{h^2 + k^2 + l^2} \quad (4.1)$$

X-ray density (d_x) of the material,

$$d_x = \frac{8M}{N(a)^3} \quad (4.2)$$

where ' M ' is the atomic weight, and ' N ' is Avogadro's number ($6.022 \times 10^{23} \text{ mol}^{-1}$). FTIR study of samples with different concentrations was obtained using alpha (II) Bruker unit, in the 400 cm^{-1} to 4000 cm^{-1} range. Transmission Electron Microscopy (2100F JEOL TEM) was employed to observe the size and shape of NPs. Magnetization field (M-H) measurements were conducted at room temperature in fields up to 15 kOe using a VSM. Easy Heat 8310 (Ambrell, UK) was used to study induction heating of as-prepared MNPs in a physiological medium at an applied fixed frequency of $\approx 277 \text{ kHz}$. The field amplitude was adjusted from 13.3 kA/m to 26.7 kA/m.

4.3. Results and Discussion

4.3.1. Structural Analysis

Crystallographic structure and crystallite size were determined using XRD patterns of $\text{Mn}_x\text{Fe}_{1-x}\text{Fe}_2\text{O}_4$ NPs with ($x = 0.0, 0.25, 0.50, 0.75$, and 1.0) shown in **Fig. 4.1a**.

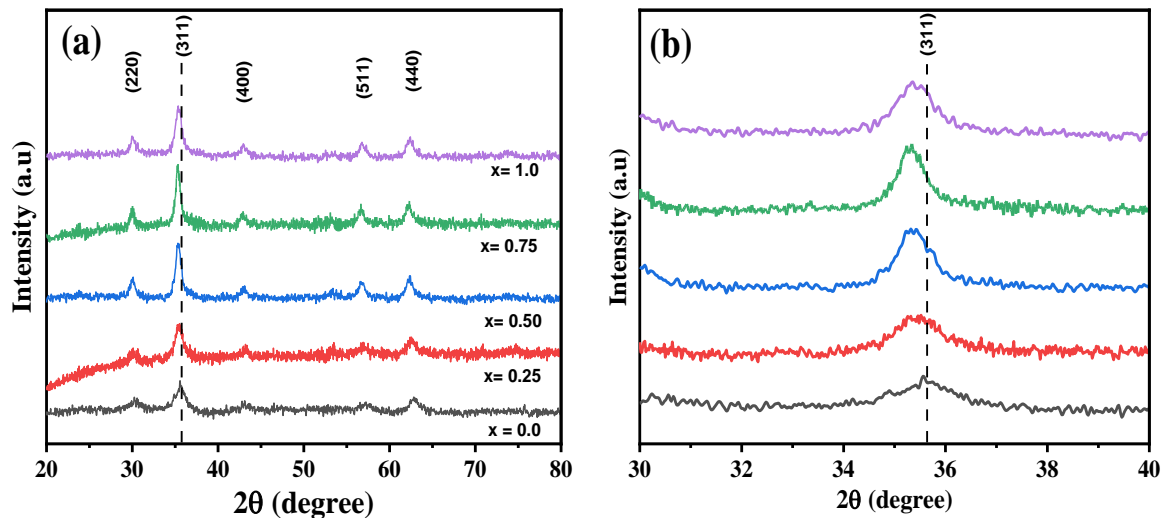


Figure 4.1 (a) XRD patterns for $\text{Mn}_x\text{Fe}_{1-x}\text{Fe}_2\text{O}_4$ ($x = 0.0, 0.25, 0.50, 0.75$, and 1.0) NPs; (b) Shift view of the region around (311) peak at different Mn^{2+}

The XRD patterns reveal broad peaks and crystallite sizes, confirming the crystalline nature of the samples. The profiles are matched with JCPDS cards No. 00-

019-0629 for Fe_3O_4 and 00-010-0319 for MnFe_2O_4 . The XRD results affirm the formation of cubic ferrite with space group $\text{Fd}\bar{3}\text{m}$. An enlarged view of the high-intensity characteristic peak (311) indicates a shift to lower angles with increasing Mn^{2+} substitution (**Fig. 4.1b**), attributed to the expansion of the unit cell as Mn^{2+} ions are incorporated into the magnetite structure [6]. The observed increase in lattice constant (a) with the rise in Mn^{2+} concentration is elucidated by considering ionic radii. The radius of Mn^{2+} (0.80 Å) is more significant than that of Fe^{2+} (0.77 Å) and Fe^{3+} (0.64 Å). This difference in ionic radii leads to lattice expansion, increasing the lattice parameter from 0.8350 nm to 0.8409 nm, reflecting the growth of the unit cell dimensions [27].

The inverse spinel manganese iron oxide will eventually expand when small-sized Fe^{3+} and Fe^{2+} ions are replaced with large-sized Mn^{2+} ions. This substitution introduces strain in the lattice, leading to linear elastic deformation. The effect is manifested in the changes in lattice plane spacing, causing the peaks to shift to lower 2θ positions in the X-ray diffraction [28]. The calculated lattice parameter ' a ' with different compositions is shown in **Table 4.1**.

Table 4.1 Lattice constant (a), Average crystallite size by XRD (D_{xrd}) and TEM (D_{TEM}), X-ray density (dx), specific surface area (S) of $\text{Mn}_x\text{Fe}_{1-x}\text{Fe}_2\text{O}_4$ NPs ($x = 0.0, 0.25, 0.50, 0.75$, and 1.0)

sample (x)	a (nm)	D_{xrd} (nm)	D_{TEM} (nm)	(dx) g/cm^3	S m^2/g
0.0	0.8354	5.784	7.6864	5.2735	236.75
0.25	0.8350	5.459	8.2154	5.2762	138.44
0.50	0.8424	10.93	9.4810	5.1324	136.84
0.75	0.8436	12.92	13.603	5.1055	113.78
1.00	0.8409	9.945	10.213	5.1590	114.83

The synthesized manganese iron oxide nanocrystals' calculated crystallite size (D_{xrd}) exhibits variation ranging from 5.7 nm to 12.92 nm, correlating with different Mn^{2+} concentrations. Concurrently, the calculated unit cell volume shows an increase from 0.583 nm^3 to 0.613 nm^3 , while the corresponding values of X-ray density (dx)

decrease from 5.27 g/cm³ to 4.99 g/cm³ with the progressive increase in Mn²⁺ concentration (Fig. 4.2) [29-30].

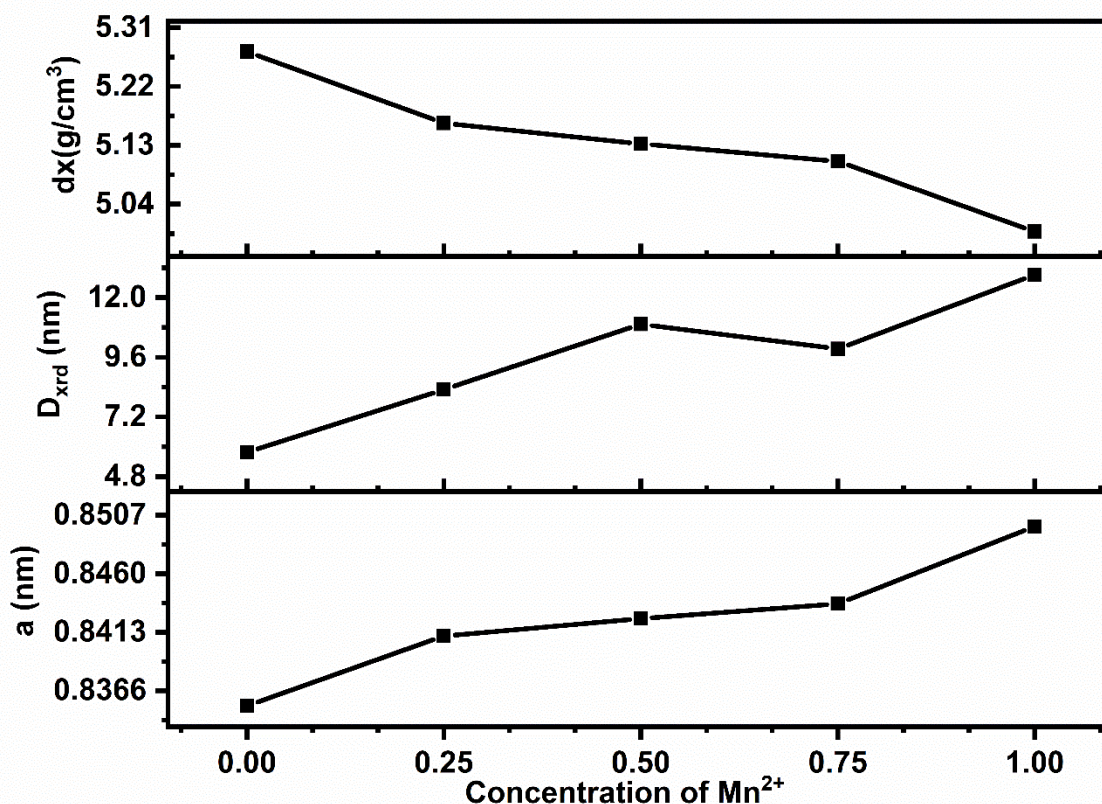


Figure 4.2 The variation of Mn_xFe_{1-x}Fe₂O₄ ($x = 0.0, 0.25, 0.50, 0.75$, and 1.0) NPs with Mn²⁺ content x in terms of their lattice parameter a (nm), crystallite size D_{xrd} (nm), and x-ray density dx (g/cm³)

4.3.2 Morphological Analysis

Fig. 4.3 (a, e, i) presents TEM images of manganese iron oxide nanoparticles (MIONPs), accompanied by corresponding histograms illustrating particle size distribution for three different compositions. The TEM analysis for samples Mn_xFe_{1-x}Fe₂O₄ ($x = 0, 0.25$, and 0.75) reveals particle size and distribution consistent with those determined by XRD. The product comprises agglomerated NPs with spherical and cubic forms, as observed in **Fig. 4.3**. Additionally, (c, g, k) shows the corresponding selected area electron diffraction (SAED) patterns of NPs, presenting spotty ring patterns that align with XRD results, confirming a good crystal structure. **Fig. 4.3** (b, f, j) depicts lattice fringes confirming the singular nature of the core, with lattice spacing approximately ranging from 0.20 nm to 0.27 nm, corresponding to the

(311) lattice plane [31]. **Fig. 4.3** (d, h, l) provides a histogram and confirms the formation of NPs with sizes around 7 ± 0.17 nm to 13 ± 0.2 nm.

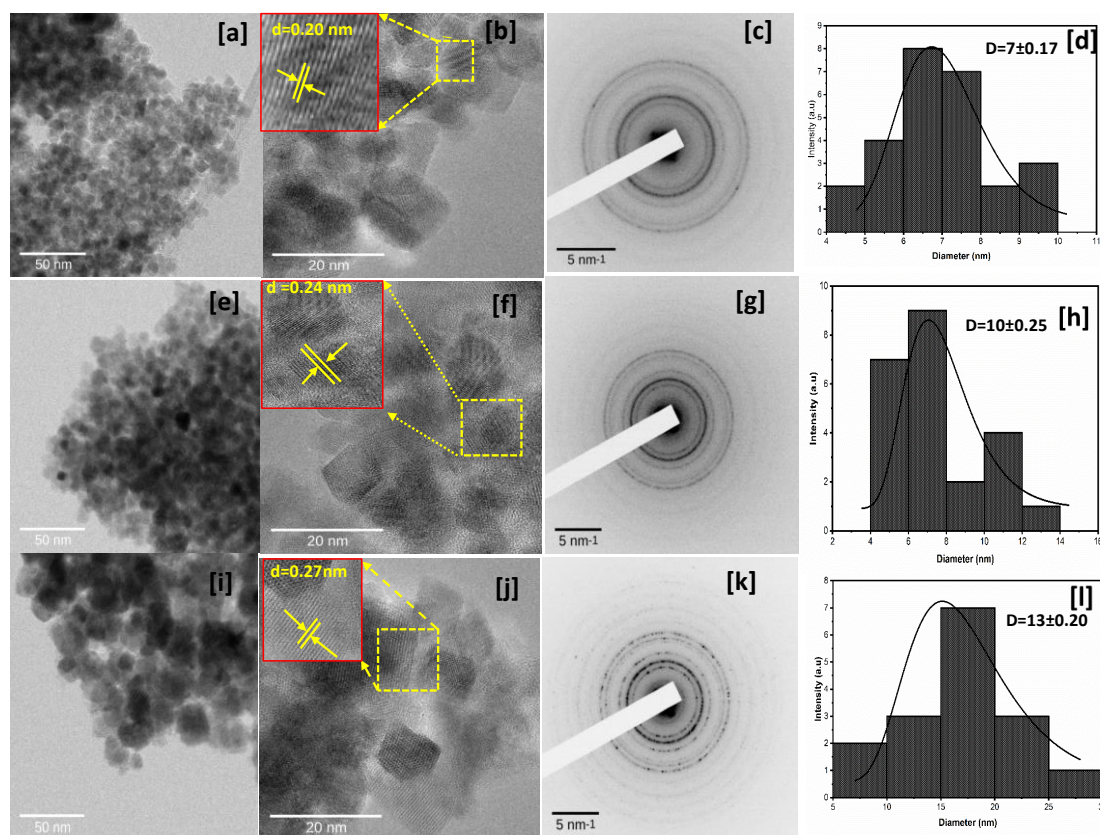


Figure 4.3 Images of (a-b, c, d), (e-f, g, h) and (I, j, k, l) represent TEM Images, SAED patterns and histograms of samples $\text{Mn}_x\text{Fe}_{1-x}\text{Fe}_2\text{O}_4$ at $x = 0, 0.25$ and 0.75 respectively

The chemical composition of the obtained $\text{Mn}_x\text{Fe}_{1-x}\text{Fe}_2\text{O}_4$ ($x = 0.0, 0.25, 0.50, 0.75$, and 1.0) NPs was investigated using energy dispersive X-ray analysis (EDX), as illustrated in **Fig. 4.4**. The analyzed results in the respective figure and **Table 4.2** confirm the percentage of Mn, Fe, and O elements. The phase purity of the samples affirms that they adhere to the expected composition ratio, indicating proper stoichiometry maintenance during preparation. The EDX spectra for the different samples and the corresponding analyzed results are shown in the following **Fig 4.4.**, confirming the percentage of Mn, Fe, and O elements.

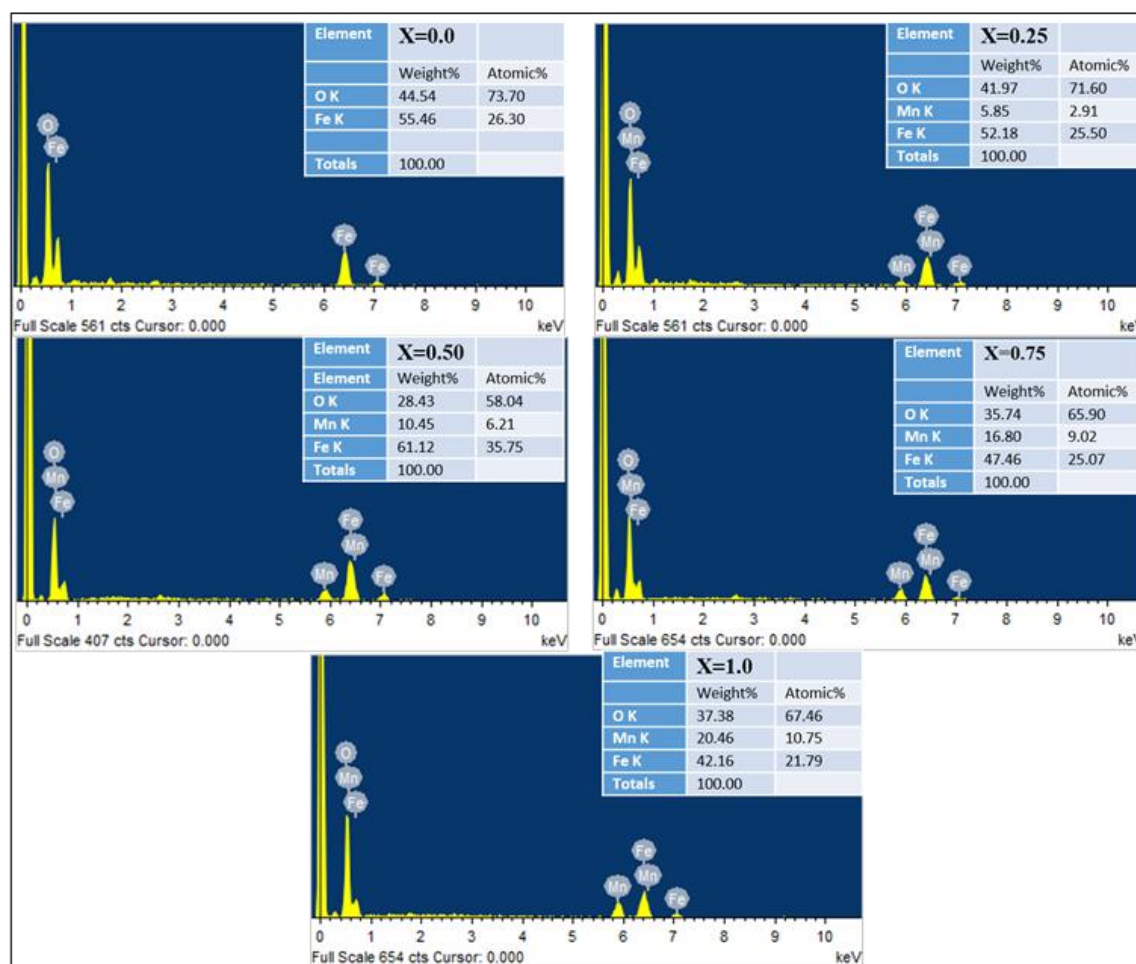


Figure 4.4. EDX spectra of the $\text{Mn}_x\text{Fe}_{1-x}\text{Fe}_2\text{O}_4$ ($x = 0.0, 0.25, 0.50, 0.75$, and 1.0) MIONPs along with their respective analyzed results as given in the inset

Fig. 4.5 depicts the FTIR absorption spectra of the $\text{Mn}_x\text{Fe}_{1-x}\text{Fe}_2\text{O}_4$ ($x = 0.0, 0.25, 0.50, 0.75$, and 1.0) NPs within the $4000\text{--}400\text{ cm}^{-1}$ range. The FTIR analysis confirms the formation of the spinel ferrite phase, revealing distinct intensity bands corresponding to covalent linkages between nanoparticles. Specifically, the $M_T\text{--}O\text{--}M_O$ stretching band at $\sim 600\text{--}500\text{ cm}^{-1}$, where M_T and M_O represent tetrahedral and octahedral sites, is evident in the spectra. The band positions of the synthesized Mn^{2+} substituted nanoferrites are shown in **Table 4.3**. As seen, the characteristic band of $\text{M}^{2+}\text{--}O$ has decreased from a value of 557.37 cm^{-1} to 553.47 cm^{-1} at tetrahedral sites and 439.52 cm^{-1} to 425.27 cm^{-1} at octahedral sites with increasing Mn^{2+} concentration. The bands around 1617 cm^{-1} and 3412 cm^{-1} are attributed to the bending vibrational modes of the adsorbed water molecules [32].

Table 4.2 Stoichiometric % concentration of the constituent elements of the $\text{Mn}_x\text{Fe}_{1-x}\text{Fe}_2\text{O}_4$ ($x = 0.0, 0.25, 0.50, 0.75$, and 1.0) NPs by EDX

Sample $\text{Mn}_x\text{Fe}_{1-x}\text{Fe}_2\text{O}_4$ (x)	Mn	Fe	O
0.0	0.0	27.30	73.70
0.25	2.91	25.50	71.60
0.50	6.21	35.75	58.04
0.75	9.02	25.07	65.90
1.00	10.75	21.79	67.46

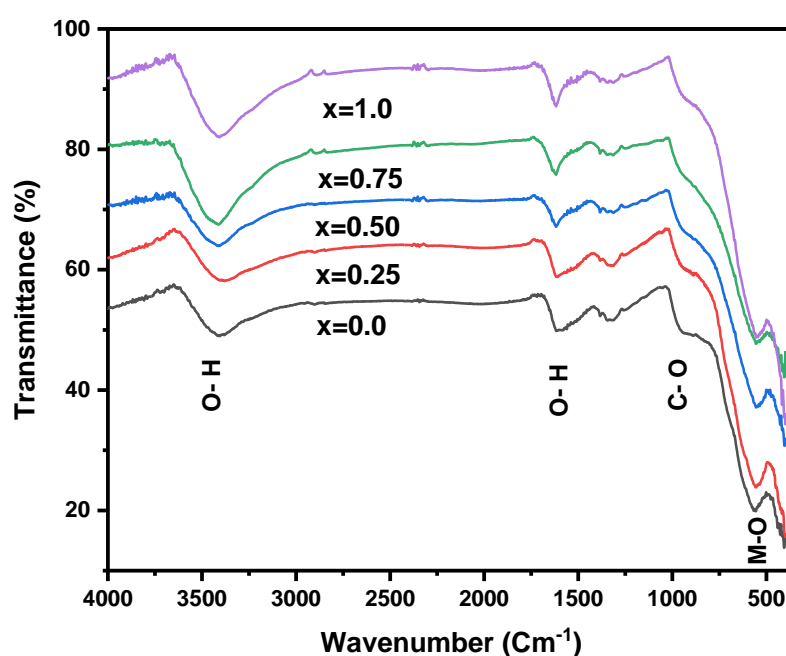


Figure 4.5 FTIR spectra of $\text{Mn}_x\text{Fe}_{1-x}\text{Fe}_2\text{O}_4$ ($x = 0.0, 0.25, 0.50, 0.75$, and 1.0) NPs

The $\text{Fe}^{3+}-\text{O}^{2-}$ stretching vibrations change when Mn^{2+} ions substitute Fe^{2+} ions at both sites in the ferrite lattice with a larger ionic radius and atomic weight. The infrared (IR) spectrum provides insights into the alterations in the molecular structure of ferrite resulting from introducing Mn^{2+} ions to the $\text{Fe}^{3+}-\text{O}^{2-}$ [21]. The shift of bands ν_1 and ν_2 to lower frequencies reveals the force constants f_T and f_O for the A and B sites, as the vibration frequency (ν) is proportionally related to the force constant f as,

$$f = 4\pi^2 C^2 \nu^2 m \quad (4.4)$$

Where ' m ' is the reduced mass for the Fe^{3+} ions and the O^{2-} ions (2.065×10^{-23} g/mol), and C is the speed of light. Far-infrared absorption is a valuable tool for studying

cation distribution as both A and B sites in the system are sensitive to changes. This method enables the examination of local symmetry, surface defects, oxidation phenomena associated with the spinel structure, and the presence or absence of Fe^{2+} ions in crystalline solids [26].

Table 4.3. Tetrahedral band (ν_1), the octahedral band (ν_2), force constants (f_T and f_O) of $\text{Mn}_x\text{Fe}_{1-x}\text{Fe}_2\text{O}_4$ ($x = 0.0, 0.25, 0.50, 0.75$, and 1.0) NPs

$\text{Mn}_x\text{Fe}_{1-x}\text{Fe}_2\text{O}_4$	ν_1	ν_2	$f_T \times 10^5$	$f_O \times 10^5$
(x)	(cm^{-1})	(cm^{-1})	(dyne/cm^2)	(dyne/cm^2)
0.00	557.32	439.52	2.2614	1.4075
0.25	556.36	433.90	2.2536	1.3707
0.50	554.43	427.15	2.2380	1.3284
0.75	555.39	426.19	2.2458	1.3224
1.00	553.47	425.27	2.2303	1.3167

4.3.3. Thermogravimetric Analysis

The thermal stability of the particles, surfactant decomposition temperature, and quantification of the surfactant ligands were determined using thermogravimetric analysis and differential thermal analysis.

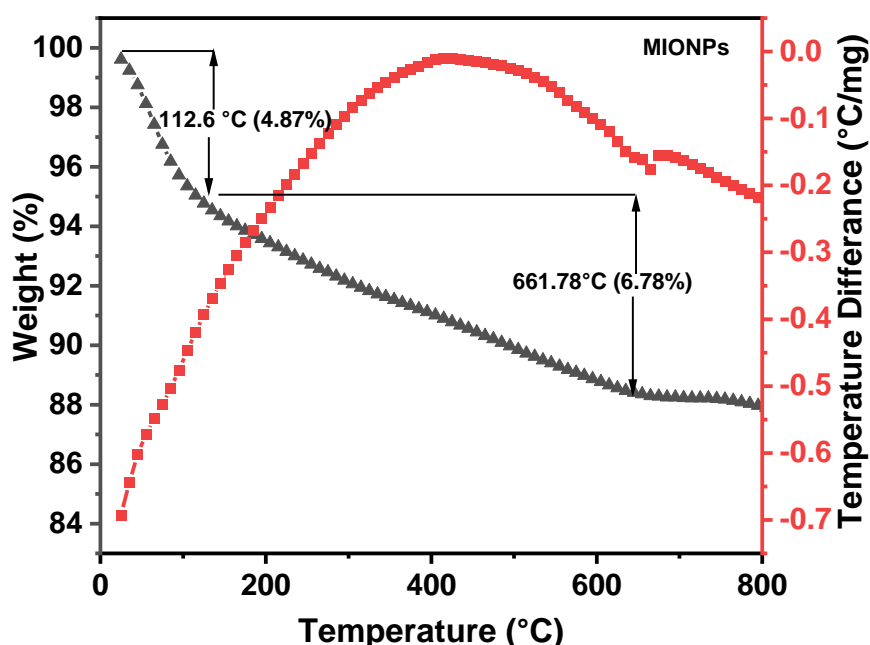


Figure 4.6 Thermogravimetric spectra of $\text{Mn}_{0.75}\text{Fe}_{0.25}\text{Fe}_2\text{O}_4$ MIONPs

TGA curves and DTA of MIONPs are shown in **Fig. 4.6**. The amount of oxidation of MIONPs decreased significantly as TG-DTA was carried out in an N₂ environment. The TGA experiments were designed to study the thermal stability of MIONPs over the range of 50–800 °C. Depending on the reaction type, each thermogram had a different stage corresponding to a different weight loss procedure. In the MIONPs samples, weight loss of 4% was noted below 110 °C due to evaporation of physically adsorbed H₂O molecules. The weight loss in the last phase of the TGA plot belongs to the phase formation of MIONPs. MIONPs achieve weight loss stability at temperatures above 600 °C.

4.3.4. Magnetic Properties

A magnetic field of 15 kOe was applied to the as-prepared samples, leading to magnetic hysteresis loops at room temperature, as illustrated in **Fig. 4.7**. The magnetic properties of the Mn_xFe_{1-x}Fe₂O₄ ($x = 0.0, 0.25, 0.50, 0.75$, and 1.0) NPs are summarized in **Table 4.4**. The net magnetization (M_s) values were determined as 37.63, 53.42, 49.45, 41.06, and 44.65 emu/g for Mn_xFe_{1-x}Fe₂O₄ ($x = 0.0, 0.25, 0.50, 0.75, 1.0$), respectively. Compared to smaller iron oxide particles that exhibited higher saturation magnetization, the observed results appear slightly distorted from the magnetization experiments for Mn_xFe_{1-x}Fe₂O₄ ($x = 0.0, 0.25, 0.50, 0.75$, and 1.0).

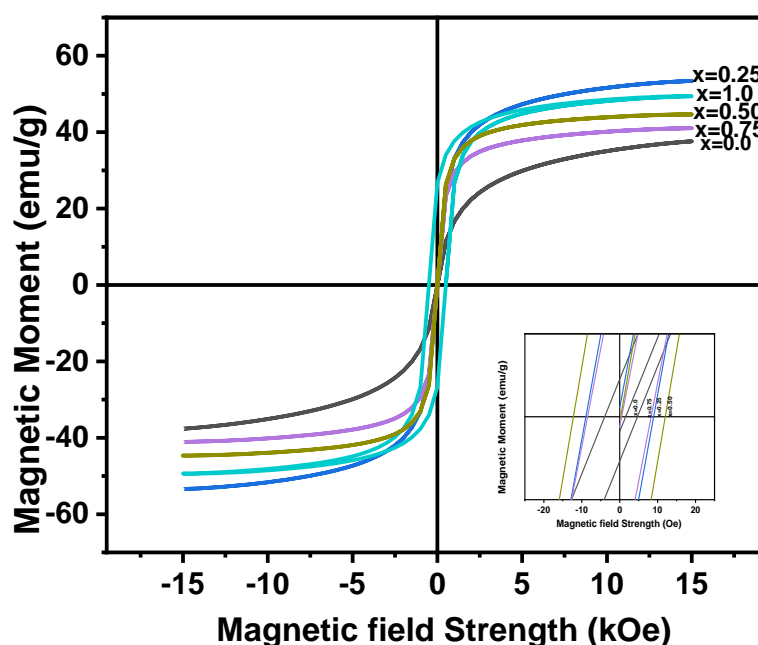


Figure 4.7 Magnetization (M) versus field (H) curves of the Mn_xFe_{1-x}Fe₂O₄ ($x = 0.0, 0.25, 0.50, 0.75$, and 1.0) NPs

This distortion could be attributed to the formation of smaller nanoparticles during synthesis and their anisotropic structural composition [25]. The variation in magnetic properties can also be understood as the distribution of cations among a tetrahedral and octahedral site of spinel ferrite.

Table 4.4 Magnetization (M_s), remanence (M_r) and remanence ratio (M_r/M_s), magnetic moment (n_B) of the $Mn_xFe_{1-x}Fe_2O_4$ ($x = 0.0, 0.25, 0.50, 0.75$, and 1.0) NPs

Sample x	M_s (emu/g)	M_r (emu/g)	H_c (Oe)	M_r/M_s	n_B Experimental.	n_B Calculated
0.0	37.63	0.09	4.32	0.0023	1.5599	4.1
0.25	53.42	0.44	8.92	0.0082	2.2121	4.25
0.50	49.45	0.15	3.12	0.003	2.0450	4.50
0.75	41.06	0.39	8.37	0.0094	1.6968	4.75
1.0	44.65	0.65	12.11	0.0145	1.8465	5.0

For the sequence $Mn_xFe_{1-x}Fe_2O_4$, the difference in the magnetic moment(n_B) with different x is determined. The magnetic moment per unit was derived using the following formula and displayed in **Table (4.4)**

$$n_B = \frac{M \times M_s}{5585} \quad (4.5)$$

Here, M represents the molecular weight. The magnetic moment values indicate that all the samples exhibit ferrimagnetic behavior. The magnetic moment of individual ions is computed considering the cation distribution. Magnetization is influenced by the distribution of cations among A -sites and B -sites. The net magnetic moment at zero Kelvin, arising from the anti-ferromagnetic coupling between the two sublattices, is simply the difference in the sublattice magnetizations. The calculation follows Neel's two-sublattice model of ferrimagnetism, expressing the magnetic moment as the magnetic moment per formula unit in B,

$$n_B(x) = M_B(x) - M_A(x) \quad (4.6)$$

M_B and M_A are the magnetic moments of the B and A sites, respectively. $Mn_xFe_{1-x}Fe_2O_4$ exhibits a cation distribution with a higher concentration of Mn^{2+} ions in the A -site than in the B -site, indicating a mixed spinel structure. Incorporating magnetic Mn^{2+} into the B sublattices, rather than magnetic Fe^{2+} in the spinel, contributes to magnetization enhancement. In the B -site, the magnetic moment is greater than that of the A -sites when Mn^{2+} is introduced. Moreover, the Mn^{2+} ion

occupying the A-site facilitates the transfer of Fe^{3+} ions from the A-site to the B-site, thereby increasing the overall magnetic moment. The results indicate that as the Mn^{2+} concentration (x) increases, both the observed and computed values of the magneton number increase. With an increase in Mn^{2+} content to counteract the growth of M_s , H_c increases. This aligns with the relationships $H_c \propto K (\mu_0 M_s)^{-1}$, where μ_0 is the permeability of free space, and K is the anisotropy constant [33]. However, IONPs are frequently reported to have lower magnetization than the bulk phase due to the canting of the spins at the surface or in the core, which is brought on by decreased coordination and broken super-exchange bonds [34]. The Mn^{2+} substituted iron oxide crystals have a slight variation in the saturation magnetization of nanocrystals. However, it was shown that the saturation magnetization had significantly improved with further Mn^{2+} substitution. We also observe that the variation in Mn^{2+} concentration affects the hysteresis curve's form. Compared to the somewhat bigger iron oxide particles leading to less saturation magnetization, the observed results of the magnetization studies for the varied x values were slightly altered. This may be caused by the particles reduced size and structural anisotropy [35]. High manganese doping levels may cause lattice distortion in manganese ferrite NPs, resulting in poor saturation magnetization, according to the analysis of XRD patterns and lattice distances [36].

4.4.5 Cation Distribution

Nanomaterials present novel properties compared to their bulk counterparts, and strains on the surface or interface are the most important basic quantities in various domains [37,12]. Nanoscale materials can modify their lattice parameters during compression or tension, thereby changing their intrinsic bond distances and electron energy levels. The grain size and micro-strain were calculated throughout the process using the line width FWHM (in radians) of the powder XRD lines. As a result of equation β , the width of the integral line is given by,

$$\beta = \beta' - \beta'' = \frac{\lambda}{D_{xrd} \cos\theta} + 4 \varepsilon \tan\theta \quad (4.7)$$

Where β' and β'' are the contributions of grain size and strain, respectively, θ is the Bragg angle, ε is the strain and ' D_{xrd} ' is the crystallite size. When the strain term $\beta'' = 4\varepsilon \tan\theta$ is negligible, ε can be evaluated in terms of β . For various XRD lines corresponding to different planes, the integral line width is measured, and **Eq. (4.8)** can be simplified as,

$$\beta \cos \theta = \lambda / D_{xrd} + \varepsilon (4 \sin \theta) \quad (4.8)$$

The values of $\beta \cos \theta$ and $4 \sin \theta$ have a linear relationship. The strain (ε) evaluated from the intercept = λ / D_{xrd} On the y-axis, when plotting $\beta \cos \theta$ (y-axis) versus $4 \sin \theta$ (x-axis).

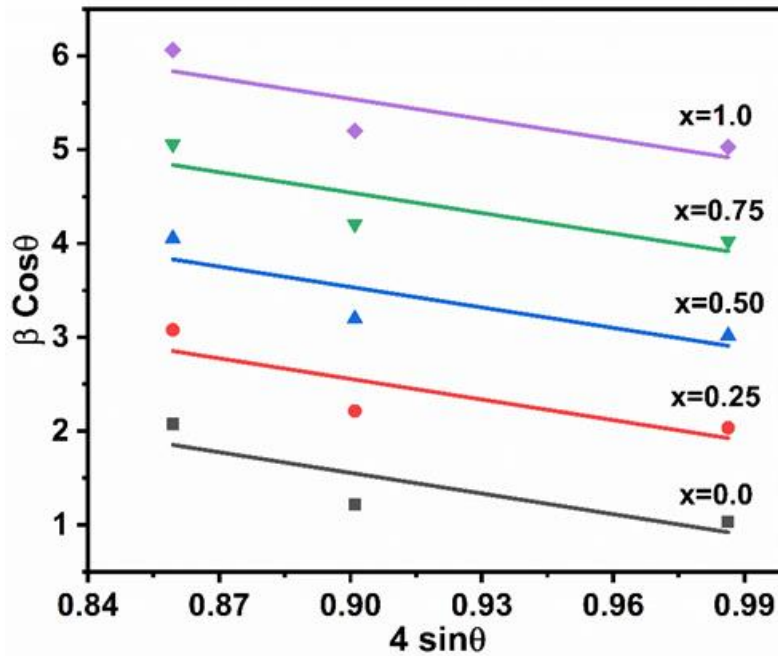


Figure 4.8 Strain graph of $\text{Mn}_x\text{Fe}_{1-x}\text{Fe}_2\text{O}_4$ ($x = 0.0, 0.25, 0.50, 0.75$, and 1.0) NPs

The strain measurements for each sample are shown in **Fig. 4.8**. It is seen that the linear difference of $4 \sin \theta$ with $\beta \cos \theta$ is for all samples. Strain measurement from the slope is more sensitive to increased Mn^{2+} content x , indicating that a more significant amount of Mn^{2+} can be accommodated in the matrix of $\text{Mn}_x\text{Fe}_{1-x}\text{Fe}_2\text{O}_4$. Differences in ionic size between the two cations account for the difference in cation distribution on tetrahedral and octahedral sites [38].

Cation distribution in crystal lattices affects spinel ferrites with structural and magnetic properties. An inverse phase cubic spinel structure has been observed for manganese iron oxide nanocrystals, with Fe^{2+} ions occupying B sites and Mn^{2+} , Fe^{3+} ions equally distributed in A and B sites. Studies of cation dispersion in spinel ferrite give useful information for improving materials with desirable characteristics [39]. In $\text{Mn}_x\text{Fe}_{(1-x)}\text{Fe}_2\text{O}_4$, XRD analysis was used to determine the distribution of cations Mn^{2+} , Fe^{2+} , and Fe^{3+} among octahedral and tetrahedral sites. The cation distribution in spinel ferrite was determined by comparing experimentally measured diffraction

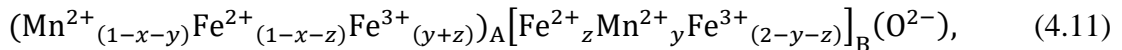
intensities to those calculated for many hypothetical crystal forms. Various distribution parameters are used to calculate intensity using the Burger formula for the planes [40],

$$I_{hkl} = |F|_{hkl}^2 PL_p \quad (4.9)$$

F is the structural component, P is multiplicity, and L_p is the Lorentz polarization factor in this equation.

$$L_p = \frac{1 + \cos^2 2\theta}{\sin^2 \theta \cos 2\theta} \quad (4.10)$$

The best information on cation distribution is obtained by comparing experimental and estimated intensity ratios for reflections whose intensities (i) are relatively independent of the oxygen parameter, (ii) change with the cation distribution in different ways, and (iii) do not differ significantly. Fe^{3+} ions have no preference for the lattice site and can occupy any of the two; Mn^{2+} ions can likewise occupy both sites. Mn^{2+} and Fe^{3+} ions have a strong A-site preference in $\text{Mn}_x\text{Fe}_{1-x}\text{Fe}_2\text{O}_4$, while Fe^{2+} and Fe^{3+} ions occupy the B sites [40]. The following cation distribution can be proposed since $\text{Mn}_x\text{Fe}_{1-x}\text{Fe}_2\text{O}_4$ ($x = 0.0, 0.25, 0.50, 0.75$, and 1.0) for inverse spinel:



where y and z are the Mn^{2+} and Fe^{2+} ion concentrations at their respective sites and ($0 \leq x \leq 1$). The following equation and an acceptable cation distribution are used to determine the mean ionic radii of tetrahedral (A) and octahedral (B) sites (r_A and r_B):

$$r_A = [1 - x - z]r\text{Fe}^{2+} + (x - y)r\text{Mn}^{2+} + (y + z)r\text{Fe}^{3+} \quad (4.12)$$

$$r_B = zr\text{Fe}^{2+} + yr\text{Mn}^{2+} + (2 - y - z)r\text{Fe}^{3+} \quad (4.13)$$

Using the value of a , the radius of oxygen ion $R_o = 1.32 \text{ \AA}$, and r_A , the oxygen positional parameter (u) can be obtained as follows:

$$u = \left[(r_A + R_o) \frac{1}{\sqrt{3}a} + \frac{1}{4} \right] \quad (4.14)$$

With increasing Mn^{2+} content x , it is apparent that r_B decreases and r_A increases. The relative value of Mn^{2+} , Fe^{2+} , and Fe^{3+} occupancy with their different ionic radii in the tetrahedral site helps to explain the difference in calculated tetrahedral or octahedral radius. The oxygen positional parameter ' u ' rises to 0.401 from 0.382. If ' u ' = $3/8 = 0.375$ in an ideal fcc structure, although the ' u ' values of most ferrites are greater than this ideal value, indicating that the oxygen ions are transferred in such a way in the A–B interaction that the distance between A and O

ions increases while the distance between B and O ions decreases. As a result, the A–A interaction decreases while the B–B interaction increases [12, 21].

Table 4.5 Distribution of cations among A- and B-sites

Com p	A-Site			B- Site			r_A Å	r_B Å	'u' Å	a_{th}	strain
x	Mn ²⁺	Fe ²⁺	Fe ³⁺	Mn ²⁺	Fe ²⁺	Fe ³⁺					
0.0	0.0	0.05	0.95	0.0	0.95	1.05	0.59	1.58	0.382	0.8352	0.7229
0.25	0.12	0.0	0.88	0.13	0.75	1.12	0.66	1.51	0.385	0.8405	0.7249
0.50	0.19	0.0	0.81	0.31	0.50	1.19	0.74	1.45	0.391	0.8423	0.7258
0.75	0.25	0.0	0.75	0.50	0.25	1.25	0.82	1.39	0.396	0.8435	0.7309
1.00	0.29	0.0	0.71	0.71	0.0	1.29	0.91	1.34	0.401	0.8497	0.7333

Using the estimated values of r_A and r_B , the theoretical lattice parameter (a_{th}) is determined as,

$$a_{th} = \frac{8}{3\sqrt{3}} [(r_A + r(o^{2-})) + \sqrt{3}(r_B + r(o^{2-}))] \quad (4.16)$$

Table (4.2) shows theoretical lattice constant values for $Mn_xFe_{1-x}Fe_2O_4$ ($x = 0.0, 0.25, 0.50, 0.75$, and 1.0) nanocrystals. As the concentration of Mn^{2+} increases, the X-ray density rises linearly because the iron atom is lighter than the manganese atom. The distance between magnetic ions is calculated in tetrahedral L_A and octahedral site L_B .

$$L_A = 0.25a\sqrt{3} \quad (4.17)$$

$$L_B = 0.25a\sqrt{2} \quad (4.18)$$

Table (4.6) shows the calculated values for L_A and L_B . It is observed that with an increase in the Mn^{2+} content, hopping length also increases. According to equations (4.19) and (4.20), one can calculate the shortest distance between A-site cations and oxygen ions and between B-site cations and oxygen ions, respectively.

$$d_{Ax} = a\sqrt{3\left(u - \frac{1}{4}\right)} \quad (4.19)$$

$$d_{Bx} = a\left[3u^2 - \left(\frac{11}{4}\right)u + \left(\frac{43}{64}\right)\right]^{\frac{1}{2}} \quad (4.20)$$

Equations (4.21), (4.22), and (4.23) were used to determine the A-site edge ' d_{AxE} ,' the shared B-site edge ' d_{BxE} ,' and the unshared B-site edge ' d_{BxEU} .'

$$d_{AxE} = a\sqrt{2\left(2u - \frac{1}{2}\right)} \quad (4.21)$$

$$d_{BxE} = a\sqrt{2(1 - 2u)} \quad (4.22)$$

$$d_{BxEu} = a[4u^2 - 3u + \left(\frac{11}{16}\right)]^{\frac{1}{2}} \quad (4.23)$$

As shown in **Table (4.6)**, substitution with Mn^{2+} indicates an increase in the octahedral bond distance d_{Bx} and the tetrahedral bond distance d_{Ax} . In manganese iron oxide nanocrystals, due to the extension of octahedral B-sites, differences between d_{Ax} and d_{BxE} increase because of the larger radius of Mn^{2+} ions compared to Fe^{2+} and Fe^{3+} ions. As a result, the oxygen anions are displaced relative to each other, causing the tetrahedral A-sites to decrease. Due to shrinkage, the force constant between the cations and anions increases because there is more covalent bonding at the A-sites than at the B-sites. There is an increase in the value of tetrahedral edge ' d_{Ax} ,' shared octahedral edge ' d_{BxE} ,' and unshared octahedral edge ' d_{BxEu} ' due to Mn^{2+} substitution is shown in **Table (4.6)**. These modifications are due to Mn^{2+} greater ionic radius, which causes the octahedral site to expand while the tetrahedral site shrinks [41-43].

Table 4.6 Hopping length (L_A) and (L_B), tetrahedral bond length (d_{Ax}), octahedral bond length (d_{Bx}), tetrahedral edge (d_{Ax}), shared (d_{BxE}) and unshared (d_{BxEu}) octahedral edges as a function of x for $\text{Mn}_x\text{Fe}_{1-x}\text{Fe}_2\text{O}_4$ ($x = 0.0, 0.25, 0.50, 0.75$, and 1.0) NPs

Sample	L_A	L_B	d_{Ax}	d_{Bx}	d_{Ax}	d_{BxE}	d_{BxEu}	α	β
$\text{Mn}_x\text{Fe}_{1-x}\text{Fe}_2\text{O}_4$ (x)	(nm)	(nm)	(nm)	(nm)	(nm)	(nm)	(nm)		
0.0	0.3617	0.2953	0.1894	0.2037	0.3095	0.2811	0.2954	0.4108	0.3871
0.25	0.3641	0.2973	0.1906	0.2051	0.3115	0.2830	0.2973	0.4155	0.2931
0.50	0.3647	0.2978	0.1910	0.2054	0.3121	0.2834	0.2979	0.4051	0.3908
0.75	0.3652	0.2982	0.1913	0.2057	0.3125	0.2838	0.2983	0.4117	0.1846
1.00	0.3679	0.3004	0.1925	0.2072	0.3148	0.2859	0.3005	0.4074	0.3426

In terms of $r_A, r_B, a_{th}, a_{exp}$, and $r(o^{2-})$, the following relationships can be used to describe the degree of ionic packing (α) and the vacancy parameter (β).

$$\alpha = \frac{32\pi}{3a_{exp}}(r_A^3 + 2r_B^3 + 4r(o^{2-})^3) \quad (4.24)$$

$$\beta = \left(\frac{a_{th}^3 - a_{exp}}{a_{th}^3} \right) \times 100\% \quad (4.25)$$

The vacancy parameter reveals the presence of vacancies at both tetrahedral and octahedral sites. It offers the normalized volume of missing ions, a total measure of vacancy concentration in the spinel structure [44]. Magnetic properties of spinel ferrites nanocrystals are attributed to octahedral and tetrahedral sites, as well as their relative strengths, which are affected by magnetic ion accumulation on the surfaces of these crystals inter-lattice and inter-sublattice interactions. Variations in the number of magnetic ions in both sites alter the magnetic properties. Ferrite nanocrystals substituted with Mn^{2+} expand the tetrahedral site, increasing the bond distance at the A site. The structural features of ferrites are influenced mainly by the variation in bond distance between a cation and cation, as well as a cation and anion, at various magnetic parameters [45].

As the unit cell volume increases, all values of inter-ionic distances increase. This is because the smaller ionic radii Fe^{2+} is replaced by a more radially large Mn^{2+} , which has a smaller interionic distance between ions (b, c, d, e, f) for $Mn_xFe_{1-x}Fe_2O_4$ ($x = 0.0, 0.25, 0.50, 0.75$, and 1.0) nanocrystals. From **Tables (4.7) and (4.8)**, it is observed that an increase in cation-anion length and cation-cation length with Mn^{2+} substituted resulted in a decreased super-exchange strength compared to iron oxides [46]. The inter-ionic lengths and angles between the cation-anion and cation-cation significantly and effectively influence magnetic interactions. Different configurations of the ion's pairs with favourable angles for the individual magnetic interactions and inter-ionic distances give the cation-anion distances p, q, r , and s , as well as the cation-cation distances (b, c, d, e , and f) and the respective bond angles $\theta_1, \theta_2, \theta_3, \theta_4$ and θ_5 . The inter-ionic distances are determined by the crystalline structure and magnetic characteristics [44].

The following equations are used to calculate these values, shown in Table (4.5), taking into account the experimental value of the lattice constant and oxygen parameters.

$$\begin{aligned}
 p &= a \left(\frac{5}{8} - u \right) \\
 q &= a\sqrt{3} \left(u - \frac{1}{4} \right) \\
 r &= a\sqrt{11} \left(u - \frac{1}{4} \right) \\
 s &= a\sqrt{3} \left(\frac{1}{3}u + \frac{1}{8} \right) \\
 b &= \sqrt{2} \left(\frac{a}{4} \right) \\
 c &= \sqrt{11} \left(\frac{a}{8} \right) \\
 d &= \sqrt{3} \left(\frac{a}{4} \right) \\
 e &= \sqrt{3} \left(\frac{3a}{8} \right) \\
 f &= \sqrt{6} \left(\frac{a}{4} \right)
 \end{aligned} \tag{4.26}$$

As a result of considering the following equations with the inter-ionic lengths measured, we can obtain the bond angles for manganese iron oxide, which are given in **Table 4.8**.

$$\begin{aligned}
 \theta_1 &= \cos^{-1} \left[\frac{p^2 + q^2 - c^2}{2pq} \right] \\
 \theta_2 &= \cos^{-1} \left[\frac{p^2 + r^2 - e^2}{2pr} \right] \\
 \theta_3 &= \cos^{-1} \left[\frac{2p^2 - b^2}{2p^2} \right] \\
 \theta_4 &= \cos^{-1} \left[\frac{p^2 + s^2 - f^2}{2ps} \right] \\
 \theta_5 &= \cos^{-1} \left[\frac{r^2 + q^2 - d^2}{2rq} \right]
 \end{aligned} \tag{4.27}$$

Table 4.7. Calculation of distances between cations and anions and between cations and cations for $\text{Mn}_x\text{Fe}_{1-x}\text{Fe}_2\text{O}_4$ ($x = 0.0, 0.25, 0.50, 0.75$, and 1.0) nanocrystals

$\text{Mn}_x\text{Fe}_{1-x}\text{Fe}_2\text{O}_4$ (x)	p (nm)	q (nm)	r (nm)	s (nm)	b (nm)	c (nm)	d (nm)	e (nm)	f (nm)
0.0	0.20	0.1808	0.3462	0.5512	0.2953	0.3462	0.3617	0.5426	0.5115
0.25	0.2102	0.1820	0.3486	0.5549	0.2973	0.3486	0.3641	0.5462	0.5149
0.50	0.2106	0.1823	0.3492	0.5559	0.2978	0.3492	0.3647	0.5471	0.5158
0.75	0.2109	0.1826	0.3496	0.5566	0.2982	0.3496	0.3652	0.5479	0.5165
1.00	0.2124	0.1839	0.3522	0.5607	0.3004	0.3522	0.3679	0.5519	0.5203

Table 4.8 Calculated values of hopping lengths and inter-ionic bond angles for $\text{Mn}_x\text{Fe}_{1-x}\text{Fe}_2\text{O}_4$ ($x = 0.0, 0.25, 0.50, 0.75$, and 1.0) nanocrystals

Sample $\text{Mn}_x\text{Fe}_{1-x}\text{Fe}_2\text{O}_4$ (x)	L_A (nm)	L_B (nm)	θ_1	θ_2	θ_3	θ_4	θ_5
0.0	0.3617	0.2953	125.24	154.93	90.00	68.11	79.99
0.25	0.3641	0.2973	125.30	154.82	90.01	68.10	79.98
0.50	0.3647	0.2978	125.28	154.74	89.98	68.10	79.97
0.75	0.3652	0.2982	123.20	154.86	89.97	68.11	79.99
1.00	0.3679	0.3004	123.27	154.85	90.00	68.11	79.99

Because these angles are related to A-B and A-A interactions, a rise in these angles verifies the strength of these bonds as bond length and angle increase with the substitution of Mn^{2+} .

4.3.6. Induction Heating Study

The effect of Mn^{2+} substitution in $\text{Mn}_x\text{Fe}_{1-x}\text{Fe}_2\text{O}_4$ ($x = 0.0, 0.25, 0.50, 0.75$, and 1.0) for hyperthermia applications is investigated by establishing a connection between their magneto-structural properties and induction heating. The induction heating studies of manganese-substituted iron oxide nanoparticles have not been previously reported in correlation with the distribution of cations, which significantly influences their magnetic properties. The heating power of the MNPs is assessed through the SAR, a crucial parameter in MHT that quantifies the fluid's ability to convert magnetic energy into heat [47, 48]. **Fig. 4.9** displays the temperature difference at various field amplitudes. MNP dissipates heat in AC magnetic fields through SAR (W/g) and ILP, calculated using equations 2.11 and 2.12 (Section 2.2). The SAR value should be as high as possible to reduce the amount of magnetic material needed to treat hyperthermia because it inversely relates to M_m . In total power loss by MNPs in an AC magnetic field, three components are involved: hysteresis loss, eddy current loss, and residual loss.

In an AC magnetic field, the hysteresis loss can be represented as **Equation 2.4 (Section 2.4.2)**, and thus, the SAR is represented as **Equation 2.5 (Section 2.4.2)**. As a result, one must consider how frequency and amplitude affect SAR. It has also been shown that a human-tolerated frequency and amplitude range is believed to be with their product $f \cdot H = C$ not exceeding $\sim 5 \times 10^9$ A/m.s [49]. The calculated values

of C are 3.5×10^9 , 5.34×10^9 and 7.12×10^9 A/m.s for 13.3, 20 and 26.7 kA/m, respectively. The critical requirement for magnetic field amplitude and frequency is fulfilled in this scenario. Since magnetic field strength and frequency are closely interrelated, SAR values cannot be directly compared to those of other systems. Consequently, discussing heat dissipation regarding ILP is more suitable [50]. Giri *et al.* synthesized $\text{Fe}_{1-x}\text{Mn}_x\text{Fe}_2\text{O}_4$ NPs by the co-precipitation method with a mean size of 10.0, 0.25, 0.50, 0.75, and 1.02 nm, and calorimetric measurements were used to determine the heating efficiency in a field with $f = 300$ kHz and $H = 10\text{--}45$ kA/m. The M_s and SAR of the material had the maximum values for $x = 0.4$ as 85 emu/g and 30 W/g, respectively [51]. Lorenzo *et al.* synthesized Manganese-doped iron oxide NPs with M_s values of 66 emu/g and SAR values of 73 W/g of Fe + Mn at $f = 183$ kHz and $H = 17$ kA/m [52].

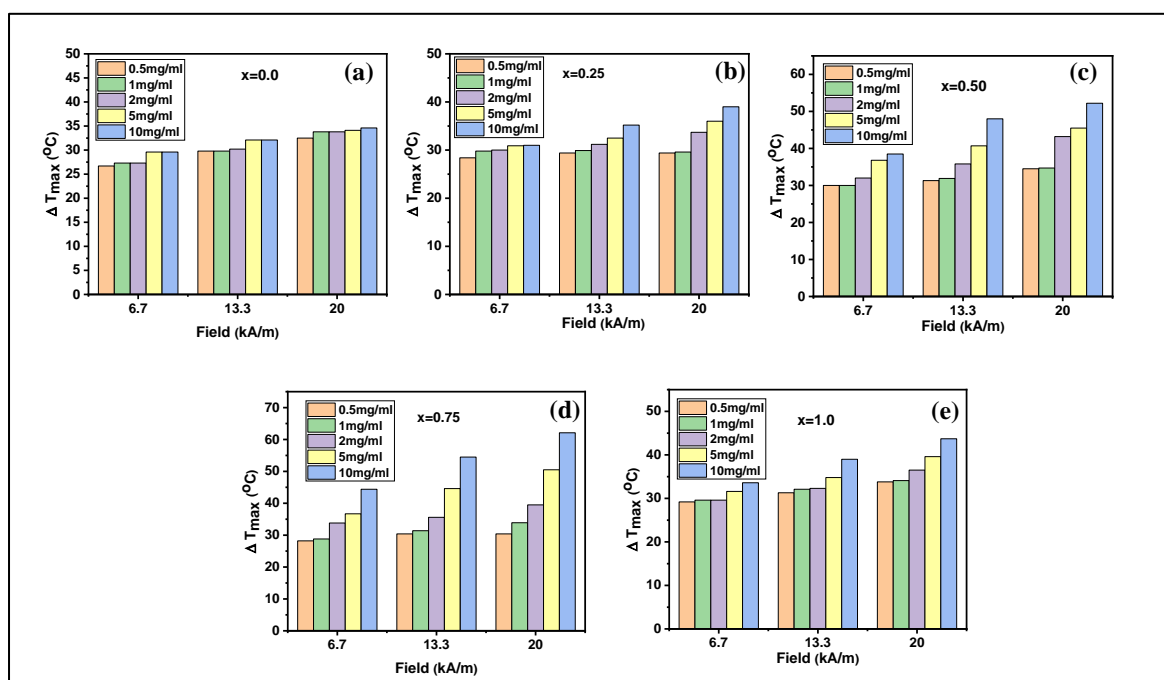


Figure 4.9 The growth in temperature versus time for $\text{Mn}_x\text{Fe}_{1-x}\text{Fe}_2\text{O}_4$ ($x = 0.0, 0.25, 0.50, 0.75$, and 1.0) NPs at different concentrations (0.5, 1, 2, 5 and 10 mg/ml) and applied fields 13.3 kA/m to 26.7 kA/m, with constant frequency (≈ 277 kHz)

When exposed to an external magnetic field, manganese iron oxide demonstrates low conductivity (approximately 10^{-3} S/cm), ensuring minimal losses from eddy currents and hysteresis [53]. The predominant heat loss mechanism in manganese iron oxide is likely attributed to Neel rotation and Brownian losses [54].

The size distribution of magnetic nanoparticles significantly influences heat dissipation in an AC magnetic field, with temperature elevation correlating with increasing field amplitude and nanoparticle concentration. Typically, temperatures ranging from 42 to 44 °C are adequate for hyperthermia therapy. At concentrations of 5 mg/ml and 10 mg/ml in water, these nanoparticles exhibited self-heating, reaching temperatures of 50.25 °C and 73.32 °C at different magnetic field amplitudes. The actual temperature increase within 10 minutes for all samples was measured at a fixed frequency (≈ 277 kHz) and various nanoparticle concentrations (0.5, 1, 2, 5, and 10 mg/ml) under changing magnetic fields of 13.3 kA/m, 20.0 kA/m, and 26.7 kA/m (See Fig. 4.9).

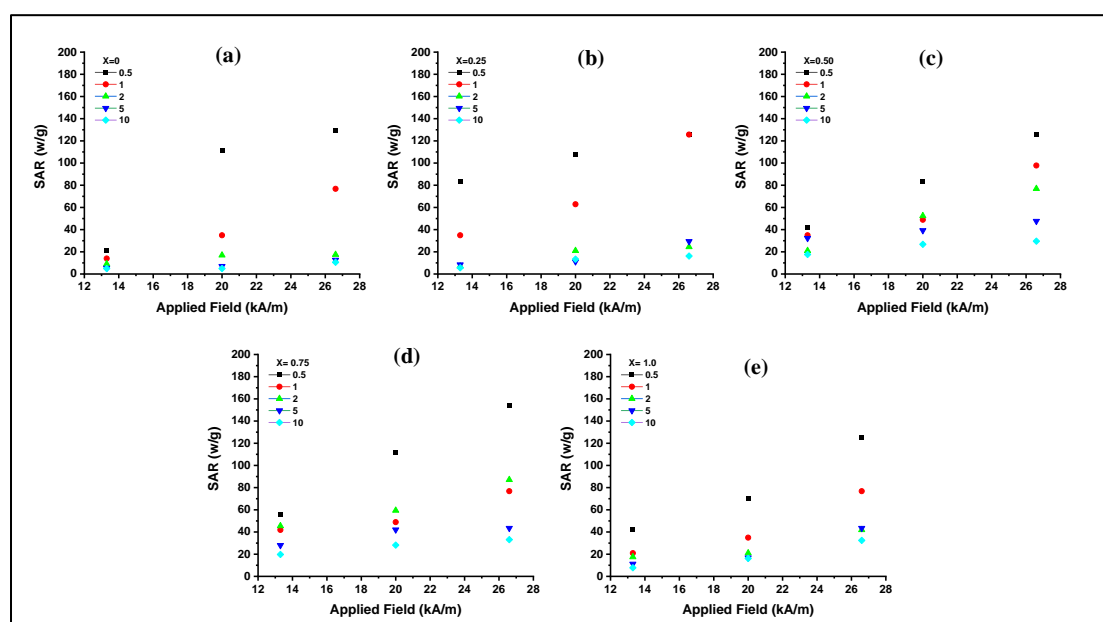


Figure 4.10 SAR value of the $\text{Mn}_x\text{Fe}_{1-x}\text{Fe}_2\text{O}_4$ ($x = 0.0, 0.25, 0.50, 0.75$, and 1.0) NPs at different concentrations (0.5, 1, 2, 5 and 10 mg/ml) and applied fields 13.3 kA/m to 26.7 kA/m, with constant frequency (≈ 277 kHz)

Dipole-dipole interactions are affected by broad particle size distributions, affecting the induction heating properties of the material. Consequently, there is an increased hysteresis loss and greater AC magnetically induced heating characteristic. Xabier *et al.* studied size-dependent magnetic hyperthermia of manganese-doped ferrite NPs. It is observed that SAR 50–90 W/g and ILP values within 1–2 nHm^2/kg [29]. Otero-Lorenzo *et al.* synthesized $\text{Mn}_{0.3}\text{Fe}_{2.7}\text{O}_4$ NPS with a solvothermal technique and found a SAR of 37 W/g, while the calculated ILP for the 5 nm particles is 4 nHm^2/kg [52]. SAR and ILP values of $\text{Mn}_x\text{Fe}_{1-x}\text{Fe}_2\text{O}_4$ ($x = 0.0, 0.25, 0.50, 0.75$,

and 1.0) NPs are calculated from **Equation (2.11 and 2.12)** shown in **Table 4.9** with an increase in field amplitude from 13.3 kA/m to 26.7 kA/m for 0.5, 1, 2, 5 and 10 mg/ml respectively.

SAR values of $\text{Mn}_x\text{Fe}_{1-x}\text{Fe}_2\text{O}_4$ ($x = 0.0, 0.25, 0.50, 0.75$, and 1.0) NPs are calculated from equation (4.30) and initial slope in **Fig. 4.10** SAR for Fe_3O_4 rises from 4.9 to 17.47 W/g (ILP = 0.09 - 0.15 nHm²/kg) with an increase in field amplitude from 13.3 kA/m to 26.7 kA/m for 2 mg/ml respectively. For sample $x = 0.25$, the value of SAR increases from 5.63 to 29.44 W/g (ILP = 0.41 - 0.59 nHm²/kg) with an increase in the field from 13.3 to 26.7 kA/m. The sample $x = 0.50$, the value of SAR increases from 17.61 to 76.89 W/g (ILP = 0.26 - 1.68 nHm²/kg) with an increase in the field from 13.3 to 26.7 kA/m. SAR increases from 19.73 to 87.12 W/g (ILP = 0.67 - 3.65 nHm²/kg) for sample $x = 0.75$ with a field increase from 13.3 to 26.7 kA/m. SAR increases from 7.75 to 41.94 W/g (ILP = 0.29 - 1.40 nHm²/kg) for sample MnFe_2O_4 , with a field increase from 13.3 to 26.7 kA/m. The $\text{Mn}_x\text{Fe}_{1-x}\text{Fe}_2\text{O}_4$ ($x = 0.0, 0.25, 0.50, 0.75$, and 1.0) NPs exhibited the highest SAR of about 153.76 W/g for the sample $x = 0.75$ at a physiological safe range of frequency and amplitude.

The magnetic field frequency and magnitude determine the ILP parameter. It is the most suitable model for 2 to 4 nHm²/kg since it can be easily compared across experiments [55]. When manganese was introduced into the network, local heating increased significantly, from 0.15 nHm²/kg (Fe_3O_4) to 1.40 nHm²/kg (MnFe_2O_4). The addition of Mn^{2+} , on the other hand, increases the material's heat, resulting in improved magnetic properties due to the distribution of cations among A and B sites. The details of SAR and ILP values of $\text{Mn}_x\text{Fe}_{1-x}\text{Fe}_2\text{O}_4$ ($x = 0.0, 0.25, 0.50, 0.75$, and 1.0) NPs with an increase in amplitudes from 13.3 kA/m to 26.7 kA/m for 0.5, 1, 2, 5 and 10 mg/ml are given in **Table 4.9**. In the context of a biological application, hyperthermia could damage cancerous cells and protect healthy cells simultaneously while keeping the temperature under control as the AMF exposure period increases. In the end, the results clearly show that high values of SAR are not a result of increasing particle concentration. Comparing these values to those reported in the literature, we used low concentration and low field to reach hyperthermia [31].

Table 4.9 SAR and ILP values of $\text{Mn}_x\text{Fe}_{1-x}\text{Fe}_2\text{O}_4$ ($x = 0.0, 0.25, 0.50, 0.75$, and 1.0) NPs with an increase in amplitudes from 13.3 kA/m to 26.7 kA/m for 0.5, 1, 2, 5 and 10 mg/ml respectively

Applied field (kA/m) for $\text{Mn}_x\text{Fe}_{1-x}\text{Fe}_2\text{O}_4$		specific absorption rate (SAR) W/g					intrinsic loss power (ILP) nHm ² /kg				
		0.5mg/ml	1mg/ml	2mg/ml	5mg/ml	10mg/ml	0.5mg/ml	1mg/ml	2mg/ml	5mg/ml	10mg/ml
$x=0.0$	13.3	20.95	13.96	-	-	4.9	1.12	1.68	-	-	0.39
	20.0	111.6	34.91	6.9	7.01	4.93	2.27	7.12	0.14	0.56	0.10
	26.7	139.6	76.81	17.47	12.6	10.57	1.25	0.69	0.15	0.11	0.09
$x=0.25$	13.3	83.76	34.91	6.99	8.41	5.63	6.7	2.80	0.56	0.67	0.45
	20.0	125.64	62.85	20.97	11.21	13.38	2.56	1.28	0.42	0.22	0.27
	26.7	107.52	125.7	24.46	29.44	16.20	1.51	1.13	0.22	0.26	0.14
$x=0.50$	13.3	41.88	34.91	20.97	32.25	17.61	3.36	2.80	1.68	2.59	1.41
	20.0	83.76	48.88	52.42	39.26	26.77	1.70	0.99	1.06	0.80	0.54
	26.7	125.64	97.77	76.89	47.67	29.59	1.13	0.88	0.69	0.43	0.26
$x=0.75$	13.3	55.84	41.90	45.43	28.04	19.73	4.49	3.36	3.65	2.25	1.58
	20.0	111.68	48.88	59.41	42.07	28.18	2.27	0.99	1.21	0.85	0.57
	26.7	153.76	76.81	87.12	43.47	33.11	1.38	0.69	0.78	0.88	0.67
$x=1.0$	13.3	41.88	20.95	17.47	11.21	7.75	3.36	1.68	1.40	0.90	0.62
	20.0	69.80	34.91	20.97	16.82	16.20	1.42	0.71	0.42	0.34	0.33
	26.7	125.64	76.81	41.94	43.47	32.41	1.13	0.69	0.37	0.39	0.29

4.4. Synthesis and Characterizations of Manganese Iron Oxide MNPs by Thermal Decomposition Method

Anisotropy is a crucial characteristic in many materials, offering direction-dependent properties like ferroelectricity and ferromagnetism, which are essential for various applications. It stems from atomic stacking arrangements and material morphologies, including shape and surface characteristics. While structural anisotropy is typically viewed as an intrinsic material property, shape and surface anisotropy are considered extrinsic and can be more precisely adjusted through controlled synthesis techniques focusing on shape and surface manipulation [56]. The performance of MNPs is strongly influenced by their structure, average size, and magnetic anisotropy. Additionally, particle ensembles provide a distinctive method for tuning their magnetic behavior by adjusting the strength of dipolar interactions between the particles [57]. The ongoing positive influence of MHT in medicine suggests significant advancements in biomedical science are on the horizon. However, a major challenge lies in the limited heating power of the currently utilized MNPs, which necessitates the local injection of substantial quantities. Therefore, optimizing the heating efficiency of MNPs remains a critical objective. The heat produced by MNPs is closely linked to their structural and magnetic characteristics. Initial studies focused on spherical MNPs, but recent advancements in synthesis have enabled the production of nanoparticles with varied and controlled sizes and shapes.

An alternative approach to enhancing the heating power of MNPs involves manipulating their shape and nanostructure, which can influence their magnetocrystalline anisotropy or facilitate cooperative magnetism. For example, recent studies have demonstrated that cubic-shaped iron oxide MNPs [57] and flower-shaped MNPs [58] exhibit significantly better MHT properties compared to optimized 20 nm spherical iron oxide MNPs [59]. Cubic-shaped spinel oxide nanocrystals have demonstrated exceptional properties compared to spherical counterparts, particularly in fields such as biomedicine. Iron oxide MNPs are the most usually used materials in MHT because of their low toxicity [57, 60]. Other ferrite MNPs, such as manganese ferrite and zinc ferrite, have been studied for their high magnetization within the ferrite family and their oxidation resistance, leading to relatively high SAR. While a high saturation magnetization (M_s) is advantageous for enhancing SAR, materials with high M_s are often metallic and face challenges related to stability and toxicity in physiological environments. A different strategy for

optimizing SAR involves adjusting the effective anisotropy of the MNPs. For instance, shape anisotropy can enhance the SAR of iron oxide nanocubes. Significant SAR values have been achieved by modifying the anisotropy of MNPs using a hard–soft exchange-coupled core/shell approach. However, these results were obtained under high field amplitudes and frequencies unsuitable for clinical applications [61]. This section synthesizes optimal Mn^{2+} into $\text{Mn}_x\text{Fe}_{3-x}\text{O}_4$ using the thermal decomposition method, establishing a correlation between induction heating studies of MNPs and their morphologies.

In a typical synthesis, a combination of iron (III) acetylacetonate (2 mmol) and manganese (III) acetylacetonate ($\text{Mn}(\text{acac})_3$, 1 mmol) was introduced into a mixture of oleic acid (1.13 g) and benzyl ether (10.4 g). The solution was degassed at room temperature for one hour and then heated to 290 °C at 20 °C per minute while stirring vigorously with a magnetic stirrer. This temperature was maintained for one hour. After cooling back to room temperature, a mixture of toluene and hexane was added to the solution. The resulting mixture was then centrifuged to separate the MnFe_2O_4 nanocubes, which were subsequently washed with chloroform [62].

4.5. Results and Discussions

4.5.1. Structural analysis

The crystallographic structure and crystallite size of $\text{Mn}_x\text{Fe}_{3-x}\text{O}_4$ ($x = 0.0, 0.25, 0.50, 0.75, \text{ and } 1.0$) (MIONCs) were determined from the XRD patterns, shown in **Fig. 4.11 (a)**. The characteristic broad diffraction peaks confirmed crystallinity of NPs and their reflection planes (220), (311), (400), (422), (511), (440), (622) indicates presence of all the diffraction peaks obtained are well-matched with JCPDS cards. 00-019-0629 and 00-10-0319 for MIONCs and spinel cubic structure is confirmed (space group $\text{Fd}\bar{3}\text{m}$). The crystallite size of synthesized nanoparticles was determined using the Williamson-Hall plot method. The average crystallite size (D_{xrd}) exhibits variation ranging from 13.48 nm to 24.27 nm, correlating with different Mn^{2+} concentrations. Concurrently, the calculated lattice parameter ' a ' shows an increase from 0.8341 nm to 0.8492 nm, while the corresponding values of X-ray density (d_x) decrease from 5.2031 g/cm^3 to 5.1908 g/cm^3 with the progressive increase in Mn^{2+} concentration (**Fig. 4.12**).

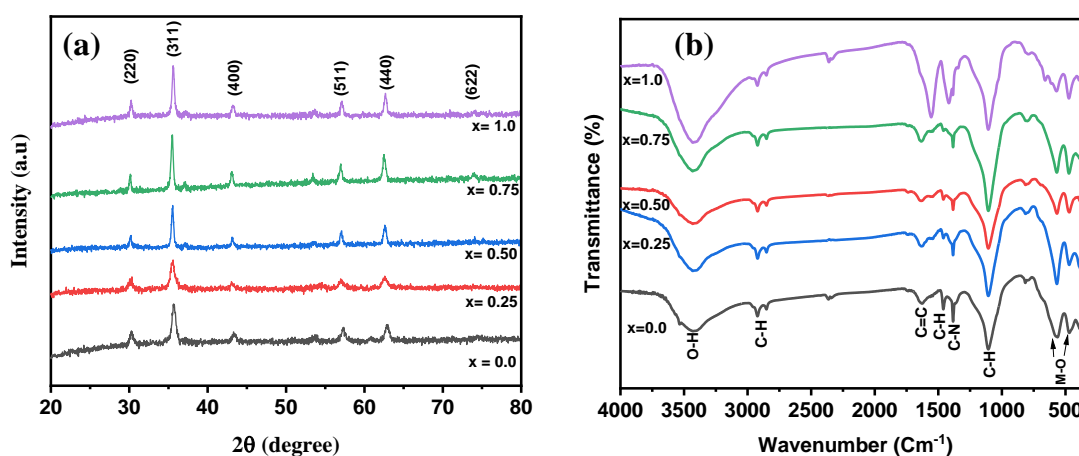


Figure 4.11 (a) XRD patterns, (b) FTIR spectra of $\text{Mn}_x\text{Fe}_{3-x}\text{O}_4$ ($x = 0.0, 0.25, 0.50, 0.75$, and 1.0) MIONCs

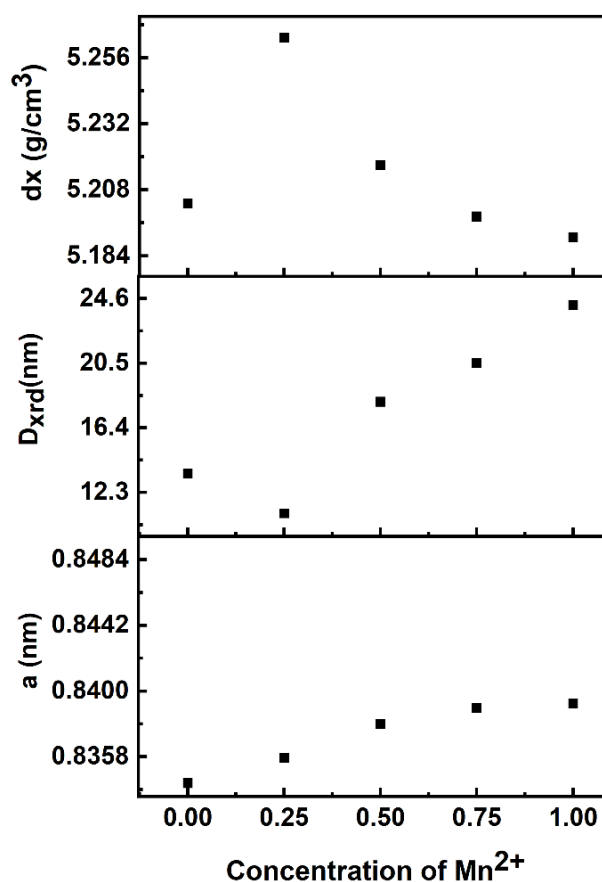


Figure 4.12 The variation of $\text{Mn}_x\text{Fe}_{3-x}\text{O}_4$ ($x = 0.0, 0.25, 0.50, 0.75$, and 1.0) MIONCs with Mn^{2+} content x in terms of their lattice parameter, crystallite size, and x-ray density

The observed increase in lattice constant (a) with the rise in Mn^{2+} concentration is elucidated by considering ionic radii. The radius of Mn^{2+} (0.80 Å) is more significant than that of Fe^{2+} (0.77 Å) and Fe^{3+} (0.64 Å). This difference in ionic radii leads to lattice expansion, increasing the lattice parameter and reflecting the growth of the unit cell dimensions [27]. The inverse spinel manganese iron oxide will eventually expand when small-sized Fe^{3+} and Fe^{2+} ions are replaced with large-sized Mn^{2+} ions. This substitution introduces strain in the lattice, leading to linear elastic deformation. The calculated lattice parameter ' a ', crystallite size D_{xrd} (nm), and x-ray density dx (g/cm^3) with different Mn compositions are shown in Fig 4.12.

Fig. 4.11 b shows the FTIR spectra of the as-synthesized MIONCs. The strong absorption bands at 451 and 576 cm^{-1} are associated with the vibration of Fe–O bonds. The absorption band at 781 cm^{-1} arises from the C–H stretching vibration. The bands at 1386 cm^{-1} and 1632 cm^{-1} occurred from the C–H and C=O bond vibrations in surfactant molecules. Absorption bands at 2920 cm^{-1} and 3416 cm^{-1} are attributed to the C–H and O–H band vibration [63].

Table 4.10. Tetrahedral band (ν_1), the octahedral band (ν_2), force constants (f_T and f_O) of $\text{Mn}_x\text{Fe}_{3-x}\text{O}_4$ ($x = 0.0, 0.25, 0.50, 0.75$, and 1.0) MIONCs

$\text{Mn}_x\text{Fe}_{3-x}\text{O}_4$ (x)	ν_1 (cm^{-1})	ν_2 (cm^{-1})	$f_T \times 10^5$ (dyne/cm^2)	$f_O \times 10^5$ (dyne/cm^2)
0.00	570	470	2.3813	1.6291
0.25	567.95	470.45	2.3642	1.6222
0.50	566.81	471.36	2.3548	1.6284
0.75	566.36	472.43	2.351	1.6358
1.00	565.45	472.73	2.3435	1.6379

The FTIR analysis confirms the formation of the spinel ferrite phase, showing distinct intensity bands related to covalent bonds between nanoparticles. Specifically, the M_T and M_O stretching band around 600–500 cm^{-1} , where M_T and M_O represent tetrahedral and octahedral sites, is visible. The band positions of Mn^{2+} -substituted nanoferrites are listed in Table 4.10. The Fe^{3+} – O^{2-} stretching vibrations shift as Mn^{2+} ions, with larger ionic radii and atomic weights, replace Fe^{2+} ions at both sites in the ferrite lattice. The IR spectrum highlights changes in the molecular structure caused by incorporating Mn^{2+} ions into the Fe^{3+} – O^{2-} framework [21].

4.5.2 Morphological analysis

The synthesized MIONCs show uniform size distribution as measured by TEM, and morphologies of the as-synthesized magnetic nanoparticles are shown in **Fig. 4.13-a and b**. The MIONCs exhibit a cubic shape and display a narrow size distribution that closely aligns with a log-normal distribution function, featuring a mean diameter of 20.85 ± 6.60 nm. The particle size distribution of the nanoparticles was determined by creating a histogram of the diameters obtained from the TEM images using ImageJ software (**Fig. 4.13 d**).

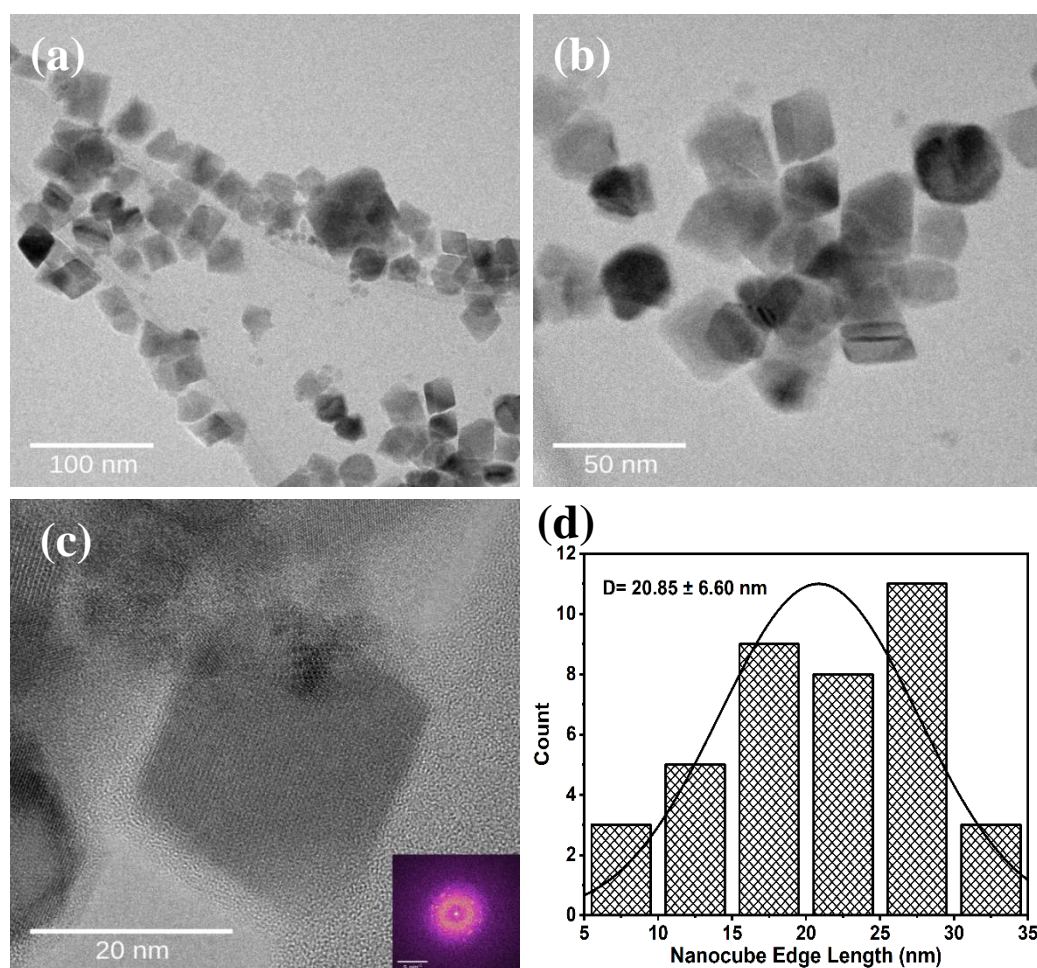


Figure 4.13 (a, b) TEM, (c), HRTEM image, (d), histogram of $\text{Mn}_x\text{Fe}_{3-x}\text{O}_4$ ($x = 1.0$) MIONCs

TEM images also reveal variations in the aggregation state of the samples. The crystalline structure and facets of the MIONCs nanocubes were further analyzed using high-resolution TEM (HRTEM) images, as depicted in **Fig. 4.13 c**. These images indicate that the nanocubes are high-quality single crystals with lattice fringe distances of 0.23 nm, corresponding to the $\{311\}$ lattice planes of MIONCs [64].

4.5.3 Thermogravimetric Analysis

The thermogravimetric analysis of MIONCs samples is shown in **Fig. 4.14**. The initial weight loss observed around 100 °C is attributed to the loss of physisorbed water. The primary decomposition occurs within the temperature range of 200–800 °C. The second weight loss step begins at approximately 250 °C and is associated with removing organic groups attached to the surface of the particles. Minimal weight loss is noted at temperatures exceeding 800 °C. Therefore, DTA was employed to gain a deeper understanding of how heat affects the molecular structure of the copolymer [65].

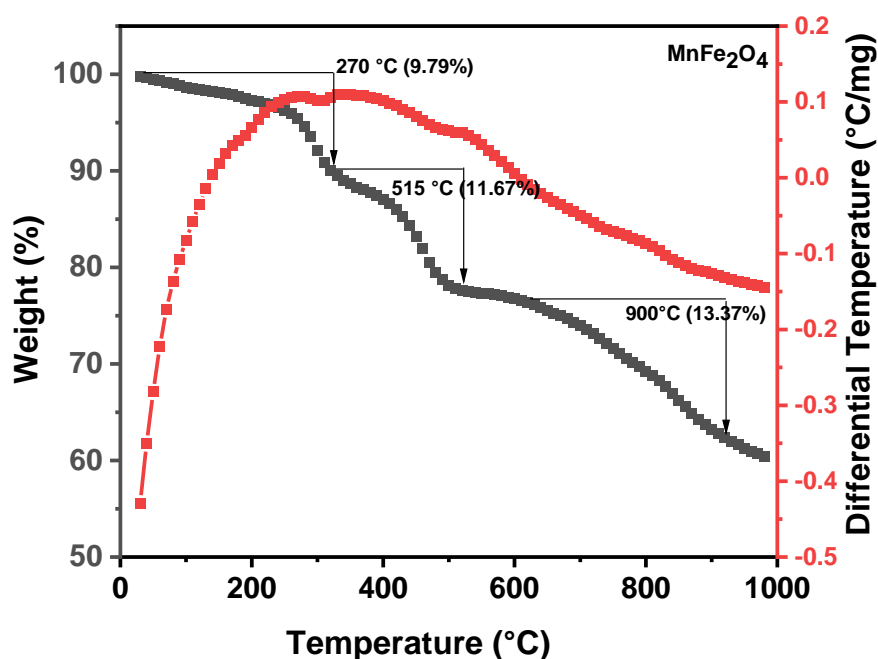


Figure 4.14 Thermogravimetric spectra of $\text{Mn}_x\text{Fe}_{3-x}\text{O}_4$ ($x = 1.0$) MIONCs

4.5.4 Magnetic Properties

To provide better insight into the relationship between the structural and magnetic properties of MIONCs, particularly in hyperthermia applications, further precise magnetic measurements were shown using VSM magnetometers. The magnetism of $\text{Mn}_x\text{Fe}_{3-x}\text{O}_4$ ($x = 0.0, 0.50$, and 1.0) MIONCs was characterized by VSM at room temperature, and the results are shown in **Fig. 4.15**. The hysteresis loop profiles of all MIONCs exhibit significant coercivity (H_c) and remnant magnetization (M_r).

The magnetic properties of the $\text{Mn}_x\text{Fe}_{1-x}\text{Fe}_2\text{O}_4$ ($x = 0.0, 0.50$, and 1.0) NPs are summarized in **Table 4.11**. The observed M_s value of MIONCs is low compared to the theoretical value of bulk MIONCs ($M_s = 92$ emu/g). Electron exchange between

the coating and surface atoms may also suppress the magnetic moment. Introducing Mn^{2+} into the B-site sublattices, rather than Fe^{2+} in the spinel, enhances magnetization due to the higher magnetic moment of Mn^{2+} at B-sites. This substitution facilitates the transfer of Fe^{3+} ions to B-sites, increasing the overall magnetic moment. As Mn^{2+} concentration increases, magneton numbers also rise. However, high Mn^{2+} content can cause lattice distortions, reducing saturation magnetization. This decrease in magnetization is attributed to particle size, structural anisotropy, and spin canting effects at the surface due to reduced coordination and broken super-exchange bonds [66].

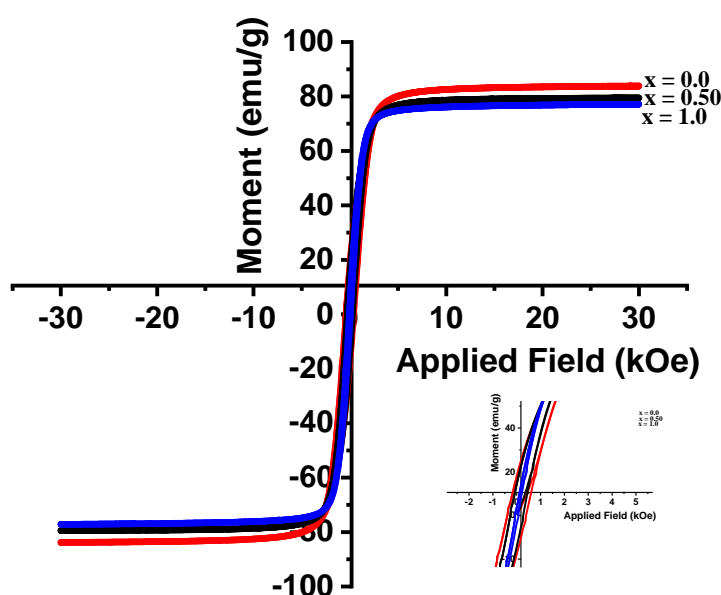


Figure 4.15 Magnetization (M) versus field (H) curves of the $\text{Mn}_x\text{Fe}_{3-x}\text{O}_4$ ($x = 0.0, 0.50$, and 1.0) MIONCs with an inset image showing the coercivity values

Mn^{2+} substitution in iron oxide nanocrystals slightly alters saturation magnetization, but further substitution significantly improves it. The variation in Mn^{2+} concentration also affects the hysteresis curve. Compared to larger iron oxide particles with lower magnetization, the changes in magnetization for different x values are likely due to reduced particle size and structural anisotropy.

Table 4.11. Summary of Saturation Magnetization (M_s), Remanence magnetization (M_r), Coercivity (H_c), Reduced Remanence (M_r/M_s), and Magnetic Moment (η_B) of the $Mn_xFe_{3-x}O_4$ ($x = 0.0, 0.50, \text{ and } 1.0$) MIONCs

$Mn_xFe_{3-x}O_4 (x)$	M_s (emu/g)	M_r (emu/g)	H_c (kOe)	M_r/M_s	Magnetic Moment (η_B)
0.0	85.85	3.27	0.2239	0.0380	3.5588
0.50	79.03	17.29	0.2029	0.2187	3.2727
1.0	78.72	24.47	0.0769	0.3108	3.2554

4.5.5 Induction Heating Study

Calorimetric measurements are highly useful for evaluating the heating efficiency of MIONCs. By measuring the heating rate of MIONCs in a solution, the specific absorption rate (SAR) can be easily determined. The impact of Mn^{2+} substitution in $Mn_xFe_{3-x}O_4$ ($x = 0.0, 0.25, 0.50, 0.75, \text{ and } 1.0$) MIONCs for hyperthermia applications is analyzed by correlating their magnetic and structural properties with induction heating performance. For each sample, the temperature was recorded over time while an AC field was applied, using a fiber optic temperature sensor inserted into the vial containing the sample, which was placed at the center of the AC coil. **Fig. 4.16** displays the temperature rise versus time for samples at various field amplitudes.

MIONCs dissipate heat in AC magnetic fields through SAR (W/g), and ILP is calculated using equations 2.11 and 2.12 (Section 2.2). The heating curves vary distinctly between samples, highlighting that the heating efficiency of these MIONCs is highly dependent on factors such as shape, size, and the strength of the applied AC field. Notably, starting from a baseline human body temperature of 37 °C, both the therapeutic window ($\Delta T = 3\text{--}7$ °C) and the thermal ablation region ($\Delta T \geq 13$ °C) for cancer treatment can be achieved in under 5 minutes by adjusting the size of the MIONCs and the applied field intensity.

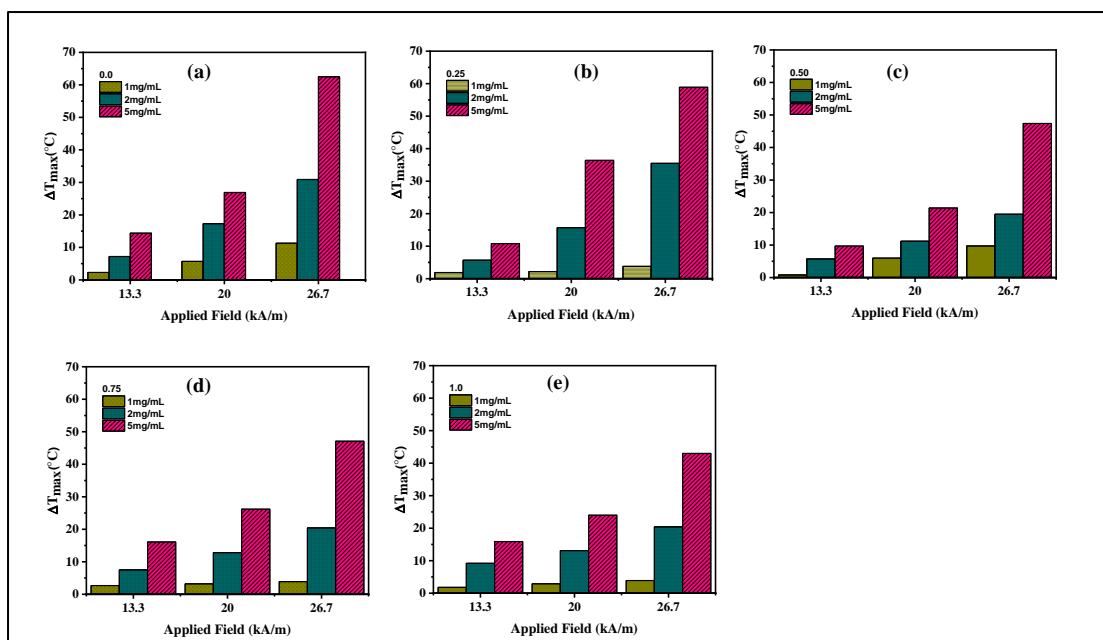


Figure 4.16 The growth in temperature versus time for samples $\text{Mn}_x\text{Fe}_{3-x}\text{O}_4$ ($x = 0.0$, 0.25, 0.50, 0.75, and 1.0) MIONCs at different field amplitudes (≈ 277 kHz)

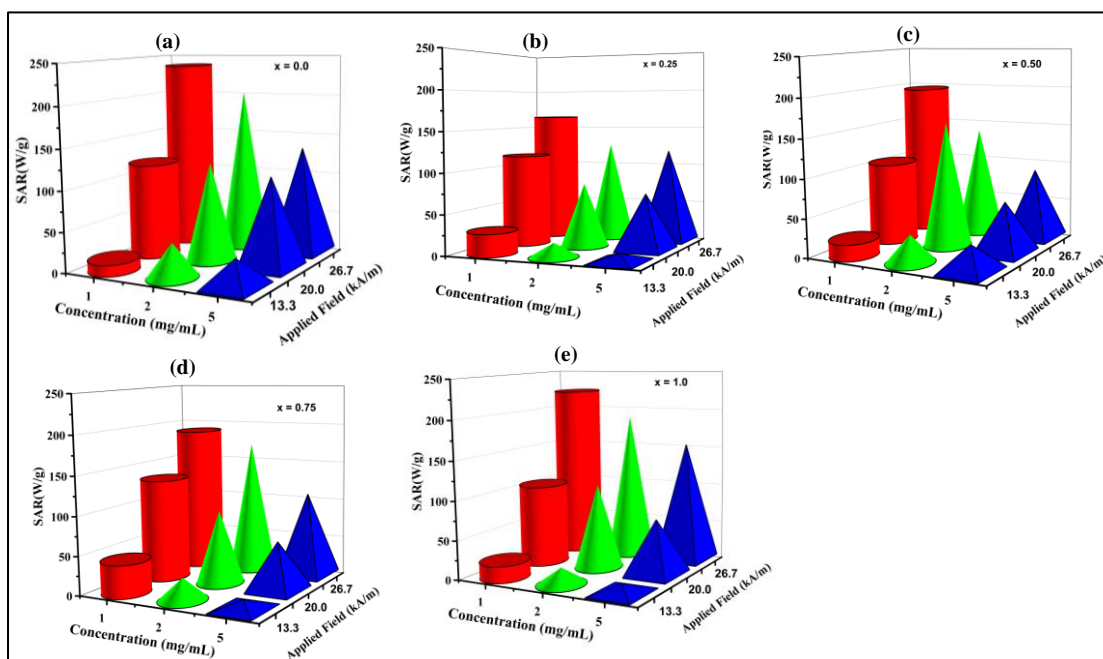


Figure 4.17 SAR value of the $\text{Mn}_x\text{Fe}_{3-x}\text{O}_4$ ($x = 0.0$, 0.25, 0.50, 0.75, and 1.0) MIONCs at different concentrations (1, 2, and 5 mg/ml) and applied fields 13.3 kA/m to 26.7 kA/m, with constant frequency (≈ 277 kHz)

From these curves, the heating efficiency or SAR of the MIONCs was determined using the initial slope method. The low SAR values observed in the smallest nanospheres may be attributed to their broader size distribution. The intrinsic

loss power (ILP) is the most suitable model, depending on the magnetic field's frequency and magnitude, allowing for easy comparison across multiple tests. Guardia et al. [57] observed a similar sharp increase in SAR in their iron oxide nanocubes, although in their case, the maximum SAR was achieved at smaller sizes, around 19 nm. They attributed this behavior to the 19 nm sample exhibiting the most precise control over shape and size distribution [67].

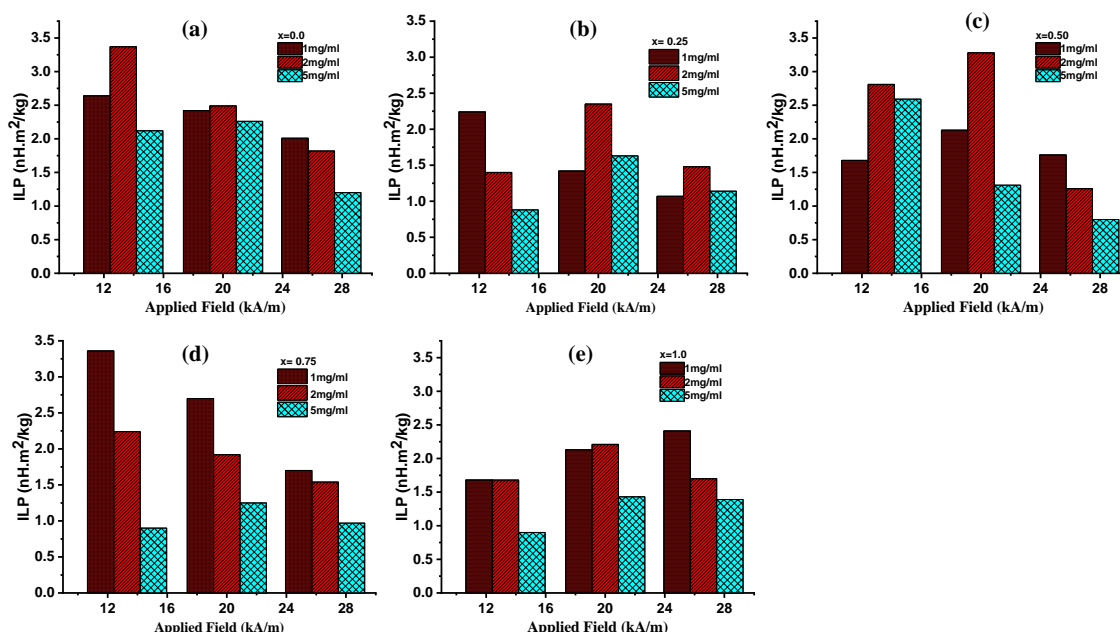


Figure 4.18 ILP value of the ($x = 0.0, 0.0, 0.25, 0.50, 0.75$, and 1.0) MIONCs at different concentrations (1, 2, and 5 mg/ml) and applied fields 13.3 kA/m to 26.7 kA/m, with constant frequency (≈ 277 kHz)

The magnetic heating properties of the samples were tested at room temperature by exposing 1 mL of MIONCs solution in water to an alternating magnetic field of different amplitudes ($H_{\max} = 13.3, 20$, and 26.7 kA/m) and frequencies ($f_{AC} = \approx 277$ kHz) for at least 600 s. SAR and ILP values of $Mn_xFe_{1-x}Fe_2O_4$ ($x = 0.0, 0.25, 0.50, 0.75$, and 1.0) MIONCs are shown in **Table 4.12** with an increase in filed amplitude from 13.3 kA/m to 26.7 kA/m for 1, 2, and 5 mg/ml respectively. Introducing manganese into the structure significantly increased local heating from 1.12 nHm²/kg (Fe_3O_4) to 3.36 nHm²/kg ($MnFe_2O_4$), attributed to enhanced magnetic properties from cation distribution between A and B sites. Analysis of these curves revealed varying temperature increases across different samples, as illustrated in the **Fig.4.16**.

Table 4.12 -SAR and ILP values of $\text{Mn}_x\text{Fe}_{3-x}\text{O}_4$ ($x = 0.0, 0.25, 0.50, 0.75$, and 1.0) MIONCs with an increase in amplitudes from 13.3 kA/m to 26.7 kA/m for $1, 2$, and 5 mg/ml respectively

$\text{Mn}_x\text{Fe}_{1-x}\text{Fe}_2\text{O}_4$	Applied field (kA/m) for	specific absorption rate (SAR) W/g			intrinsic loss power (ILP) nHm^2/kg		
		1mg/ml	2 mg/ml	5 mg/ml	1 mg/ml	2 mg/ml	5 mg/ml
$x= 0.0$	13.3	13.96	41.94	32.95	1.12	3.37	2.64
	20.0	118.72	122.33	110.78	2.42	2.49	2.26
	26.7	237.44	202.71	133.22	2.01	1.82	1.2
$x= 0.25$	13.3	27.93	17.47	9.81	2.24	1.4	0.78
	20.0	69.83	115.34	79.93	1.42	2.35	1.63
	26.7	118.72	164.27	126.41	1.07	1.48	1.14
$x= 0.50$	13.3	20.95	34.95	32.25	1.68	2.81	2.59
	20.0	104.75	160.77	64.5	2.13	3.28	1.31
	26.7	195.54	139.8	89.74	1.76	1.26	0.8
$x= 0.75$	13.3	41.9	27.93	11.21	3.36	2.24	0.91
	20.0	132.68	94.36	61.7	2.7	1.92	1.25
	26.7	188.55	171.26	107.97	1.7	1.54	0.97
$x= 1.0$	13.3	20.95	20.97	11.21	1.68	1.68	0.91
	20.0	104.75	108.35	70.11	2.13	2.21	1.43
	26.7	223.47	188.73	154.25	2.41	1.7	1.39

Generally, the temperature rises with time and frequency. Furthermore, the initial slope method can determine the corresponding SAR values from these curves. Normalizing the SAR enables a proper comparison between samples, focusing solely on their composition and concentrations [68]. **Fig. 4.17** shows the SAR and ILP (**Fig. 4.18**) values of MIONCs calculated in physiological media. For the particles, the SAR

value increases from 13.96 to 237.44 Wg^{-1} with an increase in the Mn concentrations and field from 13.3 - 26.7 kA/m. The $\text{Mn}_x\text{Fe}_{3-x}\text{O}_4$ ($x = 0.0, 0.25, 0.50, 0.75$, and 1.0) NPs exhibited the highest SAR of about 237.44 W/g for $x = 0.0$ and 223.47 for the sample $x = 1.0$ at a physiological safe range of frequency and amplitude.

4.6. Conclusions

The chemical co-precipitation approach is used to make a series of single-phased $\text{Mn}_x\text{Fe}_{1-x}\text{Fe}_2\text{O}_4$ ($x = 0.0, 0.25, 0.50, 0.75$, and 1.0) NPs with high crystallinity with diameters ranging from 5.78 to 9.94 nm. With Mn^{2+} substitution, the structural analysis revealed cubic spinel NPs, a higher lattice constant and increased particle sizes. The influence of Mn^{2+} substitution on the structural and magnetic characteristics of $\text{Mn}_x\text{Fe}_{1-x}\text{Fe}_2\text{O}_4$ ($x = 0.0, 0.25, 0.50, 0.75$, and 1.0) NPs has been investigated. It has been found that Mn^{2+} , Fe^{3+} prefers at the tetrahedral sites and Fe^{2+} , Fe^{3+} octahedral sites. Manganese incorporation significantly alters the coercivity of iron and manganese oxides by affecting A- and B-site ion interactions. At a physiologically safe frequency and amplitude range, the sample $\text{Mn}_{0.75}\text{Fe}_{0.25}\text{Fe}_2\text{O}_4$ exhibit a maximum SAR of 153.76 W/g.

Precise control over the size and morphology of $\text{Mn}_x\text{Fe}_{3-x}\text{O}_4$ nanoparticles have achieved by effectively tuning their properties through Mn^{2+} substitution in a thermal decomposition synthesis method. It has been illustrated in this work, where $\text{Mn}_x\text{Fe}_{3-x}\text{O}_4$ NPs with cubic-like shape with average sizes between 13.48 nm to 24.27 nm has been obtained. Structural and morphological analysis have been studied by XRD and TEM, it shows cubic in morphology. They have observed that their magnetic response changes as a function of their size and shape, and it has related this to the effects of the magnetic anisotropy, arrangement, and dipolar interactions. The heating efficiency of these MNPs has been analyzed by using a combination of calorimetric methods. At a physiologically safe frequency and amplitude range, the sample MnFe_2O_4 had a maximum SAR of 237.44 Wg^{-1} . These SAR values have been achieved for these cube-shaped MIONCs at a frequency and magnetic field conditions that are suitable candidates for hyperthermia treatment.

The magnetic anisotropy of MNPs influences hysteresis loop shape and heating efficiency. Nanocubes heat more efficiently than nanospheres, but as size increases, nanocube anisotropy rises more rapidly due to stronger dipolar interactions. In this respect, the nanocubes are more demanding and require higher fields than the

nanospheres in order to increase the SAR, although they can exhibit better heating values than the nanospheres. Therefore, based on these results, $\text{Mn}_{0.75}\text{Fe}_{0.25}\text{Fe}_2\text{O}_4$ nanospheres and MnFe_2O_4 nanocubes has emerged as optimized sample for further studies for that particular shapes.

4.7 References

1. S. He, H. Zhang, Y. Liu, F. Sun, X. Yu, X. Li, L. Zhang, L. Wang, K. Mao, G. Wang, Y. Lin, *Small*, 14(29) (2018) 1800135-45.
2. K. Maier-Hauff, F. Ulrich, D. Nestler, H. Niehoff, P. Wust, B. Thiesen, H. Orawa, V. Budach, A. Jordan, *Journal of neuro-oncology*, 103 (2011) 317-324.
3. H. Zhang, H. Huang, S. He, H. Zeng, A. Pralle, *Nanoscale*, 6(22) (2014) 13463-13469.
4. A. Doaga, A. Cojocariu, W. Amin, F. Heib, P. Bender, R. Hempelmann, O. Caltun, *Mater. Chem. Phys.*, 143(1) (2013) 305-310.
5. N. Thorat, H. Townely, G. Brennan, A. Parchur, C. Silien, J. Bauer, S. Tofail, *ACS Biomater Sci Eng.*, 5(6) (2019) 2669-2687.
6. S. Yazdi, P. Iranmanesh, S. Saeednia, M. Mehran, *Mater. Sci. Eng. B*, 245 (2019) 55–62.
7. P. Rajagiri, B. Sahu, N. Venkataramani, S. Prasad, R. Krishnan, *AIP Adv.*, 8 (5) (2018) 2–8.
8. V. Khot, A. Salunkhe, M. Phadatare, S. Pawar, *Mater. Chem. Phys.*, 132 (2012) 782–787.
9. D. García-Soriano, R. Amaro, N. Lafuente-Gómez, P. Milán-Rois, A. Somoza, C. Navío, F. Herranz, L. Gutiérrez, G. Salas, *J. Colloid Interface Sci.*, 578 (2020) 510-521.
10. K. Khalaf, A. Al-Rawas, H. Widatallah, K. Al-Rashdi, A. Sellai, A. Gismelseed, M. Hashim, S. Jameel, M. Al-Ruqeishi, K. Al-Riyami, M. Shongwe, *J. Alloys Compd.*, 657 (2016) 733-747.
11. D. Carta, M. Casula, A. Falqui, D. Loche, G. Mountjoy, C. Sangregorio, A. Corrias, *J. Phys. Chem. C*, 113 (20) (2009) 8606-8615.
12. D. Nikam, S. Jadhav, V. Khot, R. Bohara, C. Hong, S. Mali, S. Pawar, *RSC Adv.*, 5(3) (2015) 2338-2345.
13. G. Shahane, K. Zipare, S. Bandgar, V. Mathe, *J Mater Sci Mater Electron.*, 28 (2017) 4146–4153.
14. S. Torkian, A. Ghasemi, R. Razavi, *Ceram Int.*, 43 (2017) 6987–6995.
15. K. Vamvakidis, M. Katsikini, G. Vourlias, M. Angelakeris, E. Paloura, C. Dendrinou-Samara, *Dalt Trans.*, 44 (2015) 5396–5406.
16. A. Beeran, S. Nazeer, F. Fernandez, K. Muvvala, W. Wunderlich, S. Anil, S.

- Vellappally, M. Rao, A. John, R. Jayasree, P. Varma, *PCCP*, 17(6) (2015) 4609-4619.
17. M. Yousuf, M. Baig, N. Al-Khalli, M. Khan, M. Aboud, I. Shakir, M. Warsi, *Ceram. Int.*, 45(8) (2019) 10936-10942.
 18. S. Jesudoss, J. Vijaya, L. Kennedy, P. Rajan, H. Al-Lohedan, R. Ramalingam, K. Kaviyarasu, M. Bououdina, *J. Photochem. Photobiol. B*, 165 (2016) 121-132.
 19. M. Satakar, S. Kane, A. Ghosh, N. Ghodke, G. Barrera, F. Celegato, M. Coisson, P. Tiberto, F. Vinai, *J. Alloys Compd.*, 615 (2014) S313-S316.
 20. J. Parhizkar, M. Habibi, *Nanochem Res.*, 2(2) (2017) 166-71.
 21. V. Khot, A. Salunkhe, M. Phadatar, N. Thorat, S. Pawar, *J. Phys. D Appl. Phys.*, 46 (5) (2013).
 22. I. Malaescu, A. Lungu, C. Marin, P. Vlazan, P. Sfirloaga, G. Turi, *Ceram Int.*, 42 (2016) 16744–16748.
 23. V. Lenart, R. Turchiello, M. Calatayud, G. Goya, S. Gómez, *Braz. J. Phys.*, 49 (2019) 829–835.
 24. A. Salokhe, A. Koli, V. Jadhav, S. Mane-Gavade, A. Supale, R. Dhabbe, X. Yu, S. Sabale, *SN Applied Sciences*, 2 (2020).
 25. C. Pereira, A. Pereira, M. Rocha, C. Freire, C. Geraldes, *J. Mater. Chem. B.*, 3(30) (2015) 6261-62 73.
 26. P. Sugumaran, X. Liu, T. Heng, E. Peng, J. Ding, *ACS Appl. Mater. Interfaces*, 11 (25) (2019) 22703-22713.
 27. S. Mansour, M. Elkestawy, *Ceram Int.*, 37 (2011) 1175–1180.
 28. U. Ghodake, R. Kambale, S. Suryavanshi, *Ceram Int.*, 43 (1) (2017) 1129–1134.
 29. X. Lasheras, M. Insausti, J. Fuente, I. Muro, I. Castellanos-Rubio, L. Marcano, L. Fernández-Gubieda, A. Serrano, R. Martín-Rodríguez, E. Garaio, J. García, *Dalt Trans.*, 48 (30) (2019) 11480–11491.
 30. E. Attia, A. Zaki, S. El-Dek, A. Farghali, *J. Mol. Liq.*, 231 (2017) 589–596.
 31. D. Nikam, S. Jadhav, V. Khot, M. Phadatar, S. Pawar, *J. Magn. Magn. Mater.*, 349 (2014) 208–213.
 32. M. Arshad, M. Asghar, M. Junaid, M. Warsi, M. Rasheed, M. Hashim, M. Maghrabi, M. Khan, *J. Magn. Magn. Mater.*, 474 (2019) 98–103.
 33. M. Dojcinovic, Z. Vasiljevic, V. Pavlovic, D. Barisic, D. Pajic, N. Tadic, M. Nikolic, *J. Alloys Compd.*, 855 (2021) 157429-157466.
 34. L. Bianco, F. Spizzo, G. Barucca, M. Ruggiero, S. Crich, M. Forzan, E. Sieni, P.

- Sgarbossa, *Nanoscale*, 11(22) (2019) 10896-10910.
35. S. Sankaranarayanan, A. Thomas, N. Revi, B. Ramakrishna, A. Rengan, J. Drug Deliv. Technol., 70 (2022) 103196.
36. L. Yang, L. Ma, J. Xin, A. Li, C. Sun, R. Wei, B. Ren, Z. Chen, H. Lin, J. Gao, *Chem. Mater.*, 29(7) (2017) 3038-3047.
37. N. Thorat, R. Bohara, H. Yadav, S. Tofail, *RSC Adv.*, 6 (2016) 94967–94975.
38. A. Salunkhe, V. Khot, M. Phadatare, N. Thorat, R. Joshi, H. Yadav, S. Pawar, J. Magn. Mater., 352 (2014) 91-98.
39. Z. Heiba, M. Mohamed, H. Hamdeh, M. Ahmed, *J Alloys Compd.*, 618 (2015) 755–760.
40. F. Nakagomi, S. Silva, V. Garg, A. Oliveira, P. Moraes, A. Franco, *J. Solid State Chem.*, 182 (2009) 2423–2429.
41. V. Angadi, B. Rudraswamy, K. Sadhana, S. Murthy, K. Praveena, *J Alloys Compd.*, 656 (2016) 5–12.
42. V. Awati, S. Rathod, M. Mane, K. Mohite, *Int Nano Lett.*, 3 (2013) 1–8.
43. S. Debnath, A. Das, R. Das, *Ceram In.*, 47 (2021) 16467–16482.
44. B. Vara Prasad, K. Ramesh, A. Srinivas, *Mater Sci Pol.*, 37 (2019) 39–54.
45. T. Tatarchuk, M. Bououdina, W. Macyk, O. Shyichuk, N. Paliychuk, I. Yaremiy, B. Al-Najar, M. Pacia, *Nanoscale Res. Lett.*, 12 (2017) 1-1.
46. G. Kumar, J. Shah, R. Kotnala, V. Singh, G. Garg, S. Shirsath, K. Batoo, M. Singh *Mater. Res. Bull.*, 63 (2015) 216-225.
47. N. Thorat, R. Bohara, S. Tofail, Z. Allothman, M. Shiddiky, M. Hossain, Y. Yamauchi, K. Wu, *Eur. J. Inorg. Chem.*, 28 (2016) 4586-4597.
48. N. Thorat, S. Otari, R. Patil, V. Khot, A. Prasad, R. Ningthoujam, S. Pawar, *Colloids Surf. B Biointerfaces*, 111 (2013) 264–269.
49. R. Hergt, S. Dutz, *J. Magn. Mater.*, 311 (2007) 187–192.
50. E. Verde, G. Landi, J. Gomes, M. Sousa, A. Bakuzis, *J. Appl. Phys.*, 111 (12) (2012) 123902-123911.
51. J. Giri, P. Pradhan, T Sriharsha, D. Bahadur, *J. Appl. Phys.*, 97 (2005) 6–9.
52. R. Otero-Lorenzo, E. Fantechi, C. Sangregorio, V. Salgueiriño, *Chem. Eur. J.*, 22 (19) (2016) 6666-6675.
53. K. Rotjanasuworapong, W. Lerdwijitjarud, A. Sirivat, *Mater. Chem. Phys.*, 11 (4) (2021) 876- 895.
54. V. Khot, A. Salunkhe, N. Thorat, R. Ningthoujam, S. Pawar, *Dalt Trans.*, 42

- (2013) 1249–1258.
55. D. Cabaleiro, M. Pastoriza-Gallego, C. Gracia-Fernández, M. Piñeiro, L. Lugo, *Nanoscale Res. Lett.*, 8 (2013) 1–13.
56. Z. Ma, J. Mohapatra, K. Wei, J. Liu, S. Sun, *Chem. Rev.*, 123 (2023) 3904–3943.
57. P. Guardia, R. Corato, L. Lartigue, C. Wilhelm, A. Espinosa, M. Garcia-Hernandez, F. Gazeau, L. Manna, T. Pellegrino, *ACS Nano*, 6(4) (2012) 3080–3091.
58. E. Bertuit, E. Benassai, G. Mériguet, J. Greneche, B. Baptiste, S. Neveu, C. Wilhelm, A. Abou-Hassan, *ACS Nano*, 16(1) (2021) 271–284.
59. A. Walter, C. Billotey, A. Garofalo, C. Ulhaq-Bouillet, C. Lefevre, J. Taleb, S. Laurent, L. Elst, R. Muller, L. Lartigue, F. Gazeau, *Chem. Mater.*, 26(18) (2014) 5252–5264.
60. H. Zhang, H. Huang, S. He, H. Zeng, A. Pralle, *Nanoscale*, 6(22) (2014) 13463–13469.
61. J. Lee, J. Jang, J. Choi, S. Moon, S. Noh, J. Kim, J. Kim, I. Kim, K. Park, J. Cheon, *Nat. Nanotechnology*, 6(7) (2011) 418–422.
62. M. Li, M. Mondrinos, X. Chen, M. Gandhi, F. Ko, P. Lelkes, J. Biomed. Mater. Res., 79(4) (2006) 963–973.
63. A. Manohar, V. Vijayakanth, S. Vattikuti, P. Manivasagan, E. Jang, K. Chintagumpala, K. Kim, *ACS Appl. Nano Mater.*, 5 (2022) 5847–5856.
64. J. Pan, P. Hu, Y. Guo, J. Hao, D. Ni, Y. Xu, Q. Bao, H. Yao, C. Wei, Q. Wu, J. Shi, *ACS Nano*, 14(1) (2020) 1033–1044.
65. F. Panahi, S. Peighambaroudoust, S. Davaran, R. Salehi, *Polymer*, 117 (2017) 31–117.
66. M. Vassallo, D. Martella, G. Barrera, F. Celegato, M. Coisson, R. Ferrero, E. Olivetti, A. Troia, H. Sozeri, C. Parmeggiani, D. Wiersma, *ACS omega*, 8(2) (2023) 2143–2154.
67. Z. Nemati, J. Alonso, I. Rodrigo, R. Das, E. Garaio, J. García, I. Orue, M. Phan, H. Srikanth, *J. Phys. Chem. C*, 122(4) (2018) 2367–2381.
68. S. Fernández, O. Odio, P. Crespo, E. Pérez, G. Salas, L. Gutiérrez, M. Morales, E. Reguera, *J. Phys. Chem. C*, 126 (24) (2022) 10110.0, 0.25, 0.50, 0.75, and 1.00128.

CHAPTER-5

Surface Functionalization of Optimized Manganese Iron Oxide Nanoparticles by using Chitosan for Hyperthermia Application

The part of this chapter has published as a research article

Nanoscale



PAPER

[View Article Online](#)
[View Journal](#)



Cite this: DOI: 10.1039/d3nr02816j

Functionalized manganese iron oxide nanoparticles: a dual potential magneto-chemotherapeutic cargo in a 3D breast cancer model†

Satish S. Phalake, ^a Sandeep B. Somvanshi, ^{b,c} Syed A. M. Tofail,^d
Nanasaheb D. Thorat ^{*d,e} and Vishwajeet M. Khot ^{*a}

Localized heat generation from manganese iron oxide nanoparticles (MIONPs) conjugated with chemotherapeutics under the exposure of an alternating magnetic field (magneto-chemotherapy) can revolutionize targeted breast cancer therapy. On the other hand, the lack of precise control of local temperature and adequate MIONP distribution in laboratory settings using the conventional two-dimensional (2D) cellular models has limited its further translation in tumor sites. Our current study explored advanced 3D *in vitro* tumor models as a promising alternative to replicate the complete range of tumor characteristics. Specifically, we have focused on investigating the effectiveness of MIONP-based magneto-chemotherapy (MCT) as an anticancer treatment in a 3D breast cancer model. To achieve this, chitosan-coated MIONPs (CS-MIONPs) are synthesized and functionalized with an anticancer drug (doxorubicin) and a tumor-targeting aptamer (AS1411). CS-MIONPs with a crystallite size of 16.88 nm and a specific absorption rate (SAR) of 181.48 W g⁻¹ are reported. *In vitro* assessment of MCF-7 breast cancer cell lines in 2D and 3D cell cultures demonstrated anticancer activity. In the 2D and 3D cancer models, the MIONP-mediated MCT reduced cancer cell viability to about 71.48% and 92.2%, respectively. On the other hand, MIONP-mediated MCT under an AC magnetic field diminished spheroids' viability to 83.76 ± 2%, being the most promising therapeutic modality against breast cancer.

Received 13th June 2023,
Accepted 5th September 2023
DOI: 10.1039/d3nr02816j
rsc.li/nanoscale

5.1. Introduction

The MNPs use of applications such as heat-mediated drug delivery, catalysis, self-healing materials, MHT [1], MRI-Guided drug delivery [2], and heat-triggered remote biological process control may depend on the enhancement of the heating effectiveness of MNPs under AMF [3, 4]. Ferrite's magnetic and electrical characteristics are greatly influenced by the distribution of cations between tetrahedral and octahedral sites, which the selected synthesis method and sintering conditions can control. The practical use of these ferrimagnetic and superparamagnetic nanoparticles relies on their physical and chemical properties, which are particularly sensitive to their shape and size. Magnetic hyperthermia, which utilizes MNPs, shows great promise as an adjunct therapy for cancer treatment due to the MNPs inherent ability to dissipate heat when exposed to an AMF. To ensure the safety of MHT, we optimized the parameters of the AMF by selecting a low frequency (f) and an appropriate strength of the AMF. This optimization aimed to minimize exposure times while maintaining bio-safety. MHT utilizes MNPs to generate heat after exposure to AMF. This heat is then used to selectively treat specific tumor tissues while minimizing damage to surrounding normal tissues, as it avoids significant overall temperature elevation. The FDA has already permitted using several magnetite-based MNP products in humans [5-7]. Many synthetic functional nanomaterials have been created and are currently used in the biomedical field, most notably for cancer treatment. The newly developed nanotechnology-based approach, magneto-chemotherapy (combining magnetic hyperthermia and chemotherapy), is anticipated to enhance cancer tumor treatment in the oncological field. Meanwhile, a new aspect of magneto-chemotherapy has emerged with the development of MNPs-based MHT therapy [8, 9].

Among MNPs, significant research has focused on iron oxide and ferrite nanoparticles due to their exceptional SPM behavior and chemical stability. Spinel manganese iron oxide ($\text{Mn}_x\text{Fe}_{3-x}\text{O}_4$) systems stand out for their high magnetic moments (approximately $5 \mu_B$ per unit cell), strong chemical stability, and surfaces suitable for ligand functionalization. As soft magnets, $\text{Mn}_x\text{Fe}_{3-x}\text{O}_4$ can be saturated with low magnetic fields, offering tunable anisotropy promising for diagnostic and therapeutic uses [10]. MnFe_2O_4 has been a focal point of research due to its highest magnetization, which makes it a promising candidate for use as an MRI contrast agent

and magnetic probe that an external magnetic field can control [11, 12]. Manganese-doped iron oxide nanoparticles ($\text{Mn}_x\text{Fe}_{3-x}\text{O}_4$) are promising candidates due to their higher magnetization than magnetite nanoparticles and other metal-doped iron oxides like cobalt ferrite and nickel ferrite. Manganese ferrite has been explored due to their high magnetization among the ferrite family and stability against oxidation. These NPs have achieved relatively high SLP values. However, further increasing the SAR by increasing the M_s would be futile. Although a high M_s is beneficial for increasing AR, high M_s materials are typically metallic and face stability and toxicity issues in physiological environments [13].

To facilitate biomedical use of iron oxide nanoparticles, their surfaces must be modified with nontoxic, biocompatible stabilizers, such as natural and synthetic polymers, to ensure stability in physiological environments. Various natural polymers, including pullulan, dextran, starch, BSA, chitosan, alginate, polyethylene glycol (PEG), polyvinyl alcohol (PVA), polydopamine (PDA), polysaccharides, polyethyleneimine, polyvinylpyrrolidone (PVP), polyacid polyetherimide, and polyamidoamine (PAMAM), have been utilized as protective coatings due to their biocompatibility, high solubility, and hydrophilic properties. [14, 15]. CS offers the advantage of having aminated groups, which present a variety of active sites for additional biofunctionalization. This characteristic of CS provides further benefits. When MIONPs are exposed to an AMF, it generates localized heating, specifically within the tumor tissues. This chapter offers a practical approach for creating well-defined, high magnetic moments of MNPs and surfaces modified with chitosan.

5.2 Need for Functionalization

Surface modification is crucial for MNPs in biomedical applications, as their properties, such as hydrophobicity or hydrophilicity, vary by synthesis method; interactions depend on the surrounding media and surface molecules, with MNPs forming clusters due to Van der Waals forces and magnetic attraction, while smaller sizes increase reactivity and aggregation, leading to oxidation and loss of magnetic properties. Functionalization is essential for MNPs, even when initially stabilized, as it enhances their stability and targeting capabilities. The strategies for functionalization depend on the intended application and the initial surface chemistry of the MNPs. The primary goal is to create stable hydrophilic MNPs across various ionic strengths and pH levels. In biomedical applications, a significant challenge is to

keep the particle size below 150 nm after functionalization to preserve magnetic properties. Effective functionalization can prevent aggregation and facilitate specific interactions. At the same time, the steric hindrance from the coating influences cellular uptake and circulation time, which can help avoid the release of core materials that may lead to toxicity in the biological environment. The main objectives of surface modification of MNPs are to prevent agglomeration, enhance surface catalytic activity, improve physicochemical and mechanical properties, and boost solubility and biocompatibility [16-18].

The surface modification of MNPs influences characteristics such as size, surface chemistry, hydrophilicity, hydrophobicity, and charge, which can subsequently affect solubility, biocompatibility, biodistribution, and clearance of the resulting nanoprobes. When MNPs are coated with small molecules or polymers like dextran, starch, citrate, or polyethylene glycol (PEG), the resulting nanoprobes demonstrate improved biodistribution, longer circulation times, and more efficient uptake. Hydrophilic polymers, particularly PEG, can be conjugated to MNPs for steric stabilization, thereby preventing protein absorption and extending blood circulation for in vivo applications. The modified surface chemistry of MNPs can significantly influence their pharmacokinetic behavior in vivo, with PEG conjugation known to enhance hydrophilicity stability and reduce cytotoxicity levels [19-20]. Coating nanoparticles with small molecules effectively modifies their surface charge and stability to enhance cellular interactions. At the same time, biomolecules guide nanoparticles to specific cells for safer cancer therapies, with polymers often used as biocompatible coatings to improve bioavailability and facilitate sustained drug release [21].

5.3 Strategies and Choice of Polymer

For numerous biomedical applications, polymer coatings on MNPs are favored over simple functionalization with small organic compounds and surfactants. This preference arises because polymer coatings enhance repulsive forces, counteracting the magnetic interactions and Van der Waals attractive forces among MNPs. Polymer-engineered iron oxide nanoparticles also demonstrate enhanced blood circulation time, stability, and biocompatibility. Various studies have indicated that magnetic iron oxide/polymer composite MNPs with tailored properties can be

achieved by thoughtfully selecting the passivating and activating polymers and associated reaction parameters [22].

Surfactants influence the performance of MNPs in applications like MRI and hyperthermia, with thinner coatings causing agglomeration and thicker ones reducing magnetization. Polymers, such as chitosan from shellfish, are used to modify MNP surfaces due to their biocompatibility and unique mucoadhesive properties, enhancing nanoparticle bioavailability through various delivery routes. Chitosan's positive charge allows it to interact with negatively charged mucosal components, improving adsorption and retention [23].

5.4. Surface Functionalization of Manganese Iron Oxide Nanoparticles with Chitosan

Synthesis parameters such as concentration, pH, temperature, and particle size can be adjusted. The size distribution, shape, and formulation of MNPs influence their SAR; when exposed to an AMF, these factors may lead to inadequate heat production, reducing the effectiveness of eliminating targeted tumor cells [7]. A variety of surfactants, including both polymeric and non-polymeric materials like lipids and proteins, are used to coat manganese iron oxide nanoparticles (MIONPs) to maintain their colloidal stability and biocompatibility while preventing aggregation from magnetic dipole-dipole interactions. Polymers such as chitosan, oleic acid, starch, pullulan, and dextran are commonly applied to make MIONPs suitable for in vivo applications. Chitosan, in particular, stands out for its biocompatibility, biodegradability, film-forming ability, and bio-adhesive properties, offering aminated groups that provide multiple active sites for further biofunctionalization. This characteristic of CS offers additional benefits. The application of MNPs is constrained by their sustainability with biological radicals/ tissue. This can be overcome with the choice of suitable polymeric materials.

5.5 Experimental Details

Method

The synthesis of MIONPs has already been discussed in the previous chapter (**Chapter 4 Section 4.2**). This section provides a practical approach for creating well-defined, high magnetic moments of optimized MIONPs and surfaces modified with chitosan.

5.5.1 Surface Modification of MIONPs with Chitosan (CS- MIONPs):

Uncoated MIONPs were utilized for the coating process. A solution of 1% (w/v) chitosan (CS) in 2% (v/v) acetic acid was employed to dissolve 1% of the bare MIONPs. After 30 minutes, the mixture underwent ultrasonication. The CS-MIONPs were ultrasonically cleaned and then allowed to settle before being washed three times with distilled water to eliminate any extra CS. Following their separation, these CS-MIONPs were dried in the air at 50 °C [24]. The schematic shows the procedure for synthesizing MIONPs and their surface modification using CS in **Fig. 5.1**.

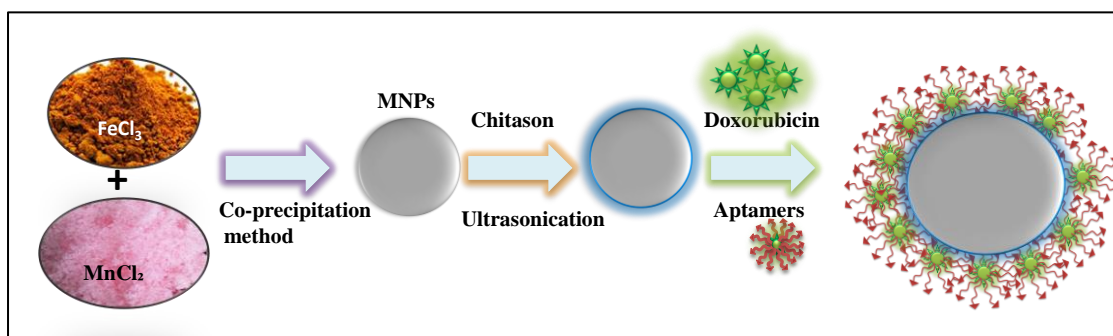


Figure 5.1: Schematic shows the procedure for the synthesis of MIONPs and their surface modification using CS

5.5.2 Structural and Magnetic Characterization

XRD analysed the crystal phase of the MIONPs. Morphology and size distribution of the MIONPs were determined using TEM, employing a JEOL JEM-2100 transmission electron microscope. The presence of a coating bounded to the surface of the MIONPs was investigated by FTIR spectroscopy. TGA was carried out for powder samples with a heating rate of 10° C/min, using SDT Q600 V20.9 Build 20 thermogravimetric analyzer up to 800 °C. DLS investigated the colloidal stability and hydrodynamic size of the MIONPs. The static hysteresis loops of dry samples were measured at room temperature by VSM, employing a Lake Shore 7410 magnetometer.

5.5.3 Magnetic hyperthermia experiment

To investigate the induction heating of the prepared nanoparticles in a physiological medium, an Easy Heat 8310 system (Ambrell, UK) was employed. A 6 cm diameter coil consisting of 3 turns was utilized for this purpose. The samples suspended in carrier liquid were positioned at the center of the coil. The suspension of

nanoparticles was loaded in the plastic microcentrifuge tube with a capacity of 2 mL. The suspensions were treated for 600 seconds with the necessary applied current (200–400 A). For the conducted experiments, the magnetic field was calculated from the relationship:

$$H = \frac{1.257ni}{L} \text{ in Oe} \quad (5.1)$$

Where n , i and L denote the number of turns, the applied current and the diameter of the turn in centimeters, respectively. Calculated values of the magnetic field (H) at 200, 300, 400, 500 and 600 A were 167.6, 251.4, 335.2, 419 and 502.8 Oe (equivalent to 13.3, 20.0, 26.7, 33.3 and 40.0 kA m⁻¹), respectively. Temperature was measured using an optical fiber probe with an accuracy of 0.1 °C. The efficiency of the nanoparticles for magnetic hyperthermia was assessed using a thermal method, employing a fixed frequency of ≈ 277 kHz and variable magnetic field amplitude ranging from 13.3 kA/m to 26.7 kA/m.

5.6. Results and Discussions

5.6.1. Structural Analysis

The powder XRD patterns were used to identify the structural investigations of the MIONPs. FTIR confirms the cubic spinel phase and examines the surfactant ligands.

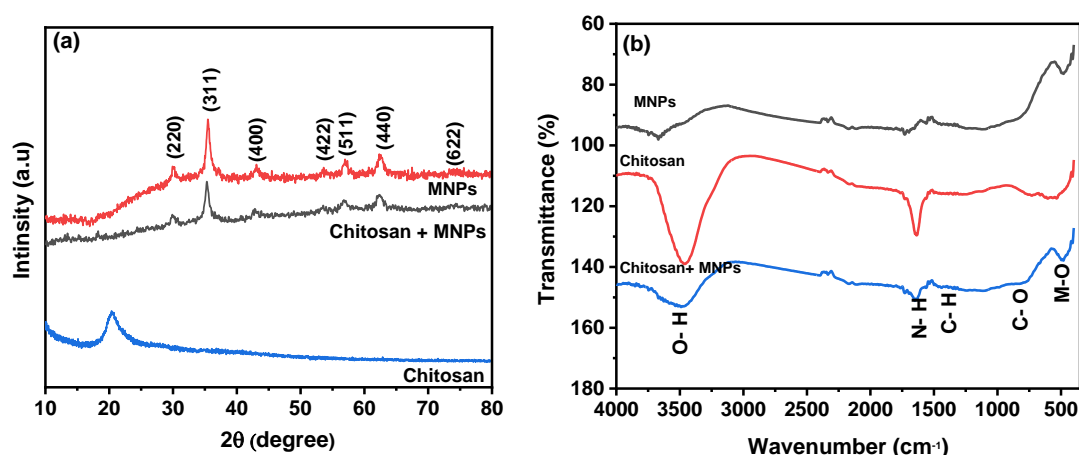


Figure 5.2 (a) XRD patterns of bare MIONPs, CS and CS- MIONPs, (b) FTIR spectra of bare MIONPs, CS and CS- MIONPs

The XRD patterns of the MIONPs and chitosan-coated MIONPs (CS-MIONPs) are shown in **Fig. 5.2a**. The characteristic broad diffraction peaks confirmed the crystalline nature of MIONPs and reflection planes (220, 311, 400,

422, 511, 440, and 622), indicating the presence of cubic spinel structure, matched with JCPDS card no. 00-10-0319. The crystallite size of synthesized MIONPs was determined using the Debye-Scherrer relation, which was determined to be 16.88 nm for uncoated and 13.91 nm for CS-MIONPs nanocomposite, respectively. The intensity decreased after capping the MIONPs with CS, and the peaks broadened, proving that the coating procedure reduced particle size. The presence of an amorphous CS polymer coating on MIONPs could lead to the micro-strain, leading to peak broadening in the coated sample [25].

The structural properties and bonding nature of synthesized MIONPs and CS-MIONPs nanocomposites were studied by infrared spectroscopy, and the FTIR spectra of bare MIONPs and CS-MIONPs along with CS are shown in **Fig. 5.2b**, respectively. The band detected at 455 cm^{-1} belongs to the $\text{Fe}_{\text{octa}}\text{-O}$ vibrational bond at octahedral sites, while the band detected at 565 cm^{-1} belongs to the intrinsic $\text{Fe}_{\text{tetra}}\text{-O}$ vibrational bond at the tetrahedral sites. Compared to the spectra of pure chitosan, the amide absorptions become stronger and move to lower wavenumbers, such as 1630 cm^{-1} , which is indicative of hydrogen-bonded amides. The CH_2 group deformation is due to the sharp peak at 1400 cm^{-1} [26]. The peaks at 1620 and 3376 cm^{-1} are attributable to stretching (ν) vibrations of the -OH group and water adsorbed on the surfaces of MIONPs, respectively. The primary amino group ($-\text{NH}_2$) in CH forms strong hydrogen bonds with the oxygen in MIONPs, as evidenced by the rise in absorption intensity at 1631 cm^{-1} [27].

5.6.2. Morphological Analysis

The morphological characterizations were studied using TEM with a JEOL JEM-2100 microscope operating at 200 kV, and an EDXS detector was used for composition studies. **Fig. 5.3-a, e** shows the TEM images for both MIONPs and CS-MIONPs and corresponding histograms illustrating particle size distribution (**d, h**). The TEM analysis of the MIONPs samples provides insights into the particle size and distribution, which align well with the results obtained from XRD analysis. The images reveal the presence of aggregated MIONPs with both spherical and irregular forms, with sizes of approximately $D=20\pm0.15\text{ nm}$ and $D=13\pm0.20\text{ nm}$, as shown in **Fig. 5.3- d, h**. The observed scattered ring patterns in the TEM images agree with the XRD analysis, showing a well-defined crystallite formation of the MIONPs. High-resolution TEM (HRTEM) images **Fig. 5.3-b, f** exhibit lattice fringes at a spacing of

approximately 0.270 nm, corresponding to the (311) plane, revealing the monophase formation.

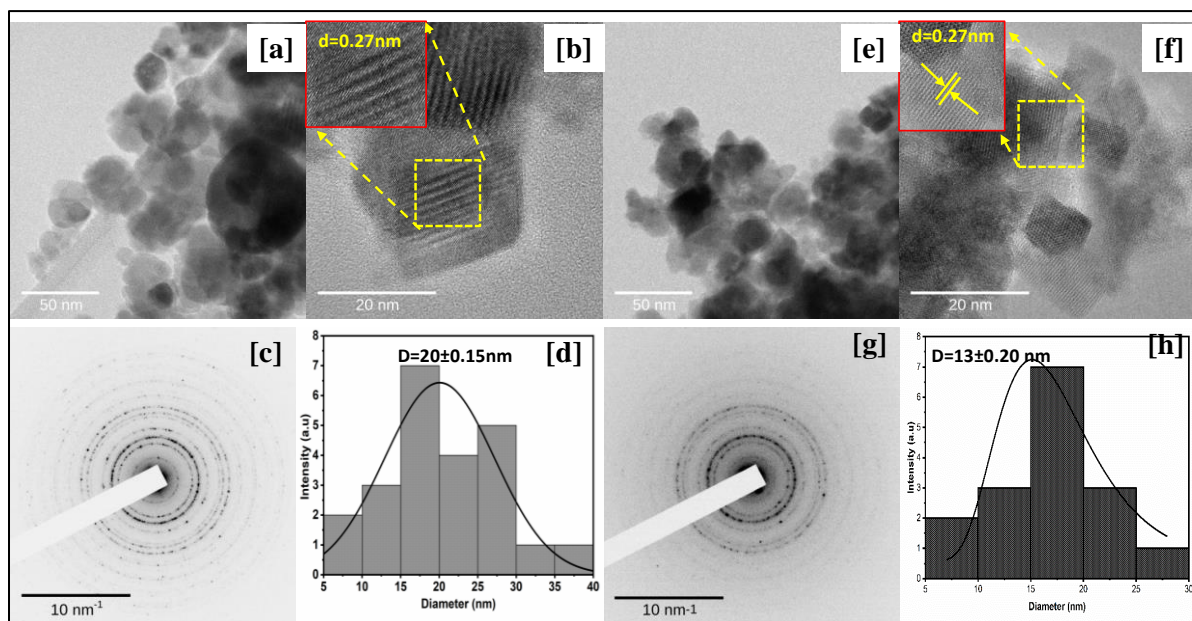


Figure 5.3 TEM, HRTEM image, SAED patterns and Histogram of bare MIONPs (a, b, c, d) and CS- MIONPs (e, f, g, h)

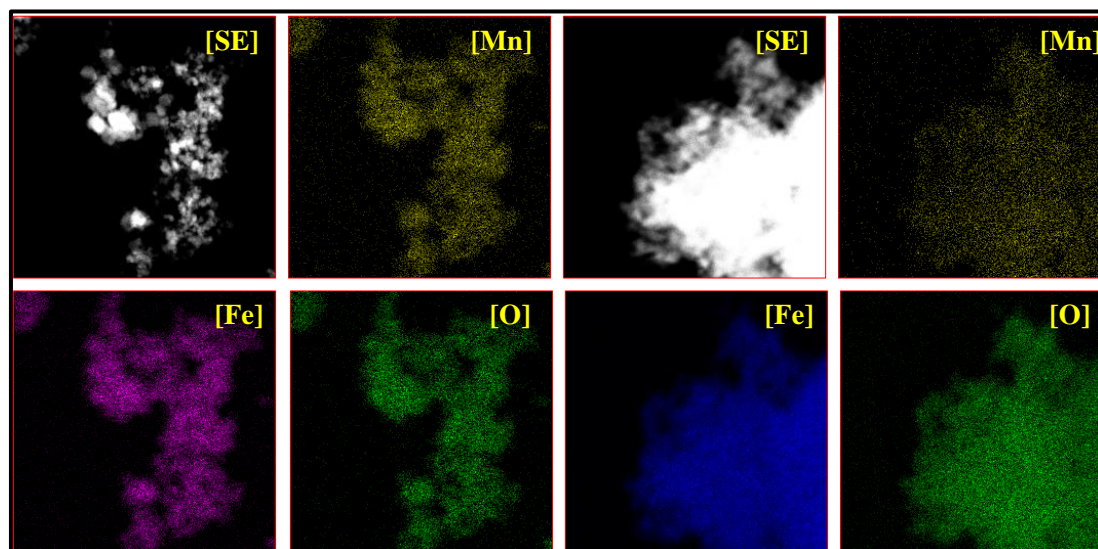


Figure 5.4 TEM-EDX chemical mapping of the samples MIONPs and CS- MIONPs

Fig. 5.3 - a, e demonstrates that the CS-coated MIONPs exhibit a nearly spherical shape and good dispersibility, with minimal agglomeration compared to the uncoated nanoparticles. Furthermore, the functionalization with CS molecules increases the average particle diameter. The non-magnetic nature of CS plays a

significant role in reducing interparticle interactions, leading to improved dispersibility after coating. The crystalline formation of MIONPs is further supported by the corresponding SAED patterns in **Fig. 5.3 (c, g)**, which exhibit bright ring patterns. The planes visible in the XRD patterns correspond to the ring motifs [25]. For a better understanding of both sample studies of the structure architecture, TEM-EDX chemical mapping was performed as shown in **Fig. 5.4**. TEM-EDX spectroscopy was used to examine further the chemical composition at the single-particle and few-particle cluster levels. Fe: Mn ratios were found for both the samples and a small cluster of particles, suggesting that the MIONPs have uniform chemical compositions. **Table 5.1** summarizes the typical chemical compositions of the MIONPs used in this study. It demonstrates that, with just slight deviations, manganese (II) and iron (III) compositions are essentially stoichiometric. The stoichiometry of the manganese and iron contents was evaluated by analyzing EDX spectra in various macroscopic sections of the samples [26].

Table 5.1 Stoichiometric percentage of the constituent elements of the $\text{Mn}_{0.75}\text{Fe}_{0.25}\text{Fe}_2\text{O}_4$ by EDX

Element	$\text{Mn}_{0.75}\text{Fe}_{0.25}\text{Fe}_2\text{O}_4$	
	Atomic %	Weight %
Mn	9.02	16.80
Fe	25.07	47.46
O	65.90	35.74

EDX was utilized to study the chemical composition of the synthesized MIONPs. The EDX spectra, presented in **Fig. 5.5**, verify the occurrence of all the desired elements in the MIONPs, and the corresponding analyzed results are depicted in the figure. The pure-phase nature of the MIONPs affirms that they align with the desired compositional ratios, indicating that the stoichiometric preparation has been accurately sustained throughout the synthesis process.

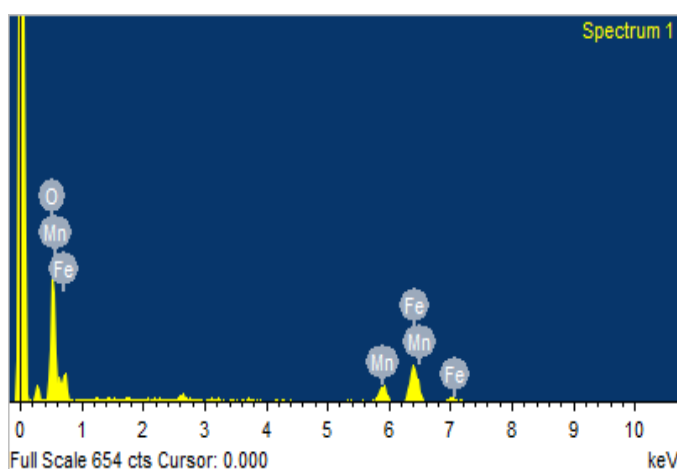


Figure 5.5 Stoichiometric % concentrations of the constituent elements of the $\text{Mn}_{0.75}\text{Fe}_{0.25}\text{Fe}_2\text{O}_4$ by EDX

5.6.3. Thermogravimetric Analysis

The thermal stability of the particles, surfactant decomposition temperature, and quantification of the surfactant ligands were determined using thermogravimetric analysis and differential scanning calorimetry. Thermogravimetric TGA curves and DTA of MIONPs and CS-MIONPs are shown in **Fig. 5.6-a, b**. Quantitative data further support the composition of the coating on the nanoparticle's surface. The amount of oxidation of MIONPs decreased significantly as TG-DTA was carried out in an N_2 environment. The TGA experiments were designed to study the thermal stability of MIONPs and CS-MIONPs over 50-800 °C. Depending on the reaction type, each thermogram had a different stage corresponding to a different weight loss procedure. For all MIONPs and CS-MIONPs samples, weight loss of 4% was noted below 110 °C due to evaporation of physically adsorbed H_2O molecules. The weight loss in the last phase of the TGA plot belongs to the phase formation of MIONPs [28]. As a result, the simultaneous oxidation and the decomposition of CS molecules cause an exothermic peak to accumulate at 200–500 °C. The decomposition of chitosan molecules causes the other peak to appear at around 160 °C. By analyzing the changes in the overall weight loss of CS-MIONPs samples, we can calculate the percentage of chitosan molecules bound to the surface of the nanoparticles. Based on this analysis, it is estimated that approximately 2% of the polymeric chitosan molecules are adsorbed onto the surface of the nanoparticles. Both samples achieve weight loss stability at temperatures above 600 °C. Magnetic particles comprised most of the remaining material after the CS completely broke down. The TGA curve showed how much CS was present in the CS-MIONPs [29].

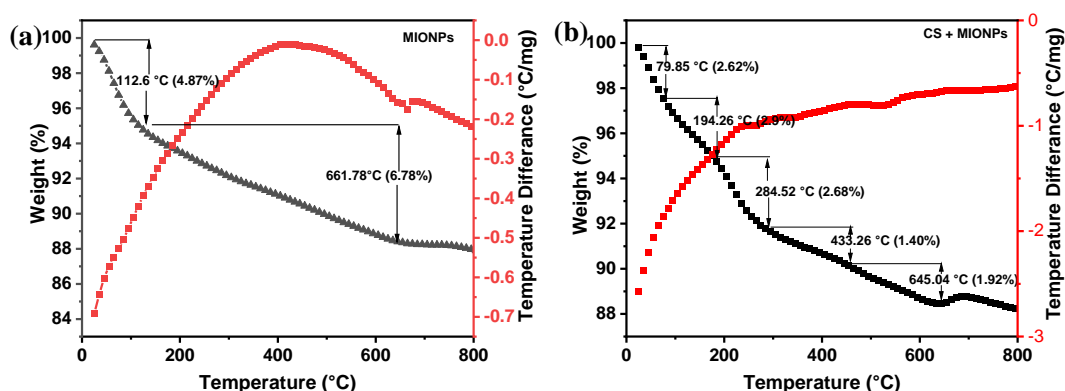


Figure 5.6 Thermogravimetric spectra of (a) uncoated MIONPs and (b) CS- MIONPs

5.6.4. Magnetic properties

Magnetic studies were performed at 300K with an applied field of ± 15 kOe using a Lake Shore 7400 Series VSM. Magnetization study is used to analyze how coating affects the magnetic characteristics of MIONPs and CS-MIONPs. The observed M_s value of bare MIONPs was 51.06 emu/g, which was low compared to the theoretical value of bulk MIONPs ($M_s = 84$ emu/g). Due to the finite size effect, M_s has been shown to diminish as MIONP particle sizes fall below 30 or 20 nm [30, 31]. **Fig. 5.7** shows the magnetization (M) versus field curves of the bare MIONPs and CS-MIONPs. In MIONPs and CS-MIONPs, coercivity and remanence are almost negligible based on VSM measurements (shown in the inset figure). As seen in the figure, under an applied field of 15 kOe, the magnetization of the sample CS-MIONPs is lower (41.60 emu/g) than that of the sample MIONPs (51.06 emu/g). The magnetization of a magnetic material is directly influenced by its weight. Consequently, the magnetization decreases as chitosan is applied as a coating. The addition of organic coating layers, such as chitosan, to magnetic materials results in an increase in the proportion of non-magnetic material, leading to a decrease in the overall magnetism of the material [25, 32].

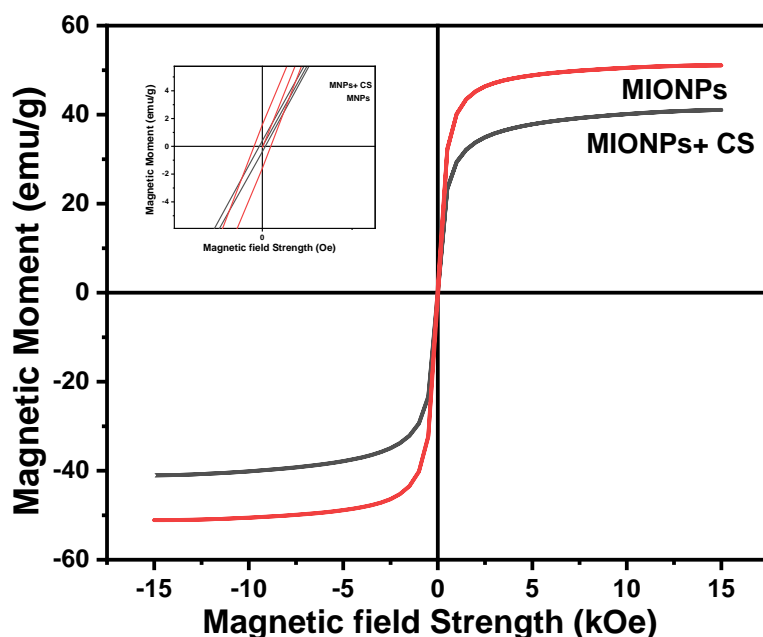


Figure 5.7 Magnetization (M) versus field curves of the bare MIONPs and CS-MIONPs

5.6.5. Stability Study

The colloidal stability was assessed by determining the Zeta potential using Malvern Instruments. As a result of DLS measurements, the hydrodynamic diameter (HDD) and zeta potential (ξ) have been determined. MIONP samples have an HDD of 362.1 nm, while CS-MIONPs have an HDD of 645.7 nm. In previous studies, MIONP content increased the hydrodynamic diameter of chitosan loaded with MIONPs. The dipole interface occurred from residual magnetic moments, and Van der Waals forces may be responsible for this. Together, they may increase particle size in magnetite nanoparticles [33].

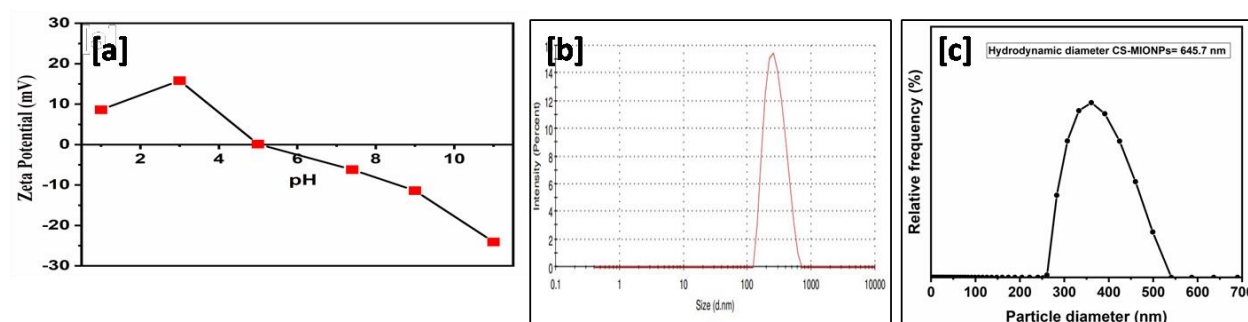


Figure 5.8 (a) Zeta potential studies at various pH of CS-MIONPs, (b, c) Hydrodynamic diameter of MIONPs and CS-MIONPs

The stability of CS-MIONPs was assessed by conducting zeta potential measurements at various conditions in the water. When the zeta potential of the nanoparticles is measured, it can be used to determine the electrostatic interaction of the nanoparticles. During nanoparticle application in biomedicine, the zeta potential measurement is a crucial factor. The zeta potentials of CS-MIONP is -7.0 mV, at pH 7.4 and the observed rise in positive zeta potential as the pH decreases is believed to be a result of the protonation of the free amino groups. This protonation process imparts a sufficient charge to ensure the stability of the coated nanoparticles. When the MIONPs are uniformly dispersed, the surface area of MIONPs is enhanced, which leads to improved heat transfer to the surrounding fluid. The HDD of MIONP nanoparticles is smaller than that of CS-MIONP nanoparticles at normal pH. CS-MIONPs show improved dispersion compared to undispersed MIONPs, enhancing their stability and uniformity. Despite this, CS-MIONPs maintain comparable energy transfer, making them a promising option for applications requiring both stability and performance.

5.6.6. Induction Heating Study

The inductive heat generation capability of MIONPs in the presence of an AC field was evaluated through SAR, which quantifies the power of heat generated by the MIONPs per gram. The calculation of SAR was performed using the formula in equations 2.11 and 2.12 (Section 2.2)

The ILP parameter, which is the most suitable model, relies on the frequency and magnitude of the magnetic field, allowing for easy comparison across multiple tests. In **Fig. 5.9 - c, d**, typically, ILP value ranges from 0.2 to 9.9 nHm²g⁻¹, while MIONPs with lower ILP values may still be sufficient to heat in magnetic hyperthermia [34]. A higher SAR value is desirable as it corresponds inversely to M_m . From the perspective of SAR measurement, a positive control denotes a reference sample possessing established and thoroughly defined electromagnetic absorption characteristics. Conversely, a negative control in SAR measurement signifies a reference sample or condition exhibiting minimal to negligible electromagnetic absorption. In this study, MIONPs are the positive control, while water is the negative control for SAR measurement. The total power loss (P) comprises three mechanisms, i.e., hysteresis losses, Neel relaxation losses, and Brownian relaxation losses [35, 36]. Under AC magnetic fields, the capability of the CS-MIONPs sample to produce heat

was evaluated. In this study, the magnetic heating experiments used a magnetic field for 10 minutes at a frequency of ≈ 277 kHz and an amplitude of $H_{max} = 13.3 - 26.7$ kAm⁻¹. The permissible limit for MHT is in the range of these parameters ($H_{max} \times f < 5 \times 10^9$ Am⁻¹s⁻¹) [37]. CS-MIONPs serve as heating mediators that translate the AMF into thermal energy, leading to an increase in temperature. The environmental viscosity and the characteristics of MNPs, including their hydrodynamic size, saturation magnetization, and anisotropy, determine how much heat is dissipated during relaxation loss [38]. **Fig. 5.9 - (a-e) and 5.10-(a-e)** illustrate the temporal temperature growth and SAR with their respective peak temperatures in an aqueous solution containing MIONPs and CS-MIONPs at dosages of 0.5, 1.0, 2.0, 5.0, and 10.0 mg/ml, under different AMF amplitudes ranging from 13.30 to 26.70 kAm⁻¹. It can be noted that the temperature difference increases with the AMF amplitude, as demonstrated in **Fig. 5.9 and 5.10** for varying heating times. A linear correlation was observed between AMF amplitude and the maximum temperature and SAR. With a calculated SAR, the highest temperature rise within 10 minutes was the corresponding value.

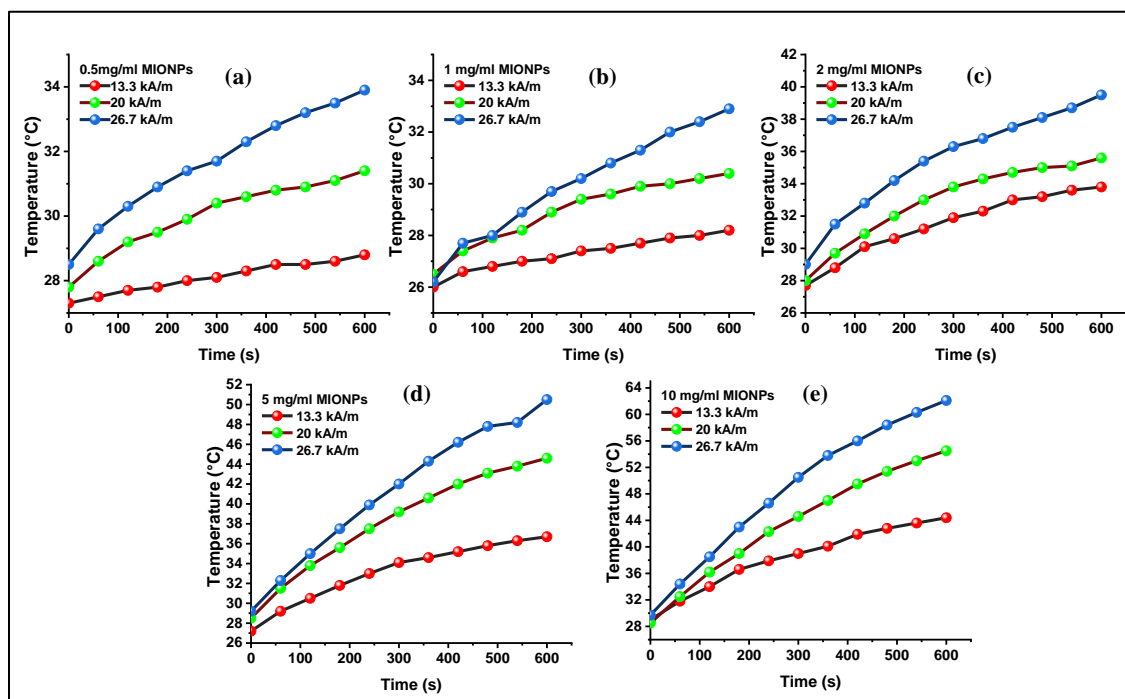


Figure 5.9 Temperature versus time curves for (a) 0.5 mg/mL, (b) 1 mg/mL, (c) 2 mg/mL, (d) 5 mg/mL and (e) 10 mg/mL of MIONPs at the applied field, 13.3 kA/m-26.7 kA/m

According to the thermal response curves, the maximum temperature rise and SAR values increased as the strength of AMF intensified [27]. When the MIONPs dosage rises from 0.5 to 10.0 mg/mL, the estimated SAR value for the CS-MIONPs initially increases from 69.76 to 181.5 W/g. As the dosage increased, the SAR value fell but remained higher than the values reported for MnFe_2O_4 MNPs made using other techniques [37]. The magnetic hyperthermia studies conducted on CS-MIONPs demonstrated the reliance of SAR on the intensity of the AMF. **Fig. 5.11-a and b** illustrate the increase in SAR performance for CS-MIONPs from 69.76 to 181.48 W/g and for bare nanoparticles from 33.11 to 153.56 W/g, as the field strength varied from 13.30 to 26.7 kA/m.

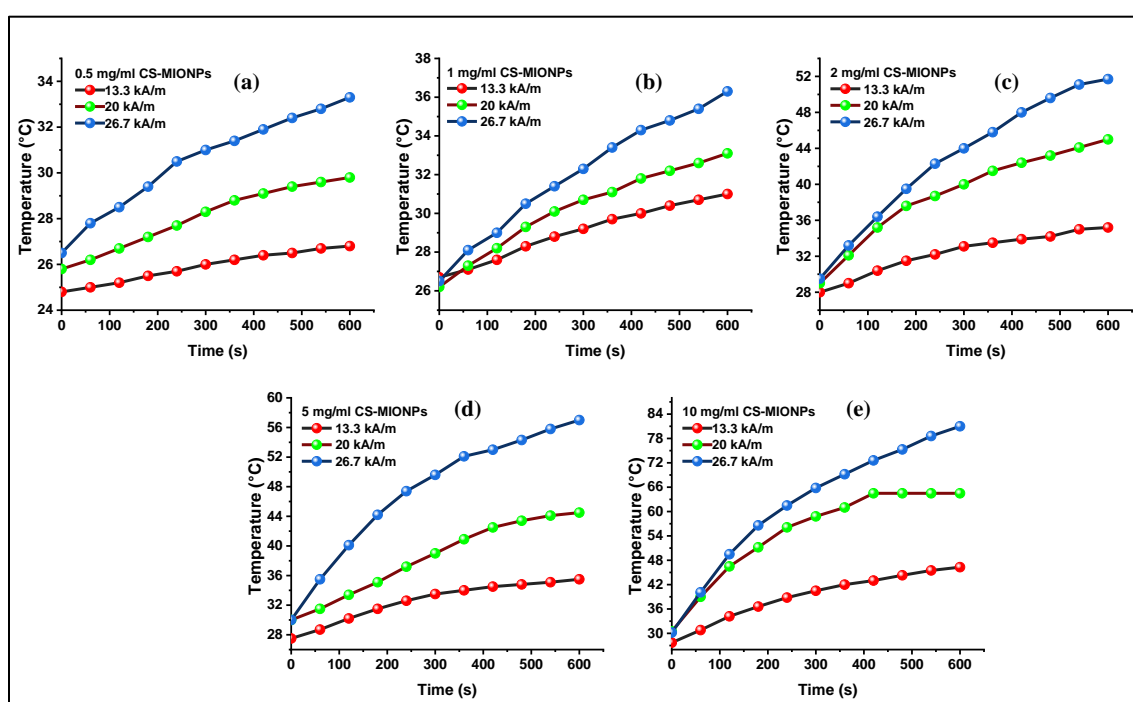


Figure 5.10 Temperature versus time curves for (a) 0.5 mg/mL, (b) 1 mg/mL, (c) 2 mg/mL, (d) 5 mg/mL and (e) 10 mg/mL of CS-MIONPs at the applied field, 13.3 kA/m - 26.7 kA/m

The correlation between SAR and the strength and intensity of the applied AC magnetic field was consistent with the findings of other suspensions following a similar procedure. It was observed that intrinsic factors like higher magnetization contributed to the increase in SAR but were not solely responsible for it. Additionally, the magneto-crystalline anisotropy energy (K_{eff}) of CS-MIONPs played a role in achieving high SAR, with particle magnetic moments influencing the K_{eff} function.

Consequently, the high magnetic moment in the current state amplified particle-particle interactions, increased exchange coupling energy, and enhanced the effectiveness of magnetic hyperthermia.

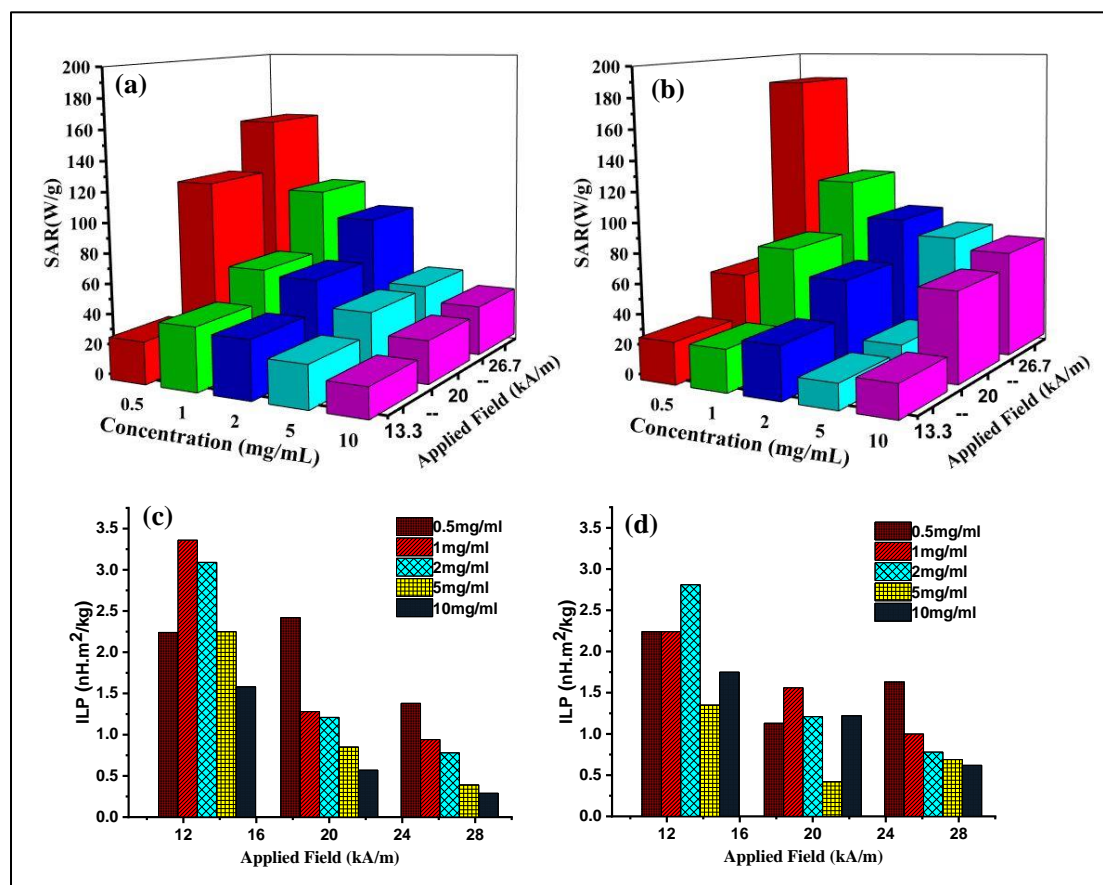


Figure 5.11 The SAR values of bare MIONPs (a) and CS-MIONPs (b), the ILP values of bare MIONPs, (c) and CS-MIONPs (d)

5.7. Conclusions

In this chapter, the successfully prepared CS-MIONPs nanofluid through co-precipitation and coating using ultrasonication has been achieved. The impact of coating on structural and morphological properties has been studied. XRD and FTIR analyses revealed the formation of a pure phase with and without CS-MIONPs. Thermogravimetric and FTIR analyses confirm the successful attachment of functional groups such as C-H on nanoparticle surface. However, chitosan-coated nanoparticles exhibit stable suspension dispersion. The stability is achieved through steric repulsion rather than electrostatic repulsion. The MIONPs and CS-coated MIONPs display soft ferrimagnetic properties with low coercivity and remanence, making them promising for biomedical use, especially in MHT. The induction heating

capability of these surface-modified nanoparticles demonstrated a notable SAR and temperature increase when subjected to an externally applied alternating magnetic field and at a magnetic field strength of 20 kA/m, the CS-coated nanoparticles achieved a maximum SAR of 181.48 W/g, compared to 153.46 W/g for the bare nanoparticles. Therefore, the MNPs synthesized using the alkaline precipitation method are suitable for MHT applications due to their smaller size, higher magnetization, and enhanced SAR values.

5.8 References

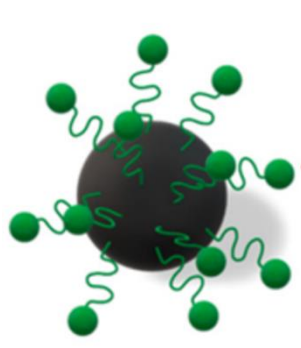
1. S. He, H. Zhang, Y. Liu, F. Sun, X. Yu, X. Li, L. Zhang, L. Wang, K. Mao, G. Wang, Y. Lin, *Small*, 14(29) (2018) 1800135-1800144.
2. K. Yang, Y. Liu, Y. Liu, Q. Zhang, C. Kong, C. Yi, Z. Zhou, Z. Wang, G. Zhang, Y. Zhang, N. Khashab, *JACS*, 140(13) (2018) 4666-4677.
3. D. Ortega, Q. Pankhurst, *Nanoscience*, 1 (2012) 60–88.
4. G. Lavorato, R. Das, Y. Xing, J. Robles, F. Litterst, E. Saitovitch, M. Phan, H. Srikanth, *ACS Appl. Nano Mater.*, 3(2) (2020) 1755-1765.
5. Y. Qu, J. Li, J. Ren, J. Leng, C. Lin, D. Shi, *ACS Appl. Mater. Interfaces.*, 6(19) (2014) 16867-16879.
6. S. Jeon, B. Park, S. Lim, H. Yoon, Y. Jeon, B. Kim, Y. Kim, K. Kim, *ACS Appl. Mater. Interfaces.*, 12(30) (2020) 33483-33491.
7. Y. Wang, *WJG, World J Gastroenterol*, 21(47) (2015) 13400-13402.
8. C. Sanson, O. Diou, J. Thevenot, E. Ibarboure, A. Soum, A. Brûlet, S. Miraux, E. Thiaudière, S. Tan, A. Brisson, V. Dupuis, *ACS Nano*, 5(2) (2011) 1122-1140.
9. A. Salunkhe, V. Khot, S. Patil, S. Tofail, J. Bauer, N. Thorat, *ACS Appl. Bio Mater.*, 3(4) (2020) 2305-2313.
10. S. Fernández, O. Odio, P. Crespo, E. Pérez, G. Salas, L. Gutiérrez, M. Morales, E. Reguera, *J. Phys. Chem. C*, 126(24) (2022) 10110-10128.
11. F. Paquin, J. Rivnay, A. Salleo, N. Stingelin, C. Silva, *J. Mater. Chem. C*, 3 (2015) 10715–10722.
12. Z. Li, S. Wang, Q. Sun, H. Zhao, H. Lei, M. Lan, Z. Cheng, X. Wang, S. Dou, G. Lu, *Adv. Healthc. Mater.*, 2 (2013) 958–964.
13. T. Zargar, A. Kermanpur, *Ceram Int.*, 43 (2017) 5794–5804.
14. A. Gupta, M. Gupta, *Biomaterials*, 26(13) (2005) 1565-1573.
15. C. Berry, S. Wells, S. Charles, A. Curtis, *Biomaterials*, 24 (2003) 4551–4557.
16. M. Mikhaylova, D. Kim, C. Berry, A. Zagorodni, M. Toprak, A. Curtis, M. Muhammed, *Chem. Mater.*, 16(12) (2004) 2344-2354.
17. C. Kalaiselvan, S. Laha, S. Somvanshi, T. Tabish, N. Thorat, N. Sahu, *Coord. Chem. Rev.*, 473 (2022) 214809-214841.
18. M. Vassallo, D. Martella, G. Barrera, F. Celegato, M. Coisson, R. Ferrero, E. Olivetti, A. Troia, H. Sozeri, C. Parmeggiani, D. Wiersma, *ACS omega*, 8(2) (2023) 2143-2154.

19. G. Sanità, B. Carrese, A. Lamberti, Sanità G, Carrese B, Lamberti A. *Front. Mol. biosci.*, 7 (2020) 587012-587032.
20. R. Thiruppathi, S. Mishra, M. Ganapathy, P. Padmanabhan, B. Gulyás, *Adv. Sci.*, 4(3) (2017) 1600279-1600293.
21. K. Kobayashi, J. Wei, R. Iida, K. Ijio, K. Niikura, *Polym. J.*, 46(8) (2014) 460-468.
22. W. Wu, C. Jiang, V. Roy, *Nanoscale*, 8 (2016) 19421–19474.
23. H. Yamamoto, Y. Kuno, S. Sugimoto, H. Takeuchi, Y. Kawashima, *J Control Release*, 102 (2005) 373–381.
24. S. Phalake, M. Lad, K. Kadam, S. Tofail, N. Thorat, V. Khot, *ACS Omega*, 7 (2022) 44187–44198.
25. D. Bharathi, R. Ranjith Kumar, S. Vasantharaj, B. Chandrashekhar, V. Bhuvaneshwari, *Int. J. Biol. Macromol.*, 132 (2019) 880–887.
26. B. Sanz, R. Cabreira-Gomes, T. Torres, D. Valdés, E. Lima, E. Biasi, R. Zysler, M. Ibarra, G. Goya, *ACS Appl. Nano Mater.*, 3(9) (2020) 8719-8731.
27. W. Mdallalose, S. Mokhosi, S. Dlamini, T. Moyo, M. Singh, *AIP Adv.*, 8 (2018) 0–6.
28. A. Beeran, S. Nazeer, F. Fernandez, K. Muvvala, W. Wunderlich, S. Anil, S. Vellappally, M. Rao, A. John, R. Jayasree, P. Varma, *PCCP*, 17(6) (2015) 4609-4619.
29. P. Hugounenq, M. Levy, D. Alloyeau, L. Lartigue, E. Dubois, V. Cabuil, C. Ricolleau, S. Roux, C. Wilhelm, F. Gazeau, R. Bazzi, *J. Phys. Chem. C*, 116(29) (2012) 15702-15712.
30. P. Shete, R. Patil, N. Thorat, A. Prasad, R. Ningthoujam, S. Ghosh, S. Pawar, *Appl. Surf. Sci.*, 288 (2014) 149-57.
31. M. Tsai, C. Hsu, C. Yeh, Y. Hsiao, C. Su, L. Wang, *ACS Appl. Mater. Interfaces.*, 10 (2) (2018) 1508-1519.
32. A. Konwar, S. Kalita, J. Kotoky, D. Chowdhury, *ACS Appl. Mater. Interfaces.*, 8 (2016) 20625–20634.
33. V. Zamora-Mora, M. Fernández-Gutiérrez, A. González-Gómez, B. Sanz, J. Román, G. Goya, R. Hernández, C. Mijangos, *Carbohydr. Polym.*, 157 (2017) 361-370.
34. X. Liu, Y. Zhang, Y. Wang, W. Zhu, G. Li, X. Ma, Y. Zhang, S. Chen, S. Tiwari,

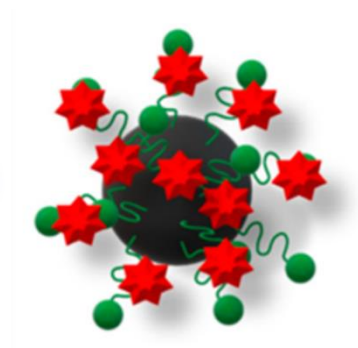
- K. Shi, S. Zhang, *Theranostics*, 10(8) (2020) 3793–3815.
35. I. Castellanos-Rubio, I. Rodrigo, A. Olazagoitia-Garmendia, O. Arriortua, I. Muro, J. Garitaonandia, J. Bilbao, M. Fdez-Gubieda, F. Plazaola, I. Orue, A. Castellanos-Rubio, *ACS Appl. Mater. Interfaces.*, 12(25) (2020) 27917-27929.
36. A. Doaga, A. Cojocariu, W. Amin, F. Heib, P. Bender, R. Hempelmann, O. Caltun, *Mater. Chem. Phys.*, 143(1) (2013) 305-310.
37. P. Nam, N. Phuc, D. Manh, D. Tung, V. Nguyen, N. Nam, P. Son, T. Bach, P. Phong, *Physica E Low Dimens. Syst. Nanostruct.*, 134 (2021) 114862-114874.
38. Y. Oh, N. Lee, H. Kang, J. Oh, *Nanotechnology*, 27(11) (2016) 115101-115122.

CHAPTER-6

Surface Functionalization of Optimized Manganese Iron Oxide Nanoparticles by using m-PEG for Hyperthermia Application



MIONCs



M-PEG MIONCs

6.1. Introduction

Many synthetic functional MNPs have been synthesized and are currently used in the biomedical field, most notably for cancer treatment. The recently emerged method based on nanotechnology is projected in oncological fields to treat cancer tumors: magneto-thermotherapy better effectively [1]. Meanwhile, a new aspect of magneto-thermotherapy has emerged with the development of MNPs-based MHT [2]. Ferrite nanoparticles, especially manganese iron oxide, exhibit characteristics such as high magnetic moments, excellent chemical stability, high saturation magnetization, minimal coercivity, exceptional biocompatibility, and a surface suitable for ligand functionalization and bioconjugation. $\text{Mn}_x\text{Fe}_{3-x}\text{O}_4$ and other ferrite MNPs have been synthesized using different methods of co-precipitation, solvothermal, and thermal decomposition. The co-precipitation method has limitations such as low crystallinity, resulting in poor heating efficiency of the MNPs, and the need for additional size-sorting steps to achieve better control over size distribution and shape [3, 4].

Anisotropy is a vital material trait offering direction-dependent properties like ferroelectricity and ferromagnetism, influenced by atomic structure, shape, and surface, with shape and surface anisotropy adjustable via controlled synthesis [5]. MNPs performance strongly depends on their structure, average size, and magnetic anisotropy. Additionally, ensembles provide a distinct method for tuning the magnetic response by altering the strength of dipolar interactions between particles [6]. Two fundamental approaches can be used to adjust particle anisotropy and enhance heating efficiency: (1) modifying crystalline anisotropy by incorporating a small amount of Mn^{2+} ions into the inverse spinel structure and (2) altering the shape of MNPs to introduce an additional source of anisotropy. Adding Mn ions results in manganese-doped ferrite nanoparticles with higher magnetization, increasing SAR values [7].

A key challenge in MHT is the low heating power of current MNPs, requiring large doses. Improving heating efficiency depends on their structure and magnetism, with shape and size adjustments boosting performance. Cubic- and flower-shaped iron oxide MNPs have shown superior results to spherical ones [6-9]. Cubic-shaped spinel oxide nanocrystals have demonstrated exceptional properties compared to spherical counterparts, particularly in fields such as biomedicine [10]. Manganese and zinc ferrite MNPs have been explored due to their strong magnetization and resistance to oxidation, resulting in high SAR. Although materials with high M_s can enhance

SAR, they often encounter stability and toxicity concerns. Adjusting anisotropy, like shape anisotropy in nanocubes or employing core/shell structures, can improve SAR, but these approaches typically require field conditions unsuitable for clinical applications [11]. Iron oxide nanoparticles require surface modification with nontoxic, biocompatible stabilizers for practical biomedical use to ensure stability in physiological environments. Synthetic polymers offer an alternative to natural polymers, providing advantages such as controllable chemical structure, molecular weight, functional groups, and tailored surfaces, making them effective stabilizers for iron oxide nanoparticles [12-14].

Thermal decomposition of metalorganic precursors typically occurs in a heated organic solvent mixed with surfactants (such as alkylamines and carboxylic acids) that regulate particle growth, prevent aggregation and act as a reducing agent. While this method may not be as straightforward as other wet chemical approaches, it is highly effective for producing monodisperse magnetic nanoparticles with precise control over their size and shape [15]. A significant drawback of the thermal decomposition method is that, although it yields nanoparticles with precise shape and size, they are hydrophobic and not directly applicable for biomedical uses such as hyperthermia. Surface functionalization is necessary to render them hydrophilic. It may negatively impact their morphological and magnetic properties, often leading to reduced saturation magnetization, changes in surface characteristics, or alterations in structural properties.

Several methods have been developed to transfer MNPs from hydrophobic to hydrophilic environments. One approach involves the bilayer technique, where various surfactants, polymers, or dendrimers form a bilayer through strong Van der Waals interactions. Another method utilizes ligand exchange reactions, introducing functional organic ligands into the organic layer during MNP synthesis and modifying them in subsequent reactions, facilitating the transfer and stabilization of MNPs in water. Ligands such as chitosan, alginate, polyethylene glycol (PEG), polyvinyl alcohol (PVA), polydopamine (PDA), polysaccharides, polyethyleneimine, polyvinylpyrrolidone (PVP), polyacid polyetherimide, and polyamidoamine (PAMAM) are commonly used as protective layers on iron oxide nanoparticles to enhance biocompatibility, solubility, and hydrophilicity [16]. Amphiphilic block copolymers are among the most effective biodegradable polymers for improving

cancer cells' uptake of superparamagnetic iron oxide nanoparticles. One hydrophilic block, methoxy-polyethylene glycol (m-PEG), is widely utilized in pharmaceutical and biomedical applications due to its excellent physicochemical and biological characteristics, including hydrophilicity, solubility, non-toxicity, ease of chemical modification, and lack of antigenicity and immunogenicity [17]. This chapter provides a practical method for synthesizing well-defined, high magnetic moments of MNPs and modifying the surface with m-PEG.

6.2 Need for Functionalization

Surface modification of MNPs is essential for their use in biomedical applications, as their surface properties, like hydrophobicity and hydrophilicity, vary with the synthesis method. The interactions of MNPs are influenced by their environment and surface molecules, leading to clustering due to Van der Waals forces and magnetic attraction. MNPs are also reactive in acidic conditions, resulting in leaching, while their small size increases surface energy, promoting aggregation. Uncoated MNPs can oxidize quickly, which diminishes their magnetic properties. Even when stabilizing agents are present, functionalization is vital to improve stability and targeting, aiming for hydrophilic MNPs that are less than 150 nm in size for practical application. Appropriate functionalization helps prevent agglomeration and enhances interactions, while coatings can affect cellular uptake and circulation time, reducing the risk of toxicity [18]. The main objectives of modifying the surfaces of MNPs are to prevent aggregation, enhance surface catalytic activity, improve physicochemical and mechanical properties, and boost solubility and biocompatibility [19].

Typically, the initial stage of surface modification involves utilizing homo- or hetero-bifunctional crosslinkers to introduce organic functional groups (such as R-NH₂ or R-COOH) that facilitate the binding of biological molecules [20]. The surface modification of nanoparticles influences various characteristics, including size, surface chemistry, hydrophilicity, hydrophobicity, and charge, which can consequently impact the solubility, biocompatibility, biodistribution, and clearance of the resulting nanoprobes. When MNPs are coated with small molecules or polymers like dextran, starch, citrate, or polyethylene glycol (PEG), the resulting nanoprobes demonstrate improved biodistribution, extended circulation time, and enhanced uptake. Hydrophilic polymers such as PEG can be conjugated to MNPs to stabilize

steric, preventing protein absorption and ensuring prolonged blood circulation for *in vivo* applications. The modified surface chemistry of MNPs can significantly influence their pharmacokinetic behavior *in vivo*, with PEG linking enhancing hydrophilicity, stability, and reducing cytotoxicity [21]. Coating nanoparticles with small molecules effectively modifies their surface charge, hydrophobicity, and stability, optimizing cellular interactions and uptake. Both small and large biomolecules can target nanoparticles to specific cells or tissues, aiding the development of safer cancer therapies and imaging agents. Polymers are also commonly used as biocompatible coatings to improve bioavailability and facilitate sustained drug release [22].

6.3 Strategies and Choice of Polymer

In many biomedical applications, polymer coatings on MNPs are favored over simple functionalization with small organic compounds and surfactants because they enhance repulsive forces, counteracting the magnetic and Van der Waals attractive forces among MNPs. Additionally, polymer-engineered iron oxide nanoparticles demonstrate improved blood circulation time, stability, and biocompatibility. Numerous studies have indicated that by selecting appropriate passivating and activating polymers and adjusting the related reaction parameters, magnetic iron oxide/polymer composite MNPs with specific desired properties can be successfully produced [23].

PEG is a synthetic polymer widely used in biomedical applications because of its biocompatibility and hydrophilic properties. Numerous commercially available PEGs come in different molecular weights and functional groups (e.g., COOH, SH), allowing for customization of nanoparticle surfaces to enhance their characteristics. Coating nanoparticles with PEG is commonly employed to improve their pharmacokinetics and bioavailability [24]. PEGs are generally recognized as safe (GRAS) and have been approved by the FDA for use in the food industry and medical and biological uses [25]. Laha et al. [26] used monodispersed PEG surfactant to substitute oleic acid to produce iron oxide nanoparticles in thermal decomposition. The optimal thickness of m-PEG resulted in enhanced performance in hyperthermia applications.

6.4. Surface Functionalization of Manganese Iron Oxide NPs with m-PEG

Thermal decomposition is one of the most straightforward processes for synthesizing MNPs in organic solutions. Various synthesis factors can be changed, including concentration, pH, temperature, and particle size. The particle size distribution, shapes, and formulations of MNPs affect their SAR; when subjected to an AMF, this may result in insufficient heat generation to effectively eliminate the targeted tumor cells [27]. A range of surfactants is used for a coating to maintain the colloidal properties and biocompatibility of MIONPs and prevent aggregation caused by magnetic dipole-dipole interactions. These surfactants encompass both polymeric and non-polymeric substances, including lipids and proteins. MIONPs are coated with different polymers, such as chitosan, oleic acid, starch, pullulan, dextran, and others, to render them suitable for *in vivo* applications. m-PEG is widely used in pharmaceutical and biomedical fields because of its biocompatibility and low toxicity. Surfaces modified with m-PEG are shown to be nonimmunogenic, non-antigenic, and resistant to protein adsorption. Studies have demonstrated that attaching m-PEG to nanoparticles enhances their uptake in cancer cells compared to unmodified nanoparticles [28].

6.5 Experimental details

6.5.1 Method

Synthesis by Thermal Decomposition Method

The synthesis of MIONCs has already been discussed in the previous chapter (Chapter 4 Section 4.4). This section provides a practical approach for creating well-defined, high magnetic moments of MIONCs and surfaces modified with m-PEG.

6.5.2 Surface Modification of MNPs with m-PEG:

To conjugate m-PEG, nanoparticles were combined with m-PEG (32 µg/mL, 1:1 by weight) and stirred at 25 °C for 24 hours. Finally, the NPs were magnetically separated and thoroughly washed with deionized (DI) water before further use [29].

6.5.3 Structural, Magnetic and Magnetic Hyperthermia Characterization

The details of material characterization and magnetic hyperthermia experiments are per Chapter 5 (Section 5.5.3).

6.6. Results and Discussion

6.6.1. Structural Analysis

The powder XRD patterns were used to identify the structural investigations of the MIONPs, FTIR confirmed the cubic spinel phase, and the surface ligands were examined.

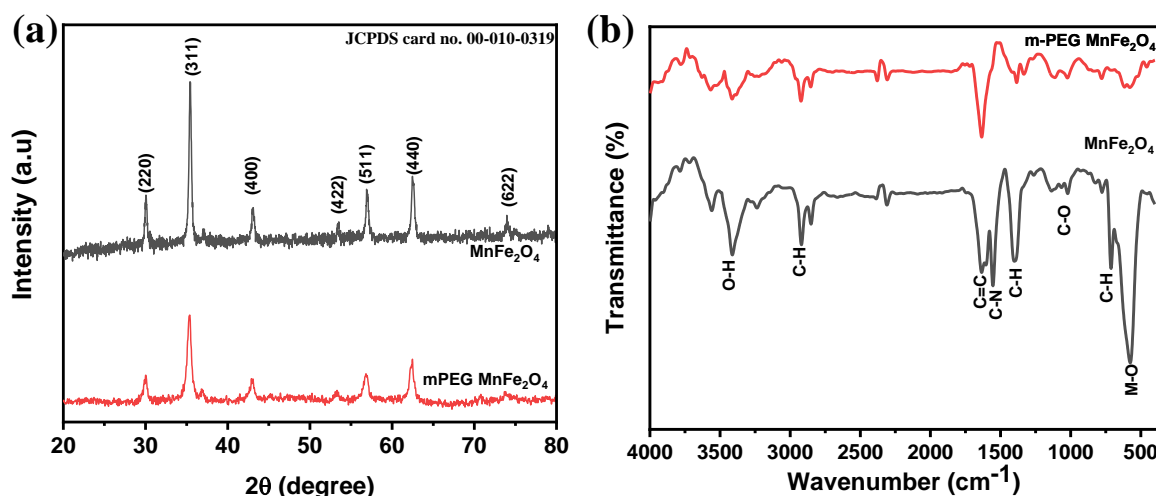


Figure 6.1 (a) XRD patterns of MIONCs NCs, (b) FTIR spectra of MIONCs and m-PEG MIONCs

Fig. 6.1 a shows the XRD patterns of MIONCs. The characteristic broad diffraction peaks confirmed crystallinity of NPs and their reflection planes (220), (311), (400), (422), (511), (440), (622) indicates presence of all the diffraction peaks obtained are well-matched with JCPDS card no. 00-010-0319 for MIONCs and spinel cubic structure is confirmed (space group Fd3m). The crystallite size of synthesized nanoparticles was determined using Scherrer's formula, and the average crystallite size of MIONCs was found to be 18.8 nm. **Fig. 6.1 b** shows the FTIR spectra of the as-synthesized MIONCs. The strong absorption bands at 451 and 576 cm⁻¹ are associated with the vibration of Fe–O bonds. The absorption band at 781 cm⁻¹ arises from the C–H stretching vibration. The bands at 1386 cm⁻¹ and 1632 cm⁻¹ occurred from the C–H and C=O bond vibrations in surfactant molecules. Absorption bands at 2920 cm⁻¹ and 3416 cm⁻¹ are attributed to the C–H and O–H band vibration [30].

The m-PEG layer on the MNP surface was characterized after coating m-PEG, as shown in **Fig. 6.1 b**. The absorption band at about 458 cm⁻¹ and 571 cm⁻¹ is due to Fe–O stretching vibration for the MIONCs. The intensity of this peak is reduced compared to synthesized MIONCs due to m-PEG coating on the MIONCs,

confirming the polymer m-PEG grafted on the surface of MIONCs [31]. In **Fig. 6.1 b**, the peaks at wavenumbers 775 cm^{-1} and 1107 cm^{-1} , associated with C-H and C-O groups, indicate the formation of carboxylic acid groups on the MIONCs. The peak at 1019 cm^{-1} likely arises from the C-O stretching vibration of ether groups, while the peaks at 947 cm^{-1} are attributed to C-H rocking in the m-PEG chain. Additionally, the emergence of two new bands around 2925 cm^{-1} and 2856 cm^{-1} , corresponding to C-H stretching vibrations, suggests the presence of the m-PEG chain in the structure of the modified MIONCs. The strong absorption bands at 1637.40 cm^{-1} are associated with the vibration of C=O stretching vibration and this confirms the polymer m-PEG grafted on the surface of MIONCs [32].

6.6.2. Morphological Analysis

The synthesized MIONCs show uniform size distribution as measured by TEM, and morphologies of the as-synthesized magnetic nanoparticles are shown in **Fig. 6.2 - a and b**.

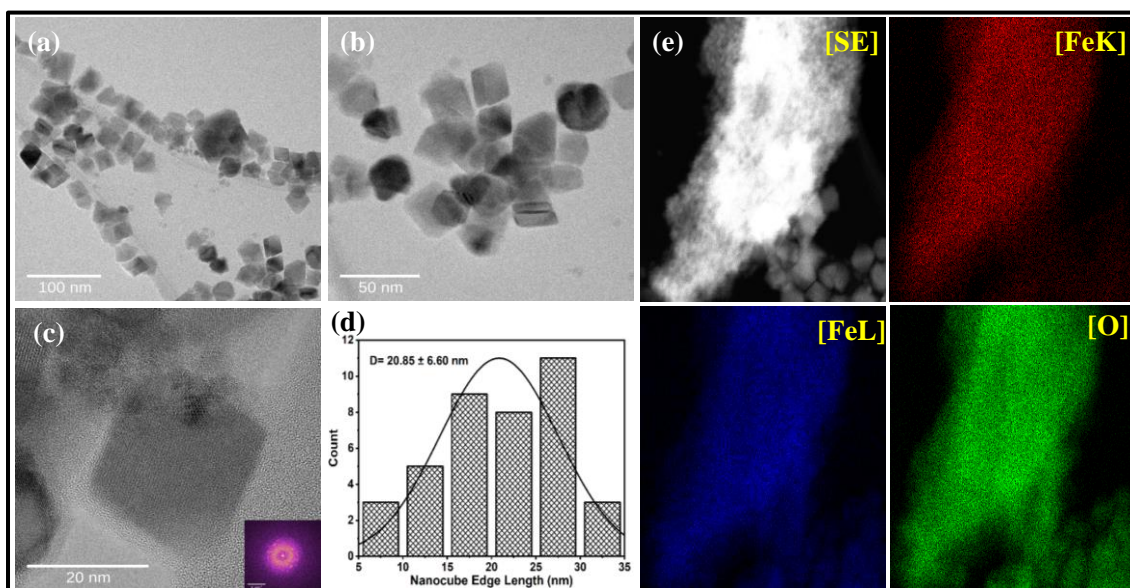


Figure 6.2 (a, b) TEM, (c) HRTEM image, (d) Histogram (e) TEM-EDX chemical mapping of the MIONCs

The MIONCs have a cubic shape and display a narrow size distribution that fits well with a log-normal distribution function, yielding a mean value of $20.85 \pm 6.60\text{ nm}$. The particle size distribution was determined by generating a histogram of diameters from the TEM images using ImageJ software (**See Fig. 6.2 d**). TEM images also reveal variations in the aggregation state of the samples. The crystalline structure

and facets of the MIONC nanocubes were further analyzed using high-resolution TEM (HRTEM) images, as shown in (See Fig. 6.2 c). These images indicate that the nanocubes are of high quality and single-crystalline, with lattice fringes measuring 0.23 nm, corresponding to the (311) lattice planes of MIONCs [33]. For a better understand of both sample studies of the structure architecture, TEM-EDX chemical mapping was performed, as shown in (Fig. 6.2 e).

6.6.3. Thermogravimetric Analysis

Moreover, TGA confirmed the presence of the m-PEG layer on the MIONCs surface. The thermogravimetric analysis of MIONCs and m-PEG MIONCs samples are shown in Fig. 6.3 a, b. The initial weight loss observed around 100 °C is attributed to the removal of physically adsorbed water. The significant decomposition occurs between 200 and 800 °C. The second weight-loss phase begins at approximately 250 °C and is linked to the release of organic groups bonded to the particle surface. For m-PEG-MIONCs, a mass loss of about 13.43% was noted, corresponding to the degradation of m-PEG. Less weight loss occurred at temperatures above 800 °C (Fig. 6.3 (a, b)). The observed weight loss indicates that more coating agents are absorbed on the surface of the MIONCs treated with m-PEG.

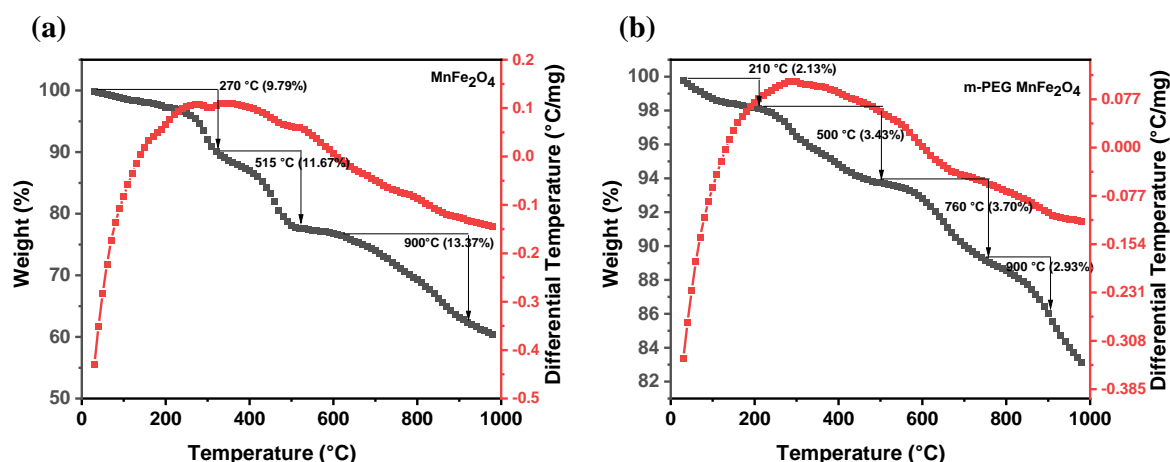


Figure 6.3 Thermogravimetric spectra of (a) MIONCs and (b) m-PEG MIONCs

The application of m-PEG in the biomedical field is influenced by its thermal properties, which are determined by its molecular structure. Therefore, DTA was employed to investigate further how heat affects the molecular structure of the copolymer. Degradation occurs due to depolymerization, exchange esterification, or oxidative processes [34].

6.6.4. Magnetic Properties

The room temperature hysteresis magnetization of dried samples was measured using SQUID with an applied magnetic field of ± 30 KOe. Both samples displayed SPM behavior, indicating that thermal energy surpasses the anisotropy energy barrier of individual particles, and the magnetization of the nanoparticle assembly is zero when there is no external magnetic field. According to theory of magnetism for exhibiting superparamagnetic behavior, the required minimum nanoparticle volume is $V = \frac{25k_B T}{K}$, where, K is the anisotropic constant, T is the room temperature and k_B is the Boltzmann constant. The magnetic behavior of nanoparticles with respect to temperature is analyzed to confirm SPM and examine the impact of temperature on magnetic properties. A widely used method for investigating superparamagnetic relaxation is FC and ZFC magnetization, which measures magnetization in a weak applied field as the temperature increases, after cooling the sample either with or without a weak magnetic field. **Fig. 6.4 b, d** presents the temperature-dependent ZFC and FC curves for the as-prepared samples.

The Temperature dependence of the magnetization at 10 K and 300 K was obtained in both samples and presented in **Fig. 6.4 a and c**. The properties such as hysteresis loops, saturation magnetization (M_s), coercive field (H_c), reduced remanent magnetization (M_r/M_s), magnetic moment (η_B), effective magnetic anisotropy constant (K_{eff}) at 300 and 10 K are summarized in **Table 6.1**. The effective magnetic anisotropy constant $K_{eff} \approx \frac{\mu_0 H_c M_s}{0.96}$ was obtained by using the low-temperature H_c and M_s Values [35]. To better understand the structural aspects and the magnetic properties of MIONCs, magnetic characterizations performed additional accurate measurements. The varying temperature has carried out magnetization (M-T) measurements after ZFC and FC, as shown in **Fig. 6.4 b, d**. The hysteresis loop profiles of all MIONCs exhibit negligible coercivity (H_c) and remnant magnetization (M_r). However, the M_s values of as-synthesized MIONCs (82.58 emu/g) and m-PEG MIONCs (79.93 emu/g) which was low compared to the theoretical value of bulk MIONCs. From M_s results, its lower value, compared to that of bulk magnetite, can be ascribed to the effects of canting or disorder of the magnetic spins at the surface of the MIONCs; the electron exchange between coating and surface atoms could also quench the magnetic moment [40].

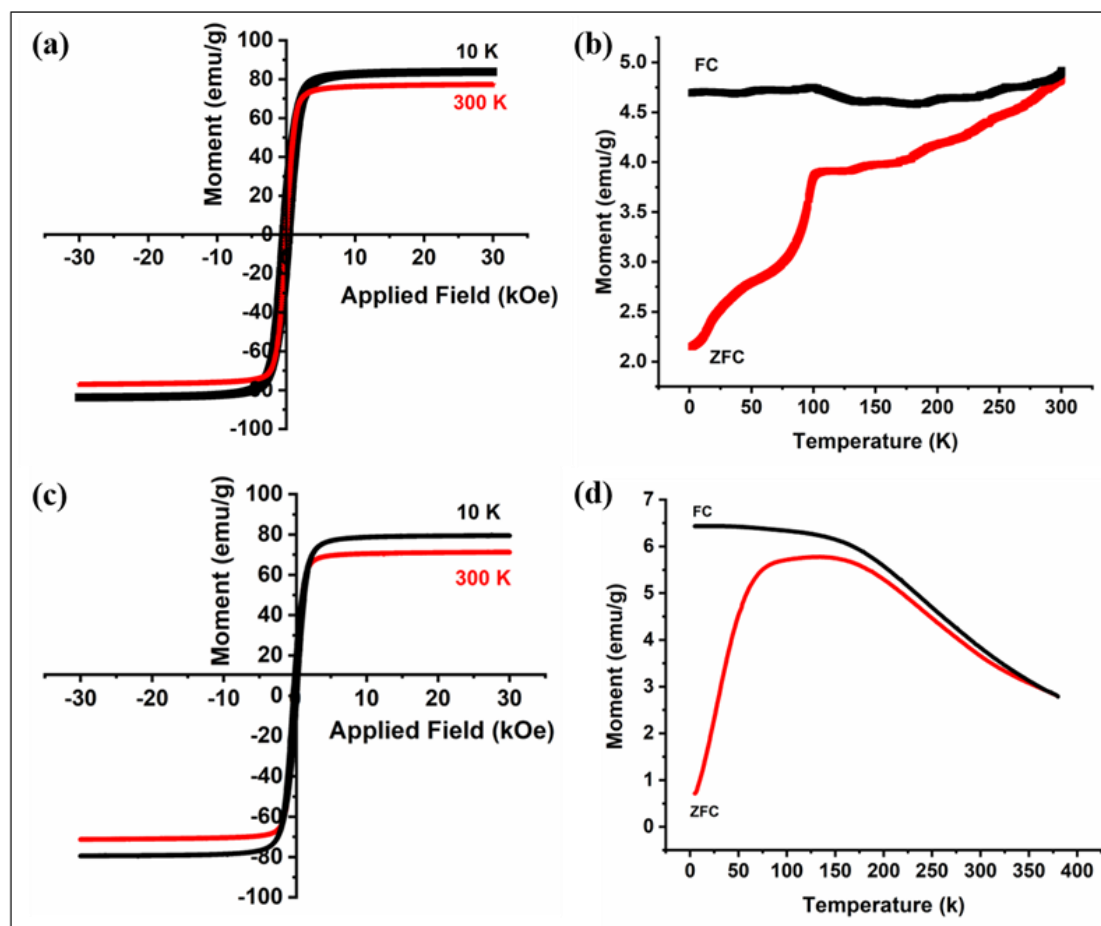


Figure 6.4 Magnetization vs applied magnetic field curves of (a) MIONCs and (c) m-PEG MIONCs samples at 300 K and 10 K (b, d) Temperature dependence of the magnetization (ZFC and FC) over the temperature range 0–400 K for (b) MIONCs and (d) m-PEG MIONCs.

The FC and ZFC curves in **Fig. 6.4 b, d** reveal irreversibility, indicative of the blocking process in superparamagnetic MIONCs. Above the blocking temperature (τ_B), magnetization decreases as temperature rises. It was also observed that all samples show a lower τ_B , which increases with particle size. The divergence of the ZFC and FC magnetization curves near τ_B , as estimated from the ZFC curve, suggests a narrow size and shape distribution. The increase in τ_B with particle size is due to insufficient spacing between particles to reduce dipolar interactions. According to the Neel Model, the transition from the blocked to superparamagnetic state occurs at different temperatures based on particle size. In this study, the ZFC and FC curves converge around τ_B , indicating minimal magnetic aggregation, consistent with the

individual particle coating and pseudoself-assembly. The ZFC curve aligns with the FC curve above 150 K, which is characteristic of superparamagnetism [36, 37].

Table 6.1. Summary of Saturation Magnetization (M_s), Coercivity (H_c), Reduced Remanence (M_r/M_s), Magnetic Moment (η_B), effective magnetic anisotropy constant (K_{eff}) obtained from the Hysteresis Loops at 300 and 10 K

Sample	M_s at 300K (emu/g)	M_s at 10K (emu/g)	H_c at 300K (emu/g)	H_c at 10K (emu/g)	M_r/M_s at (emu/g)	Magnetic Moment (η_B)	K_{eff} at 300 K (kJ/m ³)	K_{eff} at 10K (kJ/m ³)
MnFe ₂ O ₄	78.72	82.58	0.05	0.22	0.0396	3.26	9.4	9.6
m-PEG MnFe ₂ O ₄	72.08	79.93	0.02	0.92	0.0529	2.98	5.1	2.4

Consequently, a temperature scan of the magnetization at a constant field shows a sharp increase around 102 K, as the magnetic anisotropy becomes significantly larger at lower temperatures. This step-like behavior serves as a distinct fingerprint of magnetite, which disappears when the stoichiometry deviates from that of pure magnetite. As seen in **Fig. 6.4 a, c**, under an applied field, the magnetization of the sample m-PEG MIONCs is lower than that of the sample MIONCs. The reduction in magnetization after m-PEG fictionalization may be attributed to the presence of a non-magnetic polymer layer on the surface of nanoparticles, which reduces the particles-particle interaction and lowers the exchange coupling energy, reducing the magnetization [38]. The magnetization of a magnetic material is directly influenced by its weight.

Consequently, the magnetization decreases as m-PEG is applied as a coating. Introducing organic coating layers, such as m-PEG, onto magnetic materials leads to a higher proportion of non-magnetic components, decreasing the material's overall magnetic properties. **Table 6.1** presents the magnetic properties of the MIONCs and m-PEG MIONCs.

6.6.5. Stability Study

Finally, the stability of MIONCs in solution was analyzed, which is crucial for their prospective biomedical applications. The hydrodynamic size distributions, characterized by DLS, are illustrated in the figure, and the mean hydrodynamic size,

along with the ζ potential values for each sample. DLS and ζ potential measurements were conducted on uncoated and coated MIONCs to examine potential alterations in sample dispersion due to the surface coating process. DLS enables the characterization of the hydrodynamic behavior of MIONCs, specifically the size of the aggregates they form; however, this technique does not differentiate between the inorganic and organic components of the coating. The observed average hydrodynamic diameter of the MIONCs and m-PEG MIONCs is 314 ± 19 nm and 553 ± 10 nm, respectively. DLS cannot differentiate between inorganic and organic materials, measuring only the overall particle size. Consequently, this hydrodynamic size may vary considerably from the actual physical size determined by methods like XRD or TEM.

Even without an external magnetic field, magnetic dipole-dipole interactions between particles can lead to their aggregation [39]. As a result, the hydrodynamic size distributions are larger than those measured by TEM. The zeta potential for MIONCs in water at physiological pH was recorded at -14.16 mV, higher than the -9.4 mV observed for m-PEG-coated MIONCs. The lower zeta potential of uncoated MIONCs may be attributed to their hydrophobicity and the aggregation of uncoated particles, which negatively impacts stability in the dispersion medium. Coating the MIONCs with m-PEG enhances electrostatic repulsion between the particles, leading to steric stabilization [40].

6.6.6. Induction Heating Study

The heating power of MNPs is quantified in terms of SAR, a crucial parameter in magnetic fluid hyperthermia that measures the fluid's ability to convert magnetic energy into heat [41-43]. MNPs dissipate heat in AC magnetic fields through SAR (W/g) and ILP, which are calculated using the formula in equations 2.11 and 2.12 (Section 2.2). The ILP parameter, which is the most suitable model, relies on the frequency and magnitude of the magnetic field, allowing for easy comparison across multiple tests. In Fig. 6.6 -c, d, typically, ILP value ranges from 0.7 to 3.5 $\text{nHm}^2\text{g}^{-1}$, while MIONPs with lower ILP values may still be sufficient to heat in magnetic hyperthermia [44]. The heating curves exhibit significant variations between samples, demonstrating that the heating efficiency of these MIONCs is highly influenced by their shape, size, and the strength of the applied AC field. Notably, with an initial body temperature of 37 °C, either the therapeutic window ($\Delta T = 3-7$ °C) or

the thermal ablation zone ($\Delta T \geq 13$ °C) for cancer treatment can be achieved in under 5 minutes by adjusting the size of the MNPs and the applied field strength. The magnetic heating properties of the samples were tested at room temperature by exposing MIONCs solution in water to an alternating magnetic field of different amplitudes ($H_{\max} = 13.3, 20, \text{ and } 26.7$ kA/m) and frequencies ($f_{AC} \approx 277$ kHz) for at least 600 s. The solution concentrations were maintained at 1, 2, and 5 mg/mL. Measurements carried out in water aimed solely to evaluate how the magnetic and structural characteristics of the synthesized samples affected their heating performance. **Fig. 6.5 (a)** displays the temperature kinetic curves recorded after applying an alternating magnetic field to both samples dispersed in water at concentrations of 1, 2, and 5 mg/mL.

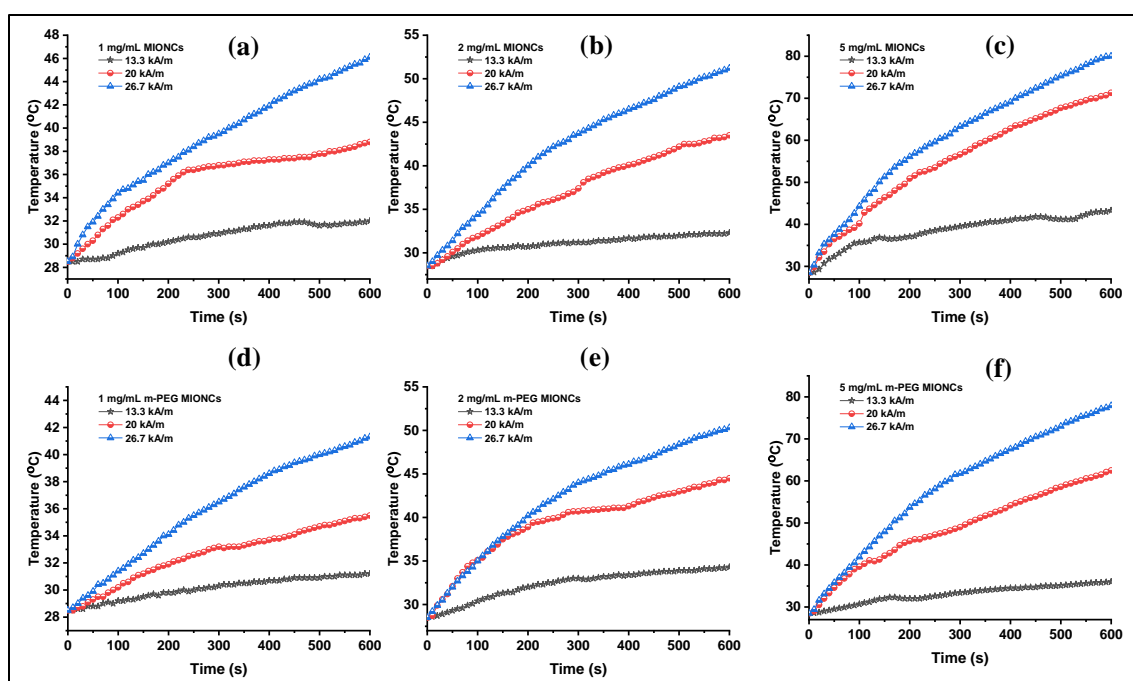


Figure 6.5 Temperature versus time curve of MIONCs ((a) 1 mg/mL, (b) 2 mg/mL, (c) 5 mg/mL) and m-PEG MIONCs ((d) 1 mg/mL, (e) 2 mg/mL, (f) 5 mg/mL) at field amplitudes 13.3 to 26.7 kA/m and frequency ≈ 277 kHz.

The temperature kinetic curves indicate that the temperature increase depends on the applied magnetic field and the concentration of MNPs. As illustrated in **Fig.6.5 (a–c)**, the coated and uncoated samples reached hyperthermia temperatures (42 to 44 °C) during the induction heating experiment at various AC magnetic fields while maintaining a constant frequency of ≈ 277 kHz. At an applied field of 26.7 kA/m, MIONCs and m-PEG MIONCs achieve temperatures of 43 and 47 °C,

respectively. From 47 to 75 °C, the maximum temperature rise was observed for MIONCs at 26.7 kA/m. In our experiment, the coated sample reached a maximum temperature of 80 °C at 26.7 kA/m with a 5 mg/mL concentration. The comparison of the heating characteristics of coated and uncoated samples shows that the time required to reach the hyperthermia temperature for coated particles is less compared to uncoated particles. We obtained the heating efficiency of the MIONCs or SAR from these heating curves using the initial slope method. **Fig. 6.6 (a, b)** represents the SAR values of MIONCs and m-PEG- MIONCs in water. SAR values also increase with increasing field strength. The very low SAR values displayed by the smallest nanospheres could be related to their broader size distribution [45].

The resulting heating curves can be found in **Fig. 6.5**. By analyzing these curves, different increases in temperature were found between samples. As a general trend, the net temperature increases as a function of time and frequency. Additionally, from these curves, the corresponding SAR values can be calculated through the initial slope method, as described in **Equation (6.1)**. The normalization of the SAR in this manner allows a proper comparison among the samples based only on their composition and concentrations [44]. **Fig. 6.6 a, b** shows the SAR values calculated in physiological media. For the uncoated particles, the SAR value increases from 44.84 to 237.44 Wg^{-1} with an increase in the field from 13.3 - 26.6 kA/m and for m-PEG MIONCs, it increases from 45.45 to 221.17 Wg^{-1} .

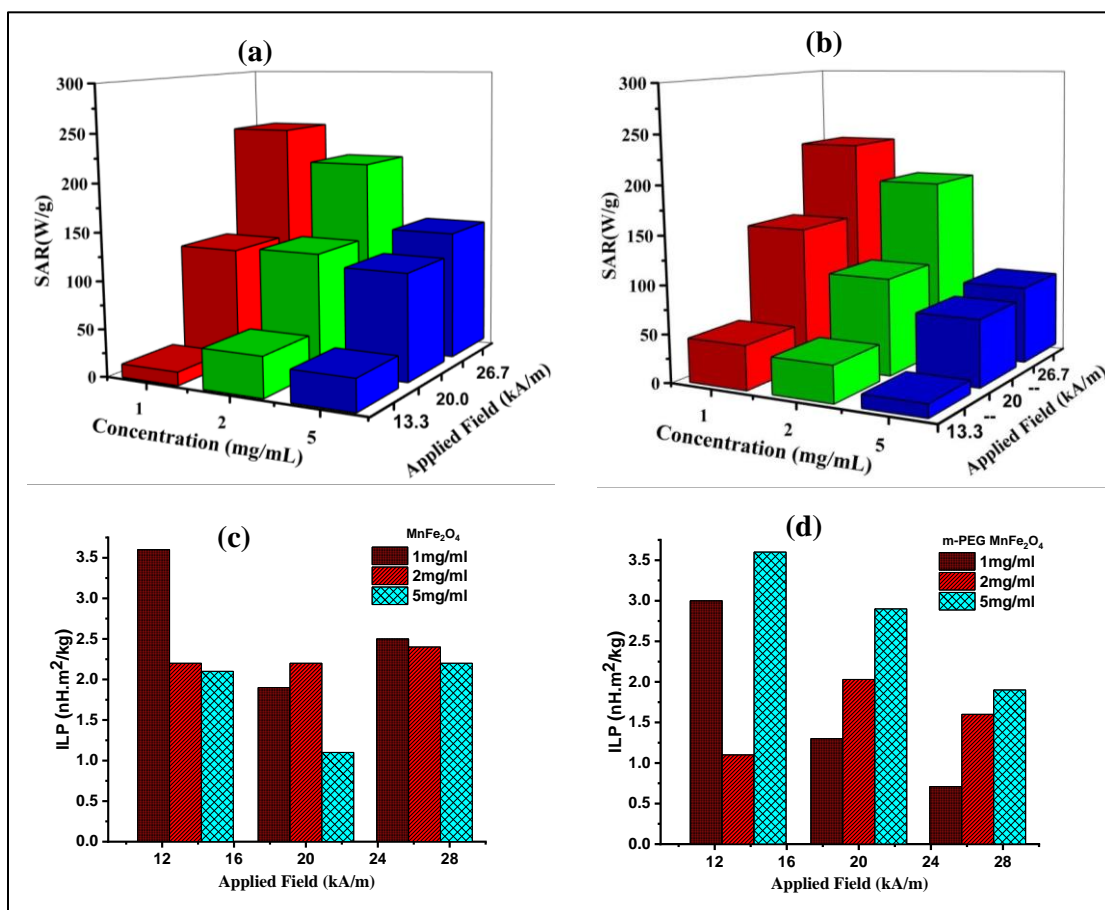


Figure 6.6 SAR vs applied magnetic field for (a) MIONCs and (b) m-PEG MIONCs, the ILP values of bare MIONCs (c) and m-PEG -MIONCs (d)

6.7 Conclusions

In this chapter, MIONCs through thermal decomposition have been successfully prepared and coated with m-PEG. The impact of coating on structural and morphological properties has been studied. XRD and FTIR analyses revealed the formation of a pure phase with and without m-PEG. Thermogravimetric and FTIR analyses confirm the successful attachment of m-PEG on the nanoparticle's surface. However, m-PEG-coated nanoparticles exhibit a stable suspension and dispersion stability. The magnetic properties, characterized by low coercivity and remanence, indicate soft ferrimagnetic SPM behavior. superparamagnetic iron oxide nanocubes have gained significant attention due to their unique magnetic properties, stability, and biocompatibility. The cubic shape of these nanoparticles enhances their magnetic response under alternating magnetic fields, enabling efficient heat generation through Néel and Brownian relaxation mechanisms.

The SAR values calculated in physiological media, for the uncoated particles increases from 13.96 to 237.44 Wg^{-1} with an increase in the field from 13.3 - 26.6 kA/m. For m-PEG MIONCs, it increases from 45.45 to 221.17 Wg^{-1} . These values of SAR obtained in the case of m-PEG MIONCs can be attributed to the superior magnetic anisotropy of nanocubes compared to spherical counterparts. This demonstrates that the synthesized m-PEG MIONCs shows induction heating characteristics and hold promise for applications in MHT for cancer.

6.8 References

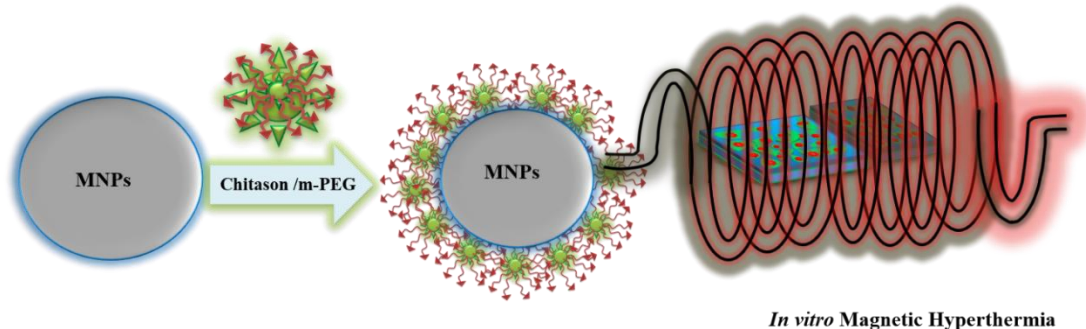
1. C. Sanson, O. Diou, J. Thevenot, E. Ibarboure, A. Soum, A. Brûlet, S. Miraux, E. Thiaudière, S. Tan, A. Brisson, V. Dupuis, *ACS Nano*, 5(2) (2011) 1122-1140.
2. A. Salunkhe, V. Khot, S. Patil, S. Tofail, J. Bauer, N. Thorat, *ACS Appl. Bio Mater.*, 3 (2020) 2305–2313.
3. J. Fortin, C. Wilhelm, J. Servais, C. Ménager, J. Bacri, F. Gazeau, *JACS*, 129(9) (2007) 2628-2635.
4. D. Forge, Y. Gossuin, A. Roch, S. Laurent, L. Elst, R. Muller, *Contrast media & molecular imaging*, 5(3) (2010) 126-132.
5. Z. Ma, J. Mohapatra, K. Wei, J. Liu, S. Sun, *Chem. Rev.*, 123 (2023) 3904–3943.
6. P. Guardia, R. Corato, L. Lartigue, C. Wilhelm, A. Espinosa, M. Garcia-Hernandez, F. Gazeau, L. Manna, T. Pellegrino, *ACS Nano*, 6(4) (2012) 3080-3091.
7. S. Del Sol-Fernández, Y. Portilla-Tundidor, L. Gutiérrez, O. Odio, E. Reguera, D. Barber, M. Morales, *ACS Appl. Mater. Interfaces.*, 11 (30) (2019) 26648-26663.
8. E. Bertuit, E. Benassai, G. Méridet, J. Greneche, B. Baptiste, S. Neveu, C. Wilhelm, A. Abou-Hassan, *ACS Nano*, 16(1) (2021) 271-284.
9. A. Walter, C. Billotey, A. Garofalo, C. Ulhaq-Bouillet, C. Lefevre, J. Taleb, S. Laurent, L. Elst, R. Muller, L. Lartigue, F. Gazeau, *Chem. Mater.*, 26(18) (2014) 5252-5264.
10. K. Maier-Hauff, F. Ulrich, D. Nestler, H. Niehoff, P. Wust, B. Thiesen, H. Orawa, V. Budach, A. Jordan, *Journal of neuro-oncology*, 103 (2011) 317-324.
11. J. Lee, J. Jang, J. Choi, S. Moon, S. Noh, J. Kim, J. Kim, I. Kim, K. Park, J. Cheon, *Nat. Nanotechnol.*, 6(7) (2011) 418-422.
12. A. Gupta, M. Gupta, *Biomaterials*, 26(13) (2005) 1565-1573.
13. C. Berry, S. Wells, S. Charles, A. Curtis, *Biomaterials*, 24 (2003) 4551–4557.
14. M. Mikhaylova, D. Kim, C. Berry, A. Zagorodni, M. Toprak, A. Curtis, M. Muhammed, *Chem. Mater.*, 16(12) (2004) 2344-2354.
15. D. Maity, P. Chandrasekharan, P. Pradhan, K. Chuang, J. Xue, S. Feng, J. Ding, J. Mater. Chem., 21 (2011) 14717–14724.
16. I. Crăciunescu, P. Palade, N. Iacob, G. Ispas, A. Stanciu, V. Kuncser, R. Turcu, J. Phys. Chem. C, 125(20) (2021) 11132-11146.
17. P. Kolhe, R. Kannan, *Biomacromolecules*, 4 (2003) 173–180.

-
18. C. Kalaiselvan, S. Laha, S. Somvanshi, T. Tabish, N. Thorat, N. Sahu, *Coord. Chem. Rev.*, 473 (2022) 214809-214841.
 19. M. Vassallo, D. Martella, G. Barrera, F. Celegato, M. Coisson, R. Ferrero, E. Olivetti, A. Troia, H. Sozeri, C. Parmeggiani, D. Wiersma, *ACS omega*, 8(2) (2023) 2143-2154.
 20. G. Sanità, B. Carrese, A. Lamberti, *Front. Mol. biosci.*, 7 (2020) 587012-587032.
 21. R. Thiruppathi, S. Mishra, M. Ganapathy, P. Padmanabhan, B. Gulyás, *Adv. Sci.*, 4(3) (2017) 1600279- 1600293.
 22. K. Kobayashi, J. Wei, R. Iida, K. Ijro, K. Niikura, *Polym. J.*, 46(8) (2014) 460-468.
 23. W. Wu, C. Jiang, V. Roy, *Nanoscale*, 8 (2016) 19421–19474.
 24. A. Morris, A. Salem, *Adv. Eng. Mater.*, 19 (2017) 1–10.
 25. M. Mohamed, A. Lila, T. Shimizu, E. Alaaeldin, A. Hussein, H. Sarhan, J. Szebeni, T. Ishida, *Science and Technology of Advanced Materials*, 20(1) (2019) 710-724.
 26. S. Laha, N. Thorat, G. Singh, C. Sathish, J. Yi, A. Dixit, A. Vinu, *Small*, 18(11) (2022) 2104855-2104885.
 27. Y. Wang, *World journal of gastroenterology*, 21(47) (2015) 13400- 13402.
 28. Y. Zhang, N. Kohler, M. Zhang, *Biomaterials*, 23 (2002) 1553–1561.
 29. S. Fu, R. Yang, J. Ren, J. Liu, L. Zhang, Z. Xu, Y. Kang, P. Xue, *Acs Nano*, 15(7) (2021) 11953-11969.
 30. A. Manohar, V. Vijayakanth, S. Vattikuti, P. Manivasagan, E. Jang, K. Chintagumpala, K. Kim, *ACS Appl. Nano Mater.*, 5(4) (2022) 5847-5856.
 31. X. Cao, B. Zhang, F. Zhao, L. Feng, *J. Nanomater.*, 1 (2012) 607296-607302.
 32. S. Khoei, A. Kavand, *J. Nanostructure Chem.*, 4 (2014) 1-6.
 33. J. Pan, P. Hu, Y. Guo, J. Hao, D. Ni, Y. Xu, Q. Bao, H. Yao, C. Wei, Q. Wu, J. Shi, *ACS Nano*, 14(1) (2020) 1033-1044.
 34. F. Panahi, S. Peighambari, S. Davaran, R. Salehi, *Polymer*, 117 (2017) 117–131.
 35. L. Félix, B. Sanz, V. Sebastián, T. Torres, M. Sousa, J. Coaquira, M. Ibarra, G. Goya, *Scientific reports*, 9(1) (2019) 4185.
 36. M. Knobel, W. Nunes, L. Socolovsky, E. De Biasi, J. Vargas, J. Denardin. *J. Nanosci. Nanotechnol.*, 8(6) (2008) 2836-2857.

-
37. Walz F. *J Phys Condens Matter.*, 14(12) (2002) R285.
 38. V. Khot, A. Salunkhe, N. Thorat, R. Ningthoujam, S. Pawar, *Dalton Trans.*, 42(4) (2013) 1249-58.
 39. A. Salunkhe, V. Khot, J. Ruso, S. Patil, *J. Magn. Magn. Mater.*, 419 (2016) 533–542.
 40. S. Jadhav, D. Nikam, V. Khot, N. Thorat, M. Phadatare, R. Ningthoujam, A. Salunkhe, S. Pawar, *New J Chem*, 37(10) (2013) 3121-3130.
 41. N. Thorat, R. Bohara, S. Tofail, Z. Alothman, M. Shiddiky, M. Hossain, Y. Yamauchi, K. Wu, *Eur. J. Inorg. Chem.*, 28 (2016) 4586-4597.
 42. N. Thorat, S. Otari, R. Patil, V. Khot, A. Prasad, R. Ningthoujam, S. Pawar, *Colloids Surf. B Biointerfaces*, 111 (2013) 264-269.
 43. X. Liu, Y. Zhang, Y. Wang, W. Zhu, G. Li, X. Ma, Y. Zhang, S. Chen, S. Tiwari, K. Shi, S. Zhang, *Theranostics*, 10(8) (2020) 3793–3815.
 44. Z. Nemati, J. Alonso, I. Rodrigo, R. Das, E. Garaio, J. García, I. Orue, M. Phan, H. Srikanth, *J. Phys. Chem. C*, 122(4) (2018) 2367-2381.
 45. S. Fernández, O. Odio, P. Crespo, E. Pérez, G. Salas, L. Gutiérrez, M. Morales, E. Reguera, *J. Phys. Chem. C*, 126(24) (2022) 10110-10128.

CHAPTER-7

***In vitro* Magnetic Hyperthermia Study of Chitosan and m-PEG Functionalized Manganese Iron Oxide Nanoparticles**



7.1. Introduction

Multifunctional MNPs present promising opportunities for safe and effective cancer treatments. Their unique structural and behavioral characteristics have garnered significant interest, as they possess distinctive magnetic properties, tunable sizes, high chemical stability, an increased surface area, the ability to be functionalized with various molecules, and compatibility with different cell types [1]. Their importance is evident in multiple applications, such as drug delivery systems, MHT, MRI contrast agents, tissue engineering, gene delivery, cell separation and selection, magneto-relaxometry, and antibacterial agents [2,3]. Chemically functionalized and colloidally stable MNPs can effectively transform electromagnetic energy into heat through several mechanisms, such as hysteresis, SPM, and eddy current losses. When electromagnetic fields are applied to surface-functionalized MNPs, the subsequent conversion of this energy into thermal energy can efficiently eliminate cancer cells, a process known as hyperthermia [4-7].

Significant efforts are underway to induce tumor destruction, both *in vitro* and *in vivo*, by utilizing low-frequency electromagnetic fields. MNPs can produce heat when subjected to an AMF and lose their magnetization once the field is removed. Upon removing the external field, they become highly dispersed in the fluid, making them suitable for clinical cancer treatments. A range of surfactants is used for a coating to maintain the colloidal properties and biocompatibility of MIONPs and prevent aggregation caused by magnetic dipole-dipole interactions. Among these is chitosan, a substance with unique characteristics like bio-compatibility, biodegradability, film formation potential, and bio-adhesion, which has received much attention regarding biodegradability and toxicity. Methoxy-polyethylene glycol (m-PEG) is a promising coating for enhancing the biocompatibility, colloidal stability, and specific absorption rate of MNPs due to its highly hydrophilic nature. It acts as a barrier against protein adsorption, thereby decreasing macrophage uptake. Additionally, m-PEG is a biocompatible, non-antigenic, and protein-resistant polymer that contains neutral hydrophilic segments, promoting a homogeneous distribution in aqueous media. Therefore, selecting the appropriate molecular weight of m-PEG for stabilizing MNPs is crucial [8, 9].

To ensure the safety of new nanomaterials, it is essential to conduct biocompatibility studies. They assessed the cytotoxicity of the synthesized chitosan and m-PEG-capped MNPs using various cell lines. This employed different cell-

based assays to determine the precise cytotoxicity and biocompatibility of the MNPs, examining several cell lines with varying incubation times and dose-dependent MNP concentrations. Comparative cytotoxicity assays were conducted on MCF7 cell lines using Trypan blue dye exclusion (TBDE) and the MTT colorimetric assay, both at different MNP concentrations. Since Trypan blue only stains cytoplasmic and nuclear components when the cell membrane is compromised, it indicates cell death by coloring only the intracellular components of dead cells [10].

7.2. The Principles of Nanotoxicology

Nanotoxicology is a branch of toxicology focused on the potentially harmful effects of nanoscale structures or particles with a diameter of less than 100 nanometers [11]. Nanomaterials, such as metals, metal oxides, ceramics, polymers, or composites, exhibit unique properties compared to traditional materials due to their nanoscale characteristics. These materials offer exciting new possibilities in oncology for cancer treatment through nanomaterial-based drug delivery systems, where anti-cancer drugs are loaded onto nanomaterials and directed to specific tumor tissues for targeted therapy. As drug carriers, nanomaterials are designed to target cancer cells actively, leading to significantly enhanced drug delivery efficiency compared to the passive diffusion of drug molecules to tumors. Nanomaterial-based drug delivery systems provide notable advantages over traditional chemotherapy, but concerns about their potential cytotoxicity persist. Nanoparticles have unique toxicity profiles due to increased surface area and molecular interactions at the bio-nano interface. Understanding these interactions is essential for recognizing nanotoxicity. Selectively targeting cancer cells can effectively destroy tumors, but unwanted toxicity from nanomaterials or their combinations may cause side effects. Since nanoparticles and therapeutic drugs share similar biological behaviors, understanding their interplay can enhance cancer treatment strategies [12].

The toxicity of nanomaterials is influenced by their size, which affects their ability to penetrate biological systems and alter structural functions, thereby disrupting essential biological processes. The behavior of MNPs in various environmental contexts is intricate and involves multiple mechanisms. MNPs possess unique properties that set them apart from conventional materials. Factors such as (1) particle size, (2) surface area and charge, (3) shape and structure, (4) solubility, and (5) surface coatings can significantly impact MNP toxicity. Variations in shapes and

structures such as planes, spheres, fibers, tubes, and polyhedral often lead to differences in toxicity. Additionally, the surface charge is critical to MNP toxicity as it governs interactions with biological systems, influencing (i) selective nanoparticle adsorption, (ii) colloidal stability, (iii) binding to plasma proteins, (iv) the integrity of the blood-brain barrier, and (v) transmembrane permeability. From a toxicological perspective, colloids and their degradation products must be eliminated from the body as quickly as possible following drug release [13, 14].



Figure 7.1 Physicochemical characteristics of engineered nanomaterials that contribute to nanotoxicity

7.3. Cytotoxicity

While toxicity refers to the overall harm a substance can inflict on an organism, cytotoxicity pertains explicitly to its harmful effects on cells. A cytotoxic agent can damage or kill cells through necrosis or apoptosis. Cytotoxicity assessments are particularly important in cancer research and developing chemotherapy drugs. Understanding the cytotoxic effects of a drug on cancer cells and its unintended impact on healthy cells is crucial. Nanotechnology is an innovative and rapidly evolving field. Although the variety of nanoparticles and nanomaterials and their applications have surged in recent decades, there is still limited research on their long-

term effects on the human body, particularly regarding potential cytotoxicity. Nanoparticles are increasingly common in diagnostic and therapeutic applications [15, 16].

Cytotoxicity refers to the general ability of a substance to be toxic to cells, which can arise from chemical stimuli, interactions with other cells, or physical/environmental factors such as radiation, extreme temperatures, or pressure. A material is deemed cytocompatibility if it does not alter the structure and functions of the tissue it contacts. The preservation of these functions is directly linked to the quality of the material's surface. Conducting cytotoxicity studies is an essential initial step in assessing the potential toxicity of various test substances, including plant extracts or biologically active compounds derived from plants. Ensuring minimal to no toxicity is crucial for the successful development of pharmaceuticals, making cellular toxicity studies vital [17].

7.4 Experimental Details for Biocompatibility Analysis

7.4.1. Hemolysis Assay

The hemolysis assay evaluated the hemolytic activity of MIONPs and CS-MIONPs using human erythrocytes. Blood from a healthy volunteer was collected using a centrifuge tube containing ethylenediaminetetraacetic acid (EDTA), and RBC pellets were washed with PBS (pH 7.4). Various concentrations of MIONPs and CS-MIONPs (20, 40, 60, 80, and 100 µg/ml) in PBS were mixed with a 5% RBC solution. Positive and negative controls used distilled water and 0.9% NaCl (Normal Saline). Samples were incubated at 37 °C for 2 h, then centrifuged, and the supernatant's absorbance at 540 nm was measured. The hemolysis percentage was calculated using a standard formula: [18]

$$\% \text{ hemolysis} = \frac{(\text{sample absorbance} - \text{negative control absorbance})}{(\text{positive control absorbance} - \text{negative control absorbance})} \times 100 \quad (7.1)$$

A similar procedure was used for the hemolysis assay of MIONCs and m-PEG MIONCs.

7.4.2. Reactive Oxygen Species (ROS) Assay

The production of reactive oxygen species (ROS), primarily contributing to the toxicity of MIONPs and CS-MIONPs, was assessed using 2',7'-dichlorodihydrofluorescein diacetate (DCFH-DA). This peroxynitrite indicator detects

nitric oxide and hydrogen peroxide inside and outside cells. Bacterial cells were treated with 200 μ M DCFH-DA, and fluorescence emission was measured at 523 nm, with excitation at 503 nm. MIONPs and CS-MIONPs (30 mg) were added at the log phase of bacterial growth, and ROS variation was determined by comparing fluorescence intensities against the positive control. For accuracy, all experiments were performed in triplicates [19].

A similar procedure was used for the ROS assay of MIONCs and m-PEG MIONCs.

7.4.3. Angiogenesis Activity/ *In Ovo* Cytotoxicity Assay:

The angiogenic activity of MIONPs and CS-MIONPs was evaluated using the Chick Chorioallantoic Membrane (CAM) assay. Fertilized chicken eggs (day 0) were obtained from a local hatchery in Kolhapur, Maharashtra, India. The eggs were surface sterilized with 70% ethanol and incubated at 37 °C with 70-80% humidity. After 5 days, a small hole was drilled at the distal end of the eggs to create a 2 cm² window, and 2 mL of albumin was extracted. The opposite side of the shell was removed to check embryo development. Whatman filter discs were soaked with phosphate-buffered saline (PBS) as a control, and 2 μ g/mL of MIONPs and CS-MIONPs were placed on the CAM. The open window was sealed with parafilm, and the eggs were incubated under the same conditions. The CAM's angiogenic capillaries were photographed at regular intervals.

A similar procedure was used for the angiogenesis activity/ in the *Ovo* cytotoxicity assay of MIONCs and m-PEG MIONCs.

7.4.4. MTT assay

Comparative *in vitro* cytotoxicity studies for both samples were conducted on MCF-7 (human adenocarcinoma cells) cell lines sourced from the National Centre for Cell Sciences in Pune, India, with detailed toxicity evaluations performed at the National Toxicology Centre, Pune, India (ISO 10993/USP 32 NF 27) using the MTT assay. The MCF-7 cells were cultured in DMEM (Dulbecco's Modified Eagle Medium) supplemented with 10% v/v fetal bovine serum, kanamycin (0.1 mg/mL), penicillin G (100 U/mL), and sodium bicarbonate (1.5 mg/mL) at 37 °C in a 5% CO₂ environment. Meanwhile, the HeLa cells were maintained in MEM with 10% fetal bovine serum and antibiotics under the same conditions.

7.5 Cell Culture

7.5.1. Cell Viability by MTT Assay

The cells were seeded at a concentration of 2×10^5 cells/mL in their respective media and incubated for 24 hours in a 96-well microtiter plate. Following this, the media was refreshed, and various concentrations of sterile CS-MIONPs (0.2, 0.4, 0.6, 0.8, and 1 mg/mL) were added to the cultured media. The plates were then incubated at 37 °C in a 5% CO₂ environment for another 24 hours. After incubation, the plates were checked under an inverted microscope for contamination and other factors. Finally, 10 µL of MTT solution, including the controls, was added to each well. The plates were incubated for 3 hours at 37 °C in a 5% CO₂ environment to allow the metabolization of MTT with the nanoparticles and cell media. After incubation, the media was removed by flicking the plates, leaving the adhered cells in the wells. The cells were washed with PBS, and the formed formazan was dissolved in 200 µL of acidic isopropanol. Absorbance was measured at 570 nm to calculate cell viability. The experiments were conducted in triplicate, and the average data were presented graphically. Relative cell viability (%) was calculated using the following equation:

$$= \{ [A_{\text{absorbance}}]_{\text{tested}} / [A_{\text{absorbance}}]_{\text{control}} \} \times 100. \quad (7.2)$$

A similar procedure was used for the MTT Assay of m-PEG MIONCs.

7.5.2. Trypan Blue Dye Exclusion (TBDE)

The cells were incubated at a concentration of 1×10^5 cells/mL for 24 hours. After treatment with MNPs, the cells were incubated at 37 °C. Following incubation, the cells were harvested through trypsinization and stained with Trypan Blue dye. A hemocytometer was used to count the cells. The cell viability (%) was determined using the following equation:

$$= \{ [A_{\text{count}}]_{\text{tested}} / [A_{\text{count}}]_{\text{control}} \} \times 100 \quad (7.3)$$

7.5.3. *In Vitro* Anti-Cancer Activity

MCF7 cells were seeded in a 96-well plate at a density of 1×10^5 cells per well. After 24 and 48 hours of incubation, the cell culture media was replaced with a fresh mixture containing MIONPs and CS-MIONPs. The cells were then incubated for 24 and 48 h before the MTT experiment. In brief, the cell culture media was aspirated, and MTT in FBS-free DMEM (10 mM) was added. After an additional 3 hours of incubation, the MTT solution was removed, and 100 µL of DMSO was

added to dissolve the formed formazan crystals. The cell viability was subsequently determined by measuring the absorbance at 570 nm. The experiments were repeated three times, and the data's mean and standard deviation (SD) were presented graphically. The relative cell viability (%) compared to the control well-containing cells without nanoparticles was calculated using the following equation:

$$= [A_{\text{absorbance}}]_{\text{tested}} / [A_{\text{absorbance}}]_{\text{control}} \times 100 \quad (7.4)$$

A similar procedure was used for the *in vitro* anti-cancer activity of MIONCs and m-PEG MIONCs.

7.5.4 In Vitro Magnetic Hyperthermia Study

To evaluate the effectiveness of *in vitro* magneto-thermotherapy, MCF7 cells were cultured with MIONCs alone and m-PEG MIONCs at a 1 mg/mL concentration. The AC magnetic fields were activated until the upper limit of hyperthermia temperature reached around 43-44 °C. The frequency applied for all *in vitro* experiments was ≈ 277 kHz, and the AC magnetic field was maintained at 20 kA/m. In the center of the coil, a media containing MIONPs and CS-MIONPs was suspended with 1 mL of cancer cells (2×10^5 cells per mL). The systems temperature was maintained at a constant 43-44 °C throughout the experiment, with a heating duration of 60 minutes provided by the samples containing nanoparticles and cells. The cells were immediately transferred to 96-well plates and cultured for 24 hours. Simultaneously, the cell samples were cultured in slide Petri dishes with 2 mL of DMEM for subsequent confocal microscopy imaging after labeling with propidium iodide (PI) and DAPI. The cell viability was assessed using the MTT assay.

7.6 Results and Discussion

7.6.1 Hemolysis Activity:

a) Hemolysis Activity of MIONPs and CS-MIONPs:

The hemolytic activity of MIONPs and CS-MIONPs was assessed across various concentrations, revealing a clear concentration-dependent increase in hemolysis for both types of nanoparticles. The concentration Vs. Absorbance and Percentage of hemolysis Vs concentration of MIONPs and CS-MIONPs are shown in **Fig. 7.2**. At 20 $\mu\text{g/mL}$, MIONPs exhibited a hemolytic activity of 0.3%, slightly higher than the 0.2% observed for CS-MIONPs. This trend continued with increasing concentrations, with MIONPs showing a maximum hemolytic activity of 3.6% at 100 $\mu\text{g/mL}$,

compared to 2.4% for CS-MIONPs. The results suggest that while both nanoparticles induce hemolysis, MIONPs are more potent than their coated counterparts, potentially due to their uncoated surface allowing for more significant interaction with red blood cells. The mechanism underlying this hemolytic effect likely involves direct interaction between the nanoparticles and the cell membrane, leading to membrane destabilization and lysis. The observed hemolysis may also contribute to particle size, surface charge, and reactive oxygen species generation. The enhanced hemolytic activities of MIONPs emphasize the importance of nanoparticle design in ensuring biocompatibility, highlighting the need for further investigation into the mechanisms involved to inform safe biomedical applications. The hemolytic efficiency of MIONPs and CS-MIONPs is shown in **Table 7.1**.

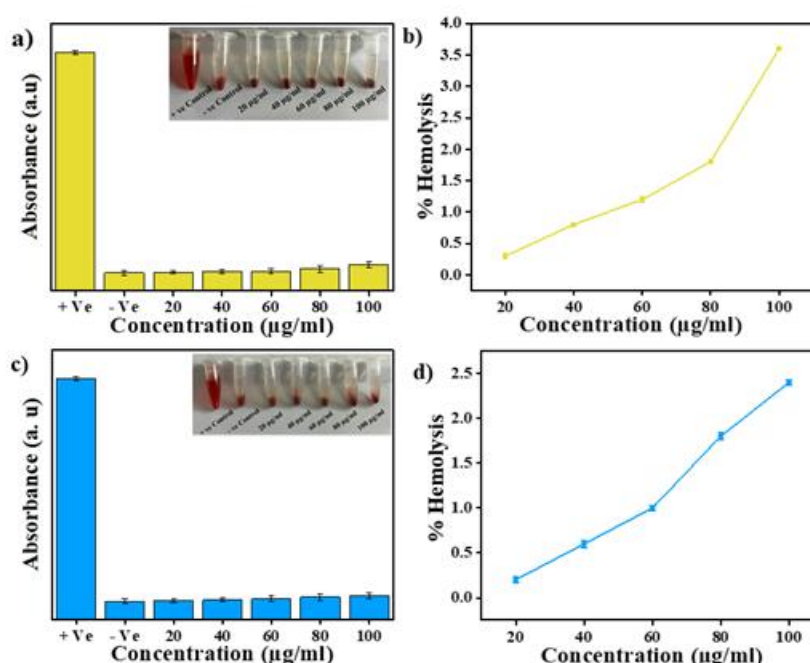


Figure 7.2 The concentration Vs. the absorbance of (a) MIONPs (c) CS-MIONPs, Percentage of hemolysis Vs concentration of (b) MIONPs (d) CS-MIONPs

b) Hemolysis Activity of MIONCs and m-PEG MIONCs:

The hemolytic activity of MIONCs and m-PEG MIONCs was assessed across various concentrations, revealing an apparent concentration-dependent increase in hemolysis for both types of nanoparticles. The concentration Vs. Absorbance and Percentage of hemolysis Vs concentration of MIONCs and m-PEG MIONCs are shown in **Fig. 7.3**. The hemolytic activity of MIONCs and m-PEG MIONCs increased with concentration, showing 0.6% hemolysis for MIONCs at 20 μg/mL

compared to 0.3% for m-PEG MIONCs. At 100 $\mu\text{g/mL}$, MIONCs reached a maximum hemolytic activity of 3.6%, while m-PEG MIONCs showed 3.3%. MIONCs are more effective in inducing hemolysis, likely due to more significant interaction with red blood cells from their uncoated surfaces. This effect may involve direct interactions with cell membranes, leading to destabilization. The results highlight the importance of nanoparticle design for biocompatibility and suggest further research into the mechanisms involved. Hemolytic efficiency data is shown in Table 7.1.

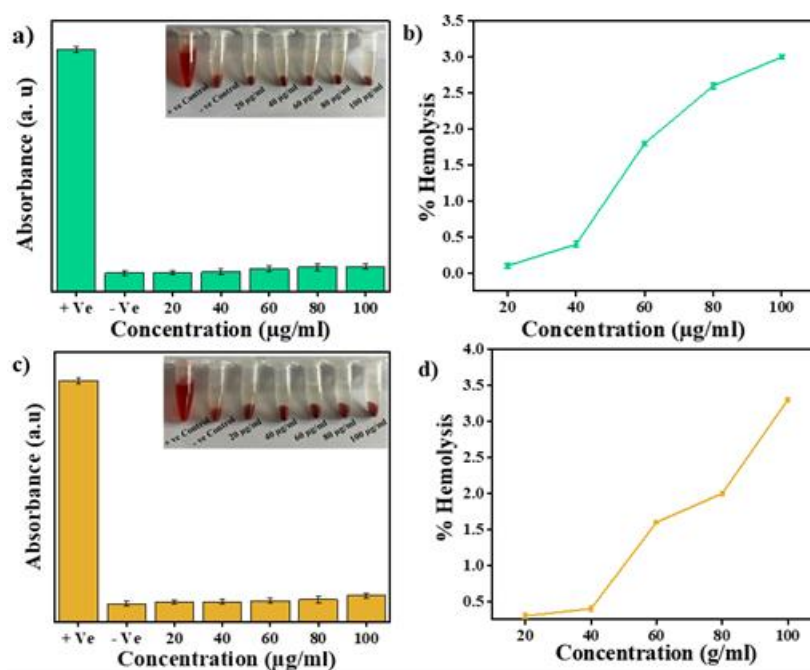


Figure 7.3 The concentration Vs. the absorbance of (a) m-PEG MIONCs, (c) MIONCs, and the percentage of hemolysis Vs concentration of (b) m-PEG MIONCs, (d) MIONCs

Table 7.1 Hemolytic efficiency of MIONPs, CS-MIONPs, MIONCs and m-PEG MIONCs

Concentrations ($\mu\text{g/mL}$)	Hemolytic activity (%) (OD 540 nm)			
	MIONPs	CS-MIONPs	MIONCs	m-PEG MIONCs
20	0.3	0.2	0.6	0.3
40	0.8	0.6	0.8	0.4
60	1.2	1.0	1.8	1.6
80	1.9	1.8	2.2	2.0
100	3.6	2.4	3.6	3.3

7.6.2 ROS Detection:

a) ROS Detection of MIONPs and CS-MIONPs:

The kinetics of DCFH-DA oxidation in bacterial cells treated with MIONPs and CS-MIONPs during the log phase of bacterial growth are shown in **Fig. 7.4**. ROS is naturally produced in the culture media even without MNP treatment, as bacteria generate ROS under non-stress conditions, which are typically neutralized by ROS-scavenging enzymes like superoxide dismutase in *E. coli*.

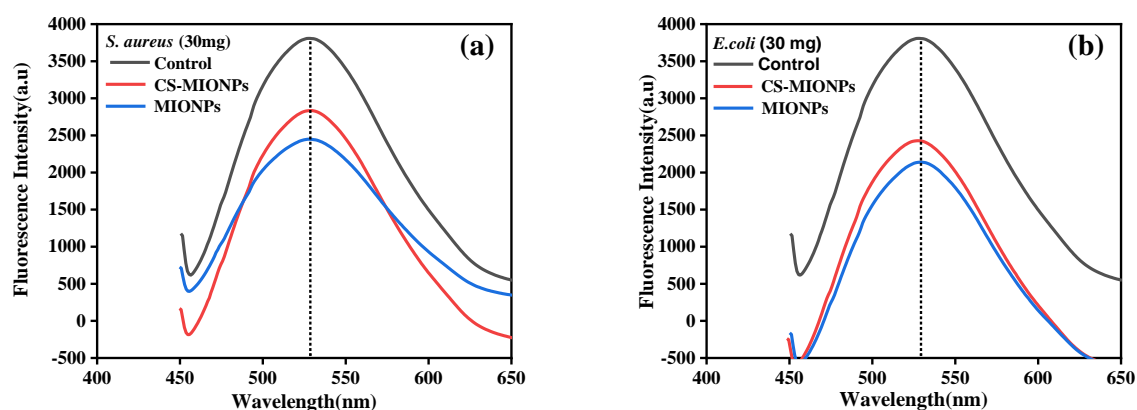


Figure 7.4 Shows the ROS determination of MIONPs and CS-MIONPs samples at a concentration of 30 mg in gram-positive and gram-negative bacteria in **a)** *E. coli* and **b)** *S. aureus*.

However, the addition of MIONPs and CS-MIONPs at a concentration of 30 mg (Fig. 7.4 a) led to a notable increase in fluorescence intensity, indicating a higher production of ROS in both *S. aureus* (Fig. 7.4 b) and *E. coli* (Fig. 7.4 a) cells. The combined findings from ROS observation and growth kinetics suggest that ROS production contributes to the antimicrobial activity of MIONPs and CS-MIONPs. Furthermore, the amount of ROS generated, as indicated by fluorescence intensity, was higher for MIONPs and CS-MIONPs at the 30 mg concentration, reflecting the changes in fluorescence intensity associated with DCFH-DA oxidation in the presence of nanoparticles for both *S. aureus* and *E. coli*. Each curve represents the average of three independent measurements and the corresponding standard error of the mean.

b) ROS Detection of MIONCs and m-PEG MIONCs:

The kinetics of DCFH-DA oxidation in bacterial cells treated with MIONCs and m-PEG MIONCs during the log phase of bacterial growth are shown in Fig. 7.5. ROS was naturally produced in the culture media even without nanoparticle treatment, indicating that bacteria generate ROS under non-stress conditions. In such cases, ROS is neutralized by scavenging enzymes like superoxide dismutase in *E. coli*.

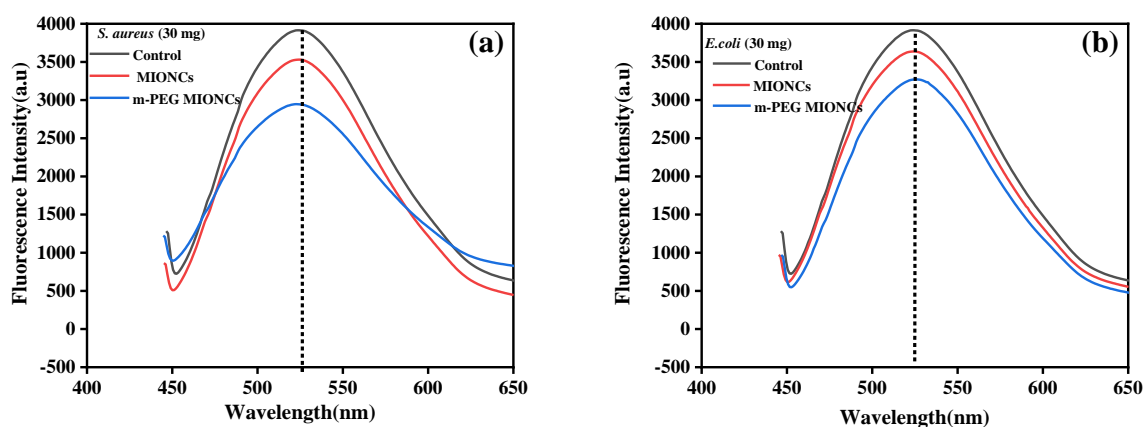


Figure 7.5 Shows the ROS determination of MIONCs and m-PEG MIONPs samples at a concentration of 30 mg in gram-positive and gram-negative bacteria in **a) *E. coli*** and **b) *S. aureus***.

However, when MIONCs and m-PEG MIONCs were introduced at a 30 mg concentration (Fig. 7.5 a), there was a significant increase in fluorescence intensity, which is directly related to elevated ROS production in both *S. aureus* (Fig. 7.5 b) and *E. coli* (Fig. 7.4 a) cells. The ROS generation and the growth kinetics study suggest

that the antimicrobial activity of MIONCs and m-PEG MIONCs is due to ROS production. Furthermore, as indicated by increased fluorescence intensity, the amount of ROS produced was higher in MIONCs and m-PEG MIONCs at 30 mg, showing a noticeable change in fluorescence with DCFH-DA oxidation in the presence of nanoparticles for both bacterial species. Each curve represents the average of three independent measurements with corresponding standard errors.

7.6.3. Angiogenesis Activity/ *In Ovo* Cytotoxicity Assay:

The chick embryo CAM is an extraembryonic membrane widely used as an *in vivo* model. MNPs are a promising option for targeted anti-tumor therapy. This study aimed to validate CAM as a suitable model for testing biological properties like biocompatibility. The CAM assay is favored for studying angiogenesis due to its extensive vascular network and ease of observation. Angiogenesis refers to the formation of new blood vessels from existing ones.

a) Angiogenesis Activity MIONPs and CS-MIONPs:

The CAM assay results reveal that MIONPs and CS-MIONPs exhibit strong biocompatibility, showing no negative impact on blood vessel formation or tissue integrity at tested concentrations. Both nanoparticle types maintained a healthy vascular network without causing inflammation, indicating their compatibility with biological systems. The surface properties of these nanoparticles likely contribute to reduced cytotoxicity and improved cellular interactions, with the CS coating potentially enhancing biocompatibility by providing a protective barrier. These findings suggest that MIONPs and CS-MIONPs are promising candidates for biomedical applications, particularly in drug delivery and tissue engineering. The hemocompatibility of MIONPs and CS-MIONPs indicates their considerable potential for use *in vitro* and *in vivo* MHT. **Fig. 7.6** shows the angiogenesis analysis of MIONPs and CS-MIONPs and the histological analysis of CAM using H&E staining.

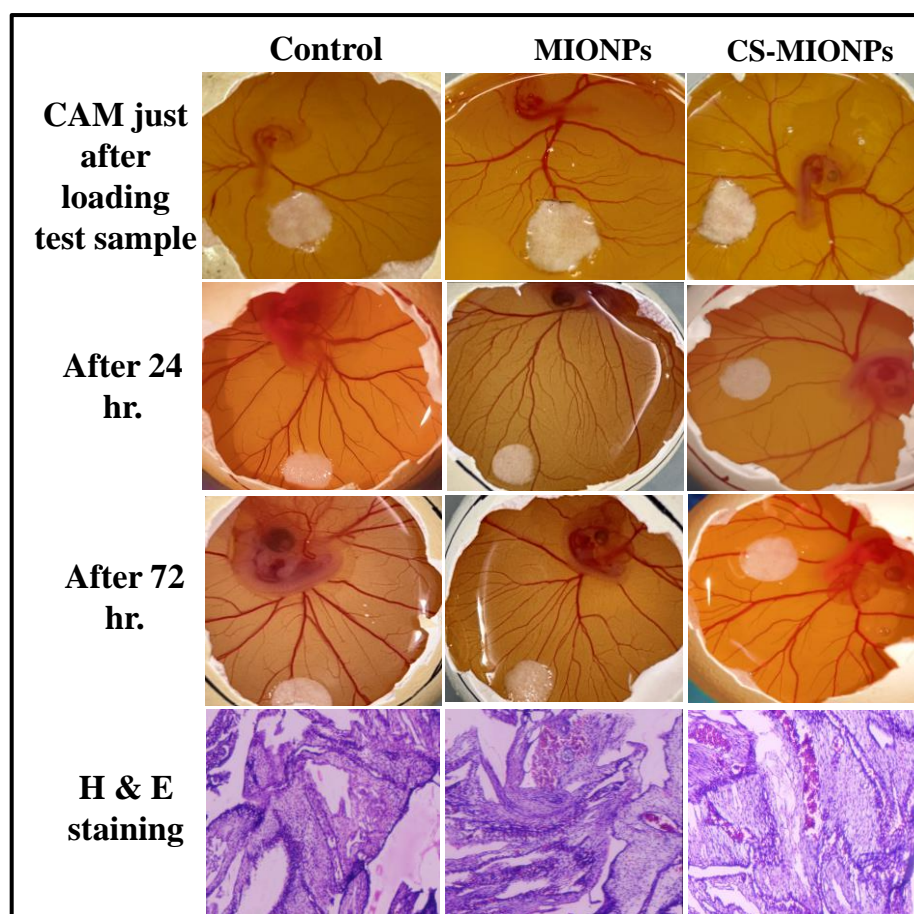


Figure 7.6 Angiogenesis analysis of MIONPs and CS-MIONPs and histological analysis of CAM using H&E staining

c) Angiogenesis Activity MIONCs and m-PEG MIONPs:

The CAM assay results show that MIONCs and m-PEG MIONCs exhibit significant biocompatibility, with no negative effects on blood vessel formation or tissue integrity at the tested concentrations. Both nanoparticles maintained a healthy vascular network and did not trigger inflammatory responses, indicating their suitability for biological systems. This biocompatibility may be attributed to the surface properties of the nanoparticles, which likely reduce cytotoxicity and encourage cellular interactions without activating immune reactions. The coating on MIONCs further enhances their biocompatibility by providing a protective layer, minimizing direct contact with cells. These findings suggest that both nanoparticle types hold promise for biomedical applications like drug delivery and tissue engineering, where maintaining tissue health is essential. Hemocompatibility, defined by less than 5% hemolysis, supports their potential in these fields. **Fig. 7.7** shows the

angiogenesis analysis of MIONCs and m-PEG MIONPs and the histological analysis of CAM using H&E staining.

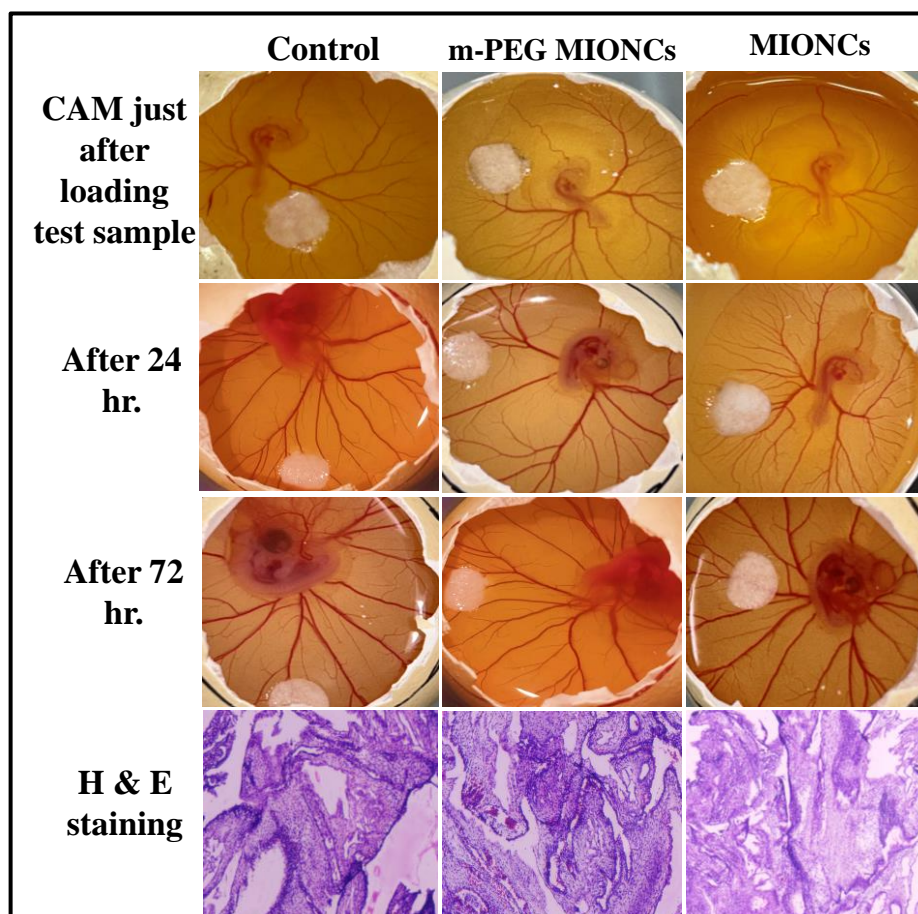


Figure 7.7 Angiogenesis analysis m-PEG MIONCs and MIONCs and histological analysis of CAM using H&E staining

7.6.4 *In vitro* Cytotoxicity of CS-MIONPs

The cytotoxicity and biocompatibility of CS-MIONPs were examined in a cell culture medium. It is essential to highlight that using a cell culture system served as a proof-of-concept, demonstrating the effectiveness and functionality of CS-MIONPs in conditions that mimic actual tumor tissues. MCF7 cell lines were used to assess the CS-MIONPs biocompatibility and cytotoxicity. The cytotoxicity of CS-MIONPs was assessed by incubating cells with varying dosages of nanoparticles (10, 25, 50, 100, 200, and 400 $\mu\text{g/mL}$) and compositions (i.e., MIONPs and CS-MIONPs) at 24h and 48h.

As mentioned above, the MTT assay was utilized to determine the cell viability, revealing no apparent toxicity of CS-MIONPs when incubated with cells at

the proper concentrations. CS-MIONPs have demonstrated biocompatibility with a mild cytotoxic effect, as previously evaluated. To investigate the anti-cancer activity of CS-MIONPs, MCF7 cells were utilized, and the effect of the concentration and time of CS-MIONPs was examined. The cytotoxicity effect of different concentrations and compositions of nanoparticles (i.e., MIONPs and CS-MIONPs) on cell viability was assessed. According to **Fig. 7.8 a**, CS-MIONPs exhibited significant cell killing, resulting in over 71.48% of cells surviving in cell culture after 48 h.

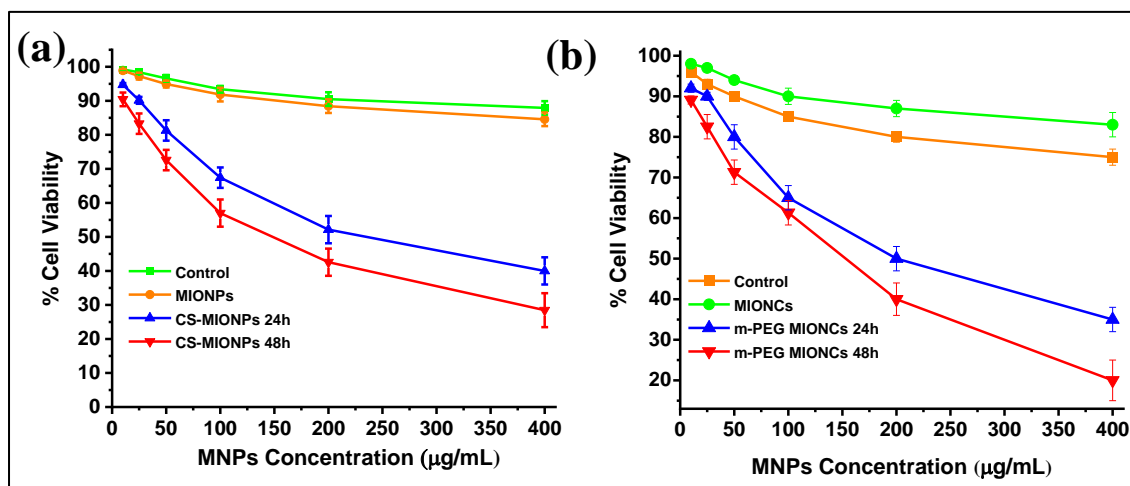


Figure 7.8 Concentration-dependent anti-cancer activity of (a) CS-MIONPs, (b) m-PEG MIONCs conjugated nanoformulations on MCF7 cells for 24h and 48h

7.6.5 *In vitro* Cytotoxicity of m-PEG MIONCs

The cytotoxicity and biocompatibility of m-PEG MIONCs were evaluated in a cell culture medium as a proof-of-concept to simulate tumor-like conditions. MCF7 cell lines were used to test the biocompatibility and cytotoxicity of m-PEG MIONCs. Cells were incubated with varying concentrations of nanoparticles (10, 25, 50, 100, 200, and 400 µg/mL) and compositions (MIONCs and m-PEG MIONCs) for 24h and 48h. The MTT assay showed no significant toxicity for m-PEG MIONCs at appropriate concentrations. However, m-PEG MIONCs demonstrated strong anti-cancer activity, with over 92.2% cell death observed after 48 h as shown in **Fig. 7.8 b**.

7.6.6. *In Vitro* Anti-cancer Activity of m-PEG MIONCs Under AC Magnetic Field

Given that the m-PEG MIONCs demonstrated high magnetic moment, good biocompatibility, and anti-cancer effect on breast cancer cells, they focused on nanoformulations *in vitro* magneto-thermotherapy performance in this study [20]. To

ensure the maximum *in vitro* therapeutic efficacy of the synergistic magnetic hyperthermia- thermotherapy approach, we modified parameters such as the hyperthermia therapeutic dose and the cellular incubation time of m-PEG MIONCs. This was done to avoid masking the effect of the synergistic platform by cell death caused by individual therapies. An improved therapeutic anti-cancer impact seen with m-PEG MIONCs was employed for a magneto-thermotherapy combo treatment. The temperature of the cellular environment, additional control samples, and suspended nanoformulations is controlled during the *in vitro* magneto-thermotherapy to remain between 43 and 44 °C without going over the MHT threshold [21]. Hence, there is sufficient localized heat ablation of MHT and release of therapeutic cargo to cause cancer cell death. A well-known molecular route of self-destruction of cells in a constructed cycle is known as ‘apoptosis,’ the term for programmed cell death. To verify magneto-thermotherapy superiority in insisting on ‘apoptosis,’ the m-PEG MIONCs were tested with an MCF7 cell line and subjected to MCT for 60 min shown in Fig.7.9 b.

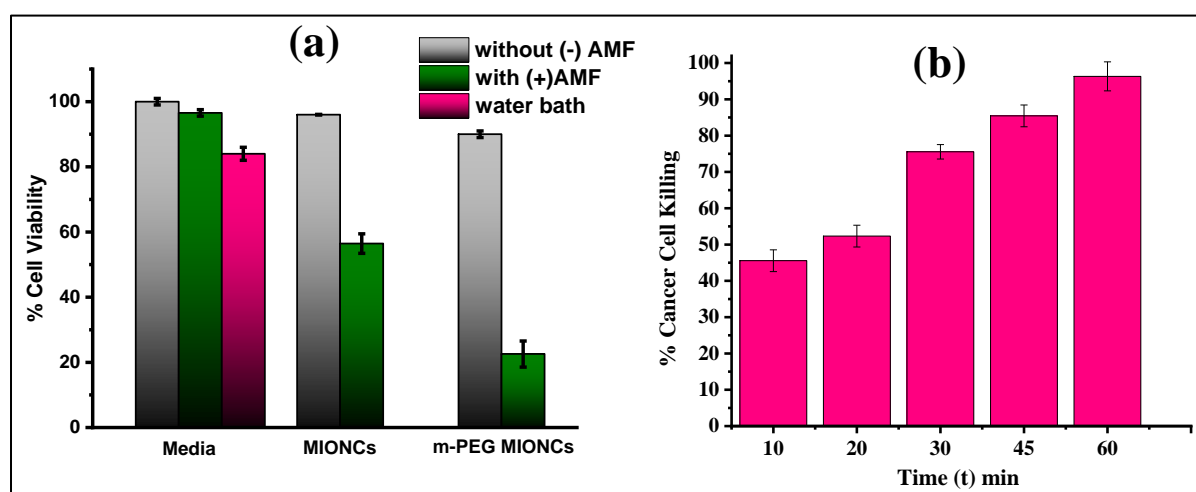


Figure 7.9 (a) The cytotoxicity of m-PEG MIONCs in Control, MIONCs, and m-PEG MIONCs with and without AMF, **(b)** Time dependent Cytotoxicity effects of m-PEG MIONCs

This finding implies that m-PEG MIONCs therapy reduced tumor growth by down-regulating the proteins' expression in cell cycle regulations and anti-apoptosis [22]. The data presented here confirmed that m-PEG MIONCs were efficiently bound and delivered to MCF-7 cells. Due to more effective internalization, m-PEG MIONCs

also demonstrated higher cytotoxicity effects on MCF-7 cells [22]. Magneto-thermotherapy can be used to treat malignant cells with superior anti-cancer therapeutic effects in a short amount of time. The developed drug-loaded nanoformulation used in this study demonstrated a sufficient anti-cancer therapeutic effect when subjected to AMF-induced hyperthermia. An optimal therapeutic dose is needed to eradicate the tumor *in vivo*. The m-PEG MIONCs synthesised in this study feature magnetic solid moments and magnetic field-responsive nanocarriers, enabling them to deliver effective hyperthermic heating deliberately and controlled. As a result, the combinational therapeutics approach is comparatively more efficient than employing just one technique, such as magneto-thermotherapy or MHT [21]. The *in vitro* cytotoxicity assay of m-PEG MIONCs is shown in **Fig. 7.9 a**.

However, the clinical application of MHT is limited due to nanosystems' reduced heat generation within the cellular environment and the development of thermotolerance, which diminishes MHT's effectiveness. Therefore, optimizing nanoparticle design is essential for creating efficient heat-generating systems to achieve therapeutic goals. The optimized m-PEG-coated MIONCs were studied for time-dependent cytotoxicity effects. The observed reduction in cell viability during hyperthermia treatment is likely due to the impact of heat on cellular processes, such as protein denaturation, increased oxidative stress, and DNA damage [23]. This study suggests that the synthesized m-PEG MIONCs could be a promising hyperthermic agent for treating solid tumors.

7.7 Conclusions

This study demonstrates the ability of CS-MIONPs to induce tumour cell death under AMF, along with their drawbacks when used with MCF7 cells. The combination of magneto-thermotherapy improves the potent efficiency of MHT in eliminating cancer cells. *In vitro* assessment of MCF-7 breast cancer cell lines in cell cultures demonstrated anticancer activity. In this study the MIONPs-mediated magneto-thermotherapy reduced cancer cell viability to about 71.48% for CS-MIONPs and 92.2% for mPEG-MIONCs, respectively. On the other hand, mPEG-MIONCs mediated magneto-thermotherapy under AC magnetic field shows the most promising therapeutic modality against breast cancer. The MHT under AC magnetic field studies ensure the potential application of mPEG-MIONCs nanoparticles in cancer theranostics.

7.8 References

1. M. Anik, M. Hossain, I. Hossain, A. Mahfuz, M. Rahman, I. Ahmed, *Nano Select*, 2(6) (2021) 1146-1186.
2. V. Cardoso, A. Francesko, C. Ribeiro, M. Bañobre-López, P. Martins, S. Lanceros-Mendez, *Adv. Healthc. Mater.*, 7(5) (2018) 1700845.
3. I. Ban, J. Stergar, U. Maver, *Nanotechnol. Rev.*, 7(2) (2018) 187-207.
4. D. Kim, E. Rozhkova, I. Ulasov, S. Bader, T. Rajh, M. Lesniak, V. Novosad, *Nat. Mater*, 9(2) (2010) 165-171.
5. M. Monopoli, C. Aberg, A. Salvati, K. Dawson, *Nano-enabled medical applications.*, (2020) 205-229.
6. R. Corato, A. Espinosa, L. Lartigue, M. Tharaud, S. Chat, T. Pellegrino, C. Ménager, F. Gazeau, C. Wilhelm, *Biomaterials*, 35 (24) (2014) 6400-6411.
7. J. Majeed, L. Pradhan, R. Ningthoujam, R. Vatsa, D. Bahadur, A. Tyagi, *Colloids and Surfaces B: Biointerfaces*, 122 (2014) 396-403.
8. N. Thorat, R. Bohara, V. Malgras, S. Tofail, T. Ahamad, S. Alshehri, K. Wu, Y. Yamauchi, *ACS Appl. Mater. Interfaces.*, 8 (23) (2016) 14656-14664.
9. S. García-Jimeno, J. Estelrich, *Colloids and Surfaces A: Physicochemical and Engineering Aspects*, 420 (2013) 74-81.
10. M. Mahmoudi, S. Saeedi-Eslami, M. Shokrgozar, K. Azadmanesh, M. Hassanlou, H. Kalhor, C. Burtea, B. Rothen-Rutishauser, S. Laurent, S. Sheibani, H. Vali, *Nanoscale*, 4(17) (2012) 5461-5468.
11. A. Singh, P. Laux, A. Luch, C. Sudrik, S. Wiehr, A. Wild, G. Santomauro, J. Bill, M. Sitti, *Toxicol. Mech. Methods.*, 29(5) (2019) 378-387.
12. Y. Wang, A. Santos, A. Evdokiou, D. Losic, *J. Mater. Chem. B*, 3 (36) (2015) 7153-7172.
13. D. Kundu, M. Khan, M. Gogoi, S. Patra, *Nanotoxicology and Nanoecotoxicology*, 1 (2021) 287-312.
14. L. Reddy, J. Arias, J. Nicolas, P. Couvreur, *Chem. Rev.*, 112 (11) (2012) 5818-5878.
15. T. Riss, A. Niles, R. Moravec, N. Karassina, J. Vidugiriene, *Cytotoxicity assay: in vitro methods to measure dead cells* (2019).
16. H. Sun, C. Jiang, L. Wu, X. Bai, S. Zhai, *Front. Bioeng. Biotechnol.*, 7 (2019) 414-436.
17. Çelik TA. *Introductory Chapter: Cytotoxicity*, 1st Edition, 1 (2018) 1-5.

18. M. Shen, H. Cai, X. Wang, X. Cao, K. Li, S. Wang, R. Guo, L. Zheng, G. Zhang, X. Shi, *Nanotechnology*, 23 (10) (2012) 105601-105611.
19. R. Bohara, N. Thorat, A. Chaurasia, S. Pawar, *RSC Adv.*, 5 (58) (2015) 47225-47234.
20. X. Han, Y. Jiang, S. Li, Y. Zhang, X. Ma, Z. Wu, Z. Wu, X. Qi, *Nanoscale*, 11 (1) (2019) 339–347.
21. T. Kumeria, S. Maher, Y. Wang, G. Kaur, L. Wang, M. Erkelens, P. Forward, M. Lambert, A. Evdokiou, D. Losic, *Biomacromolecules*, 17 (8) (2016) 2726–2736.
22. A. Salunkhe, V. Khot, S. Patil, S. Tofail, J. Bauer, N. Thorat, *ACS Appl. Bio Mater.*, 3 (4) (2020) 2305–2313.
23. R. Gupta, R. Tomar, S. Chakraverty, D. Sharma, *RSC Adv.*, 11 (28) (2021) 16942-16954.

CHAPTER-8

Summary and Conclusions



**Research work has been selected for the themed collection on
“World Cancer Day 2024: Showcasing Cancer Research across the
RSC.” Royal Society of Chemistry**

Summary and Conclusions

Cancer remains a significant global health challenge despite advances in research and treatment. Cancer remains a leading cause of death worldwide, with rising incidences attributed to factors such as aging populations and unhealthy lifestyles. While traditional cancer treatments like surgery, chemotherapy, and radiotherapy are widely used, these methods can also harm healthy tissues. The emergence of new therapies like magnetic hyperthermia (MHT) offers a non-invasive, targeted approach to cancer treatment by utilizing nanoparticles, particularly MNPs, to generate localized heat and destroy cancer cells. MNPs show great promise in various biomedical applications due to their size and magnetic properties, allowing for precision in cancer diagnosis and therapy. Research continues to explore the potential of nanotechnology for more effective, less harmful treatments, with advances like MHT contributing to improved cancer treatments. MNPs, particularly in therapies like MHT, present a promising future in cancer treatment due to their ability to selectively target and destroy cancerous cells while sparing healthy ones. Continued exploration of nanotechnology and MNPs holds potential for breakthroughs in both cancer treatment and diagnosis, offering hope for more effective and less damaging therapies.

Anisotropy, a material property that allows for direction-dependent behaviors, plays a significant role in enhancing the functionalities of MNPs. Introducing anisotropy into MNPs has proven to be an effective way of achieving specialized magnetic properties, making them crucial for various applications. The different types of anisotropies, such as magnetocrystalline, shape, and surface anisotropy influence the magnetic properties of MNPs and controlled synthesis of monodisperse MNPs. Various MNPs have been studied for MHT, including simple ferrites (MFe_2O_4 , with M being Fe, Mg, Mn, Co, Ni, Zn, Cu, etc.) and mixed ferrites ($M_xFe_{3-x}O_4$, where M is Mn, Co, Ni, Zn, and $0 < x \leq 1$). Their potential lies in the ability to engineer their magnetic configurations at the molecular level, enabling a wide range of magnetic properties through adjustments in chemical composition and M^{2+} doping levels. Among these ferrite NPs, $Mn_xFe_{3-x}O_4$ NPs have been proved to be a good candidate as they have higher magnetization than magnetite NPs. $MnFe_2O_4$ nanostructures show great promise as a theranostic platform for cancer treatment, offering unique advantages in both diagnosis and therapy.

Hence, in the present thesis, an attempt has been made to synthesize $\text{Mn}_x\text{Fe}_{1-x}\text{Fe}_2\text{O}_4$ with different molar ratios of Mn^{2+} , coated with the biocompatible polymer's chitosan and m-PEG. The study includes the formation of nanofluids and *in vitro* magnetic induction heating experiments on the MCF-7 breast cancer cell line for hyperthermia therapy applications.

The characterizations of the as-synthesized manganese iron oxide nanostructures and biocompatible polymer-coated nanostructures (chitosan and m-PEG coated manganese iron oxide) were performed using XRD, FT-IR spectroscopy, TGA, TEM with EDS, SAED, Zeta potential, and DLS techniques. Following this, the induction heating study and *in vitro* magnetic hyperthermia study of the synthesized nanoparticles were examined using an induction heating device. This chapter summarizes and concludes the extensive discussion covered in the seven chapters of this work.

Chapter I deals with the use of nanotechnology as new possibilities to meet various challenges in the field of medicine, including cancer treatment in the early 21st century. It also discusses cancer is a major global health issue, with traditional treatments often causing systemic toxicity and resistance. Nanotechnology offers a promising solution by improving drug delivery, reducing side effects, and increasing therapeutic efficacy through targeted nanoscale carriers. Traditional treatments like surgery, chemotherapy, and radiotherapy often harm healthy tissues. Innovative therapies such as MHT offer a non-invasive approach, using MNPs to generate localized heat that targets cancer cells. MNPs are promising in biomedical applications due to their size and magnetic properties, enhancing cancer diagnosis and treatment precision. Additionally, it summarizes ongoing research into nanotechnology seeks to develop more effective and less harmful treatments, with MHT showing promise for improved cancer care.

Despite advances, cancer still poses a significant health challenge, emphasizing the need for targeted strategies. MNPs, particularly in MHT, have great potential to selectively destroy cancer cells while sparing healthy ones. The chapter concludes by stating the objectives and scope of the thesis.

Chapter II includes the theoretical background and a general introduction to the use of MNPs in biomedical applications, highlighting their magnetothermal effect and excellent biocompatibility. The ferromagnetic properties of MNPs are influenced

by anisotropy, and reducing their size enhances control over their magnetic behavior. Chemical synthesis methods allow precise control over the size and shape of MNPs, further improving their applications in cancer therapy. It also covers various the specific role of MNPs in targeted drug delivery systems, magnetic resonance imaging, and their function as heating agents in MHT are elucidated. The origin, basic principles, and types of MHT are described, emphasizing heat generation through various loss mechanisms such as eddy current loss, hysteresis loss, and residual losses. Each loss mechanism is thoroughly explored. The efficiency of these mechanisms in generating heat is measured in terms of the SAR.

Consequently, extensive efforts have been dedicated to developing biocompatible, shape-selective nanostructures of manganese iron oxide that can generate a high SAR under the physiologically safe range of AC magnetic field and frequency. Properly tuned, these magnetic nanostructures are anticipated to exhibit a remarkably high SAR. The impact of different factors on SAR is discussed, aiding in the selection of mediators for MHT applications. Nanoparticles have unique physical properties, such as size, shape, high surface-to-volume ratio, and multifunctional features, including responsiveness to stimuli are discussed as potential candidates for MHT. The development of MNPs has revolutionized the potential for targeted cancer therapies, offering a way to selectively treat tumors while minimizing damage to healthy tissue.

Chapter III discusses the fundamental principles and mechanisms of syntheses and characterizations of obtained results. The standard methods for producing high-quality IONPs include co-precipitation and thermal decomposition are discussed in details. The co-precipitation method is found to be the simplest for synthesizing MNPs in aqueous solutions, allowing for controlled size by adjusting parameters like concentration, pH, and temperature. Thermal decomposition of organometallic precursors at high temperatures is a traditional approach for creating monodisperse nanocrystals. It also covers various characterization techniques used to characterize prepared materials, including X-ray Diffractometer (XRD), Transmission Electron Microscopy (TEM), Fourier Transform Infrared Spectroscopy (FTIR), Thermogravimetric Analysis-Differential Thermal Analysis (TG-DTA), and Vibrating Sample Magnetometer (VSM), were employed to assess the nanoparticles' structural, morphological, and elemental properties.

Along with characterization techniques, the other part of the chapter focuses on the methods used for biomedical applications such as for suspension/dispersion stability study: zeta potential, Dynamic Light Scattering (DLS), ultraviolet (UV)-Vis Spectroscopy, Fluorescence, Confocal Microscopy and Biocompatibility study: Cytotoxicity assays and induction heating system used for the hyperthermia study.

Chapter IV describes the synthesis of $\text{Mn}_x\text{Fe}_{1-x}\text{Fe}_2\text{O}_4$ ($x = 0, 0.25, 0.50, 0.75$ and 1) through chemical co-precipitation and thermal decomposition method. This chapter is also divided into two sections, i.e., sections 'A' and 'B'. Section A deals with synthesis of a series of single-phased $\text{Mn}_x\text{Fe}_{1-x}\text{Fe}_2\text{O}_4$ ($x = 0, 0.25, 0.50, 0.75$ and 1) NPs with good crystallinity and diameters ranging from about 5.78 to 9.94 nm by one-step capping agent-free co-precipitation route. The structural characterization shows that the Mn ferrite nanoparticles possess cubic spinel structure. Its lattice constant and particle size increase while their inversion grade decreases with the Mn substitution. It is found that the size effects dominate the influence of the cation distribution in controlling the magnetization values of our Mn ferrite nanoparticles. In addition to saturation magnetization and remanent magnetization, the coercivity of iron oxides and manganese oxides are altered significantly by manganese incorporation due to the interaction of A- and B-site ions, which directly affect the magnetic properties. The altered magnetic properties of $\text{Mn}_x\text{Fe}_{1-x}\text{Fe}_2\text{O}_4$ ($x = 0, 0.25, 0.50, 0.75$ and 1) NPs due to the distribution of cations at tetrahedral and octahedral site ultimately affect the self-heating temperature rise characteristics of MNPs. At a physiologically safe frequency and amplitude range, the sample $\text{Mn}_{0.75}\text{Fe}_{0.25}\text{Fe}_2\text{O}_4$ had a maximum SAR of 153.76 W/g.

In section B, the control over the size and morphology of $\text{Mn}_x\text{Fe}_{3-x}\text{O}_4$ nanoparticles was achieved by adjusting their properties through Mn^{2+} substitution in a thermal decomposition synthesis method. In this study, cubic-shaped $\text{Mn}_x\text{Fe}_{3-x}\text{O}_4$ nanoparticles with average sizes ranging from 13.48 nm to 24.27 nm were synthesized. Structural and morphological analyses using XRD and TEM confirmed their cubic morphology. The magnetic response of these nanoparticles varied with their size and shape, attributed to changes in magnetic anisotropy, arrangement, and dipolar interactions. Heating efficiency was assessed using calorimetric methods, with MnFe_2O_4 achieving a maximum specific absorption rate (SAR) of 223.47 Wg^{-1} at

physiologically safe frequencies and amplitudes, making these cube-shaped MNPs suitable candidates for hyperthermia treatment.

The magnetic anisotropy of MNPs affect the shape of the hysteresis loop and their heating performance. Nanocubes, which have lower anisotropy, exhibit more efficient heating compared to nanospheres. However, as their size increases, the anisotropy of nanocubes increases more quickly due to stronger dipolar interactions. As a result, nanocubes require higher magnetic fields to enhance their SAR, though they can achieve better heating efficiency than nanospheres under optimal conditions. Therefore, based on these results, $\text{Mn}_{0.75}\text{Fe}_{0.25}\text{Fe}_2\text{O}_4$ nanospheres and MnFe_2O_4 nanocubes has emerged as optimized sample for further studies.

For the use of MNPs in biomedical applications, the primary need is to transfer these nanoparticles to injectable fluid. **Chapter V** describes the polymer functionalization of optimized MIONPs and examines their induction heating performance. The FTIR spectrum of the coated MNPs revealed a significant amide absorption peak, confirming the successful chitosan (CS) coating on the MNPs. The $\text{Mn}_{0.75}\text{Fe}_{0.25}\text{Fe}_2\text{O}_4$ nanoparticles were modified with chitosan. The induction heating capability of these surface-modified nanoparticles demonstrated a notable SAR and temperature increase when subjected to an externally applied alternating magnetic field and at a magnetic field strength of 20 kA/m, the CS-coated nanoparticles achieved a maximum SAR of 181.48 W/g, compared to 153.46 W/g for the bare nanoparticles. Therefore, the MNPs synthesized using the alkaline precipitation method are suitable for MHT applications due to their smaller size, higher magnetization, and enhanced SAR values.

Chapter VI describes the synthesis of MIONCs through the thermal decomposition method and coating with m-PEG. The impact of coating on structural and morphological properties has been studied in both cases. XRD and FTIR analyses reveal the formation of a pure phase with and without iron oxide nanoparticles. Thermogravimetric and FTIR analyses confirm the successful attachment of m-PEG on the nanoparticle surface. However, m-PEG coated nanoparticles exhibit a more stable suspension and higher dispersion stability than iron oxide nanoparticles. The excellent magnetic properties with small coercivity and remanence are typical of soft ferrimagnetic characteristics. Thus, it is demonstrated that synthesized m-PEG

MIONCs, after coating with the biocompatible m-PEG polymer, have been explored for potential applications in biomedicine, especially in MHT. For the SAR values calculated in physiological media, for the uncoated particles, the SAR value increases from 13.96 to 237.44 Wg^{-1} with an increase in the field from 13.3 - 26.6 kA/m. For m-PEG MIONCs, it increases from 45.45 to 221.17 Wg^{-1} . As a result, the MNPs synthesized m-PEG MIONCs are well-suited for MHT applications because of their reduced size, increased magnetization, and improved SAR values.

Moreover, **chapter VII** demonstrates the *in vitro* cytotoxicity of chitosan and m-PEG-coated manganese iron oxide nanoparticles under an AC magnetic field. The ability of MIONPs and CS-MIONPs to induce tumor cell death under AMF is demonstrated, along with their drawbacks, when used with MCF7 cells. *In vitro* assessments of MCF-7 breast cancer cell lines demonstrated anticancer activity. In this study, the MIONPs-mediated magneto-thermotherapy reduced cancer cell viability to approximately 71.48% for CS-MIONPs and 92.2% for m-PEG MIONCs, respectively. The m-PEG MIONCs mediated magneto-thermotherapy under an AC magnetic field shows the most promising therapeutic modality against breast cancer due to superior anisotropy and heating efficiency. The studies on MHT under an AC magnetic field confirm the potential application of m-PEG MIONCs nanoparticles in cancer theranostics.

This study presents a nano-platform rationally designed using MIONPs coated with chitosan and m-PEG to be used as an effective nanomedicine in magnetically activated hyperthermia therapy.

CHAPTER-9

80-Recommendations

Recommendation

The MIONPs with high magnetic moments were synthesized and coated with chitosan, enhancing their induction heating properties, achieving a maximum SAR of 181.48 W/g compared to 153.46 W/g for uncoated particles. $\text{Mn}_{0.75}\text{Fe}_{0.25}\text{Fe}_2\text{O}_4$ nanoparticles, also chitosan-coated, showed improved hyperthermia performance. Cube-shaped $\text{Mn}_x\text{Fe}_{3-x}\text{O}_4$ MIONCs synthesized by thermal decomposition, coated with m-PEG, exhibited excellent heating efficiency, with SAR values increasing from 13.96 to 237.44 W/g for uncoated particles and from 45.45 to 221.17 W/g for m-PEG-coated ones under AC magnetic fields. *In vitro* assessment of MCF-7 breast cancer cells demonstrated anticancer activity of CS-MIONPs and m-PEG MIONCs under AMF. Magneto-thermotherapy reduced cancer cell viability by 71.48% for CS-MIONPs and 92.2% for m-PEG MIONCs, with the latter showing superior therapeutic potential due to better anisotropy and heating efficiency. These findings highlight m-PEG MIONCs as a promising candidate for magnetic hyperthermia therapy in cancer treatment. Based on the comprehensive analysis of this thesis, several recommendations arise to further the development and application of magnetic nanoparticle-based hyperthermia therapy.

- ❖ The further exploration of manganese-substituted iron oxide nanoparticles ($\text{Mn}_x\text{Fe}_{3-x}\text{O}_4$) is recommended, particularly focusing on optimizing Mn^{2+} substitution to enhance magnetic and structural properties for biomedical applications, especially hyperthermia treatment.
- ❖ Additionally, investigating the long-term stability, biocompatibility in terms of human cells, and toxicity profiles of these nanoparticles *in vitro* would be crucial to advancing their potential in clinical applications for cancer therapy.
- ❖ The *in vivo* studies should be conducted to validate the therapeutic efficacy of these nanoparticles in clinical applications, particularly for cancer theranostics.
- ❖ Exploring the *in vivo* performance and pharmaceutical properties of nanoparticles is crucial for progressing their clinical applications. Moreover, addressing existing limitations and improving their heating efficiency under an AC magnetic field will further enhance their potential in magnetic hyperthermia therapy for breast cancer.

Future findings

- ❖ Investigate the *in vivo* application of the produced $\text{Mn}_x\text{Fe}_{1-x}\text{Fe}_2\text{O}_4$ ($x = 0.0, 0.25, 0.50, 0.75$ and 1.0) nanoparticles to assess their biological performance. Histological examinations can be used to measure the impact of temperature rise on cell death.
- ❖ To develop nanoparticles with suitable magnetic properties to achieve maximum heating power under various field parameters, selecting the optimal conditions for enhanced heating efficiency. Additionally, further *in vivo* studies are required to demonstrate the therapeutic effects of these optimized nanoparticles.
- ❖ Investigating the potential of combining magnetic hyperthermia therapy (MHT) and photothermal thermal therapy (PTT) of surface functionalized MNPs to produce cumulative local heating can bring about high heating efficiency in hyperthermia therapy. The synergetic effect of MHT and PTT can be realized by magneto-optical hybrid nanostructures such as core/shell structures of magnetic NPs/semiconductor quantum dots and magnetic NPs/polypyrrole, magneto-plasmonic hybrids and composite structures of polymer-encapsulated magnetic and optical NPs.
- ❖ The further focus is on *in vitro* and *in vivo* studies of maximizing magnetothermal response at various magnetic field amplitudes by varying the doping concentration of M (Mn, Co, Zn, Cu, etc.) to optimize the magnetic anisotropy.

Publications and Conferences



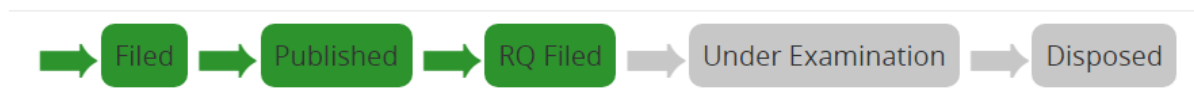
Office of the Controller General of Patents, Designs & Trade Marks
Department for Promotion of Industry and Internal Trade
Ministry of Commerce & Industry,
Government of India



Application Details	
APPLICATION NUMBER	202321038532
APPLICATION TYPE	ORDINARY APPLICATION
DATE OF FILING	05/06/2023
APPLICANT NAME	D.Y.PATIL EDUCATION SOCIETY (DEEMED TO BE UNIVERSITY),BAWADA ,KOLHAPUR
TITLE OF INVENTION	"AMINATED IRON OXIDE NANOPARTICLES FOR MAGNETIC HYPERTHERMIA APPLICATION".
FIELD OF INVENTION	CHEMICAL
E-MAIL (As Per Record)	
ADDITIONAL-EMAIL (As Per Record)	info@dypatilkolhapur.org
E-MAIL (UPDATED Online)	
PRIORITY DATE	
REQUEST FOR EXAMINATION DATE	25/09/2023
PUBLICATION DATE (U/S 11A)	15/09/2023

Application Status	
APPLICATION STATUS	Application referred u/s 12 for examination.

			View Documents
--	--	--	--------------------------------



n case of any discrepancy in status, kindly contact ipo-helpdesk@nic.in



Office of the Controller General of Patents, Designs & Trade Marks
Department for Promotion of Industry and Internal Trade
Ministry of Commerce & Industry,
Government of India



Application Details

APPLICATION NUMBER	202321073714
APPLICATION TYPE	ORDINARY APPLICATION
DATE OF FILING	30/10/2023
APPLICANT NAME	D. Y. PATIL EDUCATION SOCIETY(DEEMED TO BE UNIVERSITY), KASABA BAWADA, KOLHAPUR
TITLE OF INVENTION	" A METHOD FOR THE PREPARATION OF ASCORBIC ACID FUNCTIONALIZED COBALT IRON OXIDE NANOPARTICLES AND APPLICATION THEREOF
FIELD OF INVENTION	CHEMICAL
E-MAIL (As Per Record)	
ADDITIONAL-EMAIL (As Per Record)	info@dypatilkolhapur.org
E-MAIL (UPDATED Online)	
PRIORITY DATE	
REQUEST FOR EXAMINATION DATE	05/07/2024
PUBLICATION DATE (U/S 11A)	05/01/2024

Application Status

APPLICATION STATUS	Application Awaiting Examination
--------------------	----------------------------------

[View Documents](#)

In case of any discrepancy in status, kindly contact ipo-helpdesk@nic.in



Cite this: DOI: 10.1039/d3nr02816j

Functionalized manganese iron oxide nanoparticles: a dual potential magneto-chemotherapeutic cargo in a 3D breast cancer model†

Satish S. Phalake, ^a Sandeep B. Somvanshi, ^{b,c} Syed A. M. Tofail,^d
Nanasaheb D. Thorat ^{*d,e} and Vishwajeet M. Khot ^{*a}

Localized heat generation from manganese iron oxide nanoparticles (MIONPs) conjugated with chemotherapeutics under the exposure of an alternating magnetic field (magneto-chemotherapy) can revolutionize targeted breast cancer therapy. On the other hand, the lack of precise control of local temperature and adequate MIONP distribution in laboratory settings using the conventional two-dimensional (2D) cellular models has limited its further translation in tumor sites. Our current study explored advanced 3D *in vitro* tumor models as a promising alternative to replicate the complete range of tumor characteristics. Specifically, we have focused on investigating the effectiveness of MIONP-based magneto-chemotherapy (MCT) as an anticancer treatment in a 3D breast cancer model. To achieve this, chitosan-coated MIONPs (CS–MIONPs) are synthesized and functionalized with an anticancer drug (doxorubicin) and a tumor-targeting aptamer (AS1411). CS–MIONPs with a crystallite size of 16.88 nm and a specific absorption rate (SAR) of 181.48 W g^{−1} are reported. *In vitro* assessment of MCF-7 breast cancer cell lines in 2D and 3D cell cultures demonstrated anticancer activity. In the 2D and 3D cancer models, the MIONP-mediated MCT reduced cancer cell viability to about 71.48% and 92.2%, respectively. On the other hand, MIONP-mediated MCT under an AC magnetic field diminished spheroids' viability to 83.76 ± 2%, being the most promising therapeutic modality against breast cancer.

Received 13th June 2023,
Accepted 5th September 2023

DOI: 10.1039/d3nr02816j

rsc.li/nanoscale

1. Introduction

The future of magnetic nanoparticles' (MNPs) use in applications such as heat-mediated drug delivery, catalysis, self-heating materials, magnetic fluid hyperthermia (MFH) therapies,¹ MRI-guided drug delivery,² and heat-triggered remote

biological process control may depend on the enhancement of the heating effectiveness of MNPs under alternating magnetic fields (AMFs).^{3,4} It is projected that 297 790 women and 2800 men will be diagnosed with invasive breast cancer in the USA in 2023, and another 55 720 women will be found to have ductal carcinoma *in situ* (DCIS). In the year 2023, approximately 43 700 lives will be lost due to breast cancer, with 43 170 of those deaths affecting women and 530 impacting men.⁵ Targeted heating of cancerous tumors to temperatures between 42.0 to 44.0 °C, known as hyperthermia, is an alternative strategy for treating cancer. This method either causes direct cell death or makes the tumor more receptive to chemotherapy or radiation therapy. To ensure the safety of MFH, we optimized the parameters of the AMF by selecting a low frequency (*f*) and an appropriate strength of the AMF. This optimization aimed to minimize exposure times while maintaining bio-safety. Magnetic hyperthermia therapy (MHT) utilizes MNPs to generate heat after exposure to an AMF. This heat is then used to selectively treat specific tumor tissues while minimizing damage to surrounding normal tissues, as it avoids significant overall temperature elevation.^{6,7} Due to their superior magnetic properties, excellent biocompatibility, and

^aDepartment of Medical Physics, Centre for Interdisciplinary Research, D. Y. Patil Education Society (Deemed to be University), Kolhapur, 416 006 Maharashtra, India. E-mail: wish.khot@gmail.com

^bSchool of Materials Engineering, Purdue University, West Lafayette, USA

^cDepartment of Physics, Dr. B. A. M. University, Aurangabad-431004, Maharashtra, India

^dDepartment of Physics and Bernal Institute, Limerick Digital Cancer Research Centre (LDCRC), University of Limerick, Castletroy, Co. Limerick, Limerick, V94 T9PX, Ireland. E-mail: nanasaheb.d.thorat@ul.ie

^eNuffield Department of Women's and Reproductive Health, John Radcliffe Hospital, Medical Sciences Division, University of Oxford, Oxford OX3 9DU, UK. E-mail: thoratnd@gmail.com

†Electronic supplementary information (ESI) available: Additional details of the energy dispersive X-ray analysis (EDX) and the details of induction heating, i.e. slope values calculated from the temperature *versus* time plot and SAR values of the different concentrations of nanoparticles under an AMF of appropriate field strength. See DOI: <https://doi.org/10.1039/d3nr02816j>



Application of $\text{Mn}_x\text{Fe}_{1-x}\text{Fe}_2\text{O}_4$ ($x = 0-1$) Nanoparticles in Magnetic Fluid Hyperthermia: Correlation with Cation Distribution and Magnetostructural Properties

Satish S. Phalake, Manohar S. Lad, Ketaki V. Kadam, Syed A. M. Tofail, Nanasaheb D. Thorat,* and Vishwajeet M. Khot*



Cite This: *ACS Omega* 2022, 7, 44187–44198



Read Online

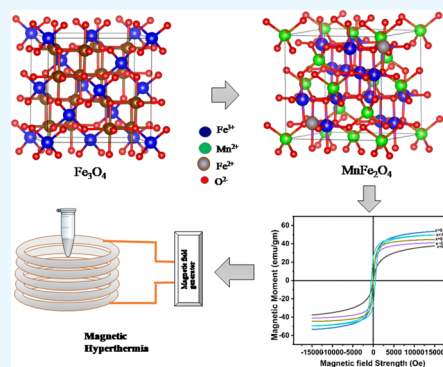
ACCESS |

Metrics & More

Article Recommendations

Supporting Information

ABSTRACT: Optimization of manganese-substituted iron oxide nanoferrites having the composition $\text{Mn}_x\text{Fe}_{1-x}\text{Fe}_2\text{O}_4$ ($x = 0-1$) has been achieved by the chemical coprecipitation method. The crystallite size and phase purity were analyzed from X-ray diffraction. With increases in Mn^{2+} concentration, the crystallite size varies from 5.78 to 9.94 nm. Transmission electron microscopy (TEM) analysis depicted particle sizes ranging from 10 ± 0.2 to 13 ± 0.2 nm with increasing Mn^{2+} substitution. The magnetization (M_s) value varies significantly with increasing Mn^{2+} substitution. The variation in the magnetic properties may be attributed to the substitution of Fe^{2+} ions by Mn^{2+} ions inducing a change in the superexchange interaction between the A and B sublattices. The self-heating characteristics of $\text{Mn}_x\text{Fe}_{1-x}\text{Fe}_2\text{O}_4$ ($x = 0-1$) nanoparticles (NPs) in an AC magnetic field are evaluated by specific absorption rate (SAR) and intrinsic loss power, both of which are presented with varying NP composition, NP concentration, and field amplitudes. $\text{Mn}_{0.75}\text{Fe}_{0.25}\text{Fe}_2\text{O}_4$ exhibited superior induction heating properties in terms of a SAR of 153.76 W/g. This superior value of SAR with an optimized Mn^{2+} content is presented in correlation with the cation distribution of Mn^{2+} in the A or B position in the Fe_3O_4 structure and enhancement in magnetic saturation. These optimized $\text{Mn}_{0.75}\text{Fe}_{0.25}\text{Fe}_2\text{O}_4$ NPs can be used as a promising candidate for hyperthermia applications.



INTRODUCTION

Due to their unique physical features, known biocompatibility, ease of production, and highly adjustable nature at the nanoscale, maghemite ($\gamma\text{-Fe}_2\text{O}_3$) and magnetite (Fe_3O_4) nanoparticles (NPs) are especially well suited for various biomedical applications.^{1,2} Magnetization in Fe_3O_4 can be tuned by replacing iron ions with transition metal cations, especially manganese ions, which have higher magnetic moments.³ It is explored for many applications which include catalysts, humidity sensors, biomedicine, MRI, microwave technologies, drug delivery, and magnetic fluid hyperthermia.² The properties of manganese ferrites such as their high electrical resistance, high Curie temperature (bulk MnFe_2O_4 is T_c 577 K), low coercivity value, and a low eddy current loss allow them to serve a wide range of applications.^{4,5} The integration of secondary cations Mn^{2+} in Fe_3O_4 and synthesis reproducibility have been studied.⁶ In the past decade, the general term MFe_2O_4 ($M = \text{Co}, \text{Mg}, \text{Ni}$, etc.) of spinel ferrites has been widely used for a variety of technological and biomedical applications.^{7,8} The magnetic and electrical properties of these compounds strongly depend on the synthesis process, chemical content, annealing temperature, and cation distribution. The cation distribution in spinel ferrite materials among two interstitial sites of the structure is one of the most challenging aspects of studying these materials due to its effect on the properties of ferrites.⁹ Shahane *et al.* reported the

MnFe_2O_4 magnetic NPs (MNPs) showing the antiparallel spin moments among Fe^{3+} , Mn^{2+} , and Fe^{2+} ions at A-sites and inverse spinel structures.¹⁰ The polycrystalline spinel ferrite $\text{Co}_x\text{Ni}_{1-x}\text{Fe}_2\text{O}_4$ ($x = 0-1$) was obtained by the sol-gel autocombustion method with the Co substitution. In Co^{2+} -substituted nickel ferrite, the density is higher than Ni^{2+} ions, owing to the higher magnetocrystalline anisotropy and the smaller particle size. The saturation magnetization (M_s) was increased to $x = 0.8$, at which point there was a small reduction in M_s for CoFe_2O_4 .¹¹ There have been several proposals for substituted magnetite NPs, $\text{M}_x\text{Fe}_{3-x}\text{O}_4$ ($M = \text{Ni}, \text{Zn}, \text{Mn}$, and Co , $0 < x \leq 1$) for various bio-applications since their magnetic properties can be easily controlled by replacing divalent or trivalent metal ions without modifying the crystal structure by either replacing them completely or partially.

$\text{Mn}_x\text{Fe}_{3-x}\text{O}_4$ NPs among these ferrites show stronger magnetization (M_s), low coercivity (H_c), and low inherent

Received: September 1, 2022

Accepted: November 8, 2022

Published: November 22, 2022





Low temperature glycine nitrate combustion synthesis of nanostructured zinc ferrites for enhanced visible light-driven methylene blue degradation

K. V. Kadam¹ · S. S. Phalake¹ · M. S. Lad¹ · V. G. Parale² · J. L. Gunjekar¹ · V. M. Khot¹

Received: 17 December 2023 / Accepted: 3 March 2024 / Published online: 18 March 2024
© Qatar University and Springer Nature Switzerland AG 2024

Abstract

In this study, we present the efficient degradation of methylene blue (MB) under visible light using nanostructured zinc ferrite (ZnFe_2O_4) photocatalysts. The ratio of glycine and nitrate as a fuel and oxidant, respectively employed for the preparation of ZnFe_2O_4 nanoparticles by using the combustion method. The ratio variation of glycine and nitrate shows an effect on crystal structure, texture, and pores formation which is supported for photodegradation. The X-ray diffraction and scanning electron microscopy study exhibited cubic spinel structure and highly porous morphology respectively. X-ray photoelectron spectroscopy, and ultra-violet diffuse reflectance spectroscopy techniques utilized for the confirmation of ZnFe_2O_4 material and band gap energy measurement. Furthermore, the adiabatic flame temperature (T_{ad}) and the properties of the resulting product were studied in various combinations of nitrates and glycine. Thermodynamic analyses reveal that both the number of gases produced, and adiabatic flame temperature increase with a rising fuel-to-oxidant ratio. The synthesized photocatalysts are evaluated for their efficacy in the MB dye degradation under visible light ($\lambda \geq 400$ nm). The ZnFe_2O_4 nanoparticles (GN⁻¹ ratio of 0.48 (Z1)) showed efficient photocatalytic activity up to 90.65% degradation of MB dye in 5 h (h). These results played a crucial role due to the formation of hydroxyl radicals ($\bullet\text{OH}$) reactive species, leading to the efficient degradation of MB under visible light irradiation. ZnFe_2O_4 (Z1) nanoparticles demonstrated excellent recyclability and stability study. The highly porous morphology as well as the reduced band gap enabled the photodegradation of MB dye. Also, this work highlights the influence of the fuel-to-oxidizer ratio for MB dye degradation under visible light.

Keywords Combustion method · Nanoparticles · Photocatalysis · Porous morphology · Zinc-iron-oxide

1 Introduction

Water pollution is a critical environmental issue primarily caused by the release of harmful substances, including organic dyes and heavy metals, in industrial wastewater [1]. These pollutants pose a serious threat to humans, animals, plants, and aquatic ecosystems [2]. Various types of dyes, such as synthetic, azo, acidic, basic, reactive, diazo, and anthraquinone, further contribute to water pollution

[3]. Cationic dyes like methylene blue (MB) are challenging to remove from wastewater due to their harmful effects, and they are commonly used in industries for applications like coloring paper, clothing dye, photosensitizers, and redox indicators [4–6]. Several wastewater treatment methods exist, including physical–chemical processes like coagulation, irradiation, ozonation, chemical oxidation, ion exchange, adsorption, and reverse osmosis [7]. Photocatalysis, particularly visible light-driven photocatalysis, has emerged as a promising technology for wastewater cleanup, effectively breaking down dyes by absorbing a broad spectrum of light and promoting the formation of hydroxyl groups [8]. Nanoparticles responding to visible light, such as zinc ferrite (ZnFe_2O_4), have shown effectiveness in photocatalytic degradation of MB and other dyes, making them promising for wastewater treatment [9–13]. Their choice is driven by affordability, non-toxicity, and magnetic properties, especially under visible light exposure [14, 15].

✉ V. M. Khot
wish.khot@gmail.com

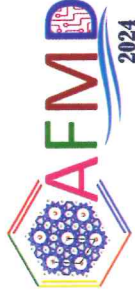
¹ Centre for Interdisciplinary Research, D. Y. Patil Education Society (Deemed to Be University), Kolhapur 416 006, India

² Department of Materials Science and Engineering, Yonsei University, 50 Yonsei-Ro, Seodaemun-Gu, Seoul 03722, Korea



SRM
INSTITUTE OF SCIENCE & TECHNOLOGY
(Deemed to be University u/s 3 of UGC Act, 1956)

*International Conference on
Advanced Functional Materials and Devices
(AFMD-2024)*



Certificate of Participation



This is to certify that

Mr. Satish Sambhaji Phalake


Dr. Y. Patil Education Society University

has presented the work entitled

Synthesis of m-PEG functionalized manganese iron oxide nanoparticles by using thermal decomposition method in magnetically activated hyperthermia therapy

in the International Conference on Advanced Functional Materials and Devices (AFMD-2024) organized by Nanotechnology Research Centre (NRC), SRM Institute of Science and Technology, Kattankulathur, Tamil Nadu, India, held during February 26-29, 2024.


Dean Sciences
SRMIST


Convener
AFMD - 2024, SRMIST


Co-Convenor
AFMD - 2024, SRMIST



D. Y. PATIL EDUCATION SOCIETY
(Deemed to be University), KOLHAPUR
NAAC 'A' Grade in 3rd Cycle

Certificate

This is to certify that **Mr. /Ms. Phalake Satish Sambhaji** of Centre for Interdisciplinary Research, DYPES, Kolhapur has delivered invited talk/ chaired the session/ presented oral/ presented poster/ participated in the **International Conference on Nanotechnology Addressing the Convergence of Materials Science, Biotechnology and Medical Science (IC-NACMBM-2024)** held at the Centre for Interdisciplinary Research, D. Y. Patil Education Society (Deemed to be University), Kolhapur, Maharashtra, India during 12th to 14th February 2024. His/ Her contribution to the conference is highly appreciated.

Dr. Jayavant L. Gunjekar

Convener

Prof. Meghnad G. Joshi

Convener

Prof. Chandrakant D. Lokhande

Chairman



"Education through self-help is our motto." - Karmaveer

Rayat Shikshan Sanstha's

RAJARSHI CHHATRAPATI SHAHU COLLEGE, KOLHAPUR

(Reaccredited 3rd Cycle by NAAC at 'A' Grade with CGPA 3.07)



DEPARTMENT OF PHYSICS and IQAC

Organizes Under G20 University Connect Program

One Day International Conference on

"Recent Trends in Fabrication of Nanomaterials and Their Applications (ICRTFNA-2023) "

Certificate

This is to certify that, Dr. /Prof./Mr./Ms./Mrs. Satish Phalake of

D. Y. Patil

has participated /worked as Resource

Person/Chairperson/Organizing committee member in One Day International Conference on 'Recent Trends in Fabrication of Nanomaterials and Their Applications (ICRTFNA-2023) ' Organized by Department of Physics

and IQAC held on March 15, 2023. He/She has presented paper entitled _____

Dr. A. R. Patil

Coordinator

Dr. V. V. Killedar

Organizing secretary

Dr. L. D. Kadam

Principal

TRAINING PROGRAM

on

Advanced Instrumentation Techniques for Material Characterization & Analysis

12th July-19th July 2022


Under


"STUTI" – Synergistic Training program Utilizing the Scientific and Technological Infrastructure



Certificate of Participation

Awarded to Satish Phalake, Research Scholar at DY Patil Education Society, Kolhapur, Maharashtra for participating in the 7 days Training Program organized by the Central Instrumentation Laboratory (CIL) & Department of Physics, DCRUST, Murthal in association with Sophisticated Analytical Instrumentation Facility (SAIF), Panjab University, Chandigarh.


Prof. Ashok K Sharma
Director, CIL
STUTI Training coordinator
DCRUST, Murthal, Haryana


Prof. G. R. Chaudhary
Director, SAIF/CIL
STUTI Program Coordinator (PMU)
Panjab University, Chandigarh



**“A++” Accredited by NAAC (2021)
with CGPA 3.52**



**SCHEME FOR TRANS-DISCIPLINARY RESEARCH
FOR INDIA'S DEVELOPING ECONOMY**

**Five days Hands on Training Workshop on
“Basic Techniques in Nanoscience and Nanotechnology”**

For UG, PG and Research students



This is to certify that Prof./Dr./Mr./Mrs./Ms. Phalake Satish Sambhaji
From D.Y. Patil Education Society, Kolhapur has participated/delivered a talk/
conducted practical/worked as committee member in five days **Hands on Training Workshop**
on **"Basic Techniques in Nanoscience and Nanotechnology"** organized by School of Nano
science and Technology, Shivaji University, Kolhapur **Under UGC-STRIDE (Component I)** during
21st to 25th March 2022.

Wimmer

Director

Prof. (Dr.) K. K. Sharma
SNST, SUK



Co-ordinator

Dr. P. J. Patil

Assistant Professor, SNST, SUK



D. Y. PATIL EDUCATION SOCIETY,
(Institution Deemed to be University) Kolhapur
Accredited NAAC with 'A' Grade

Certificate

DNYANSHODH -2022

(Search For Knowledge)

On the occasion of National Science Day

This is to certify that

Mr/Ms. Satish Sambhaji Phalake

has got IIIrd prize in Poster presentation on topic

Magnetic Induction Heating Application

on 28th February 2022 , in Dnyanshodh -2022 organized by Centre for Interdisciplinary Research (CIR)

D. Y. Patil Education Society (Deemed to be University), Kolhapur-416006

Chairman

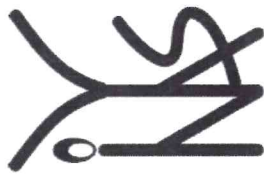
Prof. (Dr.) C. D. Lokhande

Dean,
Centre for Interdisciplinary Research

Convener

Dr. Arpita Pandey - Tiwari

Associate Professor,
Department of Medical Biotechnology.



INYAS SCIENCE CAMP-2022

CERTIFICATE



DYP
SALOKHE NAGAR

This is to certify that

Mr./Mrs.

Satish Phalke

has served as a volunteer in the “INYAS Science Camp -2022” organized by
D. Y. Patil Education Society (Institution Deemed to be University), Kolhapur,
Indian National Young Academy of Science (INYAS),
Indian National Science Academy (INSA) and D. Y. Patil Knowledge Campus, Salokhenagar,
Kolhapur

at D. Y. Patil Vidyaniketan School, Salokhenagar, Kolhapur during 16 - 17 December 2022.

Gunjekar

Dr. J. L. Gunjekar
DYPES, INYAS Member

Dr. V. V. V. Parker

Dr. V. V. V. Parker
BARC, INYAS Member

Prof. C. D. Lokhande

Prof. C. D. Lokhande
Dean CIR, DYPES



UNIVERSITY OF
OXFORD

INTERNATIONAL SYMPOSIUM on

Nanotechnology for Healthcare:
Clinical and Industrial Perspectives

Nuffield Department of Women's
& Reproductive Health,
Medical Sciences Division

UNIVERSITY OF OXFORD

Certificate of Attendance

This certificate is presented to

Satish Sambhaji Phalake

**D Y patil Education Society (Institution
Deemed to be University), Kolhapur**

For attending

the 2022 International Symposium

on Nanotechnology for Healthcare: Clinical and Industrial Perspectives
organised by Nuffield Department of Women's & Reproductive Health,
Medical Sciences Division, UNIVERSITY OF OXFORD (UK)

10th JUNE 2022

Organisers :

Dr. Nanasaheb Thorat M.Sc.Ph.D., MRSC

Nuffield Department of Women's & Reproductive Health
Medical Sciences Division, John Radcliffe Hospital
UNIVERSITY OF OXFORD (UK)

Prof. Helen Townley

Nuffield Department of Women's & Reproductive Health
Medical Sciences Division, John Radcliffe Hospital
UNIVERSITY OF OXFORD (UK)